BERGISCHE
UNIVERSITÄT
WUPPERTAL

Fakultät für Mathematik und Naturwissenschaften
Fachgruppe Physik

Search for a heavy Scalar Boson in the 2 Higgs Doublet Model with the ATLAS Detector

Dissertation zur Erlangung des Grades
Doktor der Naturwissenschaften (Dr. rer. nat.)

vorgelegt der
Bergischen Universität Wuppertal
Fakultät für Mathematik und Naturwissenschaften

von Gunar Ernis

Referent: Prof. Dr. Wolfgang Wagner (Universität Wuppertal)
Koreferentin: Dr. Corinne Mills (University of Edinburgh)

Eingereicht am 2. Oktober 2015
Tag der mündlichen Prüfung: 22. Januar 2016

Die Dissertation kann wie folgt zitiert werden:

urn:nbn:de:hbz:468-20160128-101729-9
[http://nbn-resolving.de/urn/resolver.pl?urn=urn%3Anbn%3Ade%3Ahbz%3A468-20160128-101729-9]

– There's something very important I forgot to tell you.

– What?

– Don't cross the streams.

– Why?

– It would be bad.

– I'm fuzzy on the whole good/bad thing.
What do you mean, "bad"?

– Try to imagine all life as you know it stopping instantaneously and every molecule in your body exploding at the speed of light.

– Total protonic reversal.

– Right. That's bad. Okay. All right.
Important safety tip. Thanks, Egon.

(*Ghostbusters*. Dir. Ivan Reitman. Columbia Pictures, 1984)

Contents

List of Figures

List of Tables

1 | Introduction

The principal task of physical theories is to explain observations. Any given new theory must be able to explain the things we already know, on the other hand, predictions are essential for the investigation of any theory. Theories that gained our trust must be put to test – using their predictions – in order to preserve it.

In the physical regime of subatomic scales, the most successful theory is the Standard Model of particle physics (SM) [1, 2], which combines three major themes of modern physics: Field theory [3, 4], quantum mechanics [5, 6] and the relativistic principle [7]. Each of these concepts passed a long evolution and uncountable tests in which they could not be falsified and therefore are considered as cornerstones in our understanding of (particle) physics. The SM summarises the description of the known elementary particles and their interactions in terms of relativistic quantum fields and is considered as one of the best-tested physical theories [8]. Several predictions, starting with the existence of W and Z bosons [9–11], the anticipation of the top and bottom quarks [12] to the presence of a Higgs boson [13–15], have all been confirmed [16–21] by experiments hosted at the Conseil Européen pour la Recherche Nucléaire (CERN), Fermilab and other laboratories around the globe.

However, while being successful as a theory for fundamental interactions, the SM lacks explanations for the strong charge/parity (CP) problem [22], which is the question why the strong interaction does not break CP symmetry while electroweak interaction does. Further the observed baryon asymmetry in our universe [23] and dark matter [24] can also not be explained by the SM. In order to address these issues, the SM is tested against a set of models called 2-Higgs-Doublet Models (2HDMs) [25], which are constructed as an extension of the SM, and allow the explanation of the baryon asymmetry in the universe [26] and the strong CP problem [27]. While the Higgs sector of the SM is composed of a single doublet of complex scalar fields, the 2HDMs introduce two of such doublets which give rise to five Higgs bosons: two CP even scalar fields h and H with $m_h \leqslant m_H$, a CP odd pseudo scalar field A and two charged fields $H^{\pm}$.

The discovery of a light Higgs-like boson [20, 21] with a mass of approximately 125 GeV in 2012 by the A Toroidal LHC Apparatus (ATLAS) and Compact Muon Solenoid (CMS) collaborations utilising proton-proton collisions produced at the Large Hadron Collider (LHC) hosted at CERN lead to much attention of 2HDMs in current phenomenological research [28–35]. A dedicated experimental investigation is therefore attractive, since the rate of the light Higgs-like boson provides constraints on 2HDMs [36]. The first direct search by the ATLAS collaboration at the LHC has already been conducted [37] and lead to large parameter space being ruled out. Further searches for generic 2HDMs have been performed by the Collider Detector at Fermilab (CDF) collaboration at the Tevatron [38, 39] and a combined analysis, regarding the rates of the light Higgs-like boson from both ATLAS and CMS collaborations, has been performed [40]. But none of the investigated scenarios can be ruled out with the current data set. Furthermore an indirect search has been performed by the ATLAS collaboration [41], which reduces the possible parameter space for the 2HDMs.

The analysis presented in this thesis investigates the possibility that the boson observed by the ATLAS and CMS experiments at a mass of approximately 125 GeV originates from a Higgs boson that is part of a 2HDM, where the CP symmetry is – at most – softly broken. In particular, it is assumed that the observed particle is the light CP-even Higgs boson h of a 2HDM and the analysis searches for additional signal contributions from the heavy CP-even Higgs boson H of the model. Both Higgs bosons are reconstructed in the $h/H \to WW^{(*)} \to e^-\bar{\nu}\mu^+\nu/e^+\nu\mu^-\bar{\nu}$ decay channel, where gluon-gluon fusion (ggF), vector-boson fusion (VBF) and Higgs-strahlung or associated production with a vector boson (VH) are considered as production modes of the Higgs bosons. In order to obtain sensitivity for both production mechanisms, different final states are considered: In the first channel two charged leptons and large missing transverse momentum $E_{\mathrm{T}}^{\mathrm{miss}}$ are required (0-jet channel), in the second (which is most sensitive to the VBF process) two jets with high transverse momentum are required (2-jet channel) in addition. The final state with an additional single high transverse momentum jet (1-jet channel) is also taken into account and is considered as overlap of the former production modes: The ggF process with an additional jet and the VBF process with a missing jet.

The analysis is based on data which correspond to 20.3 fb^{-1} of integrated luminosity, recorded with the ATLAS detector with a centre-of-mass energy of 8 TeV in 2012. The mass interval of 135 GeV $\leqslant m_H \leqslant$ 1000 GeV for a heavy Higgs boson H is investigated in hypothesis tests utilising large numbers of pseudo experiments. In case of no evidence for a second, heavier Higgs boson excluded parameter regions are computed in terms of the heavy Higgs boson mass m_H and the coupling to the vector bosons.

2 | Theoretical Background

In the following sections an overview of the theoretical framework of gauge theories which describes the SM is given. An extra section is devoted to the Brout-Englert-Higgs mechanism (BEH mechanism), where the effect of spontaneous symmetry breaking, and how this gives rise to a Higgs boson, is explained. The final section of this chapter deals with one of the simplest extensions of the SM, the 2HDMs, which lead to an enriched Higgs sector.

2.1 The Standard Model of Particle Physics

The SM [1, 2] describes the known elementary particles and their interactions which can be grouped in two ways: according to their interactions and according to their mass. All fermions (spin-$\frac{1}{2}$ particles) are able to take part in weak interactions and if they have an additional electrical charge, they can interact electromagnetically. Fermions that only participate in electroweak interactions are called leptons and those that also interact via the strong force are denoted quarks. Quarks, however, do not appear isolated in nature and form hadrons due to the so-called confinement which is a property of the strong interaction. The family of hadrons includes baryons like the proton or the neutron, which consist of three quarks and mesons like the pion, which are composed of a quark-antiquark pair. Most of these hadrons are short-lived particles which decay quickly. Therefore, observable objects involving hadrons are seen as so-called jets in the detector, with a jet being a collimated bundle of decay products originating from a single quark or gluon.

The particles can further be categorised into generations, where each consists of a quark pair and a lepton pair. These generations are identical copies of each other and differ by the masses of the particles and their flavour quantum numbers. The particles of the first and lightest generation are the up (u) and the down quark (d) with an electrical charge of 2/3[1] and $-1/3$ respectively, the electron (e) with an electrical charge of -1 and the uncharged and massless electron neutrino (ν_e). These are the only stable particles from which nuclei and atoms are built. Quarks with the charge of 2/3 are denoted up-type quarks while those with the charge of $-1/3$ are called down-type quarks. The up-type quarks of the second and third generation are called charm (c) and top (t), while the down-type quarks are named strange (s) and bottom (or beauty) (b). The leptons of the second and third generation are the muon (μ) and the tau lepton (τ) with their corresponding massless neutrinos ν_μ and ν_τ. Each particle has a partner, the so-called antiparticle. Particles and antiparticles differ by their charge (and charge-like quantum numbers) and their magentic momentum while mass, lifetime and spin remain the same. They are either denoted by a different charge sign (i.e. the antiparticle of the electron e^- is denoted as e^+) or by a "bar" symbol (i.e. the antiparticle of the up quark u is denoted as $\bar{u}$).

[1] All charges are given in terms of the elementary charge.

In addition to the fermions, which contain the building blocks of matter, the SM consists of four kinds of gauge bosons (spin-1 particles), which mediate the different interactions between particles. The gauge bosons of the strong interaction are called gluons (g), the ones of the weak interaction are the W and the Z bosons and the gauge boson of the electromagnetic interaction is the photon (γ). Gauge bosons couple only to a specific charge which is different for each interaction: In case of the strong interaction the charge is called colour charge and it can take the values (anti-)red, (anti-)green and (anti-) blue. In case of the weak interaction the corresponding charge is the third component of the weak isospin T_3 and all fermions have either $T_3 = +\frac{1}{2}$ or $T_3 = -\frac{1}{2}$. Finally, the electromagnetic interaction responds to the well known electric charge. Moreover the SM contains a scalar particle, the Higgs boson [42] which generates the mass of the gauge bosons and fermions. An overview of the particle properties is given in Figure 2.1.

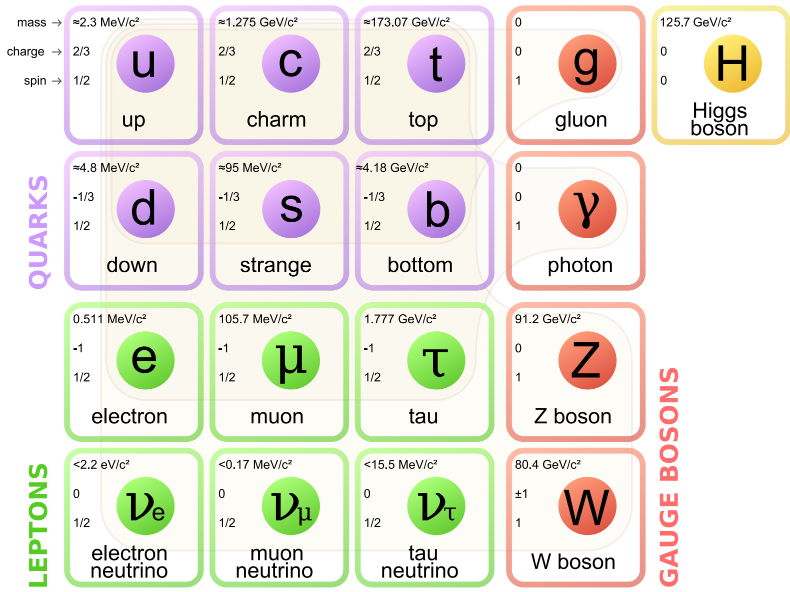

Figure 2.1: Properties of the elementary particles of the SM [43]. The values of the particle properties are taken from [2].

As mentioned above, quarks appear only in bound states. The theoretical framework of particle physics, which is described in the following sections, relies on the assumption of asymptotically free particles. This means, that the strength of the strong interaction becomes weaker at high energies (and small distances) and therefore particles can be considered as free at some high energy (small distance) scale. This behaviour is parametrised by the factorisation scale μ^2, which describes the separation of long-ranged and short-ranged interactions of the proton. For colliders like the LHC, this is true for the collisions themselves but not for the description of the colliding protons, consisting of three valence quarks (two up quarks and one down quark) bound by gluons. In addition, the splitting of gluons into quark-antiquark pairs (so-called sea quarks) gives rise to plenty of partons inhabiting the proton which share its momentum. The parton distribution functions (PDFs) $f_i(x_i, \mu^2)$ describe the probability to find a parton of the flavour i carrying the momentum fraction x_i, defined by $x_i \cdot$

$p^{\mu}_{\mathrm{proton}} = p^{\mu}_{i}$ inside the proton and have to be taken into account when calculating observables. In Figure 2.2 the CT10 [44, 45] PDFs are shown for the factorisation scale $\mu^2 = 125^2\ \mathrm{GeV}^2$.

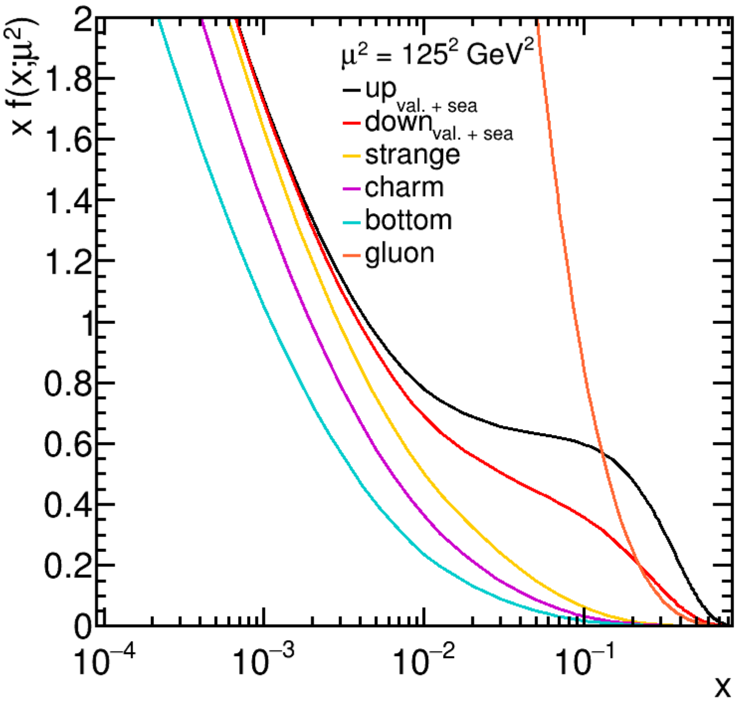

Figure 2.2: CT10 [44, 45] Parton distribution functions (PDFs) of the proton as a function of the parton momentum fraction x. The PDFs are shown for the factorisation scale $\mu^2 = 125^2\ \mathrm{GeV}^2$. Valence-quark and sea-quark densities of the up and down quarks are summed together respectively. The plot uses data from Ref. [46].

2.1.1 Symmetries and Gauge Theories

Symmetries play an important role when describing nature with quantum field theories (QFTs). Physically, a symmetry is a set of transformations of (quantum-)fields, under which the equations of motion are invariant. Usually these sets form a group and in the case of the SM the so-called gauge group is:

$$SU(3)_C \times SU(2)_L \times U(1)_Y, \tag{2.1}$$

where $SU(n)$ is the special unitary group[2] and $U(n)$ is the unitary group of degree n. Each group corresponds to a physical interaction (denoted by the indices C and Y, while the index L denotes that the $SU(2)$ affects left-handed states only)and provides a coupling and a

[2]The $SU(n)$ consists of all unitary $n \times n$ matrices with determinant 1.

number of gauge bosons. Particles that have a non-trivial transformation under $SU(3)_C$ underlie the strong interaction or Quantum Chromodynamics (QCD) [47–49] with the coupling g_s and eight gluons G^a_μ, $a = 1, \ldots, 8$ as gauge bosons. The two other gauge groups $SU(2)_L \times U(1)_Y$ build the electroweak theory [9–11], with the two couplings g and g' and the four unphysical gauge bosons A^a_μ, $a = 1, 2, 3$ and B_μ. In the SM the latter symmetries are spontaneously broken and linear combinations of A^a_μ and B_μ form physical states which can be identified with the massive $W^\pm$ and Z bosons and the massless photon γ. The equations of motion for each particle described by the SM can be obtained from the principle of least action, where the action S can be defined in terms of a Lagrangian density (or simply Lagrangian) $\mathcal{L}$, which is a function of one or more fields $\phi(x)$ and their derivatives $\partial_\mu \phi(x)$ [50]:

$$S = \int d^4x \, \mathcal{L}(\phi, \partial_\mu \phi). \tag{2.2}$$

The Lagrangian $\mathcal{L}_{\text{SM}}$ for the SM can be written as[3]:

$$\mathcal{L}_{\text{SM}} = \mathcal{L}_{\text{kin.}} + \mathcal{L}_{\text{coup.}} + \mathcal{L}_{\text{Higgs}} + \mathcal{L}_{\text{Yukawa}}, \tag{2.3}$$

where $\mathcal{L}_{\text{kin.}}$ contains the kinetic terms for the fermion and gauge fields,

$$\begin{aligned} \mathcal{L}_{\text{kin.}} &= \mathcal{L}_{\text{ferm.}} + \mathcal{L}_{\text{gauge}} \\ &= i\bar{\psi}\gamma^\mu \partial_\mu \psi - \left(\frac{1}{2} G^a_{\mu\nu} G^{a,\mu\nu} + \frac{1}{2} A^a_{\mu\nu} A^{a,\mu\nu} + \frac{1}{4} B_{\mu\nu} B^{\mu\nu} \right). \end{aligned} \tag{2.4}$$

Here, ψ denotes the implicit sum over Dirac spinors for doublets of the $SU(2)_L$ and triplets of the $SU(3)_C$ respectively and γ^μ denote the Dirac matrices, while $G^a_{\mu\nu}$, $A^a_{\mu\nu}$ and $B_{\mu\nu}$ denote the field strength tensors of the $SU(3)_C$, $SU(2)_L$ and $U(1)_Y$ gauge fields:

$$\begin{aligned} G^a_{\mu\nu} &= \partial_\mu G^a_\nu - \partial_\nu G^a_\mu + i g_s f_s^{abc} G^b_\mu G^c_\nu \\ A^a_{\mu\nu} &= \partial_\mu A^a_\nu - \partial_\nu A^a_\mu + i g f^{abc} A^b_\mu A^c_\nu \\ B_{\mu\nu} &= \partial_\mu B_\nu - \partial_\nu B_\mu. \end{aligned} \tag{2.5}$$

Greek indices run from 0 to 3 and denote the Lorentz structure of the gauge bosons, while latin indices run over the number of group generators (1 to 8 for $SU(3)_C$ and 1 to 3 for $SU(2)_L$). Finally, f_s^{abc} and f^{abc} denote the structure constants, which determine the commutation relations of the group generators, for the non-abelian groups $SU(3)_C$ and $SU(2)_L$ respectively.

The second term on the r.h.s of the Lagrangian in (2.3) $\mathcal{L}_{\text{coup.}}$ describes the coupling of the fermions to the gauge bosons:

$$\mathcal{L}_{\text{coup.}} = -\bar{\psi}\gamma^\mu \left(g_s \frac{1}{2} G^a_\mu \lambda^a + g \frac{1}{2} A^b_\mu \sigma^b + g' \frac{1}{2} Y B_\mu \right) \psi, \tag{2.6}$$

[3] All expressions are given in "God given" units [50], where $\hbar = c = 1$. Further the Einstein notation is used, which implies summation over repeated indices.

where λ^a are the Gell-Mann matrices, σ^a are the Pauli matrices and Y is the weak hypercharge. Here fermions are put into doublets under $SU(2)$ and quarks are additionally put into triplets under $SU(3)$.

This term arises directly from local gauge invariance which requires that the Lagrangian is invariant under a local gauge transformation:

$$\psi'(x) = \underbrace{\exp\left(i\frac{1}{2}\theta^a(x)\lambda^a\right)}_{\in SU(3)} \underbrace{\exp\left(i\frac{1}{2}\eta^a(x)\sigma^a\right)}_{\in SU(2)} \underbrace{\exp(i\frac{1}{2}\kappa(x))}_{\in U(1)} \psi(x). \tag{2.7}$$

This is only the case if the gauge fields are transformed in the following way:

$$\begin{aligned} G_\mu^{a\prime} &= G_\mu^a + \frac{1}{g_s}\partial_\mu\theta^a(x) + f_s^{abc} G_\mu^b \theta^c(x) \\ A_\mu^{a\prime} &= A_\mu^a + \frac{1}{g}\partial_\mu\eta^a(x) + f^{abc} A_\mu^b \eta^c(x) \\ B_\mu' &= B_\mu + \frac{1}{g'}\partial_\mu\kappa(x) \end{aligned} \tag{2.8}$$

where the f^{abc}, f_s^{abc} terms are self-interaction terms and lead to interactions among the gauge bosons.

To combine $\mathcal{L}_{\text{kin.}}$ with $\mathcal{L}_{\text{coup.}}$ one can replace the ordinary derivative ∂_μ in (2.3) by the covariant derivative:

$$D_\mu = \partial_\mu + ig_s\frac{1}{2}G_\mu^a\lambda^a + ig\frac{1}{2}A_\mu^b\sigma^b + ig'\frac{1}{2}YB_\mu. \tag{2.9}$$

The terms apart from ∂_μ in (2.9), which are necessary to preserve gauge invariance, generate the interactions between fermions and the gauge fields. Therefore, one may say that fundamental interactions are caused by the principle of local gauge invariance of the Lagrangian.

Unfortunately, the arguments above lead to the conclusion, that all vector bosons have to be massless since the necessary mass terms $m_G^2 G_\mu G^\mu$, $m_A^2 A_\mu A^\mu$ and $m_B^2 B_\mu B^\mu$ are not gauge invariant. Since it is clear, that the weak interaction is mediated by massive vector bosons a mechanism is needed which provides mass to the gauge bosons. This problem can be solved, if at least one of the symmetries of the Lagrangian is spontaneously broken. The last two terms of the SM Lagrangian in (2.3) are discussed in the following section, after the concept of spontaneous symmetry breaking has been reviewed.

2.1.2 The Brout-Englert-Higgs Mechanism

Before discussing the mass terms of the Lagrangian (2.3), the concept of spontaneous symmetry breaking [42] has to be introduced, since it is crucial for the BEH mechanism [15, 51, 52]. A gauge theory is called spontaneously broken, if the solutions of the field equations possess less degrees of freedom than the symmetry group of the Lagrangian. This is the case, if

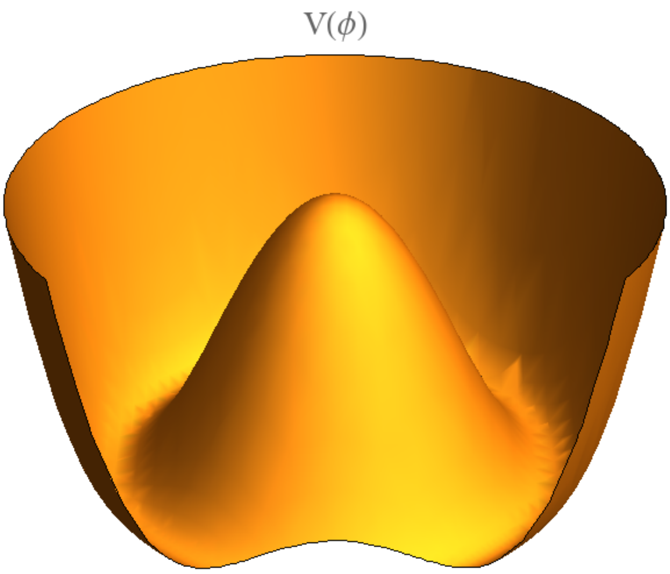

Figure 2.3: Illustration of the potential $V(\Phi)$ (2.11) which causes spontaneous symmetry breaking.

the ground state is not invariant under the whole group of symmetry transformations of the Lagrangian [53].

In order to break the electroweak symmetry a complex doublet of scalar fields

$$\Phi = \begin{pmatrix} \phi^+ \\ \phi^0 \end{pmatrix}, \tag{2.10}$$

where ϕ^+ denotes a charged and ϕ^0 denotes a neutral complex scalar field, with a potential (depicted in Figure 2.3)

$$V(\Phi) = -\mu^2\Phi^\dagger\Phi + \lambda\left(\Phi^\dagger\Phi\right)^2, \quad \mu^2, \lambda > 0 \tag{2.11}$$

and a positive weak hypercharge is introduced in the Lagrangian. The relevant part of the Lagrangian looks like

$$\mathcal{L}_{\text{Higgs}} = \left(D_\mu\Phi^\dagger\right)\left(D^\mu\Phi\right) - V(\Phi), \tag{2.12}$$

where only the $SU(2)\times U(1)$ part

$$D_\mu^{\text{ew}} = \partial_\mu + ig\frac{1}{2}A_\mu^b\sigma^b + ig'\frac{1}{2}YB_\mu \tag{2.13}$$

of the covariant derivative is considered since the $SU(3)$ symmetry is not broken. The potential (2.11) develops a minimum at:

$$|\Phi_0| = \frac{1}{\sqrt{2}}\sqrt{\frac{\mu^2}{\lambda}} = \frac{1}{\sqrt{2}}v \tag{2.14}$$

and therefore Φ has a non-vanishing vacuum expectation value (vev). Due to the freedom to choose a specific gauge[4] one may cast the ground state of Φ into the following form:

$$\langle \Phi_0 \rangle = \frac{1}{\sqrt{2}} \begin{pmatrix} 0 \\ v \end{pmatrix}. \tag{2.15}$$

The fact that the ground state is different from 0 causes the spontaneous symmetry breaking and is crucial for the gauge bosons as well as the fermions to acquire a mass. The fluctuations around the ground state can be parametrised by a single field h, which is called Higgs field in the following

$$\Phi = \frac{1}{\sqrt{2}} \begin{pmatrix} 0 \\ v + h \end{pmatrix}. \tag{2.16}$$

Inserting (2.16) into the potential (2.11) leads to:

$$V(h) = h^2 v^2 \lambda + h^3 v \lambda + \frac{\lambda}{4} h^4. \tag{2.17}$$

Two features are now apparent: Firstly, the original symmetry of the potential is broken since the $O(h^3)$ term neither has the $\Phi \to -\Phi$ symmetry nor the full $SU(2)_L \times U(1)_Y$ symmetry of the original potential left. Secondly, the $O(h^2)$term corresponds to a mass term of the Higgs field with $m_h = \sqrt{2\lambda v^2}$. The vev can be expressed in terms of m_W, the mass of the W boson and g, the weak coupling constant [54] $v = \frac{2m_W}{g} \approx 246$ GeV, while λ, and therefore the Higgs boson mass, is a free parameter of the theory.

In addition, the doublet (2.10) obeys the following transformation rule:

$$\Phi' = \underbrace{\exp\left(i\frac{1}{2}\eta^a(x)\sigma^a\right)}_{\in SU(2)_L} \underbrace{\exp(i\frac{1}{2}\kappa(x))}_{\in U(1)_Y} \Phi, \tag{2.18}$$

where Φ' describes the Higgs-doublet after a local gauge transformation. It is straightforward to calculate the mass terms of the gauge bosons from the kinetic term of the scalar field [50]:

$$\begin{aligned}(D_\mu\Phi)(D^\mu\Phi)|_{\Phi=\Phi_0} &= \left(\partial_\mu\Phi - igA^a_\mu\frac{\sigma^a}{2}\Phi - i\frac{g'}{2}YB_\mu\Phi\right)\left(\partial^\mu\Phi - igA^{\mu a}\frac{\sigma^a}{2}\Phi - i\frac{g'}{2}YB^\mu\Phi\right)\Bigg|_{\Phi=\Phi_0} \\ &= -\frac{1}{2}\frac{v^2}{4}\left(g^2\left[(A^1_\mu)^2 + (A^2_\mu)^2)\right] + \left[gA^3_\mu - g'B_\mu\right]^2\right) + \text{int. terms} \end{aligned} \tag{2.19}$$

It is very important that there are three massless (unphysical) scalar fields (the Goldstone bosons) appearing in the Lagrangian in general (one for each broken generator). However, they disappear due to the specific gauge choice of (2.18) and become the longitudinal degrees of freedom of the (now) massive gauge fields.

[4]In this case, the vev is chosen to be proportional to the eigenvector of the third generator $t^3 = \frac{1}{2}\sigma^3$ of the $SU(2)$, where σ^3 denotes the third Pauli matrix.

Introducing the following quantities:

$$\begin{aligned} W^{\pm}_{\mu} &= \frac{1}{\sqrt{2}}\left(A^1_\mu \mp iA^2_\mu\right) \qquad & Z_\mu &= \frac{1}{\sqrt{g^2+g'^2}}\left(gA^3_\mu - g'B_\mu\right) \\ A_\mu &= \frac{1}{\sqrt{g^2+g'^2}}\left(gA^3_\mu + g'B_\mu\right) \qquad & m_W &= \frac{v}{2}g,\ m_Z = \frac{v}{2}\sqrt{g^2+g'^2} \end{aligned} \tag{2.20}$$

and inserting them into (2.19) one obtains [50]:

$$(D_\mu\Phi)(D^\mu\Phi)|_{\Phi=\Phi^0} = \frac{1}{2}(\partial_\mu h)(\partial^\mu h) + [m_W^2 W^+_\mu W^{-\mu} + \frac{1}{2}m_Z^2 Z_\mu Z^\mu]\left(1+\frac{h}{v}\right)^2 \tag{2.21}$$

for a scalar doublet with hypercharge $Y = 1$. The terms proportional to h and h^2 describe the couplings of the gauge bosons and the Higgs boson which are proportional to their masses squared.

For further simplification, the weak mixing angle [11] can be introduced:

$$\begin{pmatrix} Z^0_\mu \\ A_\mu \end{pmatrix} = \begin{pmatrix} \cos\theta_W & -\sin\theta_W \\ \sin\theta_W & \cos\theta_W \end{pmatrix} \begin{pmatrix} A^3_\mu \\ B_\mu \end{pmatrix}, \tag{2.22}$$

$$\cos\theta_W = \frac{g}{\sqrt{g^2+g'^2}},\ \sin\theta_W = \frac{g'}{\sqrt{g^2+g'^2}} \tag{2.23}$$

and the elementary charge e can be identified [50] as:

$$e = g\sin\theta_W. \tag{2.24}$$

All observable quantities which only involve the exchange of W and Z bosons can be described in terms of m_W, e and θ_W.

For fermions the field Φ can also be used to generate the respective mass terms for the Lagrangian. In general, a fermion field ψ can be split into left- and right-handed fields ψ_L and ψ_R. When coupling to a gauge field, ψ_L and ψ_R can be assigned to different representations of the gauge group, which means that they have different covariant derivatives and therefore different couplings [50]. In the electroweak theory, left-handed fields are given as doublets under $SU(2)$, while right-handed fields are given as singlets under $SU(2)$:

$$\begin{aligned} q^1_L &= \begin{pmatrix} u \\ d \end{pmatrix},\ q^1_{R_u} = u_R,\ q^1_{R_d} = d_R \quad & \ell^1_L &= \begin{pmatrix} \nu_e \\ e \end{pmatrix},\ \ell^1_R = e_R \\ q^2_L &= \begin{pmatrix} c \\ s \end{pmatrix},\ q^2_{R_u} = c_R,\ q^2_{R_d} = s_R \quad & \ell^2_L &= \begin{pmatrix} \nu_\mu \\ \mu \end{pmatrix},\ \ell^2_R = \mu_R \\ q^3_L &= \begin{pmatrix} t \\ b \end{pmatrix},\ q^3_{R_u} = t_R,\ q^3_{R_d} = b_R \quad & \ell^3_L &= \begin{pmatrix} \nu_\tau \\ \tau \end{pmatrix},\ \ell^3_R = \tau_R \end{aligned} \tag{2.25}$$

This leads to the problem, that mass terms like

$$m_\ell \bar{\ell}\ell = m_\ell\left(\bar{\ell}_L\ell_R + \bar{\ell}_R\ell_L\right) \tag{2.26}$$

are prohibited by gauge invariance because left-handed and right-handed fields transform differently [55]. The Higgs field, again,provides a way out of this dilemma. Indeed, the Higgs doublet (2.10) can be used in order to generate couplings (Λ^ℓ_i for leptons and $\Lambda^{d/u}_{ij}$ for up-type or down-type quarks respectively, where i and j run over the number of generations) which connect left- and right-handed fermion fields:

$$\begin{aligned}\mathcal{L}_{\text{Yukawa}} = &- \Lambda^\ell_i \bar{\ell}^i_L \, \Phi \, \ell^i_R + \text{h.c.} \\ &- \left(\Lambda^d_{ij} \bar{q}^i_L \, \Phi \, q^j_{R_d} + \Lambda^u_{ij} \bar{q}^i_L \, \Phi^C \, q^j_{R_d}\right) + \text{h.c.},\end{aligned} \tag{2.27}$$

with Φ^C given as:

$$\Phi^C = i\sigma^2 \Phi^\dagger, \tag{2.28}$$

with the second Pauli matrix σ^2. Expanding Φ around its ground state as in (2.16) and inserting it into (2.27) yields:

$$\begin{aligned}\mathcal{L}_{\text{Yukawa}} = &\left[-\frac{v}{\sqrt{2}} \Lambda^\ell_i \, v \, \bar{\ell}^i_L \, \ell^i_R + \text{h.c.}\right] \left(1 + \frac{h}{v}\right) \\ &\left[-\left(\frac{v}{\sqrt{2}} \Lambda^d_{ij} \, v \, \bar{q}^i_L \, q^j_{R_d} + \frac{v}{\sqrt{2}} \Lambda^u_{ij} \, v \, \bar{q}^i_L \;\; q^j_{R_u}\right) + \text{h.c.}\right] \left(1 + \frac{h}{v}\right),\end{aligned} \tag{2.29}$$

which in turn leads to the mass terms:

$$m^i_\ell = \frac{1}{\sqrt{2}} \Lambda^\ell_i \, v \quad \text{and} \quad m^i_{q_a} = \frac{1}{\sqrt{2}} \Lambda^a_{ii} \, v, \text{ (no summation) with } a = u, d. \tag{2.30}$$

Similar to equation (2.21), the terms in equation (2.30) which are proportional to h describe the interaction of the fermions and the Higgs boson with the coupling proportional to the mass of the particle.

Having more than one generation of quarks can lead to additional couplings, which mix generations and result in off-diagonal terms in the coupling matrix Λ^a, with $a = u, d$. This can be addressed by choosing a new basis for the quark fields, where the Higgs couplings are diagonal and which leads to the Cabibbo-Kobayashi-Maskawa (CKM) matrix [12, 56].

2.1.3 Higgs-Boson Production and Decay Modes in the Standard Model

The most important production modes for the Higgs boson at the LHC are depicted in Figure 2.4. The dominant production mechanism is the ggF ($pp \to H$, 2.4(a)), mediated by a virtual quark loop (mainly top and bottom quarks), followed by VBF ($pp \to qqH$, 2.4(b)), whose cross section is about one order-of-magnitude smaller than the ggF cross section. The ggF cross section is known up next-to-next-to-leading order (NNLO) accuracy in QCD, where the next-to-leading order (NLO) contributions have been calculated in Ref. [57–59] and the NNLO contributions have been calculated in Ref. [60–62]. Soft-gluon resummations are included up to next-to-next-to-leading log (NNLL) [63] and the electroweak corrections are taken into account up to NLO [64, 65].

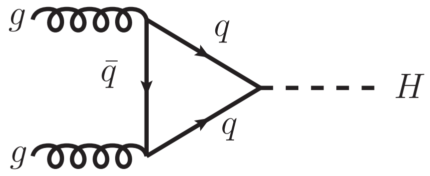

(a) Gluon-gluon fusion (ggF).

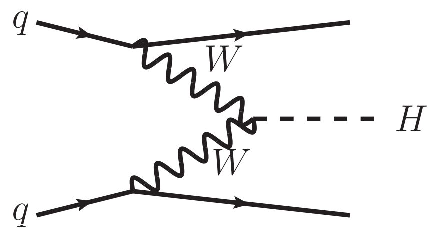

(b) Vector-boson fusion (VBF).

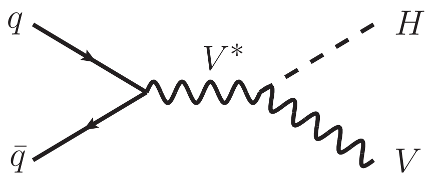

(c) Higgs-strahlung or associated production with a vector boson (VH).

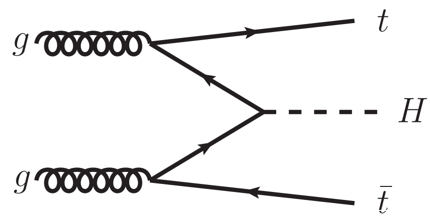

(d) Associated production with a $t\bar{t}$ pair (ttH).

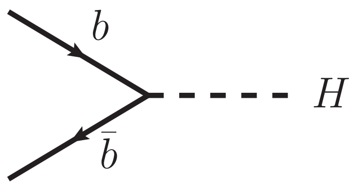

(e) Bottom-quark annihilation.

Figure 2.4: Higgs-boson production processes at the LHC. Figure (a) shows gluon-gluon fusion, (b) vector-boson fusion, (c) Higgs-strahlung, (d) associated production with a $t\bar{t}$ pair and (e) shows the annihilation of $b\bar{b}$ pair into a Higgs boson.

Despite the smaller cross section, VBF is an important mechanism of Higgs-boson production due to two forward jets which can be exploited to suppress relevant background processes. While the ggF production mode gives access to the Yukawa couplings of the Higgs boson to the top and bottom quarks through the quark loop, the VBF production mode makes it possible to examine the nature of the coupling of the Higgs boson to the massive gauge bosons. Especially in the light of an extended Higgs sector this is of great relevance, since both, Yukawa couplings and gauge-boson couplings, are predicted to be different from the SM. The VBF process is known up to NLO QCD and electroweak accuracy [68–70] with approximate NNLO QCD corrections [71].

The VH (Figure 2.4(c)), which also allows access to the gauge-boson couplings, is suppressed at the LHC, since it needs an antiquark in the initial state. As described in Section 2.1 antiquarks are occur only as sea quarks in the proton which reduce the probability of a collision compared to valence quarks. This argument about PDFs, and the lower centre of mass energy, is the reason why VH production was the most important production process at the Tevatron [72]. The cross

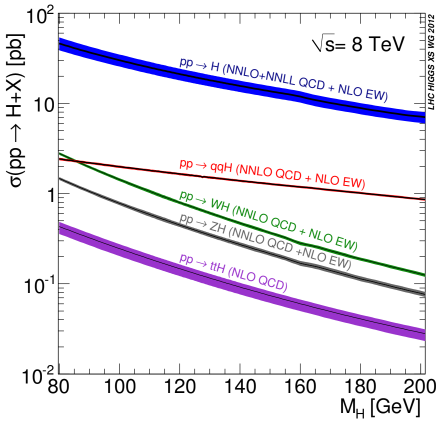

(a) Higgs-boson production cross sections.

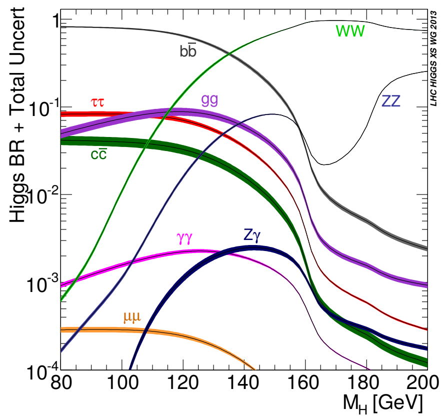

(b) Higgs-boson branching ratios.

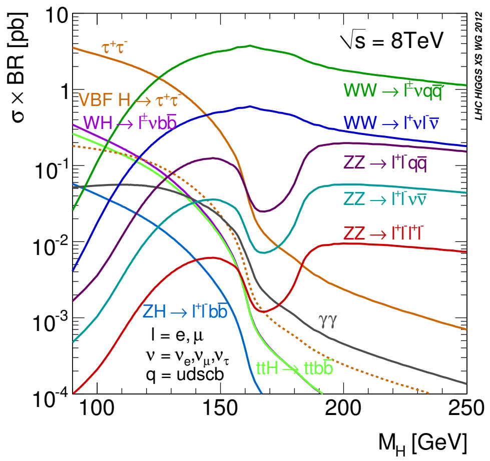

(c) Product of Higgs-boson production cross sections and branching ratios.

Figure 2.5: Higgs-boson production cross sections (a), branching ratios (b) and the product of the former (c) for the SM as function of the Higgs-boson mass [66, 67]. The SM-like Higgs boson is assumed to have a mass of $m_H = 125$ GeV.

sections for VH processes are calculated at NLO [73] and at NNLO [72] in QCD, and NLO electroweak radiative corrections [74] are applied.

The least important production processes for the Higgs boson are the associated production with a $t\bar{t}$ pair (ttH) (Figure 2.4(d)) which is strongly suppressed in the SM and not considered further and the bottom-quark annihilation (Figure 2.4(e)). While the latter also has almost no impact in the SM it can have an influence on the production of Higgs bosons in beyond Standard Model (BSM) scenarios like the 2HDMs described in Section 2.2.

Since the coupling strength of the Higgs boson is proportional to the mass of the interacting particle, heavier particles are preferred for the Higgs boson decay if the decay is kinematically allowed. Figure 2.1 shows the masses of the different SM particles and the relation $m_h < 2m_{W/Z}$ holds. Therefore, in case of a Higgs-boson decay in to a massive vector-boson pair, at least one the bosons will be off-shell.

The production cross sections and branching ratios of the Higgs boson in the SM as a function of the Higgs boson mass are shown in Figure 2.5. In the low mass region the decay into bottom-quark pairs is the dominant but also – due to large QCD multijet background at the LHC – the most challenging mode. Because of its clean experimental signature the decay into two photons, mediated by a quark or gauge-boson loop, is far more important and played a crucial role in the observation of the 125 GeV Higgs boson [20, 21]. The other channel that substantially supported the discovery was the $h \to ZZ^* \to \ell^-\ell^+\ell^-\ell^+$ channel, also due to its clean signature and good mass resolution. Due to the high branching ratio of the $h \to WW$ decay over a large mass range as depicted in Figure 2.5(b) this decay channel is well suited for the search for heavy Higgs bosons. Therefore the $H \to WW^* \to \ell^-\bar{\nu}\ell^+\nu$ channel is used for the search of a heavy Higgs boson H in this thesis.

2.1.4 Properties of the Higgs Boson in the Standard Model

As mentioned before, the mass of the Higgs boson is a free parameter and therefore has to be determined by experiments. After the discovery of a particle with a mass of about 125 GeV [20, 21] the properties (mass, spin, signal strength and couplings) of the particle have been measured in detail. Figure 2.6 shows the recent results of the Higgs-boson mass measurement [75], which gives a central value of 125.09 GeV.

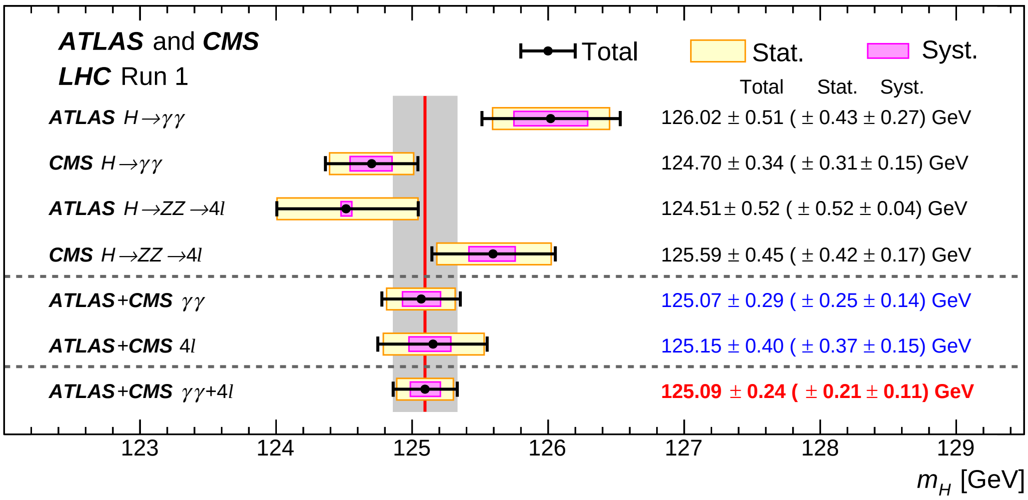

Figure 2.6: Summary of Higgs boson mass measurements from the individual analyses of ATLAS and CMS and from the combined analysis. Systematic, statistic and total uncertainties are indicated with magenta and yellow shaded bands and black error bars respectively. The red line shows the central value of 125.09 GeV with its total uncertainty of the combined measurement depicted by the grey band [75].

The spin of the Higgs boson has also been measured in various decay channels [76, 77] and found to be compatible with the $J^P = 0^+$ hypothesis, predicted by the SM.

The signal strength μ, defined as the ratio of the measured cross section times branching ratio and the predicted SM cross section times branching ratio, has been measured [78] and the result is shown in Figure 2.7. For the last two channels ($h \to \mu\mu$ and $h \to Z\gamma$) no evidence for signals are observed [79, 80] and therefore upper limits on the signal strengths are set. In the $h \to \mu\mu$ channel the observed limit on the signal strength is $\mu < 7.0$ [79] and in the $h \to Z\gamma$ channel the observed limit on the signal strength is $\mu < 11.0$ [80] at the 95% confidence level (CL). The combined result of $\mu = 1.18^{+0.15}_{-0.14}$ [78] is compatible with the SM prediction.

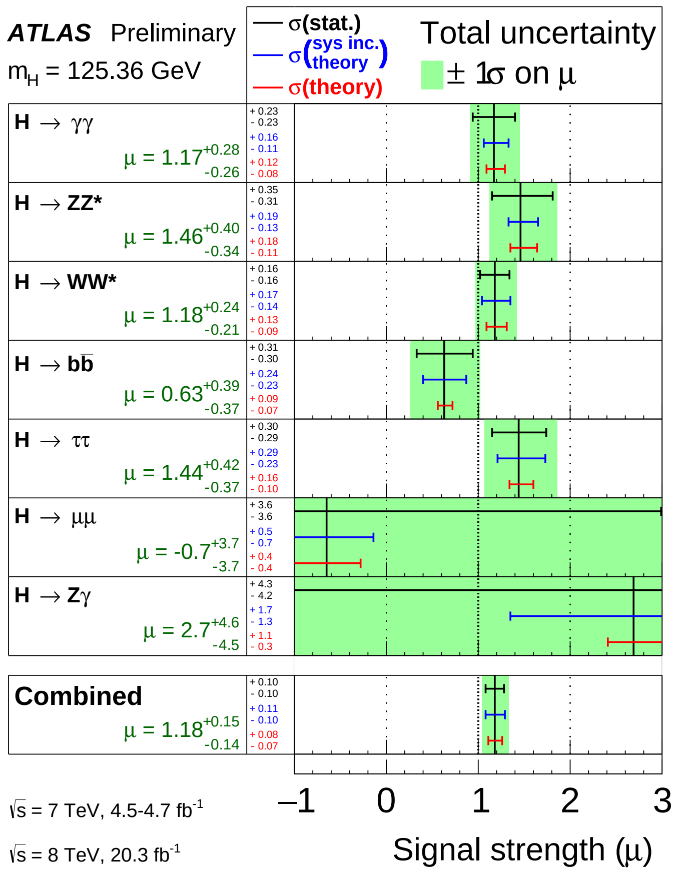

Figure 2.7: The observed signal strengths and uncertainties for different Higgs boson decay channels and their combination for $m_h = 125.36$ GeV. The statistical uncertainties are given by the black band (top), the experimental uncertainties combined with theoretical uncertainties are given by the blue band (middle) and the theoretical uncertainties alone are given by the red band (bottom). The green shaded band shows the total uncertainties [78].

The coupling of the Higgs boson to vector bosons and fermions is usually parametrised in terms of scale factors κ_i which describe deviations from the SM couplings [81]. They are defined such, that the cross sections σ_{ii} and the partial decay widths Γ_{ii} associated with the SM particle i are scaled with a factor κ_i^2 comparing to the SM prediction. In the case, where only universal fermion couplings κ_F and universal vector-boson couplings κ_V with

$$\begin{aligned} \kappa_F &= \kappa_t = \kappa_b = \kappa_\tau = \kappa_g = \kappa_\mu \\ \kappa_V &= \kappa_W = \kappa_Z \end{aligned} \tag{2.31}$$

are considered, the best fit values are [78]:

$$\begin{aligned} \kappa_F &= 1.11^{+0.17}_{-0.15} \\ \kappa_V &= 1.09^{+0.07}_{-0.07} \end{aligned} \tag{2.32}$$

which are compatible with the SM. In addition, Figure 2.8 shows the dependence of the so-called reduced coupling strength factors y_F and y_V, which are defined as

$$\begin{aligned} y_F &= \kappa_F \frac{m_F}{v} \\ y_V &= \sqrt{\kappa_V} \frac{m_V}{v}, \end{aligned} \tag{2.33}$$

from the mass of the regarded decay products. The result is again compatible with the SM prediction.

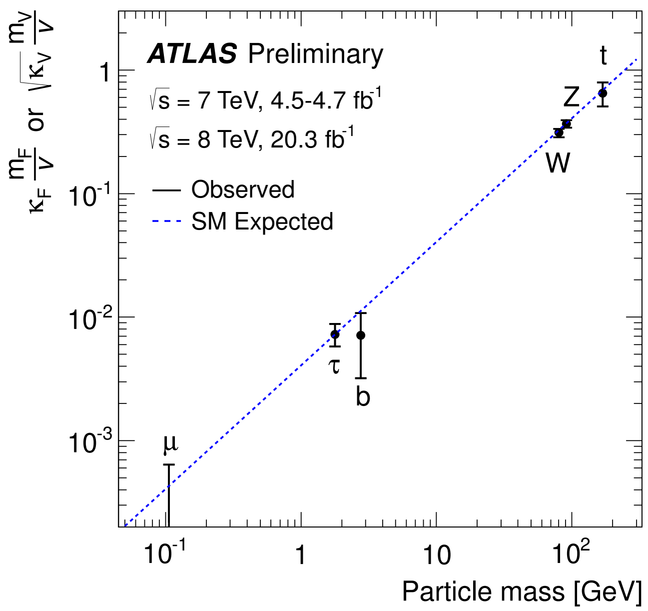

Figure 2.8: Fit results for the reduced coupling strength scale factors y_F and y_V (see text for definition) as a function of the particle mass, assuming a SM-like Higgs boson with a mass of 125.36 GeV [78].

2.2 The 2-Higgs-Doublet Model

A simple and natural extension of the SM is the inclusion of two Higgs doublets instead of one:

$$\Phi_1 = \begin{pmatrix} \phi_1^+ \\ \phi_1^0 \end{pmatrix}, \quad \Phi_2 = \begin{pmatrix} \phi_2^- \\ \phi_2^0 \end{pmatrix}, \tag{2.34}$$

where Φ_1 and Φ_2 have positive hypercharge like the SM doublet in equation (2.10) and the superscripts $\pm$ and 0 denote the electric charge of the scalar fields ϕ. The set of models which include two Higgs doublets are therefore called 2-Higgs-Doublet Models (2HDMs) [25]. Similar to (2.11) a potential can be introduced including both Higgs doublets, which – in its most general form – can be written as [82]:

$$\begin{aligned} V(\Phi_1, \Phi_2) = {} & m_{11}^2 \Phi_1^\dagger \Phi_1 + m_{22}^2 \Phi_2^\dagger \Phi_2 - (m_{12}^2 \Phi_1^\dagger \Phi_2 + \text{h.c.}) \\ & + \frac{1}{2}\lambda_1 (\Phi_1^\dagger \Phi_1)^2 + \frac{1}{2}\lambda_2 (\Phi_2^\dagger \Phi_2)^2 + \lambda_3 (\Phi_1^\dagger \Phi_1)(\Phi_2^\dagger \Phi_2) + \lambda_4 (\Phi_1^\dagger \Phi_2)(\Phi_2^\dagger \Phi_1) \\ & + \left[\frac{1}{2}\lambda_5 (\Phi_1^\dagger \Phi_2)^2 + \left(\lambda_6 (\Phi_1^\dagger \Phi_1) + \lambda_7 (\Phi_2^\dagger \Phi_2)\right) (\Phi_1^\dagger \Phi_2) + \text{h.c.} \right] \end{aligned} \tag{2.35}$$

with $m_{11}^2, m_{22}^2, \lambda_1, \ldots, \lambda_4 \in \mathbb{R}$ and $m_{12}^2, \lambda_5, \lambda_6, \lambda_7 \in \mathbb{C}$. This potential is symmetric under $U(2)$ transformations, therefore one has a free choice of gauge. Here, particular gauges can be parametrised in terms of the vevs of the doublets:

$$\langle \Phi_1 \rangle = \frac{v}{\sqrt{2}} \begin{pmatrix} 0 \\ \cos\beta \end{pmatrix}, \langle \Phi_2 \rangle = \frac{v}{\sqrt{2}} \begin{pmatrix} 0 \\ e^{i\xi} \sin\beta \end{pmatrix}, \tan\beta = \frac{|\langle \Phi_2 \rangle|}{|\langle \Phi_1 \rangle|}. \tag{2.36}$$

A particular gauge can now be fixed by a specific choice of $\tan\beta$. The exponential term $e^{i\xi}$ in equation (2.36) arises from the electromagnetic $U(1)$ symmetry and an non-zero phase ξ leads to a vacuum state which spontaneously breaks CP symmetry [83]. Since CP-violating effects are beyond scope of this thesis, ξ is set to zero and further CP-conservation is achieved by introducing a discrete $\mathbb{Z}_2$ symmetry

$$\Phi_1 \to \Phi_1, \Phi_2 \to -\Phi_2. \tag{2.37}$$

Such a symmetry requires m_{12}^2, λ_6 and λ_7 to be 0 unless this symmetry is softly broken [84], which allows $m_{12}^2 \neq 0$. The latter is assumed, because it extends the parameter space of the 2HDMs which are investigated in this thesis.

Similar to (2.16) excitations of the different Higgs fields around their vevs can be examined [85]

$$\Phi_1 = \begin{pmatrix} \phi_1^+ \\ (v\cos\beta + \rho_1 + i\eta_1)/\sqrt{2} \end{pmatrix}, \Phi_2 = \begin{pmatrix} \phi_2^- \\ (v\sin\beta + \rho_2 + i\eta_2)\sqrt{2} \end{pmatrix} \tag{2.38}$$

with $\rho_1 = \text{Re}(\phi_1^0) - v\cos\beta$, $\rho_2 = \text{Re}(\phi_1^0) - v\sin\beta$ and $\eta_i = \text{Im}(\phi_i^0)$, $i = 1, 2$. From these fields the Goldstone bosons G^0 and $G^\pm$, which can be absorbed to generate the mass of the W

and Z bosons, and five physical Higgs particles can be formed [86]: Two scalar (CP-even) particles h and H with $m_h < m_H$, a pseudo scalar (CP-odd) particle A and two charged Higgs-bosons $H^{\pm}$:

$$\begin{pmatrix} H^{\pm} \\ G^{\pm} \end{pmatrix} = \begin{pmatrix} \cos\beta & \sin\beta \\ -\sin\beta & \cos\beta \end{pmatrix} \begin{pmatrix} \phi_1^{\pm} \\ \phi_2^{\pm} \end{pmatrix} \tag{2.39}$$

$$\begin{pmatrix} G^{0} \\ A \end{pmatrix} = \begin{pmatrix} \cos\beta & \sin\beta \\ -\sin\beta & \cos\beta \end{pmatrix} \begin{pmatrix} \eta_1 \\ \eta_2 \end{pmatrix}. \tag{2.40}$$

These transformations diagonalise the mass matrices for the charged and pseudo scalar Higgs bosons and their masses can be obtained from the quadratic terms of the 2HDM potential (2.35) [86]:

$$m_A^2 = \frac{m_{12}^2}{\sin\beta\cos\beta} - v^2\lambda_5 \text{ and} \tag{2.41}$$

$$m_{H^{\pm}} = m_A^2 + \frac{1}{2}v^2(\lambda_5 - \lambda_4). \tag{2.42}$$

However, the mass matrix for the scalar particles is not diagonal by coincidence. Therefore, a mixing angle α has to be introduced as follows:

$$\begin{pmatrix} H \\ h \end{pmatrix} = \begin{pmatrix} \cos\alpha & \sin\alpha \\ -\sin\alpha & \cos\alpha \end{pmatrix} \begin{pmatrix} \rho_1 \\ \rho_2 \end{pmatrix} \tag{2.43}$$

in order to diagonalise the corresponding mass matrix.

The masses of the two scalar Higgs bosons can also be obtained from the 2HDM potential (2.35) and they read [83, 86, 87]:

$$\begin{aligned} m_{h,H}^2 &= \frac{1}{2}\left(\mathcal{M}_{11}^2 + \mathcal{M}_{22}^2 \pm \sqrt{\left(\mathcal{M}_{11}^2 - \mathcal{M}_{22}^2\right) + 4\left(\mathcal{M}_{12}^2\right)^2}\right), \quad \text{with:} \\ \mathcal{M}_{11}^2 &= m_A^2 \sin^2\beta + v^2[\lambda_1 \cos^2\beta + \lambda_5 \sin^2\beta] \\ \mathcal{M}_{12}^2 &= -m_A^2 \sin\beta\cos\beta + v^2(\lambda_3 + \lambda_4)\sin\beta\cos\beta \\ \mathcal{M}_{22}^2 &= m_A^2 \cos^2\beta + v^2[\lambda_2 \sin^2\beta + \lambda_5 \cos^2\beta] \end{aligned} \tag{2.44}$$

Similar to the SM the particle masses are free parameters of the theory and a particular choice of the masses m_h, m_H, m_A and $m_{H^{\pm}}$ of the physical particles, the ratio of the vevs $\tan\beta$, the mixing angle α and the soft breaking parameter m_{12}^2 fix all parameters which are left in the 2HDM potential (2.35) and therefore define a particular model.

A feature of all 2HDMs is the possibility of tree level flavour-changing neutral currents (FCNCs) which are avoided in the SM by a crucial coincidence. In order to pay regard to experimental constraints on FCNCs [88, 89], only 2HDMs without FCNCs are taken into account in this thesis. It is possible to remove FCNCs from the theory by assuming the discrete symmetry of (2.37) for all right-handed quarks, which does not permit FCNCs at tree level since it forces any given type of fermions to couple to not more than one doublet (also known as Glashow-Weinberg condition) [90]. Regarding the quark sector of a 2HDM, there are only two possibilities to realise such a behaviour: Either both, right-handed u- and d-type quarks, couple to the same doublet Φ_2 or they each couple to a different one, e.g d-type to Φ_1 and u-type to Φ_2.

Extending this symmetry to right-handed leptons, which are also allowed to couple to exactly one doublet to prevent FCNCs, gives two more possibilities for the coupling of fermions to Higgs doublets. Table 2.1 [85] shows the possible combinations, usually denoted as Type I to Type IV. In this analysis no distinction between model Type I and III and Type II and IV is possible, since in the regarded channel $H \to WW \to \ell\nu\ell\nu$ no coupling between Higgs bosons and leptons occur. Therefore, the discussion focuses on model Types I and II keeping in mind that these are proxies for Type III and IV respectively.

Table 2.1: 2HDM Types which lead to natural flavour conservation. The doublets Φ_1 and Φ_2 are the Higgs doublets introduced in equation (2.35) while $q^i_{R_u}$, $q^i_{R_d}$ and ℓ^i_R are the fermions introduced in equation (2.25) with $i = 1, 2, 3$ [85].

	Type I	Type II	Type III	Type IV
$q^i_{R_u}$	Φ_2	Φ_2	Φ_2	Φ_2
$q^i_{R_d}$	Φ_2	Φ_1	Φ_2	Φ_1
ℓ^i_R	Φ_2	Φ_1	Φ_1	Φ_2

2.2.1 Higgs-Boson Production and Decay Modes in the 2HDM

As described in Section 2.1.4, the parametrisation of the coupling of fermions and vector bosons to the Higgs boson is described by scale factors κ. In case of the 2HDM these scale factors can be predicted [28] and they depend on the particle mass, the ratio of the Higgs vevs $\tan\beta$ and on the mixing angle α, which diagonalises the (H, h) mass matrix. The scale factors in terms of α and β relative to the SM are given in Table 2.2. Here, $\kappa^{V/u/d/\ell}_{h/H}$ describes the coupling of the light/heavy Higgs boson (h/H) to a vector boson (V), an up/down-type quark (u/d) or a lepton (ℓ).

In order to create appropriate predictions for 2HDM, cross sections and branching ratios of the SM obtained by Monte-Carlo (MC) simulations, have to be scaled according to the factors in Table 2.2. The calculation of 2HDM cross sections is performed with `SusHi` [91] (ver. 1.1.1), a program which calculates Higgs-boson production cross sections in various models. Initially it was designed to evaluate cross sections for the process $pp/p\bar{p} \to \phi + X$, in ggF and bottom-quark annihilation in the SM and the Minimal Supersymmetric Standard Model (MSSM), where ϕ is any of the neutral Higgs bosons within these models. Starting from version 1.0.3 however, it is also possible to calculate the cross sections within the several types of 2HDMs.

The accuracy of the predictions calculated by `SusHi` is "partially" NNLO which means that NNLO QCD corrections (implemented by `ggh@nnlo` [60]) are taken into account in the heavy-

Table 2.2: The couplings of the light and the heavy Higgs bosons h and H in the different 2HDM Types in terms of α and β relative to the couplings of the SM [28].

	Type I	Type II	Type III	Type IV
κ_h^V	$\sin(\beta-\alpha)$	$\sin(\beta-\alpha)$	$\sin(\beta-\alpha)$	$\sin(\beta-\alpha)$
κ_h^u	$\cos\alpha/\sin\beta$	$\cos\alpha/\sin\beta$	$\cos\alpha/\sin\beta$	$\cos\alpha/\sin\beta$
κ_h^d	$\cos\alpha/\sin\beta$	$-\sin\alpha/\cos\beta$	$\cos\alpha/\sin\beta$	$-\sin\alpha/\cos\beta$
κ_h^ℓ	$\cos\alpha/\sin\beta$	$-\sin\alpha/\cos\beta$	$-\sin\alpha/\cos\beta$	$\cos\alpha/\sin\beta$
κ_H^V	$\cos(\beta-\alpha)$	$\cos(\beta-\alpha)$	$\cos(\beta-\alpha)$	$\cos(\beta-\alpha)$
κ_H^u	$\sin\alpha/\sin\beta$	$\sin\alpha/\sin\beta$	$\sin\alpha/\sin\beta$	$\sin\alpha/\sin\beta$
κ_H^d	$\sin\alpha/\sin\beta$	$\cos\alpha/\cos\beta$	$\sin\alpha/\sin\beta$	$\cos\alpha/\cos\beta$
κ_H^ℓ	$\sin\alpha/\sin\beta$	$\cos\alpha/\cos\beta$	$\cos\alpha/\cos\beta$	$\sin\alpha/\sin\beta$

top approximation, while the NLO QCD contributions of all quarks are fully taken into account. Electroweak corrections are also considered up to NNLO, implemented as tabulated correction factors. For the $b\bar{b}$-annihilation process, `SusHi` uses `bbh@nnlo` [92] and rescales the results by the factors given in Table 2.2 for any of the 2HDM scenarios described in the last section.

Similar to `SusHi`, which calculates the cross section in the 2HDM scenario, `2HDMC` [83] (ver. 1.6.1) is used for the calculation of the branching ratios. The program features the conversion between different parametrisations of the 2HDM potential, it allows the specification of Yukawa couplings with choice of different $\mathbb{Z}_2$ symmetries and has the possibility to calculate all two-body decay modes of the Higgs bosons. In addition, it checks the following theoretical constraints:

- Positivity of the Higgs potential: The potential (2.35) has to be positive in any field space direction for asymptotically large values of the fields [93, 94] which provides constraints for some coefficients λ_i [83].
- Tree-level unitarity: Since the scattering matrix S has to be unitary, the eigenvalues of the S-matrix [95] also deliver constraints for coefficients λ_i.
- Perturbativity: Perturbativity can be achieved by constraining the quartic Higgs coupling [83].

The input parameters for `SusHi` and `2HDMC` are the masses of the Higgs particles from the 2HDM m_h, m_H, m_A and $m_{H^\pm}$, the mass parameter m_{12} from the potential (2.35), the ratio of the vevs $\tan\beta$ and the coupling of the light scalar Higgs boson h to the vector bosons $\sin(\beta-\alpha)$. The parameter m_h is fixed at 125 GeV, since the new boson is assumed to be the light scalar boson h of the 2HDM. To obtain valid values in terms of positivity, unitarity and perturbativity, the values of m_A and $m_{H^\pm}$ are set to m_H or 350 GeV, whatever is smaller. The parameter m_{12} is set to $m_{12}^2 = m_A^2 \frac{\tan\beta}{1+\tan^2\beta}$, which corresponds to the MSSM choice [83].

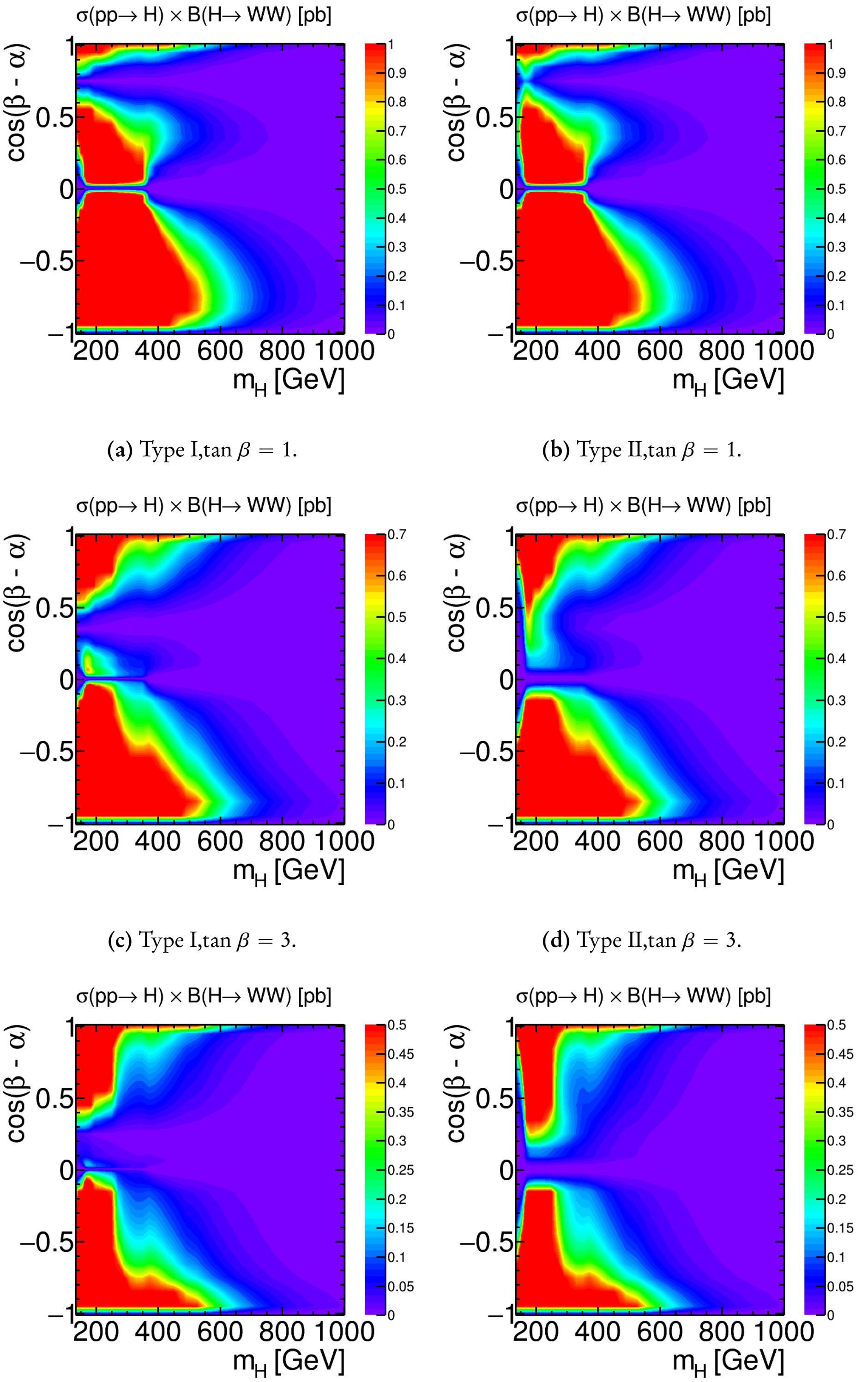

(a) Type I,tan β = 1.

(b) Type II,tan β = 1.

(c) Type I,tan β = 3.

(d) Type II,tan β = 3.

(e) Type I,tan β = 6.

(f) Type II,tan β = 6.

Figure 2.9: ggF cross section times branching ratio of the $H \to WW$ decay mode for the 2HDMs Type I and Type II in pb in the m_H-$\cos(\beta - \alpha)$ plane for selected values of $\tan\beta$. The maxima of the plots are fixed at 1 pb, 0.7 pb and 0.5 pb for the different values of $\tan\beta$ respectively in order to get a better resolution of the progression of the cross section times branching ratio in the high-m_H regime.

To get an understanding where to expect sensitivity for an additional heavy Higgs boson, Figures 2.9 and 2.10 show the values of cross section times branching ratio of the $H \to WW$ decay mode in the m_H-$\cos(\beta - \alpha)$ plane for several values of $\tan\beta$ and divided into ggF and VBF production modes. The ggF mode provides good sensitivity in the negative range of $\cos(\beta - \alpha)$, while the VBF mode adds sensitivity mostly in the positive range of $\cos(\beta - \alpha)$. The maximum in these plots is fixed at a small value in order to get an impression of the structure in the high-m_H range.

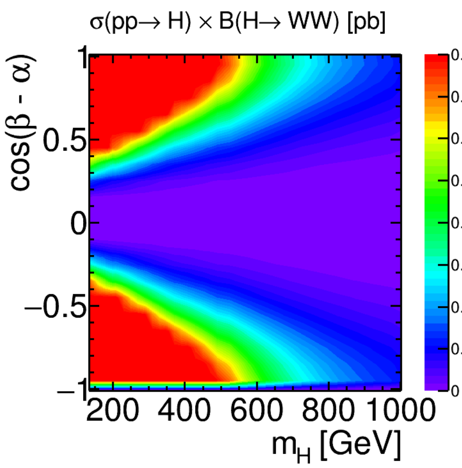

(a) $\tan\beta = 1$.

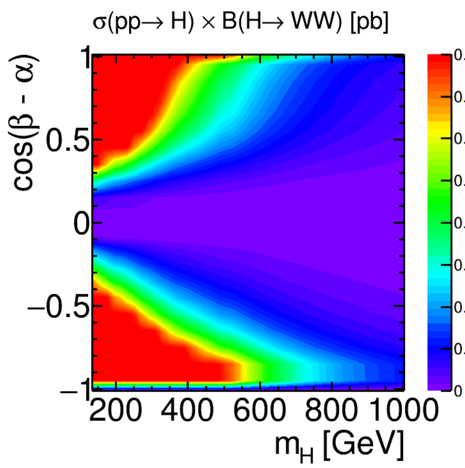

(b) $\tan\beta = 3$.

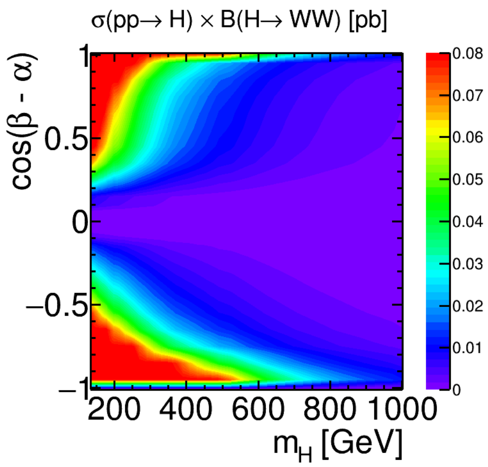

(c) $\tan\beta = 6$.

Figure 2.10: VBF cross section times branching ratio of the $H \to WW$ decay mode for the 2HDMs in pb in the m_H-$\cos(\beta - \alpha)$ plane for selected values of $\tan\beta$. The maxima of the plots are fixed at 0.08 pb in order to get a better resolution of the progression of the cross section times branching ratio in the high-m_H regime. Only Type I of the 2HDM is shown, since the relative couplings κ_H^V from Table 2.2 are similar for Type I and II.

In addition Figure 2.11 shows the cross section times branching ratio of the light Higgs boson of the 2HDM in terms of $\cos(\beta-\alpha)$ for several values of $\tan\beta$ separated into ggF and VBF. In both production modes of 2HDM Type I the sensitivity moves to the alignment limit ($\cos(\beta-\alpha) \to 0$) as $\tan\beta$ increases, while it moves away from the alignment limit in Type II. Therefore a larger impact in the total sensitivity for $\cos(\beta-\alpha) \to 0$ is expected in Type I than for Type II.

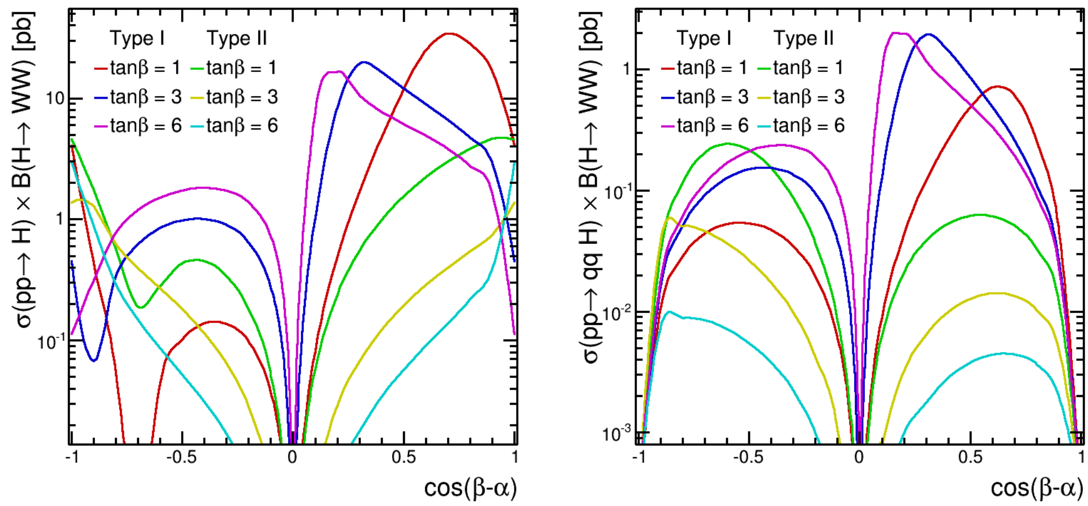

(a) Cross section times branching ratio in the ggF production mode.

(b) Cross section times branching ratio in the VBF production mode.

Figure 2.11: Cross section times branching ratio in the ggF (a) and VBF (b) production modes for the light scalar Higgs boson h ($m_h = 125$ GeV) of the 2HDM in terms of $\cos(\beta-\alpha)$.

2.2.2 Constraints on the 2HDM phase space

The discovery of the Higgs boson with $m_h \approx 125$ GeV does not only allow precise measurements but also constrains the phase space of the 2HDMs, assuming that the new observed particle coincides with the light neutral CP-even Higgs boson h [41]. Figure 2.12 shows the regions of the $\cos(\beta-\alpha)$-$\tan\beta$ plane which can be excluded with at least 95% CL for the 2HDM Types I and II using only the properties of the light Higgs boson as input. In the regarded analysis, the production and decay rates are rescaled with the appropriate factors described in Table 2.2, but no assumptions on the other Higgs particles predicted by the 2HDM are made. Due to its SM-like nature, large parts of the $\cos(\beta-\alpha)$ range can be excluded while an exclusion in the alignment limit is not possible.

Figure 2.13 shows some results of an earlier version of this analysis [37] for a heavy scalar Higgs boson in the 2HDM framework. In these plots, the coloured area shows the observed exclusion in the m_H-$\cos\alpha$ plane, while the area limited by the black solid (dashed) line shows the expected exclusion at 99% (95%) CL. The 2HDMs are tested against the SM as null hypothesis, including the SM-like Higgs Boson, which is also adopted in this thesis (see Chapter 9). In the regarded scenarios, neutral heavy Higgs bosons with masses up to 250 GeV and in some regions up to 300 GeV could be excluded at 95% CL.

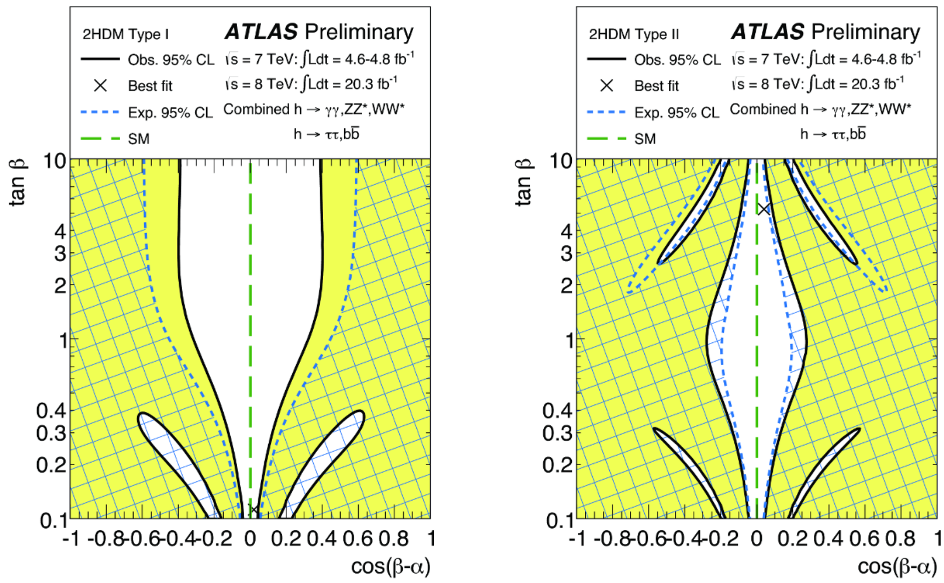

Figure 2.12: Regions of the $\cos(\beta-\alpha)$-$\tan\beta$ plane of two types of 2HDMs excluded by fits to the measured rates of Higgs boson production and decays. The contours corresponding approximately to 95% CL are indicated for both the data and the expectation assuming the SM Higgs sector. The cross in each plot marks the observed best-fit value. The light shaded and hashed regions indicate the observed and expected exclusions, respectively [41].

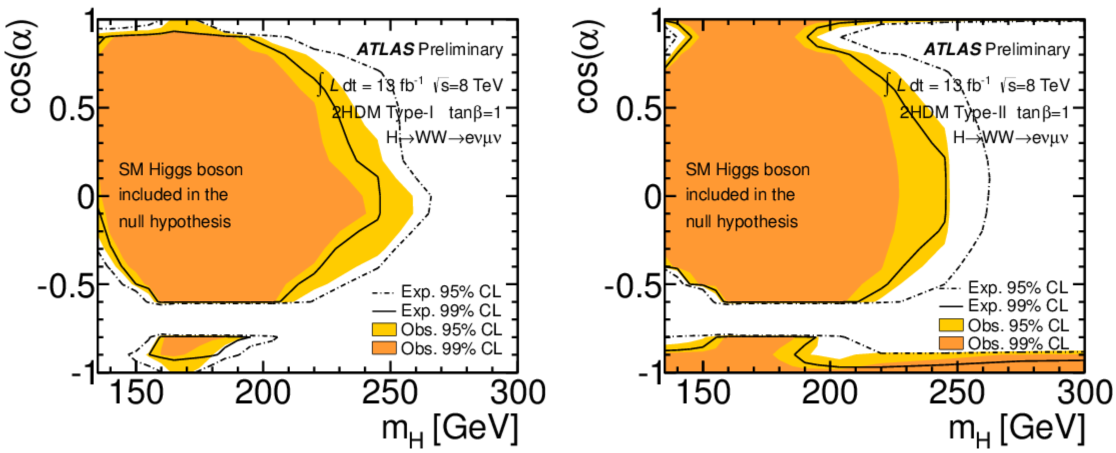

Figure 2.13: Exclusion contours of 2HDM Type I (left) and Type II (right) for $\tan\beta = 1$ in the m_H-$\cos\alpha$ plane. The coloured areas show the observed exclusion at 99% and 95% CL respectively, while the area limited by the black solid (dashed) line shows the expected exclusion at 99% (95%) CL [37].

3 | The LHC and the ATLAS Experiment

Currently, the most powerful facility – in terms of energy and collision rate – for particle physics is the LHC [96] hosted at CERN. It was built in a 26.7 km tunnel which originally has been constructed for the Large Electron-Positron Collider (LEP) and is designed to collide proton or lead beams with centre-of-mass energies of 14 TeV and 2.8 TeV per nucleon respectively. The LHC provides four interaction points, where experimental facilities are placed.

Out of the four main experiments A Large Ion Collider Experiment (ALICE) [97], A Toroidal LHC Apparatus (ATLAS) [98], Compact Muon Solenoid (CMS) [99] and Large Hadron Collider beauty (LHCb) [100], ATLAS and CMS are so-called multi-purpose detectors designed to cover the widest possible range of physics at the LHC. One of the main goals – finding a Higgs boson – has already been achieved [20, 21], while others like probing for BSM physics are still ongoing [101, 102].

The two other experiments ALICE and LHCb are designed for more customised physics programmes: ALICE is specialised in analysing lead-ion collisions which are used to produce a quark-gluon plasma [103] in which quarks and gluons are no longer confined. LHCb focuses on the slight asymmetry between matter and antimatter which is present in interactions containing bottom quarks [104].

Since the analysis described in this thesis uses data collected by the ATLAS experiment, it is described in more detail in Section 3.2.

3.1 The Large Hadron Collider

The acceleration chain [105] of protons and lead ions can be tracked based on the sketch of the CERN accelerator complex in Figure 3.1. The acceleration starts by injecting protons into Linear Accelerator 2 (LINAC2), accelerating them up to 50 MeV and handing them over to the Proton Synchrotron Booster (PSB) [106], where the protons are accelerated to 1.4 GeV. The beam is then transferred to the Proton Synchrotron (PS) [107] where the particles are further accelerated to 25 GeV. From there, protons are sent to the Super Proton Synchrotron (SPS) [108] which brings them to an energy of 450 GeV before they are injected to the LHC. In the LHC protons are further accelerated to get their final design beam energy of 7 TeV per beam. So far, the LHC has been running with centre-of-mass energies of 7 TeV in 2011 and 8 TeV in 2012. After the long shutdown 1 (from February 2013 to April 2015) the LHC will be running with a centre-of-mass energy of 13 TeV.

In order to accelerate protons, the LHC[5] uses eight cavities per beam, each delivering a field of 5 MV/m at 400 MHz and an operation temperature of 4.5 K. To keep the particles on a nearly

[5]Details on the technical design can be found in Ref. [96]

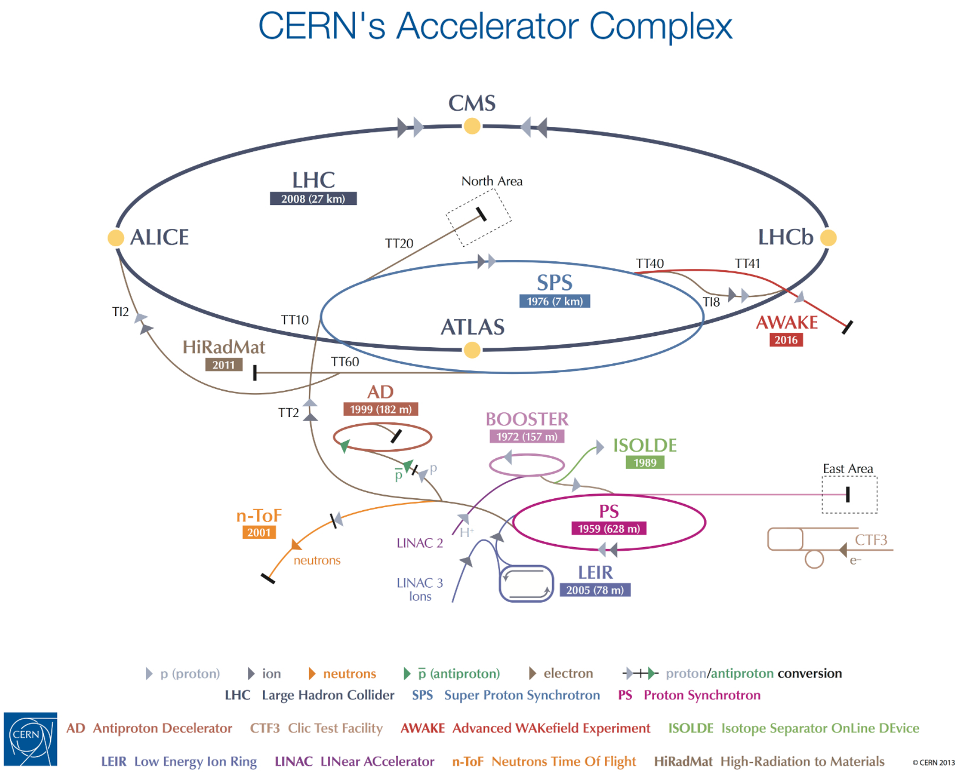

Figure 3.1: The CERN accelerator complex [109] with the four main experiments ATLAS, ALICE, CMS and LHCb.

circular orbit at 7 GeV beam energy, a magnetic field of 8.33 T is necessary which is provided by 1232 superconducting dipole magnets. These have to be operated at a temperature of 1.9 K to preserve the superconductivity of the magnets which is reached by pumping super-fluid helium into their cryogenic system. The beam is hold together with the aid of 392 main quadrupole magnets and 6208 magnets with higher multipole moments.

Apart from the beam energy the most important parameter for colliders is the instantaneous luminosity $\mathcal{L}$ which describes the rate of particle interactions per area:

$$\mathcal{L} = \frac{\gamma}{4\pi} \frac{N_b n_b^2 f_{\text{rev}}}{\epsilon^* \beta^*} F, \quad \text{with:} \quad F = \frac{1}{\sqrt{1 + \left(\frac{\theta_c \sigma_{\text{T}}}{2\sigma_{\text{L}}}\right)^2}}, \tag{3.1}$$

where N_b is the number of bunches per beam, n_b is the number of particles per bunch, f_{rev} is the revolution frequency, ϵ^* is the normalised beam emittance at the interaction point, β^* is the beta function at the interaction point, γ is the relativistic Lorentz factor and F is the geometric reduction factor, depending on the crossing angle θ_c and the transversal/longitudinal beam sizes σ_{T} and σ_{L}. A comparison of design values and achieved values in the 2012 run is given in Table 3.1.

Table 3.1: Overview of the LHC performance parameters [110].

Parameter	Design value	Value in 2012
Beam energy	7 TeV	4 TeV
β^* in int. points 1, 2, 3, 4	0.55 m	0.6 m, 3.0 m, 0.6 m, 3.0 m
Bunch spacing	25 ns	50 ns
Bunches per beam	2808	1374
Particles per bunch	$1.15 \cdot 10^{11}$ p/bunch	$1.6 - 1.7 \cdot 10^{11}$ p/bunch
ϵ^* at start of fill	3.75 mm mrad	2.5 mm mrad
Peak luminosity	10^{34} cm^{-2} s^{-1}	$7.33 \cdot 10^{33}$ cm^{-2} s^{-1}
Max. mean number of events per crossing	~ 19	~ 40
Stored beam energy	~ 362 MJ	~ 140 MJ

The integrated luminosity $\mathcal{L}_{\text{int}} = \int dt \mathcal{L}$ is a measure for the number of collisions in a given time period, since the number of events N of a process with cross section σ is given as $N = \sigma \mathcal{L}_{\text{int}}$. The integrated luminosity for the data-taking in 2012 with a centre-of-mass energy of $\sqrt{s}$ = 8 TeV is 20.3 fb^{-1}. Table 3.2 gives an overview of the luminosity performance of the LHC.

Table 3.2: Overview of the LHC luminosity performance [110].

Max. luminosity delivered in one fill	237 pb^{-1}
Max. luminosity delivered in 7 days	1.35 fb^{-1}
Longest time in stable beams (2012)	22.8 hours
Longest time in stable beams over 7 days	91.8 hours

3.2 The ATLAS Experiment

As mentioned in the last section, ATLAS is a multi-purpose detector built to cover a wide range of physics including tests of the SM and BSM physics. It is built symmetrically around the interaction point with different layers of subdetectors which are described in the following sections. An overview sketch of the ATLAS experiment is given in Figure 3.2.

For the event description in ATLAS a right handed coordinate system, adjusted to the barrel geometry of the experiment, is used. The nominal interaction point is used as origin of the coordinate system with the z-axis pointing into beam direction. The x-y plane is perpendicular to the beam with the x-axis pointing to the centre of the LHC and the y-axis pointing upward. The azimuthal angle ϕ is measured in the x-y plane, with respect to the x-axis and

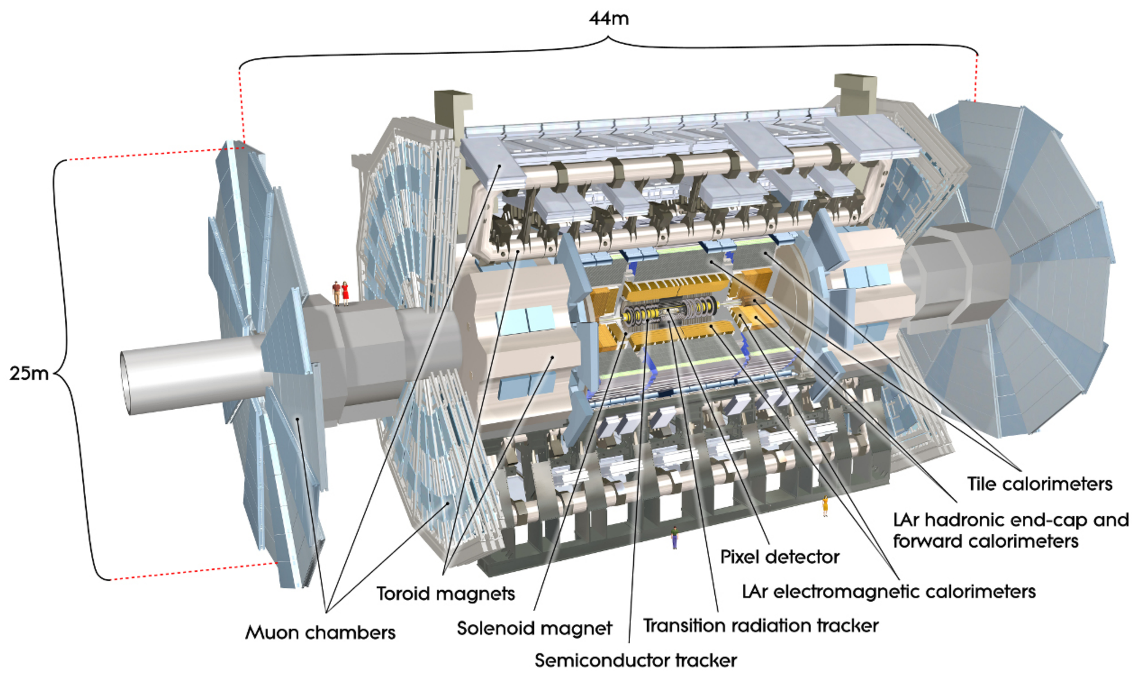

Figure 3.2: Overview of the ATLAS experiment [111].

the polar angle θ is measured with respect to the beam axis. Instead of θ the pseudorapidity

$$\eta = -\ln \tan\left(\frac{\theta}{2}\right) \tag{3.2}$$

is often used to describe the direction of particles, which is identical to the rapidity

$$y = \frac{1}{2}\ln\left(\frac{E+p_z}{E-p_z}\right) \tag{3.3}$$

for massless particles. The angular distance of two objects as seen from the origin of the coordinate system is defined as:

$$\Delta R = \sqrt{\Delta\eta^2 + \Delta\phi^2}\,. \tag{3.4}$$

and the momentum transverse to the beam axis p_{T} is defined as the projection of the momentum to the x-y plane:

$$p_{\mathrm{T}} = \sqrt{p_x^2 + p_y^2}\,. \tag{3.5}$$

For objects which leave a trace in the calorimeters, the so-called transverse energy E_{T} is defined as:

$$E_{\mathrm{T}} = E \cosh\eta\,. \tag{3.6}$$

Finally, neutrino activity or BSM physics signals can cause an imbalance of the transverse energy, which should add up to zero (in the limit of perfect detector resolution) since the colliding particles have only longitudinal momentum.

The missing transverse momentum is defined as:

$$\begin{aligned}\vec{E}_{\mathrm{T}}^{\mathrm{miss}} &= -\sum_{\text{rec. objects}} \vec{p}_{\mathrm{T}},\\ E_{\mathrm{T}}^{\mathrm{miss}} &= \left|\vec{E}_{\mathrm{T}}^{\mathrm{miss}}\right|\end{aligned} \tag{3.7}$$

where the sum runs over all reconstructed objects. In the reconstruction of $E_{\mathrm{T}}^{\mathrm{miss}}$ all visible particles are included, therefore all subdetector systems of ATLAS are relevant. The sum of the transverse momenta can be determined by track information, calorimetric information or a combination of both.

3.2.1 Inner Detector

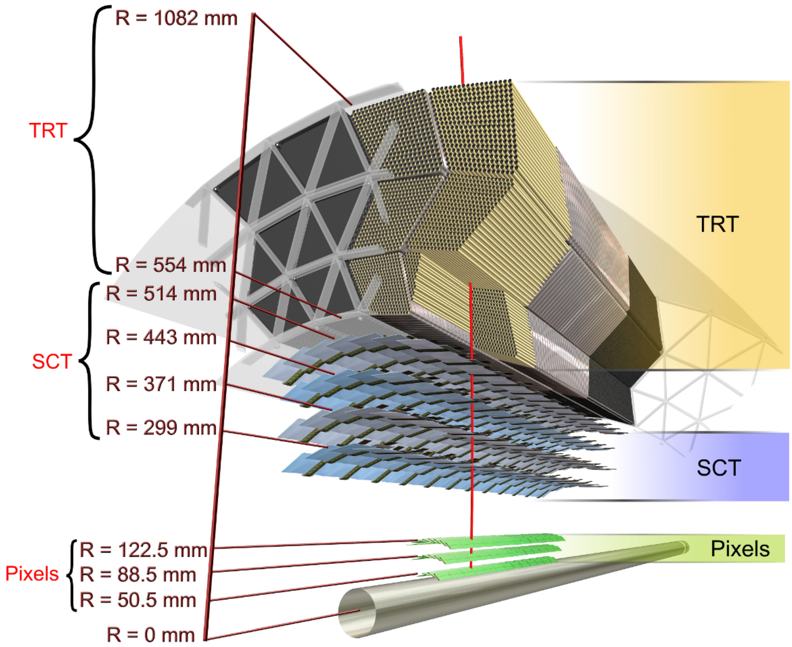

Figure 3.3: Overview of the Inner Detector system of the ATLAS experiment [112]. The image shows a cross section of ATLAS's barrel at $\eta = 0.3$.

The Inner Detector (ID), as depicted in Figure 3.3, consists of three independent subdetectors: the pixel detector, Semiconductor Tracker (SCT) and Transition Radiation Tracker (TRT) which allow the measurement of the trajectories (or tracks) of charged particles with high spatial, angular and momentum resolution. While the first two are semiconductor detectors, the latter is a straw detector which enhances the pattern recognition and improves the momentum resolution over $|\eta| < 2.0$ [98]. The ID is 6.2 m long, has a diameter of 2.1 m and covers a pseudorapidity range of $|\eta| < 2.5$. The silicon detectors must be kept at -5 °C to -10 °C in order to maintain adequate noise performance after radiation damage [98] while the TRT can be operated at room temperature. The deflection of charged particles, which allows the measurement of the particle momenta, is enforced by a solenoid magnetic field with the field strength of 2 T.

The innermost detector is a three-layered pixel detector [113, 114] arranged in concentric cylinders of overlapping staves (barrel) and disks (end-cap) with 1744 pixel sensors in total which cover a pseudorapidity range of $|\eta| < 2.5$. It contains about 80 million readout channels which provide the capability for pattern recognition and track reconstruction at the full LHC luminosity. The pixel detector is most important for the identification and reconstruction of secondary vertices and jets originating from b quarks. In addition to pseudorapidity coverage the performance requirements are [114]:

- A resolution better than 15 μm in the x-y plane;
- Good resolution in longitudinal direction, allowing primary vertex reconstruction of charged tracks with $\sigma(z) < 1$ mm;
- Very good identification of jets which contain bottom quarks both in the high-level trigger and in the offline reconstruction;
- Radiation hardness of the pixel detector elements to operate after a total dose of 500 kGy.

The design choices meeting these requirements are the three-layer design which allow three pixel hits over the full pseudorapidity range [115], the minimal radius of 5.5 cm around the beam axis of the innermost layer due to limitations of the beam pipe vacuum system and the smallest available pixel size of 50×400 μm^2 (about 90% of the pixels) and 50×600 μm^2 (about 10% of the pixels). Typical resolution values in r-ϕ direction are about 10 μm and about 115 μm in beam direction. In order to improve the resolution further, during the long shutdown 1 the ID has been equipped with an additional innermost pixel layer called Insertable B-Layer (IBL) [116]. It was installed between the existing pixel detector and a new beam pipe at a radius of 3.3 cm and the pixels used for the IBL have a finer granularity of 50×250 μm^2 compared to the ones used for the pixel detector. Together with the improved b-tagging algorithms [117], the IBL increases the rejection of light flavour jets by a factor of 4 at low p_{T} compared to run 1 [118].

The SCT [119] is built around the pixel detector and has a similar structure: In the barrel it consists of four layers and in the end-cap region it has nine disks. In contrast to the pixel detector, SCT uses 80 μm $\times$ 6.5 cm micro-strip sensors instead of pixel sensors with 6.3 million readout channels. To improve measurements in beam direction, the modules are rotated by ± 20 mrad around their geometrical centres. This configuration allows at least four space-point measurements over the coverage of the detector. The resolution of the SCT is about 17 μm in r-ϕ direction and about 580 μm in beam direction.

The outermost component of the ID is the TRT [120] which contains thin-walled proportional drift tubes or straws in the barrel and in the end-caps. In the barrel 52 544 straws with a length of 144 cm oriented parallel to the beam axis are used while the end-caps contain 122 880 straws with a length of 37 cm each. Particles which are emitted in a pseudorapidity range of $|\eta| < 2$ and with a transverse momentum of $p_{\mathrm{T}} > 0.5$ GeV traverse $35 - 40$ straws of the detector in the barrel, providing tracking at higher radii in the ID. In the end-caps ($0.8 < |\eta| < 1.0$) only 22 hits in the detector are possible. Each straw has a inner diameter of 4 mm and is filled with a xenon-gas mixture which is ionised if it is hit by a charged particle which in turn can be detected. In addition, high energetic particles (mostly electrons) generate X-rays which also ionise the xenon and therefore amplify the signal. The intrinsic resolution in r-ϕ direction is 130 µm.

3.2.2 Calorimetry

Around the ID and the solenoid magnet the calorimetric system of ATLAS can be found. It consists of two sampling calorimeters, the first an electromagnetic calorimeter (ECAL) used for the energy measurement of electrons and photons and the second a hadronic calorimeter (HCAL) which measures the energy of hadrons and jets respectively. An overview of the calorimetric system is given in Figure 3.4.

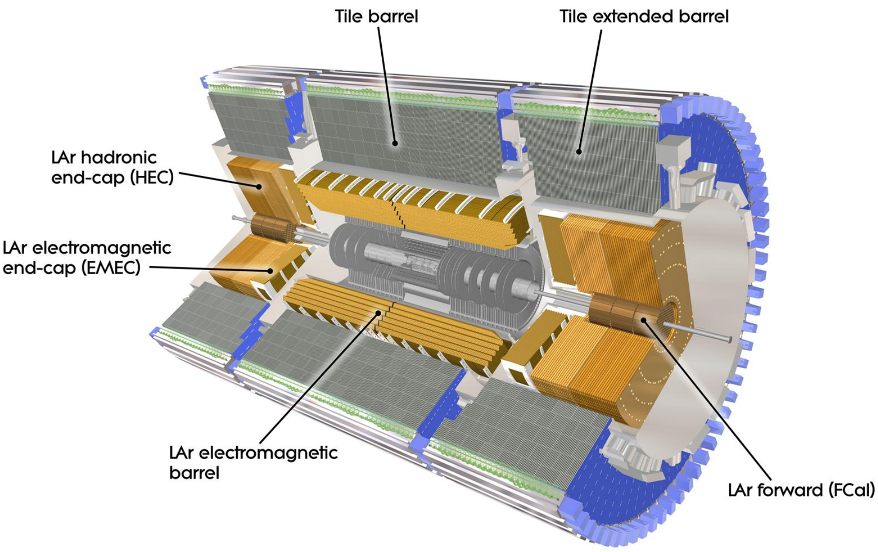

Figure 3.4: Overview of the calorimetric system of the ATLAS experiment [121].

The ECAL [122] consists of liquid-argon detectors with accordion-shaped absorbers and electrodes [98], which ensure a full azimuthal symmetry. It is separated into three parts: the barrel, which covers $|\eta| < 1.5$, two end-caps, covering $1.5 < |\eta| < 3.2$ and two forward calorimeters [123] which cover $3.1 < |\eta| < 4.9$. Due to the liquid argon, which acts as active material for the shower detection, the calorimetric system has be cooled to a temperature of 88 K.

The absorbing materials are lead (barrel) and copper (forward calorimeters). In the precision-measurement region $|\eta| < 2.5$ three active layers are deployed, while in the region with higher pseudorapidity $2.5 < |\eta| < 3.2$ and in the overlap region between barrel and end-caps two active layers are used. The first layer has the finest granularity in η and its main task is to measure the direction of the particle shower. The second layer is designed to collect the largest fraction of energy of the electromagnetic shower and the last layer collects the tail of the shower and therefore has a coarse granularity but is also used for trigger events. The ECAL is built from two half-barrels that are centred around the beam axis. One of the half-barrels covers the positive z range ($0 < \eta < 1.475$) while the other one covers the negative z range ($-1.475 < \eta < 0$). Each of them has a length of 3.2 m and inner/outer radii of 1.4 m and 2 m respectively, which corresponds to about 24 radiation lengths. The end-caps are 63 cm thick, corresponding to about 26 radiation lengths.

Around the ECAL, the HCAL [124] with the inner and outer radii of 2.28 m and 4.25 m, is built. It is divided into three barrel modules, two end-caps and two forward calorimeters. The barrel module covers the pseudorapidity range of $|\eta| < 1.0$, the two extended barrel modules cover $0.8 < |\eta| < 1.7$, the end-caps cover $1.5 < |\eta| < 3.2$ and the forward calorimeters have a coverage of $3.1 < |\eta| < 4.9$. Similar to the ECAL, the HCAL is segmented into three layers in the barrel and the extended barrel with steel absorber plates and scintillator tiles as active medium. Each layer corresponds to 1.5, 4.1 (2.6), 1.8 (3.3) interaction lengths for the (extended) barrel. In the end-caps and in the forward calorimeters liquid argon is used as active material and copper (tungsten) as absorber in the end-caps (forward calorimeters). Due to the liquid argon, the end-caps and the forward calorimeters are housed in the same cryostats as the ECAL end-caps. The angular segmentation of the barrel-shaped calorimeters is 0.1×0.1 ($\Delta\phi \times \Delta\eta$), which provides a good resolution for high-energetic jets and missing transverse momentum.

3.2.3 Muon Spectrometer

The outermost detector of the ATLAS experiment is the muon spectrometer (MS) [125] which is designed to detect charged particles, that are not stopped in the calorimeters. The main tasks of the MS are the precise measurement of the momentum of muons in a pseudorapidity range of $|\eta| < 2.7$ and triggering events with high-energetic muons with $|\eta| < 2.4$.

The muon chambers (see Figure 3.5) are located between and on top of the eight coils of the superconducting toroid magnet which surrounds the barrel, while the end-cap chambers are in front and behind the two end-cap toroid magnets [98]. In order to measure the particle momentum, the coils of the barrel toroid provide a magnetic field strength of 0.5 T perpendicular to the particle trajectories, while the magnetic field strength of the end-cap magnets is 1 T. The magnetic field is monitored by about 1800 Hall sensors distributed throughout the MS.

For the MS four different detector techniques are utilised: In the barrel three layers of monitored drift tubes (MDTs) provide the muon tracking in a pseudorapidity region of $|\eta| < 2.7$, in the

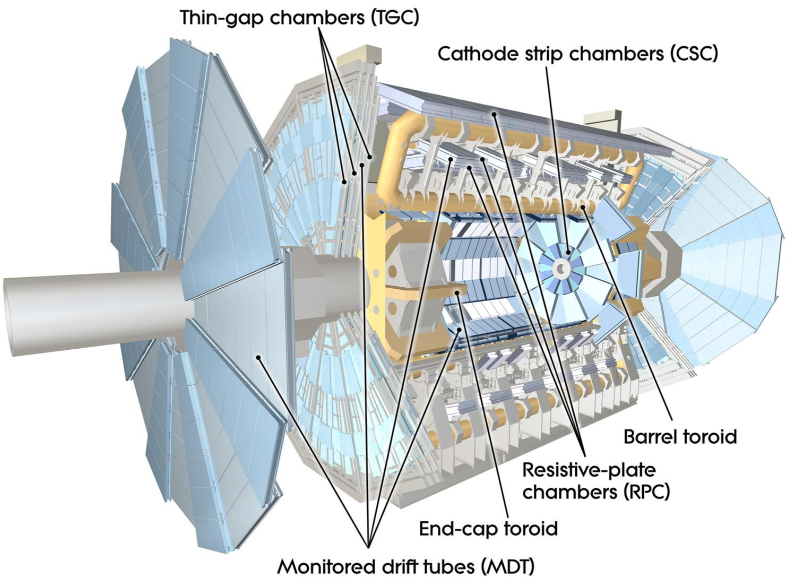

Figure 3.5: Overview of the muon system of the ATLAS experiment [126].

end-caps an additional layer of cathode strip chambers (CSCs) is used, since CSCs have a higher rate capability and time resolution. In the pseudorapidity range of $|\eta| < 2.4$ resistive plate chambers (RPCs) in the barrel and thin gap chambers (TGCs) in end-caps are used as additional trigger chambers.

The MDTs are arranged in three concentric layers around the beam axis with radii of 5 m, 7.5 m and 10 m. They are built from aluminium tubes filled with an argon-gas mixture with a pressure of 3 bar and provide a resolution of 80 µm (35 µm in beam direction) per chamber in the pseudorapidity range $|\eta| < 2.7$. The additional CSCs, which cover a pseudorapidity range of $2.0 < |\eta| < 2.7$, provide a spatial resolution of 40 µm in the y-z-plane (bending plane) and of 5 mm in the transverse plane.

3.2.4 Forward Detectors

Additional to the ATLAS main detectors three so-called forward detectors are placed around ATLAS to measure the luminosity.

The first detector is situated ± 17 m away from the interaction point and is called Luminosity measurement using Cerenkov Integrating Detector (LUCID) [127]. It is a relative luminosity detector and its main purposes are the measurement of the integrated luminosity and the monitoring of the instantaneous luminosity and the beam conditions. Therfore, it surrounds the beam pipe in a distance of 10 cm and measures inelastic pp collisions in the forward direction of about $|\eta| \approx 5.8$.

The second system, seen from the interaction point, is Large Hadron Collider forward (LHCf) [128] which is designed to measure particles which are produced very close to the beam direction in proton-proton collisions to test models used to estimate the energy of cosmic rays. It is located ± 140 m away from the interaction point.

Finally, with ± 240 m the most remote system of the forward detectors, is Absolute Luminosity for ATLAS (ALFA) [129]. It is used to determine the absolute luminosity via elastic scattering at small angles. The total cross section – and therefore the luminosity – can be measured exploiting the optical theorem [130], which connects the forward scattering amplitude with the total cross section. To get as close as possible to the beam, Roman pot technology is used which allows to get as close as 1.5 mm to the beam line. In 2012 ALFA was not running and therefore no measurement has been performed.

3.2.5 Trigger System

As seen in Table 3.1 with a bunch spacing of 25 ns the event rate is 40 MHz and with an average size of 1.5 MB per event there is no technology available to readout and store all events delivered by the LHC. Therefore a trigger system is utilised to reduce the output rate and to enrich the selected sample with events of rare processes.

In ATLAS a three-levelled trigger system [131, 132] is used, which reduces the output rate from 40 MHz to 200 Hz after the full trigger chain. The level 1 (L1) trigger is hardware based with custom-made electronics, while the level 2 (L2) trigger and the event filter (EF) (combined referred to as high-level trigger (HLT)) are software triggers, almost entirely based on commercially available computers and networking hardware [98].

In the L1 trigger, the output rate is reduced to 75 kHz based on kinematic and energetic characteristics from the event. The selected events contain signatures of high-p_{T} muons, electrons and photons, jets and tau leptons, which decay into hadrons. Since it is very hard to deflect particles from the beam line, events passing the L1 trigger need a large total transverse energy and large fraction of missing transverse momentum $E_{\mathrm{T}}^{\mathrm{miss}}$, indicating neutrino activity. The L1 trigger uses the RPCs and TGCs to gather information about the muon-p_{T}, while the identification of the other particles is based on calorimetric information with reduced granularity.

Events passing the L1 trigger are processed, supported by fine-granularity data of the detectors, by the L2 trigger in so-called region of interests (ROIs) that have been defined during the L1 trigger process. The ROIs consist of geometrical information about events which have been retained in the muon and calorimeter trigger processors [98]. In addition, the L2 trigger uses ID information which is not available for the L1 trigger, reducing the output rate to 2 kHz.

The last step after the event building process in the trigger chain is the EF. It uses offline analysis procedures including complex pattern recognition algorithms and has access to the fully reconstructed event in order to reduce the output rate to 200 Hz. The full granularity and precision of the calorimeter, the muon chamber data and the ID is used to thin out the trigger selections in the HLT.

3.3 Performance of the ATLAS Experiment

The general performance goals for ATLAS's subdetector systems in Table 3.3 allow precise measurement of tracks, momentum, energy and electric charge of the proton collision's decay products.

Table 3.3: Performance goals for the ATLAS subdetector systems [98].

Detector component	Required resolution	η coverage Measurement	Trigger
Inner detector	$\sigma_{p_T}/p_T = 0.05\%/p_T \oplus 1\%$	± 2.5	–
EM calorimetry	$\sigma_E/\sqrt{E} = 10\%/\sqrt{E} \oplus 0.7\%$	± 3.2	± 2.5
Hadronic calorimetry			
barrel and end-cap	$\sigma_E/\sqrt{E} = 50\%/\sqrt{E} \oplus 3\%$	± 3.2	
forward	$\sigma_E/\sqrt{E} = 100\%/\sqrt{E} \oplus 10\%$	$3.1 < \lvert\eta\rvert < 4.9$	
Muon spectrometer	$\sigma_{p_T}/p_T = 10\%$ at $p_T = 1$ TeV	± 2.7	± 2.4

The reconstruction efficiencies of the various objects have been determined and are briefly described for electrons, muons and the energy calibration, since those are the important objects regarding this analysis. All efficiencies lie within the design goals.

The electron/photon and muon reconstruction efficiencies have been measured, documented in Refs. [133, 134]. The reconstruction efficiency for electrons has increased by 5% compared to the data taken in 2010. After averaging over η the efficiency is between 97% for electrons with an $E_T = 15$ GeV and 99% at $E_T = 50$ GeV while the uncertainty is between 0.5% and 1.5%. For muons, the reconstruction efficiency is 99% for $|\eta| < 2.5$ and $p_T > 10$ GeV with an uncertainty smaller than 0.2% [134].

The energy calibration has been performed with electrons from Z-boson decays [135] and its uncertainties lie between 0.05% for high-E_T electrons in the central part of the detector and 0.2–1% for electrons with $E_T = 10$ GeV. The relative uncertainty of the detector energy resolution is less than 10% for electrons with $E_T < 50$ GeV and asymptotically rises to 40% for electrons with high energy [135].

In 2012 ATLAS collected an integrated luminosity of 21.3 fb^{-1}, with a peak luminosity of $7.33 \cdot 10^{33}$ cm^{-2} s^{-1} [136] from which 20.3 fb^{-1} can be used for physics. Figure 3.6 shows the data delivered by the LHC, the data collected by ATLAS and the fraction which fulfils quality criteria and is declared as good for physics.

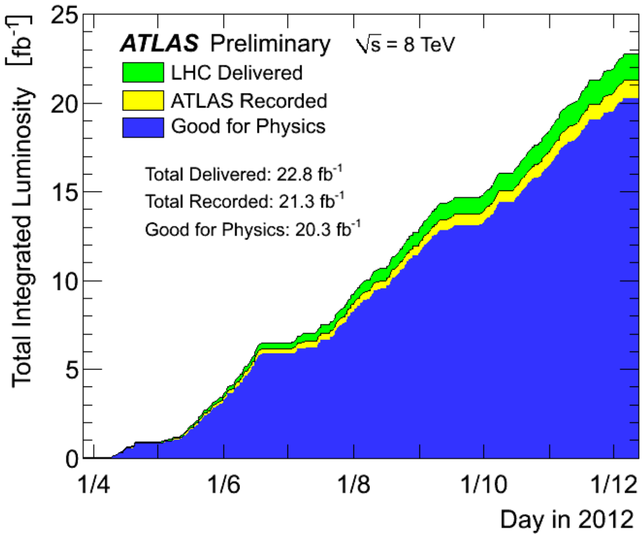

Figure 3.6: Cumulative luminosity versus time, delivered to (green) and recorded by ATLAS (yellow) during stable beams and for *pp* collisions at 8 TeV centre-of-mass energy in 2012. The amount of luminosity which is certified to be good quality data is depicted in blue [137].

The reason that not the full amount of data delivered by the LHC could be recorded by ATLAS is mainly due to the data-taking efficiencies of the detector subsystems which are described in Ref. [136] and are summarised in Table 3.4.

Table 3.4: Data-taking efficiency for the ATLAS subdetector systems [136].

Detector component	Operational fraction	Data taking efficiency
Inner detector		
Pixel	95.0%	99.9%
SCT	99.3%	99.1%
TRT	97.5%	99.8%
EM calorimetry	99.9%	99.1%
Hadronic calorimetry		
Tile calorimeter	98.3%	99.6%
End-cap calorimeter	99.6%	99.6%
Forward calorimeter	99.8%	99.6%
Muon spectrometer		
MDTs	99.7%	99.6%
CSCs	96.0%	100%
RPCs	97.1%	99.8%
TGCs	98.2%	99.6%
Trigger	100%	100%

4 | Object Definitions and Data Sets

After the LHC and the ATLAS detector systems have been briefly described in the previous chapter, in the following it is described how to determine charged particle tracks and energy clusters from the detector information. These tracks and clusters can be classified as electron, muon or jet candidates and are used for physics analyses.

4.1 Reconstruction and Object Definitions

In the following sections an overview is given how the physics objects, which are used in data analysis, are obtained from the information available by the detector readout. Similar to the description of the ATLAS detector systems in Chapter 3, the description of the object reconstruction starts from the ID with track and vertex reconstruction followed by the reconstruction of particle candidates aided by calorimeter and muon spectrometer information.

4.1.1 Tracks and Vertices

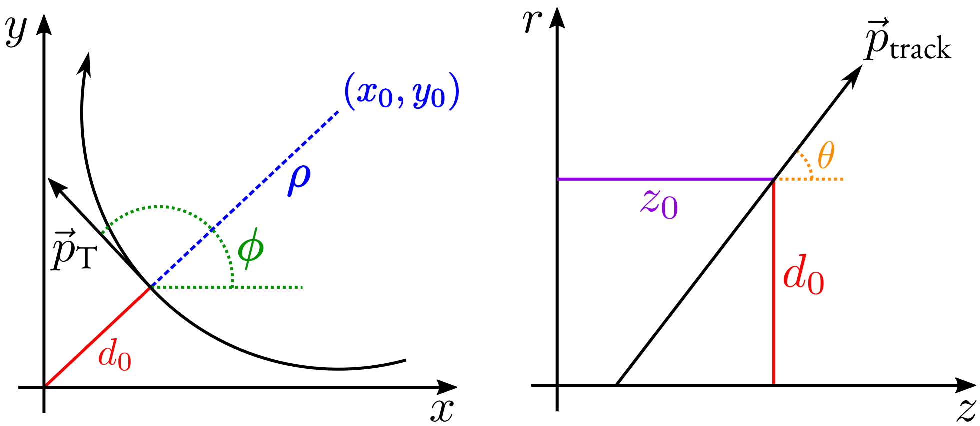

(a) Track parametrisation in the x-y plane. **(b)** Track parametrisation in the r-z plane.

Figure 4.1: Parametrisation of a charged particle track in the x-y plane (a) and in the r-z plane (b). Due to the magnetic field, the particle is only deflected in the x-y plane [138].

The trajectories of charged particles in uniform magnetic fields have the shape of a helix. Track candidates are parametrised in terms of the two impact parameters d_0 and z_0 in the transverse and longitudinal plane respectively, as depicted in Figure 4.1. Further parameters of the track are the polar and azimuthal angles θ and ϕ, its momentum $\vec{p}_{\text{track}}$ and its transverse momentum $\vec{p}_{\text{T}}$.

In ATLAS, tracks are reconstructed using the measurements of all ID subdetectors: Pixel, SCT and TRT. The main reconstruction strategy is called *inside-out strategy* [138], since it starts with exploiting pixel and SCT measurements and extending the particle trajectories to the TRT for a full ID track reconstruction. The inside-out track reconstruction is performed in three steps: Pattern recognition, ambiguity solving and TRT track extension.

For the pattern recognition, pixel and SCT hits are used to define three-dimensional space points. A track seed for the pattern recognition is found, if the trajectory, defined by at least three space points, is compatible with a transverse momentum larger than 500 MeV. A Kalman-filter algorithm [139, 140] is applied to the seed in order to follow the trajectory and a track candidate is formed if the track seeds can be extended to contain at least seven hits in the silicon detectors.

Since many of the track candidates share hits, are incomplete, or are fake tracks, they are ranked according to the likelihood, that the track candidate originated from a real particle. In general, a higher number of hits of the track candidate increases the likelihood in order to favour fully constructed tracks over smaller segments, while lower numbers of hits or holes (reconstructed tracks through a disabled detector element) deprecate the likelihood [138]. After the selection of the track candidates a global χ^2 fit to the space points is performed to obtain the track parameters and the trajectory.

Finally the TRT hits are included to obtain the complete track. The track, fitted with hits from Pixel and SCT, is used to define a path through the TRT where hits within a drift radius of 10 mm around this path are assigned to the track. The track is then refitted with the additional TRT information and compared with the pixel/SCT track where finally the track with the highest likelihood is selected.

As can be seen in Figure 4.2, signal events which are triggered and reconstructed in the ATLAS detector can be superimposed by many proton-proton interactions with low transverse momentum (also called pile up). The determination of the primary vertex – the vertex of the triggered event – is therefore a crucial task. The region where collisions can take place is confined by the beam spot which can be described by a Gaussian profile with a standard deviation of about 5 cm in beam direction and about 15 µm in the transverse plane.

The reconstruction of primary vertices consists of two intersecting stages: The vertex finding and the vertex fitting [141]. In the finding step, the association of reconstructed tracks to vertex candidates is performed while in the fitting step the actual position and refitted tracks are obtained. The ATLAS software provides two approaches for the vertex reconstruction, namely *fitting-after-finding* and *finding-through-fitting*.

In the *fitting-after-finding* method, the tracks are ordered according to their impact parameter in beam direction and the obtained clusters are regarded as primary vertex candidates. Each of the candidates is reconstructed by a vertex fitter [142] and ordered according to their value of the z_0-impact parameter. The track clusters, obtained by a search with a sliding window

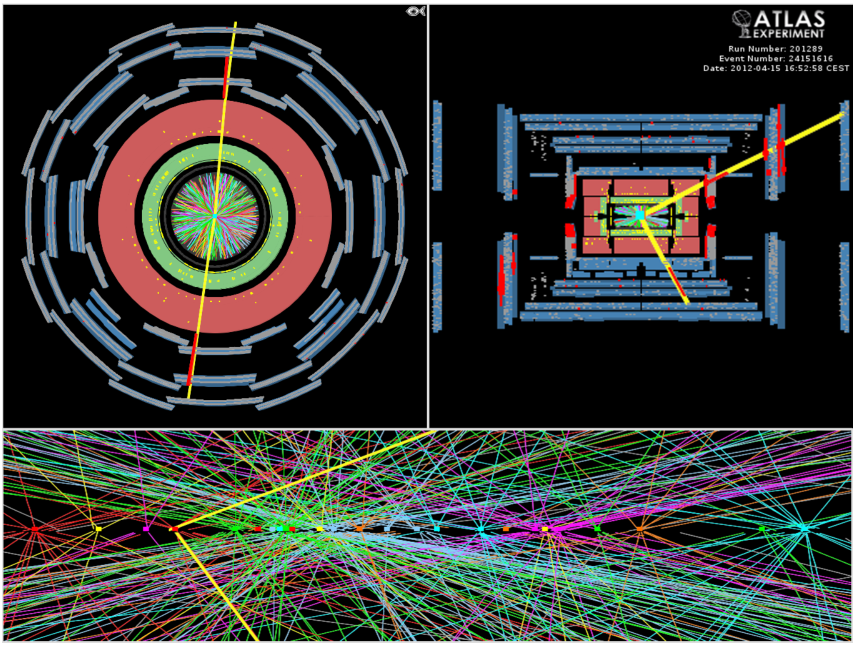

Figure 4.2: A candidate Z boson event in the dimuon decay with 25 reconstructed vertices. This event was recorded on April 15th 2012 and demonstrates the high pile up environment in 2012 running. For this display the track p_{T} threshold is 0.4 GeV and all tracks are required to have at least 3 Pixel and 6 SCT hits [143].

approach utilising the projection of z_0 to the beam axis, are regarded as initial primary vertex candidates. Each candidate is then reconstructed and iteratively cleaned from outliers. The number of reconstructed primary vertices in this approach is determined at the seeding stage and once a track is rejected from a vertex candidate it is never used in another cluster [141].

In contrast, the *finding-through-fitting* approach has a better way of dealing with outlying tracks and is therefore used in this analysis. Similar to the *fitting-after-finding* method, the reconstruction starts with a preselection of tracks coming from the bunch crossing region. A single vertex candidate is reconstructed from the selected tracks and the tracks which are considered as outliers form a new vertex seed. At the following iteration the fitting of two vertices is performed and the number of vertices grows in each further iteration. Since each track is downweighted with the number of vertices, they compete with each other in order to attain more tracks [141].

While most of the collisions take place at the primary vertex, some long-lived particles e.g. b-hadrons can decay at a significant distance from the primary vertex and tracks associated with such decays can be used to identify secondary vertices. While a primary vertex is often formed by the intersection of 20 or more tracks, secondary vertices are often fitted by only 2 or 3 tracks.

4.1.2 Electron Candidates

The reconstruction and identification of electrons plays an important role in this analysis since electrons are one of the final state objects of the regarded decay channel. The reconstruction separates between so-called central electrons ($|\eta| < 2.5$), where ID information can be used, and forward electrons ($|\eta| > 2.5$) which is not equipped with tracking detectors. In this analysis only central electrons are used.

The reconstruction of central electrons is a three-step process [144]: It starts with cluster reconstruction, where electromagnetic clusters are built from seeds with energy deposits of $E_{\mathrm{T}} > 2.5$ GeV in the second layer of the ECAL. From MC simulations of the leptonic decay of W and Z bosons, the reconstruction efficiency is expected to be about 97% at $E_{\mathrm{T}} = 7$ GeV and almost 100% at energies $E_{\mathrm{T}} > 20$ GeV [144].

In the next step tracks are associated with the electromagnetic clusters. Tracks are extrapolated to the cluster seed in the second layer of the ECAL and matched successfully if the distance between the track impact point and the centre of the cluster is small ($|\Delta\eta| < 0.05$, $\Delta\phi < 0.1$). If at least one track can be matched with a cluster, the electron candidate is considered to be reconstructed. In case of more than one matched track, the one with the smallest ΔR distance is chosen.

Finally, the cluster sizes of the reconstructed electron candidates are optimised to take the energy distributions in the different regions of the ECAL into account. In the barrel region the cluster is enlarged to 3×5 cells and in the end-caps the size is increased to 5×5 cells. The total energy of the electron candidate is determined by the estimated energy deposit in the material in front of the ECAL, the measured energy deposit in the cluster, the estimated energy deposit outside of the cluster (lateral leakage) and the estimated energy deposit beyond the ECAL (longitudinal leakage) [144].

In order to allow a good separation between isolated and non-isolated electrons, misidentified electrons from hadrons and electrons from photon conversions, the electron identification relies on sequential cuts on calorimeter and tracking variables optimised in 10 η and 11 E_{T} bins, where the number of bins is motivated by the detector structure. For physics analyses three sets of selection criteria, also called operation points, are available called *loose*, *medium* and *tight*. As the names suggest, they are designed hierarchical and provide increasing background rejection at the cost of identification efficiency. The rejection power is achieved by adding discrimination variables at each step and tightening the requirements on the other variables.

The *loose* electron selection uses shower-shape variables in the first two layers of the ECAL. Further requirements on the track quality (at least 7 hits in the silicon detectors and $|\Delta\eta| < 0.015$ between the hit position in the first layer and the extrapolated track) and the association of clusters and tracks improve the rejection of hadronic backgrounds in the transverse energy range $30\ \mathrm{GeV} < E_{\mathrm{T}} < 40\ \mathrm{GeV}$ by a factor of about 5 while keeping a high identification efficiency of up to 97%, see Figure 4.3(a).

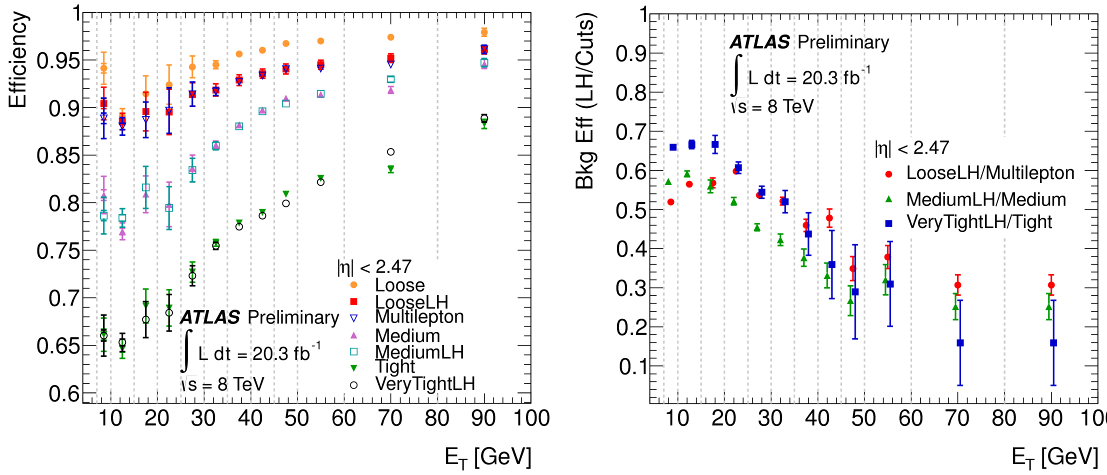

(a) Measured identification efficiency for the various cut-based and LH selections as a function of E_T. The uncertainties are statistical (inner error bars) and statistical+systematic (outer error bars) [133].

(b) Ratio of background efficiencies for a LH and the closest-efficiency cut-based selections as a function of E_T. The uncertainties are statistical as well as systematic [133].

Figure 4.3: Identification efficiencies for electron and background candidates in different selections.

Figure 4.3(a) shows the electron identification efficiency of the cut-based selections compared to the likelihood selections where both perform equally well. Figure 4.3(b) shows the ratio of the background identification efficiencies of the different selections where the likelihood selections clearly have an advantage.

The *medium* selection is based on the *loose* selection and adds the requirement of a measured hit in the innermost pixel layer, which allows a good rejection of photon conversions. Further a basic selection is required on the transverse impact parameter and signals in the TRT to reject charged-hadron background. The background rejection is increased by an order of magnitude by tightening the *loose* requirements.

The *tight* selection uses all identification tools available to increase the rejection power by a factor of two compared to the *medium* selection. In comparison to the *medium* selection the requirements on the discriminating variables and the track quality in presence of an extension in the TRT are tightened. Additionally, a cut on the cluster-energy to track-momentum ratio is performed and a veto on reconstructed photon conversion vertices is applied.

An overview of the exact cuts applied in the different identification selections is given in Ref. [144].

In addition, ATLAS uses multivariate-analysis (MVA) techniques for the electron identification, since they allow a combined evaluation of several variables and their correlation. In ATLAS the likelihood (LH) technique [133] is used, which utilises the signal and background probability density functions (pdfs) of the discriminating variables. Based on these, a discriminant is defined on which a cut is applied.

Similar to the cut-based approach different selections are available called *LooseLH*, *MediumLH* and *Very Tight LH* (*VTLH*) which are designed to roughly match the selection efficiencies of the cut-based *loose*, *medium* and *tight* selections, but to perform better at the rejection of light-flavour jets and conversions. For each operation point the bin division for E_{T} is 6 bins and 9 bins for $|\eta|$. The binning is similar but coarser compared to the cut-based selection and it is chosen to balance the available data statistics with the variation of the pdf shapes of the input variables in E_{T} and $|\eta|$ [133].

In this analysis two different selections are used depending on the E_{T} range of the electron candidate. In the low range 10 GeV $< E_{\mathrm{T}} <$ 25 GeV where the contribution of W + jets/QCD multijet background is largest, the *VTLH* selection is used since it performs best in the background rejection, while being comparable with the electron identification efficiency of the *tight* selection which can be seen in Figure 4.3.

In the high-E_{T} range $E_{\mathrm{T}} >$ 25 GeV the cut-based *medium++* identification is used for which, compared to the *medium* selection, additional requirements against photon-to-electron conversion are taken into account and which improves the rejection efficiency against conversion background and increases the electron purity.

Table 4.1: Electron identification and isolation cuts as a function of E_{T}.

<table>
<tr><th>E_{T} [GeV]</th><th>Electron ID</th><th>Calo. isolation</th><th>Track isolation</th><th>Impact parameters</th></tr>
<tr><td>10 – 15</td><td rowspan="3">VTLH</td><td>$E_{\mathrm{T}}^{\mathrm{cone30}}/E_{\mathrm{T}} < 0.20$</td><td>$p_{\mathrm{T}}^{\mathrm{cone40}}/E_{\mathrm{T}} < 0.06$</td><td rowspan="4">$d_0/\sigma_{d_0} < 3.0$
$z_0 \sin\theta < 0.4$ mm</td></tr>
<tr><td>15 – 20</td><td>$E_{\mathrm{T}}^{\mathrm{cone30}}/E_{\mathrm{T}} < 0.24$</td><td>$p_{\mathrm{T}}^{\mathrm{cone30}}/E_{\mathrm{T}} < 0.08$</td></tr>
<tr><td>20 – 25</td><td rowspan="2">$E_{\mathrm{T}}^{\mathrm{cone30}}/E_{\mathrm{T}} < 0.28$</td><td rowspan="2">$p_{\mathrm{T}}^{\mathrm{cone30}}/E_{\mathrm{T}} < 0.10$</td></tr>
<tr><td>> 25</td><td>medium++</td></tr>
</table>

In addition to the identification efficiencies so-called isolation criteria are also applied in order to reject further W + jets/QCD multijet background. The isolation is performed by cuts on $E_{\mathrm{T}}^{\mathrm{cone}X}/E_{\mathrm{T}}$ and $p_{\mathrm{T}}^{\mathrm{cone}X}/p_{\mathrm{T}}$ which describe the sum of energy deposited in the calorimeter/sum of track momentum in a cone $\Delta R < X\%$, where the E_{T} or p_{T} of the regarded object is subtracted. Further cuts on the longitudinal impact parameter $z_0 \sin\theta$, where θ is the angle between beam axis and electron track and on the transverse impact parameter d_0 relative to its uncertainty σ_{d_0} are applied in order to select the correct vertex. The applied cuts are summarised in Table 4.1

4.1.3 Jet Candidates

As described in section 2.1, strongly interacting particles cannot be observed solitarily in the detector, but they form particle jets during their hadronisation process. In ATLAS, jets are reconstructed from topological clusters in the calorimeters using the anti-k_{T} algorithm [145]. As a part of a broader class of sequential recombination algorithms, the anti-k_{T} algorithm mainly relies on a specific distance measure d_{ij} between the jet candidates i and j (combined topological clusters of the calorimeters) and d_{iB}, which is the distance measure between the jet candidate i and the beam axis B. The distance measures are given by:

$$d_{ij} = \min\left(p_{\mathrm{T},i}^{2n}, p_{\mathrm{T},j}^{2n}\right)\frac{\Delta R_{ij}^2}{R^2}, \tag{4.1}$$

$$d_{iB} = p_{\mathrm{T},i}^{2n}, \tag{4.2}$$

where ΔR_{ij} is the angular distance for jet candidates i and j from equation (3.4) and n parametrises the different types of algorithms. For $n = 1$, the algorithm is known as k_{T} algorithm [146], for $n = 0$ it is known as Cambridge/Aachen algorithm [147, 148] and for $n = -1$ it is called anti-k_{T} algorithm. The parameter R describes the radius of the cone, in which soft partons are accumulated into the jet and is set to $R = 0.4$.

In the first step of the algorithm, the minimum d_{min} of all d_{ij} and d_{iB} is determined. If d_{min} is found to be of the type d_{iB}, the object i is considered as jet and removed from the list of candidates. On the other hand, if d_{min} is found to be one of the d_{ij} the objects i and j are merged into a new object and the minimisation continues.

An important feature of the presented algorithms is their infrared and collinear safety which means, that the number and the shape of jets should not be altered neither by soft-gluon radiation (which accounts for infrared divergences in scattering amplitudes) nor by the splitting of a hard parton into two collinear ones (which accounts for collinear divergences in scattering amplitudes). In the case of the anti-k_{T} algorithm, soft partons within a circle of radius R are simply accumulated into the jet at the end of the clustering process and if a parton splits into two with collinear momenta, the algorithm recombines them immediately producing the same result as before [146].

As described above, jet candidates are reconstructed from topological clusters in the calorimeters, where the baseline for the jet energy scale (JES) calibration is the electromagnetic scale, determined using test-beam measurements for electrons and muons in the ECAL and HCAL [149]. In addition to this initial scale, jets need to be corrected on two levels: using the properties of clusters or cells in the HCAL and using jet kinematics. The correction of jet kinematics can be derived independently of the cluster-level corrections, however the latter needs an overall JES correction.

The cluster-level correction method used in this analysis is called local-cluster-weighting (LCW) method, which relies on differences in shower profiles between electromagnetic and hadronic signals [150]. In the LCW method electromagnetic and hadronic clusters are distinguished based on shower depth, cell-energy density, cluster energy and pseudorapidity. These variables are used to weight the clusters of the HCAL in order to correct for the hadronic response, dead material and out-of-cluster deposits [151].

The jet-level corrections are performed in four steps [150]:

1. The LCW jets are first calibrated by a correction to account for the energy offset caused by pile-up interactions.

2. The jet direction is corrected to back to the primary vertex instead of the centre of the ATLAS detector.
3. The jet calibration is derived by relating the reconstructed jet energy to the truth jet energy, obtained by MC events. After this stage, the jets are referred to as LCW+EW (electroweak) jets.
4. The so-called *in situ* derived correction [150] is applied to jets in data, where the balance of the jet's transverse momentum compared to a reference object is used to determine the final JES.

After the calibration, jet candidates are selected if they have a $p_{\mathrm{T}} > 25$ GeV in the central part ($|\eta| < 2.4$) or if they have a $p_{\mathrm{T}} > 30$ GeV in the forward part ($2.4 < |\eta| < 4.5$) of the detector in addition with the following requirements:

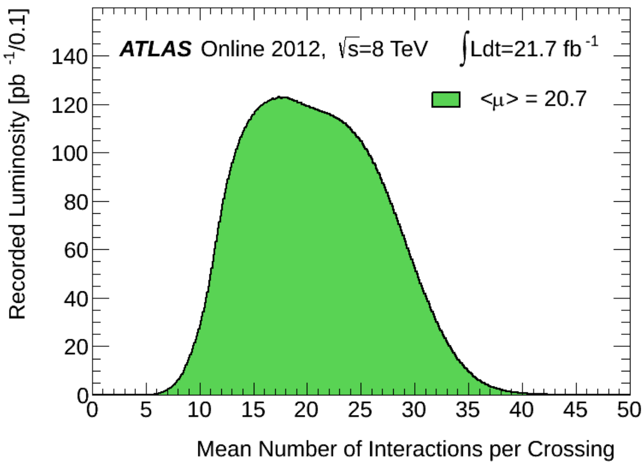

Figure 4.4: The luminosity-weighted distribution of the mean number of interactions per bunch crossing for 2012 (full *pp* collisions data set) [137].

As depicted in Figure 4.4 on average there are 20.7 interactions per bunch crossing which can produce a large number of jets. In order to find only the jets associated with the relevant primary vertex a cut on the so-called jet vertex fraction (JVF) [152] is performed which acts as a discriminant between jets from hard processes and pile-up jets. The JVF is defined as:

$$\mathrm{JVF}(\mathrm{jet}_i, \mathrm{vtx}_j) = \frac{\sum_k p_{\mathrm{T},k}(\mathrm{jet}_i, \mathrm{vtx}_j)}{\sum_n \sum_l p_{\mathrm{T},l}(\mathrm{jet}_i, \mathrm{vtx}_n)}, \tag{4.3}$$

where $p_{\mathrm{T},k}(\mathrm{jet}_i, \mathrm{vtx}_j)$ is the scalar transverse momentum of the track k, lying in jet i and coming from vertex j. The numerical range of JVF is between 0 and 1 and a requirement of JVF > 0.5 for all jets with $p_{\mathrm{T}} < 50$ GeV and $|\eta| < 2.4$ is applied.

Finally, it is necessary to identify jets which originate from a b quark (also called b tagging) in order to suppress background events originating from top-quark decays. A sketch of a b-hadron decay is depicted in Figure 4.5. Several b-tagging algorithms have been deployed in ATLAS [153], which range from simple algorithms based on impact parameters (IP3D) and secondary vertices (SV1) to a more sophisticated algorithm (JetFitter) which exploits the topology of weak b- and c-hadron decays.

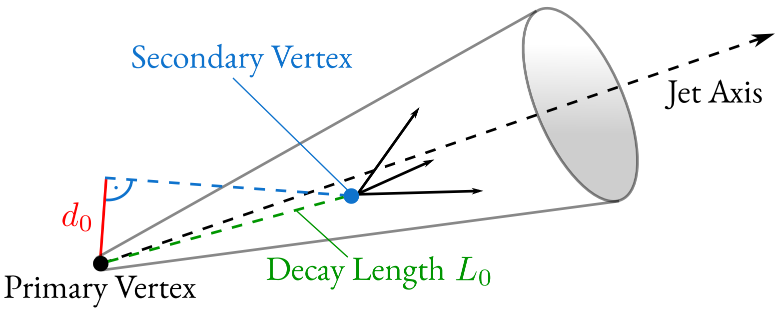

Figure 4.5: Schematic view of displaced tracks forming a secondary vertex, which is reconstructed by tracks with a large impact parameter d_0.

In the MV1 algorithm [154], which is used in this analysis, the output of the former algorithms is used in a neural network in order to generate output weight pdfs for b, c and light-flavour jets. It is trained to separate b jets from light flavour jets and computes a tag weight for each jet. The performance of the MV1 algorithm has been calibrated at several working points, corresponding to b-tagging efficiencies in simulated top/anti-top quark pair events. In this analysis a working point of 85% efficiency is used.

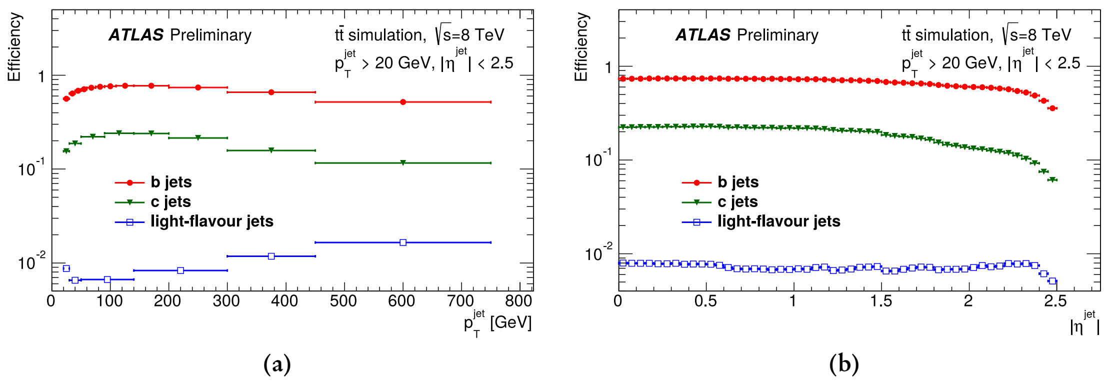

Figure 4.6: Efficiency of the MV1 algorithm to select b, c and light jets, as a function of p_T (a) and $|\eta|$ (b). The working point is 70% efficiency (for a sample of simulated top/anti-top quark pair events) for b jets defined with $p_T > 20$ GeV and $|\eta| < 2.5$ [155].

The b-, c- and light-jets tagging efficiency of the MV1 algorithm for a working point of 70% is depicted in Figure 4.6, again for simulated top/anti-top quark pair events [155].

4.1.4 Muon Candidates

The identification of muons is performed according to several reconstruction criteria, leading to different muon "types" depending which informations of the detector parts are used. The different types are [134, 156]:

- Stand-alone (SA) muons: The muon trajectory is reconstructed using only MS information. Flight direction and impact parameters of the muon are determined by extrapolating the muon track from the MS to the point of closest approach to the beam line.
- Combined (CB) muons: The muon track is reconstructed independently in the ID and in the MS. A combined track is formed from the successful combination of ID and MS track.
- Segment-tagged (ST) muons: A track, extrapolated from the ID to the MS, is identified as muon if it is associated with at least one track segment in the MDT or CSC.
- Calorimeter-tagged (CaloTag) muons: An ID track which can be associated to an energy deposit in the ECAL as expected from a minimum ionising particle. While having the lowest purity of all muon types, it recovers acceptance in the uninstrumented region of the MS.

CB muon candidates have the highest muon purity and are therefore used in this analysis. The combination of the information from the different detector parts is performed by the so-called STACO-algorithm [157, 158] for muon tracks in the pseudorapidity range $|\eta| < 2.5$. The algorithm performs a statistical combination of tracks with vertices to obtain the full track parameters [158].

The reconstruction efficiency has been measured with the tag-and-probe method [134] using large reference samples of $J/\psi \to \mu\mu$ and $Z \to \mu\mu$ decays in the data sets obtained in 2011 and 2012. Over the most covered phase space ($|\eta| < 2.7$ and $5\ \text{GeV} \lesssim p_\text{T} \lesssim 100\ \text{GeV}$), the efficiency is above 99% and was measured with per-mille precision, which is shown in Figure 4.7. The momentum resolution depends on the pseudorapidity and ranges from 1.7% to 4% for small/large pseudorapidity and transverse momentum combinations [134].

In the pseudorapidity regions $\eta \approx 0$ and in the region between barrel and end-caps $1.1 < |\eta| < 1.3$ the reconstruction efficiency is strongly affected by acceptance losses since in the former region the MS is only partially equipped with muon chambers in order to provide space for services for the ID and the calorimeters and in the latter region there are regions where only one layer of chambers is traversed muons in the MS [134, 156], due to the fact that some chambers of that region were not yet installed[6].

Similar to electrons, muon candidates are only used if they have $p_\text{T} > 10$ GeV and in addition the following conditions from the ID are required: At least one hit in the pixel detector, at least 5 hits in the SCT, at most 2 active Pixel or SCT elements traversed by the track without hits and a successful TRT-track extension (at least 9 hits) has to be found if the track lies within its acceptance.

[6]During the LHC shutdown from 2013-2014, the installation of muon chambers has been completed.

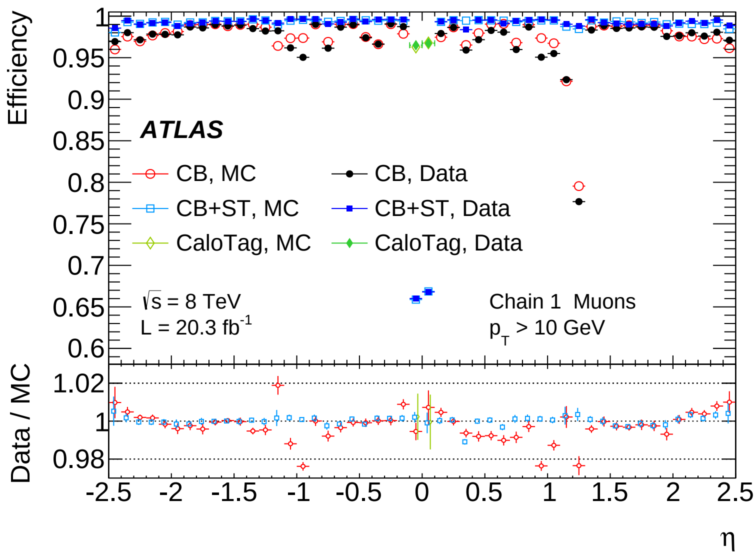

Figure 4.7: Muon reconstruction efficiency as a function of η measured in $Z \rightarrow \mu\mu$ events for muons with $p_T > 10$ GeV and different muon reconstruction types. CaloTag muons are only shown in the region $|\eta| < 0.1$, where they are used in physics analyses. The error bars on the efficiencies indicate the statistical uncertainty. The panel at the bottom shows the ratio between the measured and predicted efficiencies. The error bars on the ratios are the combination of statistical and systematic uncertainties [134].

The reconstructed muons have to fulfil a set of isolation criteria as well as cuts on on the impact parameter, which reject cosmic muons. The isolation variables used for muons are the same ones as for electrons, presented in section 4.1.2. The applied cuts are summarised in Table 4.2.

Table 4.2: Muon isolation cuts as a function of E_T.

E_T [GeV]	Calo. isolation	Track isolation	Impact parameters
$10 - 15$	$E_T^{cone30}/E_T < 0.06$	$p_T^{cone40}/E_T < 0.06$	$d_0/\sigma_{d_0} < 3.0$, $z_0 \sin\theta < 1.0$ mm
$15 - 20$	$E_T^{cone30}/E_T < 0.12$	$p_T^{cone30}/E_T < 0.08$	
$20 - 25$	$E_T^{cone30}/E_T < 0.18$	$p_T^{cone30}/E_T < 0.12$	
> 25	$E_T^{cone30}/E_T < 0.30$		

4.1.5 Missing Transverse Momentum

Due to the two neutrinos in the investigated final state, the missing transverse momentum $\vec{E}_T^{miss}$, as defined in equation (3.7), is an important observable. For the calculation of $\vec{E}_T^{miss}$, reconstructed physics objects are used whose calorimeter deposits are associated with reconstructed electrons, photons, hadronically decaying tau leptons, jets and muons [159]. The missing transverse momentum can be reconstructed using tracking information, calorimeter information or a combination of both. In the latter approach, the reconstruction mainly uses tracking information while for jets the calorimeter information is added. In comparison to same flavour final states (two electrons or two muons), where the track-based reconstruction is used, in the different flavour final state (one electron and one muon), as regarded in this analysis, the combination of calorimeter and track information delivers the best resolution and is therefore used [160].

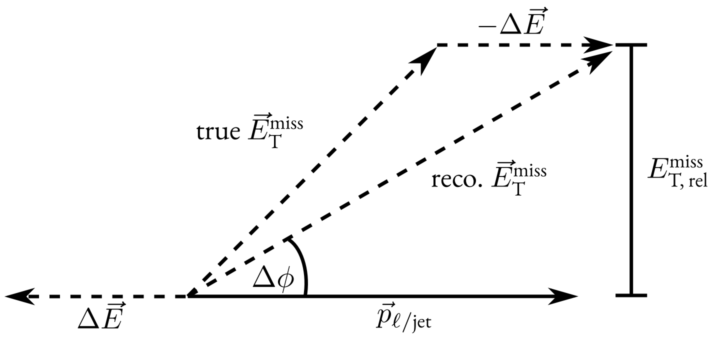

Figure 4.8: Illustration of the definition of $E_{\mathrm{T,\,rel}}^{\mathrm{miss}}$. The component of $\vec{E}_{\mathrm{T}}^{\mathrm{miss}}$ orthogonal to the direction of the lepton or jet $\vec{p}_{\ell/\mathrm{jet}}$ is called $E_{\mathrm{T,\,rel}}^{\mathrm{miss}}$. As depicted, $E_{\mathrm{T,\,rel}}^{\mathrm{miss}}$ does not change if the energy of the next hard object (lepton or jet) is mismeasured by an amount of ΔE.

In order to reduce variations on $\vec{E}_{\mathrm{T}}^{\mathrm{miss}}$ caused by mismeasured leptons and jets the projection of the missing transverse momentum to an axis defined by the closest hard object is used:

$$\begin{aligned} E_{\mathrm{T,\,rel}}^{\mathrm{miss}} &= E_{\mathrm{T}}^{\mathrm{miss}} \sin\Delta\phi, \text{ for } \Delta\phi < \frac{\pi}{2} \\ E_{\mathrm{T,\,rel}}^{\mathrm{miss}} &= E_{\mathrm{T}}^{\mathrm{miss}}, \text{ otherwise.} \end{aligned} \tag{4.4}$$

The angle $\Delta\phi$ is measured between $\vec{E}_{\mathrm{T}}^{\mathrm{miss}}$ and the considered object (lepton or jet). The advantage of $E_{\mathrm{T,\,rel}}^{\mathrm{miss}}$ over $E_{\mathrm{T}}^{\mathrm{miss}}$ is that the former is more robust against inaccurate energy measurements of leptons and jets as illustrated in Figure 4.8.

4.2 The 2012 Data Set

The analysis described in this thesis uses pp LHC collision data at a centre-of-mass energy of 8 TeV collected with the ATLAS detector between March and December 2012. Only data fulfilling a certain set of quality requirements, which correspond to the functionality of the ATLAS subdetector systems, are used. The necessary information about the luminosity and physics runs are provided in so-called good run lists (GRLs).

Table 4.3: Summary of the collected luminosity in different data-taking periods in fb^{-1} [161].

Data period	Stable delivered	ATLAS recorded
A1–8	0.929	0.867
B1–14	5.682	5.403
C1–8	1.674	1.577
D1–8	3.666	3.453
E1–4	2.605	2.423
F1	0.000	0.000
E5	0.308	0.292
G1–5	1.407	1.321
H1–6	1.683	1.583
I1–3	1.176	1.084
J1–8	2.981	2.777
L1–3	1.000	0.913
M1	0.015	0.010

The 2012 data set has been split into data periods numbered from A to M in which is assured that LHC beam conditions and detector states were uniform. A summary of the collected luminosity in the different periods is given in Table 4.3, where the first column gives the data period, the second column shows how much luminosity could be delivered by the LHC with stable beam conditions and the last column shows how much luminosity was recorded by ATLAS. In the data period F1 (12. and 13. September 2012) no data was taken, since a special physics run was performed.

As described in section 3.2.5, triggers play are crucial role in the data-taking process since their decisions substantially define the available data. For electron and muon candidates of the considered $h/H \to WW \to e\nu\mu\nu$ process the triggers define the lowest possible lepton p_{T}. Events containing these candidates are recorded with unprescaled[7] single lepton triggers logically alternated with dilepton triggers to maximise the total trigger efficiency. Table 4.4 shows the setup for the 2012 run.

Table 4.4: Trigger setup for 2012 run.

$e\mu$ & μe channels	$p_{\mathrm{T}}(e) > 24$ GeV, vhi, *medium* or $p_{\mathrm{T}}(e) > 60$ GeV, *medium* or $p_{\mathrm{T}}(\mu) > 24$ GeV, i, *tight* or $p_{\mathrm{T}}(\mu) > 36$ GeV, *tight* or ($p_{\mathrm{T}}(e) >$ 12 GeV, Tvh, *medium* and $p_{\mathrm{T}}(\mu) > 8$ GeV)

[7] A prescale factor is used to reduce the amounts of events accepted by the trigger chain. For example, with a prescale factor of 10 only one out of ten events which fulfil the trigger chain is accepted.

The labels *loose, medium* and *tight* summarise quality criteria applied for electrons and muons while the suffixes *vh, Tvh* and *i* describe η and p_{T} dependent selection criteria for the reduction of hadronic leakage and isolation requirements respectively. Details on the different selections are given in Refs. [162, 163] for electrons and in Ref. [164] for muons.

5 | Process Description and Event Generation

A crucial point in understanding the collected collision data described in Chapter 4 is the comprehension of the considered signal and background processes in this analysis. The signal processes have been briefly described in Section 2.1.3 and are summarised in Section 5.1 in addition with a discussion about the relevant background processes. This theoretical knowledge is exploited in MC generators in order to simulate events with predictions according to the regarded physical model. A general description of MC event generation is given in Section 5.2 followed by the description of the MC programs used to create the predictions in Section 5.3.

5.1 Signal and Background processes

As described in Section 2.1.3 the main production mechanisms of the Higgs boson are the ggF and the VBF modes. The considered decay mode is $h/H \to WW \to e\nu\mu\nu$ as depicted in Figure 5.1.

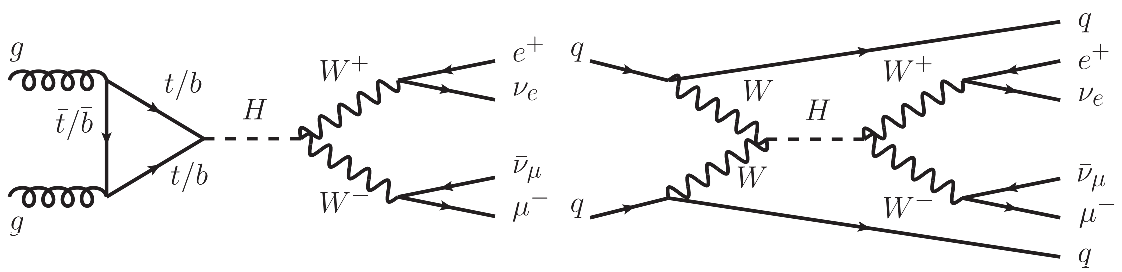

(a) Gluon-gluon fusion (ggF). **(b)** Vector-boson fusion (VBF).

Figure 5.1: Full signature of Higgs-boson production by ggF (a) and VBF (b) and its decay into two W bosons, which in turn decay into a electron/neutrino (muon/neutrino) pair.

The experimental signature of the considered processes consist of two different-flavoured leptons with opposite charge and a large amount of missing transverse momentum due to the presence of two neutrinos. The analysis is further split into jet multiplicity bins, with 0, 1 or 2 jets in the final state in addition to the leptons. As depicted in Figure 5.1, the ggF production has its largest contribution in the 0-jet channel, while the VBF production is accompanied with 2 jets. In the 1-jet channel ggF and VBF production are both present, mainly driven by the higher order corrections of the ggF process (which add jets to the final state) and with smaller contributions coming from the VBF process with a missing jet.

Every process that has the same final state as the signal processes above gives rise to an irreducible background which means, that these processes can only be distinguished from the signal due to its kinematics, as described in Chapter 6. The second source of (reducible) background arises from processes with large cross sections and a similar final state which lead to higher probabilities to imitate the signal process due to erroneously reconstructed objects.

For the analysis of the $h/H \to WW$ channel four different classes of background processes are relevant: The diboson-background, where simply two W bosons are produced in the final state in addition with processes having any combination of two vector bosons $W/Z/\gamma$ in the final state and the top-quark background, where either a $t\bar{t}$ pair or a single top quark is produced. Furthermore the Drell-Yan or Z + jets background where a leptonically decaying Z boson is produced and finally W-boson production in association with quarks or W + jets background, where a W boson is produced in association with jets.

5.1.1 Diboson Background

The diboson background is dominated by the WW boson pair production, which produces the same final state as the ggF signal process and therefore is the dominant background in the 0-jet channel. The corresponding Feynman graphs are depicted in Figure 5.2

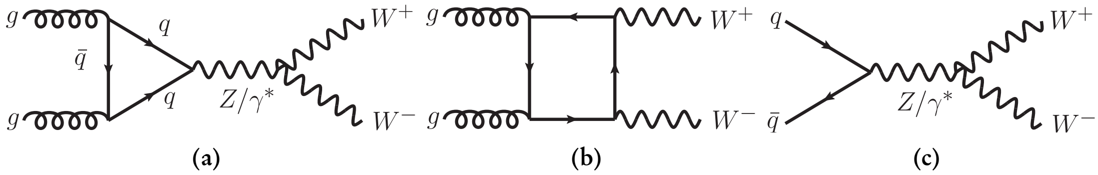

Figure 5.2: WW boson pair production background processes.

In addition, events having a WZ/ZZ boson pair final state, where one W/Z boson decays hadronically and the other Z boson decays into a lepton pair, imitate the VBF final state apart from missing transverse momentum. Events containing a $W\gamma^*$ final state may also lead to the signal signature if the W boson decays hadronically and the photon splits into a lepton pair. Feynman graphs leading to other than WW boson background are displayed in Figure 5.3.

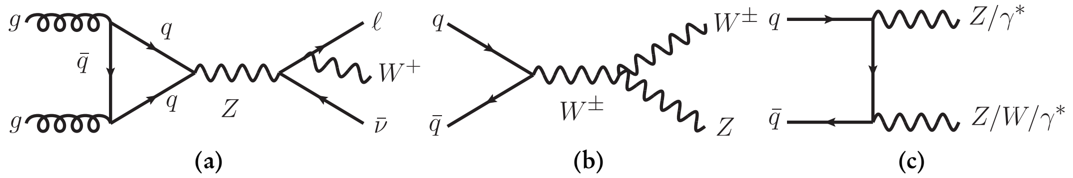

Figure 5.3: Diboson pair production background processes.

5.1.2 Top-Quark Background

Figure 5.4 shows the Feynman graphs of processes contributing to the top-quark background, which are dominant in the 2-jet channel. Due to its large mass the top quark does not hadronise, but decays immediately into a bottom quark and a W boson. The decay into lighter quarks is strongly suppressed by small CKM matrix elements.

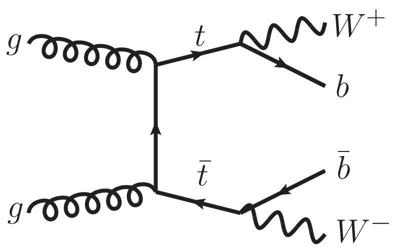

(a) Top-quark pair production.

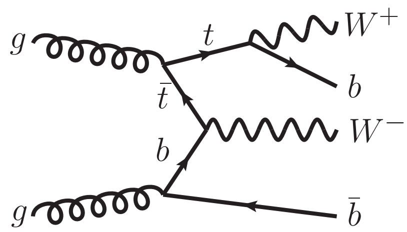

(b) Associated single top-quark production.

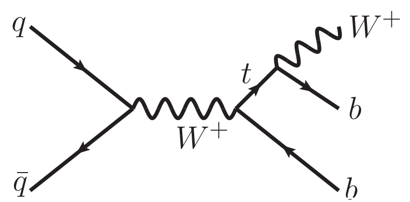

(c) Single top-quark production mediated through the s channel.

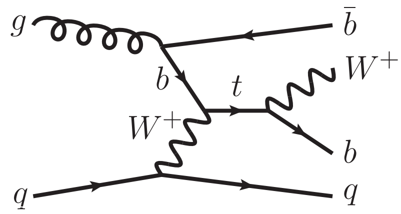

(d) Single top-quark production mediated through the t channel.

Figure 5.4: Background processes arising from top-quark production.

If the W bosons in the top-quark pair production in Figure 5.4(a) and the associated single top-quark production in Figure 5.4(b) decay into leptons, they imitate the final state of the VBF process except for the presence of two b jets. However, the presence of b jets can be exploited by categorising events by the number of reconstructed jets and vetoing events with b-tagged jets which strongly reduces the top-quark background. The s- and t-channel mediated single top-quark production in Figures 5.4(c) and 5.4(d) can also contribute to the background by jets, which are falsely identified as leptons.

5.1.3 Drell-Yan and Jets Associated W Boson Production Background

During the Drell-Yan [165] process as depicted in Figure 5.5(a) two oppositely charged leptons are produced. In case of a leptonically decaying $\tau^+\tau^-$ pair, the signal final state requiring an $e\mu$ pair and missing transverse momentum can be imitated if one τ decays into an electron and a neutrino while the other τ decays into a muon and a neutrino. In the case of the Z + jets process as depicted in Figure 5.5(b), a misreconstructed jet or a mismeasurement in the calorimeters can in addition lead to a signal-like final state. The processes depicted in Figures 5.5(c) and 5.5(d) can imitate the signal final state, if one of the jets is misidentified as a lepton. Due to the fact that the processes described above do not have the same final state as the signal (reducible background) they are less important compared to the diboson/top-quark backgrounds.

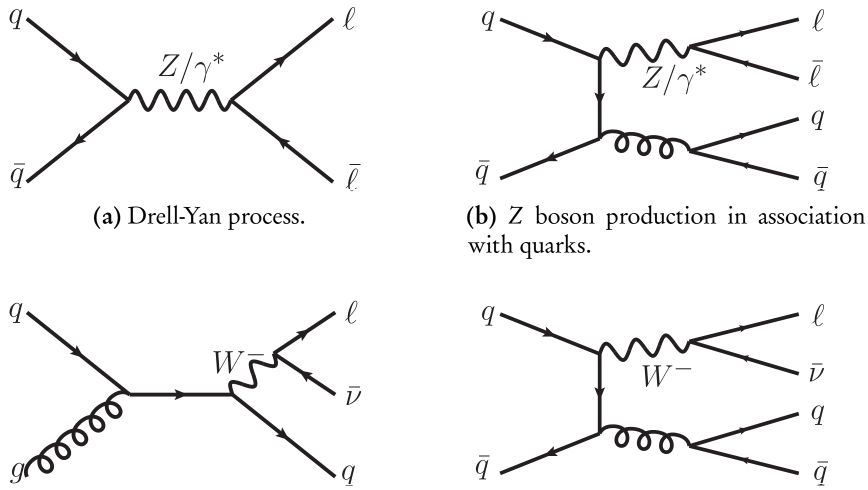

(a) Drell-Yan process.

(b) Z boson production in association with quarks.

(c) W boson production in association with one quark (W + jets).

(d) W boson production in association with two or more quarks.

Figure 5.5: W and Z boson production in association with quarks. Graphs (a) and (b) show the Drell-Yan and Z + jets background processes, while graphs (c) and (d) show the production of a W boson in association with quarks.

5.2 Monte Carlo Event Generation

The interpretation of data delivered by LHC and ATLAS is only possible if the theoretical predictions, as described in the previous section, can be carried out in a way which allows them to be compared with observed events. Tools providing these predictions are called Monte-Carlo (MC) generators, since they make extensive use of numerical MC techniques. Their main goals are the provision of a complete picture of final states in hadron collisions which include the description of particle types and their momenta for each event as well as the absolute production rates for the different possible processes. After the generation of simulated events, these pass a detector simulation where the interactions between the simulated particles and the different detector materials are evaluated. Finally the same algorithms and techniques which are used for the reconstruction of the observed events are used for the reconstruction of the simulated events as well, which allows a direct comparison of the prediction and the observed data. Basically, MC generators should be able to emulate Nature's behaviour in a real experiment.

The fundamental physical concept making these predictions possible is called factorisaton [166] which is the ability to isolate separate independent phases of the overall collision process [167]. These phases are ruled by different dynamics which enable to split the description of the proton structure and the final-state hadronisation from the hard interaction of elementary particles which can be described perturbatively. An overview of the general structure of a proton-proton collision is given in Figure 5.6.

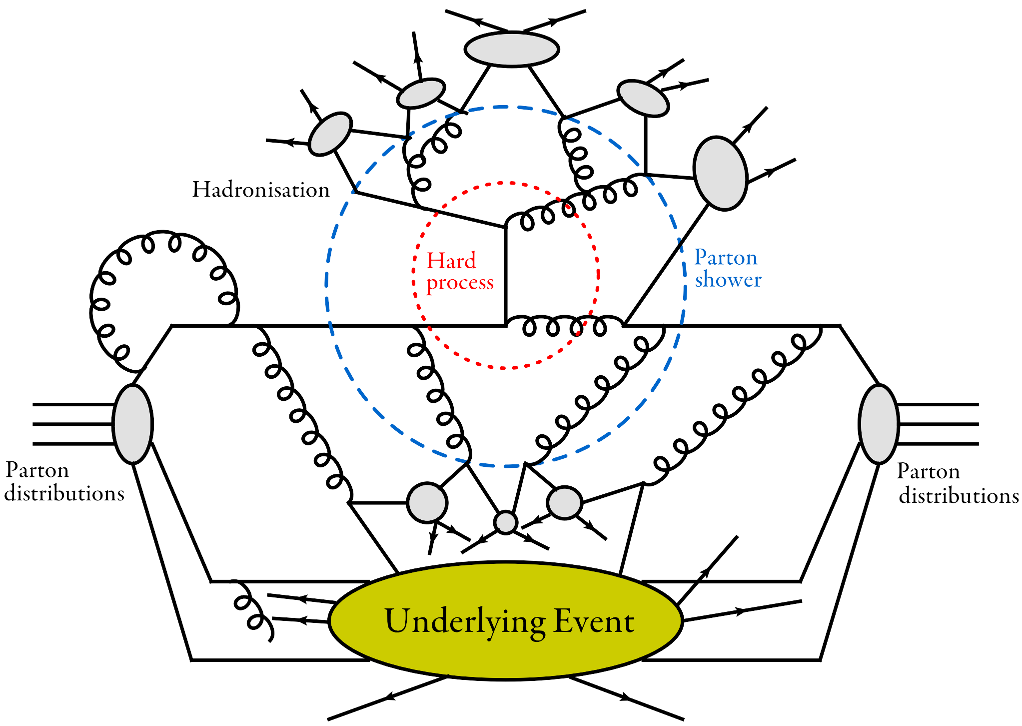

Figure 5.6: General structure of a proton-proton collision. The different processes are indicated: The hard process inside the red dotted line, the showering phase inside the blue dashed line and the underlying event in yellow. The hadronisation takes place just outside the blue dashed line which indicates the showering [167].

The description of the hard interaction is mainly driven by the scattering-matrix of the respective process which can be calculated perturbatively in powers of the strong coupling constant $\alpha_s(Q^2)$ with the help of Feynman graphs. The truncation of the perturbative expansion for an observable quantity like the cross section or the decay width to a finite order of $\alpha_s(Q^2)$ generates an intrinsic uncertainty to the predictions. The description above relies on the fact, that the strong coupling is small at large energy scales Q^2 and therefore can be treated as perturbative parameter. Higher order corrections lead to so-called virtual corrections, indicated by particle loops in Feynman graphs, and initial-state/final-state radiation (ISR/FSR), where real partons (usually gluons) are emitted from the initial or final states. Since the interacting particles are not free but originate from the colliding protons any quantity calculated at parton level must be convoluted with the appropriate PDFs that describe the proton in order to obtain observables for the whole process.

Due to large momentum transfers during the hard process, the involved colour-charged partons are intensely accelerated and will – similar to the radiation of an accelerated electric charge – emit QCD radiation in form of gluons. Since gluons themselves carry colour charges they can emit further radiation which leads to so-called parton showers. The showers represent higher-order corrections of the hard processes which are usually not feasible to calculate [53]. Therefore the calculation of parton shower uses approximations where mainly the collinear parton splitting and soft gluon radiation – the dominant contributions – are included. After the showering, the resulting partons with a small distance in phase space are combined into colour singlets. Due to the factorisaton properties of QCD this hadronisation process is decoupled and tuned to reference processes. Since no calculations based on first principles regarding the hadronisation are available, the simulations are based on phenomenological models [167].

The collisions of fragments of the hadron left over from the primary hard interaction is called underlying event. It goes through the showering and hadronisation phase like the hard process, on which it depends since the hard process and the underlying event have colour dependencies in order to enforce overall colour neutrality. Finally pile-up events and other effects which may occur during a bunch crossing are added to the simulation.

5.3 Monte Carlo Generators

Due to factorisaton, the different stages of proton-proton collisions can be separated into different programs: Matrix-element generators provide the simulation of hard processes and their cross sections and multi-purpose generators simulate the showering and the hadronisation making use of the output of the former. However, this combination leads to some difficulties. Higher order corrections (NLO, NNLO, etc.) for matrix elements allow for a good description of the emission of hard particles, while it is more challenging to perform the simulation of soft particles at this stage. The modelling of the latter is performed better by parton showers but since the different programs are independent of each other, this might lead to double counting, which means that the emission of particles is counted in the matrix-element generator and in the showering. To avoid this unwanted feature, so-called matching schemes [168–171] have to be used which remove double counting.

The MC generators used in this analysis are split into parton-shower (PS) and matrix-element (ME) generators. Events originating from ME generators need to undergo the showering process and are usually used as input for the PS generators. The PS generators used in this analysis are given in the following:

- `PYTHIA6/8` [172, 173] are used as interface for other generators in order to simulate ISR/FSR, hadronisation and further decays. While `PYTHIA6` was written in the programming language `Fortran`, `PYTHIA8` has been rewritten and further developed in `C++`. `PYTHIA` is designed to generate complete events having a focus on such where QCD effects are important. For the description of the hadronisation the so-called Lund model [174, 175] is utilised, which treats gluons as field lines which in turn form a string due to their self interaction.

- HERWIG [176] is a general-purpose MC event generator, which uses the parton-shower approach for ISR/FSR QCD radiation, including colour coherence effects and azimuthal correlations both within and between jets. Since multiple parton interactions are not available HERWIG is interfaced to JIMMY [177] which allows for the simulation of multi-parton interactions and the underlying event. For the modelling of the hadronisation, a cluster-based model [178] is used.

In addition to the generators described above, the following programs are used for the calculation of MEs of the different signal and background processes as described in Table 5.1:

- POWHEG [179] stands for Positive Weight Hardest Emission Generator and is a method to interface matrix-element MC calculations (currently with NLO accuracy) with parton-shower generators. In order to avoid radiation double counting of the first hard emission, the interfaced parton-shower generator has either to be p_{T}-ordered or it should be able to apply a p_{T}-veto [180].

- GG2WW [181] is a parton-level integrator and event generator for the loop induced $gg(\to h) \to WW \to \ell\nu\ell\nu$ process. In the loop contributions the top and bottom quark are taken into account, and in the Higgs boson contributions spin, decay angle, off-shell and interference effects are considered. In addition it is also possible to choose an arbitrary value for the W-boson mass.

- SHERPA [182] stands for Simulation of High-Energy Reactions of Particles and contains a flexible tree-level matrix element generator for the calculation of hard scattering processes. The initial- and final-state radiation is implemented by a parton-shower model and the hadronisation is described by a cluster-based model [178]. The latter is composed of two phases: cluster formation caused by the splitting of (non-perturbative) gluons into quark-antiquark pairs and the creation of light-flavour pairs by the decay of the clusters.

- AcerMC [183] is dedicated to the generation of SM background processes which were recognised as critical for the searches at LHC. The program provides a library of the massive matrix elements and native phase space modules for the generation of a set of selected processes in leading order (LO) accuracy.

- ALPGEN [184] is used to generate events of multi-parton processes in hadronic collisions. Matrix elements are calculated at LO (QCD and electroweak) for a large set of processes. In order to avoid double counting the so-called MLM matching scheme [185] is used.

The following programs are used in order to implement the interference effects between Higgs-boson signals a non-resonant diboson background processes for Higgs-boson masses larger than 400 GeV. The implementation is performed by reweighting the SM signal samples produced with the MC generators described above.

- MCFM [186, 187] is a parton-level MC program which gives NLO predictions for a range of processes at hadron colliders. Here the generator is used to implement the interference effects between Higgs-boson ggF signals and the diboson background processes.

- `REPOLO` stands for REweighting POwheg events at Leading Order and is used to reweight SM Higgs-boson events to different BSM scenarios. It is written by the authors of `VBFNLO` [70, 188, 189] and in this analysis `REPOLO` is used to implement the interference effects between Higgs-boson VBF signals and the diboson background processes.

Table 5.1 gives an overview about the different processes and the MC generators which are used to simulate them.

Table 5.1: MC generators used to model the signal and background processes, and corresponding cross sections (given for a $m_h = 125$ GeV Higgs boson). Leptonic decays of W/Z bosons are always assumed, and the quoted cross sections include the branching ratios and are summed over lepton flavours.

Process	Generator	$\sigma \cdot$ Br (pb)
ggF $h/H \to WW$	`POWHEG` [190]+`PYTHIA8` [173]	0.435
VBF $h/H \to WW$	`POWHEG` [191]+`PYTHIA8`	$3.6 \cdot 10^{-2}$
VH $h/H \to WW$	`PYTHIA8` (`PYTHIA6` [172])	$2.5 \cdot 10^{-2}$
$q\bar{q}/g \to WW$	`POWHEG`+`PYTHIA6`	5.68
$gg \to WW$	`GG2WW` [181]+`HERWIG` [176]	0.20
$WW + 2$ jets (QCD)	`SHERPA` [182]	0.568
$WW + 2$ jets (electroweak)	`SHERPA`	0.039
$t\bar{t}$ dileptonic	`POWHEG`+`PYTHIA6`	26.6
tW/tb leptonic	`POWHEG`+`PYTHIA6`	4.17
tqb leptonic	`AcerMC` [183]+`PYTHIA6`	28.4
inclusive W	`ALPGEN` [184]+`HERWIG`	$37 \cdot 10^3$
inclusive $Z/\gamma^\star(m_{ll} \geqslant 10GeV)$	`ALPGEN`+`HERWIG`	$16.5 \cdot 10^3$
Electroweak $Z/\gamma^\star$	`SHERPA`	5.36 (inc. t-ch)
$W(Z/\gamma^*)$	`POWHEG`+`PYTHIA8`	12.7
$W(Z/\gamma^*)(m_{(Z/\gamma^*)} < 7$ GeV)	`SHERPA`	12.2
$Z^{(*)}Z^{(*)} \to 4l(2l2\nu)$	`POWHEG`+`PYTHIA8`	0.73(0.50)
Electroweak $WZ + 2$ jets	`SHERPA`	$13 \cdot 10^{-3}$
Electroweak $ZZ + 2$ jets $(4l, ll\nu\nu)$	`SHERPA`	$73 \cdot 10^{-5}(12 \cdot 10^{-4})$
$W\gamma$	`ALPGEN`+`HERWIG`	369
$Z\gamma(p_T^\gamma > 7GeV)$	`SHERPA`	163

After the generation of MC events the interaction with the detector and its response is simulated with Geant4 [192, 193], a toolkit for the simulation of the passage of particles through matter. The geometry of the ATLAS detector has been translated into a Geant4 representation [194], so that it is possible to study the different interactions of the colliding particles with the detector.

5.3.1 Subtleties of High Mass Signal Samples

In the mass range below 130 GeV the width Γ_h of the SM Higgs boson is more than four orders of magnitude smaller than its mass m_h [195] which makes the narrow-width approximation (NWA) an excellent approximation with an error estimate of $O(\Gamma_h/m_h)$. Unfortunately this is not the case for Higgs bosons with higher masses. The Higgs-boson production cross sections are therefore sampled with a Breit-Wigner distribution which allows for a finite width and the description of an enhanced tail of the lineshape. However, as it turns out this description also breaks down for Higgs masses larger than 400 GeV and must be replaced by the so-called complex pole scheme (CPS) [196], which describes resonances of instable particles as complex energy poles in their scattering matrix amplitudes. In case of this analysis, signal samples with a width described by a Breit-Wigner distribution are used up to Higgs-boson masses of 400 GeV, while CPS samples are used for Higgs-boson masses of 400 GeV and larger. Regardless of its lineshape, the signal samples are generated with `POWHEG+PYTHIA`.

Another important aspect which alters the signal model for Higgs masses larger than 400 GeV is the interference between the signal and the non-resonant WW boson background [81, 197]. The interference is known to LO accuracy in QCD but not included in the `POWHEG + PYTHIA` samples. In order to take them into account, the signal samples are weighted according to the interference effect. The weights are calculated with `MCFM` at LO and rescaled to the NNLO cross section for the ggF process and with `REPOLO` for the VBF process.

Finally, the off-shell contributions of the Higgs-boson production which originates from the Higgs-boson mass dependence of its decay matrix element is also taken into account. In the $h/H \to WW^*$ decay modes energy scales of $Q^2 > (2M_V)^2$ cause an enhanced off-shell cross section [81]. Since this effect is smaller compared to the ones described above, it is taken into account by a systematic uncertainty as described in Chapter 8.

5.3.2 Jets Associated W Boson Production

Events in which W bosons are produced in association with jets can imitate the signal process, if the jets are misidentified as leptons. Since this process is not accurately described in simulated MC events a data-driven method [198, 199] called *Fake Factor Method* is used to estimate the background processes with one jet (W + jets) and two jets (QCD multijet production). In this method [200] three exclusive samples are defined: The signal sample, the W + jets control sample and the QCD control sample. The signal sample contains two fully identified leptons in data and its event number $N_{(\mathrm{id+id})}$ can be written as:

$$N_{(\mathrm{id+id})} = N_{(\mathrm{id+id})}^{W\text{ + jets}} + N_{(\mathrm{id+id})}^{\mathrm{QCD}} + N_{(\mathrm{id+id})}^{\mathrm{EW}}, \tag{5.1}$$

where $N_{(\mathrm{id+id})}^{W\text{ + jets}}$ is the number of events in the W + jets sample, $N_{(\mathrm{id+id})}^{\mathrm{QCD}}$ is the number of events in the QCD sample and $N_{(\mathrm{id+id})}^{\mathrm{EW}}$ is the number of all other background events to the Higgs-boson signal sample. In the W + jets control sample an alternative lepton definition, where the chance that jets are misidentified as leptons is enhanced, is used. Objects passing this alternative definition are called anti-id objects and the W + jets control sample is constituted of events containing one fully identified lepton and one anti-id object. These events are then passed to the diboson event selection, where the anti-id object is treated as fully identified lepton. The event composition of the W + jets control sample can be expressed as:

$$N_{\text{(id+anti-id)}} = N^{W\text{ + jets}}_{\text{(id+anti-id)}} + N^{\text{QCD}}_{\text{(id+anti-id)}} + N^{\text{EW}}_{\text{(id+anti-id)}}, \tag{5.2}$$

where $N^{W\text{ + jets}}_{\text{(id+anti-id)}}$ is the number of W + jets events, $N^{\text{QCD}}_{\text{(id+anti-id)}}$ is the number of QCD multijet events and $N^{\text{EW}}_{\text{(id+anti-id)}}$ is the number of background events to the Higgs-boson signal in the W + jets control sample which neither originate from W + jets nor QCD multijet events.

Similar to the W + jets control sample the QCD control sample is defined with two anti-id objects and its composition can be expressed similar to equation (5.2):

$$N_{\text{(anti-id+anti-id)}} = N^{W\text{ + jets}}_{\text{(anti-id+anti-id)}} + N^{\text{QCD}}_{\text{(anti-id+anti-id)}} + N^{\text{EW}}_{\text{(anti-id+anti-id)}}, \tag{5.3}$$

where $N^{W\text{ + jets}}_{\text{(anti-id+anti-id)}}$ is the number of W + jets events, $N^{\text{QCD}}_{\text{(anti-id+anti-id)}}$ is the number of QCD multijet events and $N^{\text{EW}}_{\text{(anti-id+anti-id)}}$ is the number of other background events to the Higgs-boson signal in the QCD multijet production control sample.

The estimation of the W + jets background is performed by applying an extrapolation (or fake factor) f_ℓ to the W + jets control sample. The fake factor is defined as:

$$f_\ell = \frac{N_{\text{(id+id)}}}{N_{\text{(id+anti-id)}}}, \text{ with } \ell = e, \mu. \tag{5.4}$$

The fake factor is defined separately for electrons and muons and is measured in data using Z + jets and dijet events. The number of W + jets events in the signal region is calculated by scaling the number of events in the W + jets control sample by the measured fake factor:

$$\begin{aligned} N^{W\text{ + jets}}_{\text{(id+id)}} &= f_\ell \cdot N^{W\text{ + jets}}_{\text{(id+anti-id)}} \\ &= f_\ell \cdot \left(N_{\text{(id+anti-id)}} - N^{\text{QCD}}_{\text{(id+anti-id)}} - N^{\text{EW}}_{\text{(id+anti-id)}} \right), \end{aligned} \tag{5.5}$$

where $N^{\text{EW}}_{\text{(id+anti-id)}}$ is subtracted using simulated MC events and $N^{\text{QCD}}_{\text{(id+anti-id)}}$ is subtracted using $N_{\text{(anti-id+anti-id)}}$ events. Figure 5.7 [199] shows the muon and electron fake factors in terms of p_{T} (muons) and E_{T} (electrons) respectively.

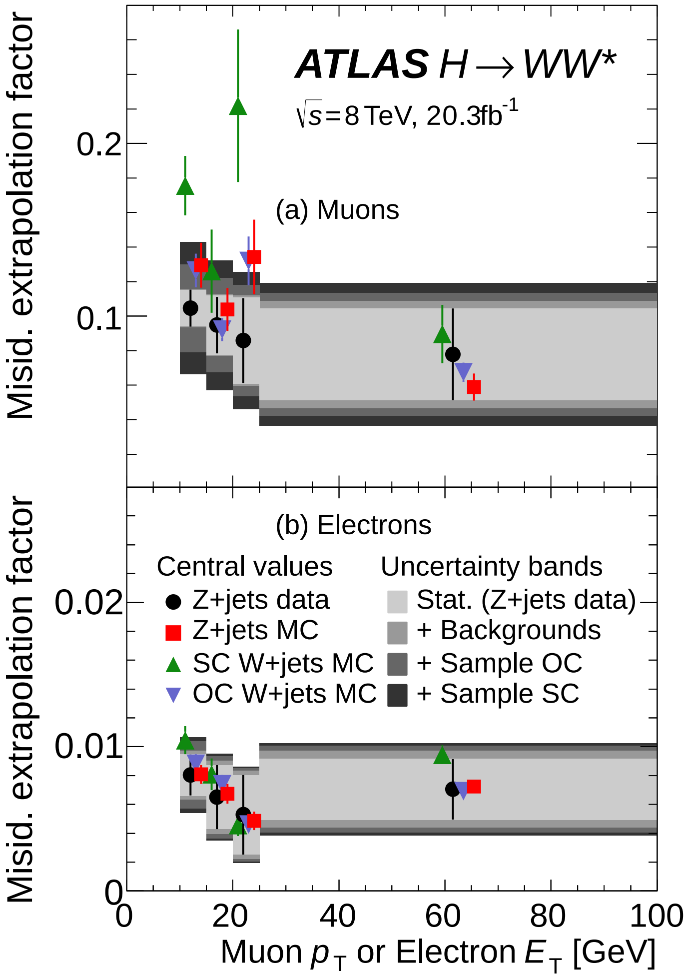

Figure 5.7: Misidentified lepton extrapolation factors, f_ℓ, for anti-identified (a) muons and (b) electrons. The symbols represent the central values of the Z + jets data and the three ALPGEN+PYTHIA6 MC samples: Z + jets, opposite-charge (OC) W + jets, and same-charge (SC) W + jets. The bands represent the uncertainties: Stat refers to the statistical component, which is dominated by the number of jets identified as leptons in Z + jets data; Background is due to the subtraction of other electroweak processes present in Z + jets data; and Sample is due to the variation of the f_ℓ ratios in Z + jets to OC W + jets or to SC W + jets in the three MC samples. The symbols are offset from each other for presentation [199].

6 | Process Features and Event Selection

The analysis conducted in this thesis relies on MC simulations of the signal and background processes as described in the previous chapter. In this chapter some features of the signal processes are presented and examined if they are apparent in the kinematic distributions and other observables. After this a set of cuts is presented in order to remove events which are most likely background events and to enhance the signal-to-background ratio. Before the distributions are processed further with the MVA method (described in detail in Chapter 7) used to discriminate between signal and background events, the agreement between the simulated and observed events is checked, since the modelling of the distributions is an important factor for the MVA.

6.1 Features of the Signal

Since the considered final state contains two neutrinos, the signal processes are expected to have a large amount of missing transverse energy compared to the background processes. Further, the Higgs-boson decay chain features a characteristic topology due to (angular) momentum conservation and the $V - A$ structure of the electroweak interaction. Figure 6.1 shows the decay chain of the Higgs boson in its rest frame, where the W bosons are emitted back-to-back. Due to angular momentum conservation, the spins of the W bosons have to point into opposite directions and therefore they both have the same helicity.

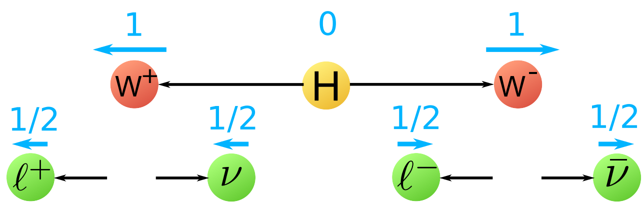

Figure 6.1: Illustration of spin correlation in the Higgs-boson decay in its rest frame. The black arrows indicate the momentum of the particles in the rest frame of the mother particle while the blue arrows indicate their spin. The leptons are emitted in the same direction due to the $V - A$ structure of the electroweak interaction.

Since W bosons only interact with left-handed fermions and right-handed antifermions, the helicity of their decay products is also fixed: In the decay of the W^- boson the antineutrino has to be right-handed, while the charged lepton is left-handed and vice versa for the W^+ boson. A consequence of this decay topology is, that the charged leptons are emitted in the same direction in the Higgs-boson rest frame and therefore have a small opening angle between each other. Figure 6.2 shows the relative missing transverse momentum as defined in equation (4.4) and opening

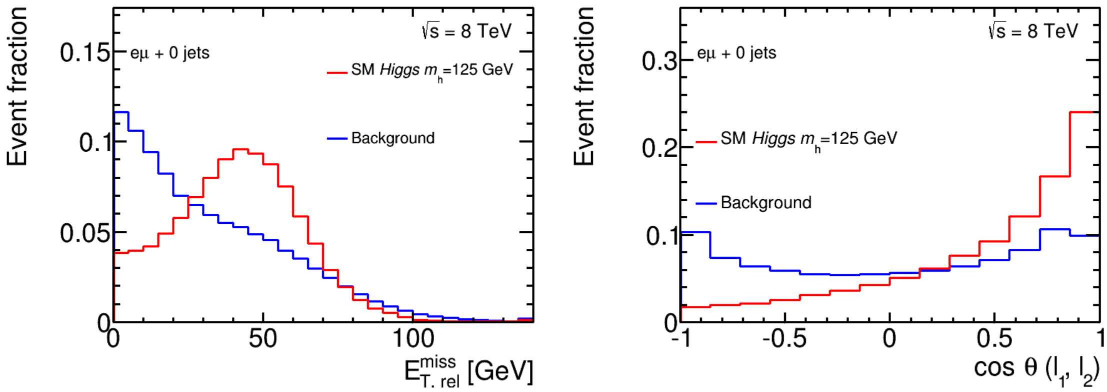

(a) Relative missing transverse momentum. **(b)** Opening angle of the final-state leptons.

Figure 6.2: Normalised distributions of the relative transverse missing energy $E_{\mathrm{T,\,rel}}^{\mathrm{miss}}$ (a) and $\cos\theta(\ell_1, \ell_2)$, the cosine of the opening angle between the final-state leptons (b) in the 0-jet channel. The SM Higgs-boson signal for $m_h = 125$ GeV is depicted in red, while the total background is depicted in blue.

angle distributions of the two final-state leptons for a SM Higgs with 125 GeV in the 0-jet channel.

In case of the Higgs-boson production via VBF two jets are added to the signal signature which are likely to point into forward/backward directions of the detector which leads to a characteristic gap in the pseudorapidity distributions of the jets. Together with the dijet-mass distribution they provide a good discrimination between signal and background as can be seen in Figure 6.3.

Furthermore, it is not possible to fully reconstruct the Higgs boson mass due to the presence of two neutrinos. In order to constrain the mass, the so-called transverse mass is introduced [2]:

$$m_{\mathrm{T}} = \sqrt{\left(E_{\mathrm{T}}(\ell\ell) + E_{\mathrm{T}}^{\mathrm{miss}}\right)^2 - \left(\vec{p}_{\mathrm{T}}(\ell\ell) + \vec{E}_{\mathrm{T}}^{\mathrm{miss}}\right)^2}, \tag{6.1}$$

where $E_{\mathrm{T}}(\ell\ell)/E_{\mathrm{T}}^{\mathrm{miss}}$ is the transverse energy of the leptons/missing transverse momentum in the final state and $\vec{p}_{\mathrm{T}}(\ell\ell)/\vec{E}_{\mathrm{T}}^{\mathrm{miss}}$ is the transverse momentum/missing transverse momentum vector of the leptons or neutrinos respectively. This variable is invariant under Lorentz boosts in beam direction and values of m_{T} are smaller or equal than the invariant mass of the decaying particle. Due to this feature, the mean values of m_{T} distributions move to higher values for higher Higgs-boson masses as shown in Figure 6.4 and Table 6.1.

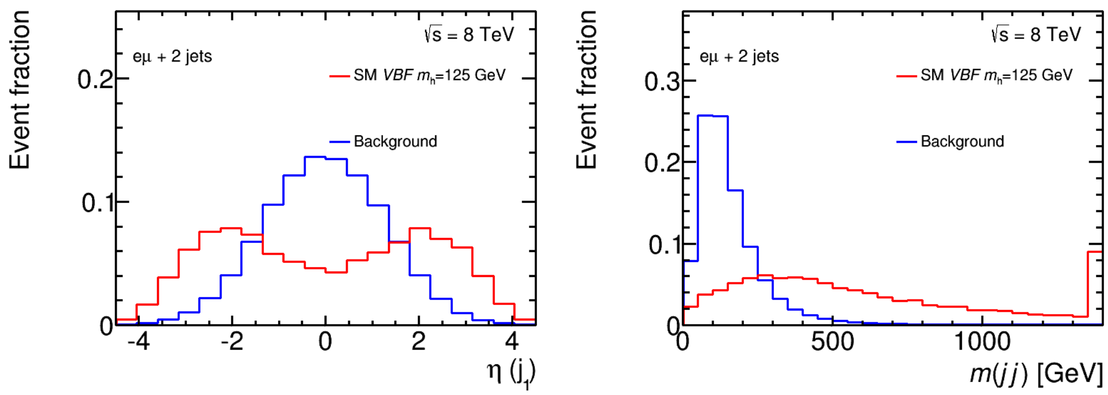

(a) Pseudorapidity of the first jet.

(b) Invariant dijet mass.

Figure 6.3: Normalised distributions of the pseudorapidity of the first jet $\eta(j_1)$ (a) and the invariant dijet mass $m(jj)$ (b) in the 2-jet channel. The VBF Higgs-boson signal for m_h = 125 GeV is depicted in red, while the total background is depicted in blue.

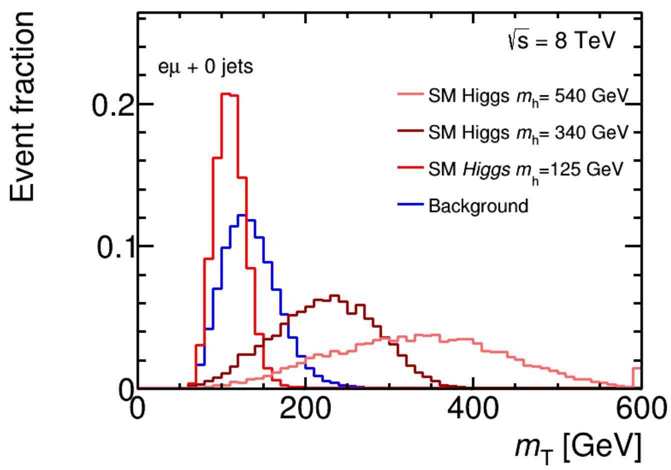

Figure 6.4: Transverse mass distribution for Higgs boson signals with m_h = 125 GeV, m_h = 340 GeV and m_h = 540 GeV depicted in different shades of red and the total background in blue. With the Higgs boson mass progressing to higher values, the mean of the corresponding distribution also progresses to higher values.

Table 6.1: Mean and RMS values of the m_T distribution for different values of the Higgs boson mass m_h in GeV.

m_h	mean	RMS
125	111.50	20.86
150	125.13	21.81
340	224.00	60.98
540	333.02	100.21
750	392.16	117.83
950	406.15	117.62

6.2 Event Selection

The $h/H \to WW \to e\nu\mu\nu$ events are recorded according to the objects and triggers described in Chapter 4. A common preselection for all search regions is performed in order to enhance the signal-to-background ratio and to remove regions, which are almost completely dominated by background events. After this, different sets of cuts are applied depending on the search region of the Higgs-boson mass and the jet multiplicity bins.

6.2.1 Preselection

The following preselection of $h/H \to WW \to e\nu\mu\nu$ event candidates is imposed:

- Exactly two opposite sign leptons with different flavour passing the lepton selection defined in Section 4.1 are required. In addition the leading lepton ℓ_1 is required to have $p_T > 25$ GeV and the subleading lepton ℓ_2 is required to have $p_T > 15$ GeV.
- The invariant mass of the two leptons $m(\ell\ell)$ has to be larger than 10 GeV.
- The relative transverse missing energy $E_{T, rel}^{miss}$ is required to be at least 25 GeV. This provides a strong suppression of W + jets/QCD multijet and Z + jets/Drell-Yan backgrounds (the latter mainly originating from $Z \to \tau^+\tau^-$ decays).

6.2.2 Selection

As described in Section 6.1, the shape of the Higgs-boson signals depend on the regarded Higgs-boson mass. Therefore it is advantageous to adjust the cuts applied on kinematic variables for different search settings. For example (see Figure 6.4) keeping all events with $m_T < 150$ GeV might be fitting when searching for a Higgs boson with the mass of 125 GeV, since it would mainly remove background events and keeping signal events, but it would also remove the bulk of events of a Higgs boson with the mass of 340 GeV or more. Reverting the cut would lead to the opposite result: The bulk of the light Higgs-boson signal and background events are rejected while the events containing a heavy Higgs signal are kept.

In order to take this feature into account, the analysis is split into five (non-orthogonal) selection regions (see Table 6.2) where different optimisation of cuts are performed.

Table 6.2: Search regions in terms of the Higgs-boson mass, where different cuts are applied.

Low mass 1	Low mass 2	High mass 1	High mass 2	High mass 3
135 – 160 GeV	165 – 195 GeV	200 – 300 GeV	320 – 500 GeV	> 500 GeV

In each search region, the analysis is further split in terms of jet multiplicity where in the 0-jet channel zero jets are required, in the 1-jet channel exactly one jet is required and in the 2-jet channel exactly two jets are required. In the 1- and 2-jet channel any event which contains a b-tagged jet is rejected to suppress backgrounds originating from top-quark decays. In addition, in the 2-jet channel it is required, that the jets are identified in opposite hemispheres to take the special VBF topology into account.

Table 6.3 shows the cuts of the different mass regions and jet channels which are applied in addition to the preselection cuts. The cuts on the dilepton opening angle $\Delta\phi(\ell_1, \ell_2)$ and on the dilepton invariant mass $m(\ell\ell)$, depicted in Figure 6.5, are applied to reduce the number of background events in regions, where only a negligible signal contribution is expected. In the low-mass regions, the different cuts on $m(\ell\ell)$ exploit the mass dependence of the heavy Higgs boson signal.

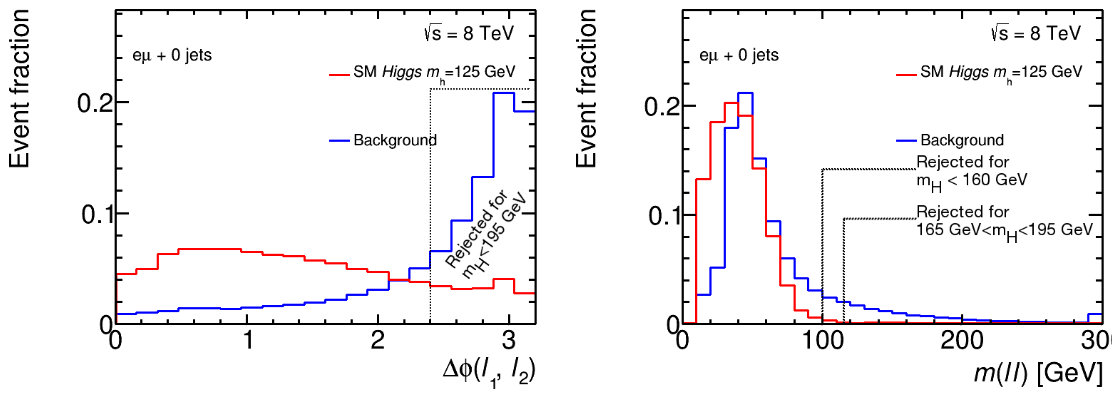

(a) Dilepton opening angle. **(b)** Invariant dilepton mass.

Figure 6.5: Normalised distributions of the dilepton opening angle $\Delta\phi(\ell_1, \ell_2)$ (a) and the invariant dilepton mass $m(\ell\ell)$ (b) in the 0-jet channel with the rejected region marked. The SM Higgs-boson signal for $m_h = 125$ GeV is depicted in red while the total background is depicted in blue.

In the high-mass regions the mass dependence of the heavy Higgs-boson signal is respected with the cuts on m_{T} as can be seen in Figure 6.6. In the high-mass region 1 the transverse mass is also constrained from above because in the regarded phase space of $m_{\mathrm{T}} > 290$ GeV only background events and (almost) no signal events can be found. In order to avoid those regions, these background events are rejected.

The additional cuts on transverse momentum of the leading lepton $p_{\mathrm{T}}(\ell_1)$ and the transverse momentum of the dilepton system $p_{\mathrm{T}}(\ell\ell)$ are also used to remove background-dominated phase space.

Finally, a cut on the invariant dijet mass $m(jj)$ is placed in the 2-jet channel. While the other cuts where aiming for a minimal loss of signal events, applying this cut rejects a lot of signal events. However, it can be stated, that it is very hard to distinguish between signal and background events in the region of $m(jj) < 250$ GeV and therefore the events are completely removed (see Figure 7.6 in Chapter 7). This helps to focus on phase space regions where a discrimination between signal and background events is feasible. The event yield of the signal and background events after the selection is shown in Table 6.4.

Table 6.3: Applied cuts in the different mass regions. The definitions correspond to the available Higgs-boson samples: For 135 GeV $\leqslant m_H < 200$ GeV samples are available in 5 GeV steps, for 200 GeV $\leqslant m_H < 600$ GeV the step width is 20 GeV and for 600 GeV $\leqslant m_H$ the step width is 50 GeV.

Low-mass region 1: 135 – 160 GeV			
Variable	0 jets	1 jet	2 jets
$\Delta\phi(\ell_1, \ell_2)$	< 2.4	–	–
$m(\ell\ell)$	< 100 GeV	< 100 GeV	< 100 GeV
$m(jj)$	–	–	> 250 GeV
Low-mass region 2 : 165 – 195 GeV			
Variable	0 jets	1 jet	2 jets
$\Delta\phi(\ell_1, \ell_2)$	< 2.4	–	–
$m(\ell\ell)$	< 115 GeV	< 115 GeV	< 115 GeV
$m(jj)$	–	–	> 250 GeV
High-mass region 1: 200 – 300 GeV			
Variable	0 jets	1 jet	2 jets
$p_{\mathrm{T}}(\ell_1)$	–	–	> 30 GeV
m_{T}	120 GeV $< m_{\mathrm{T}} <$ 290 GeV	145 GeV $< m_{\mathrm{T}} <$ 290 GeV	–
$p_{\mathrm{T}}(\ell\ell)$	> 20 GeV	–	–
$m(jj)$	–	–	> 250 GeV
High-mass region 2: 320 – 500 GeV			
Variable	0 jets	1 jet	2 jets
$p_{\mathrm{T}}(\ell_1)$	> 35 GeV	> 40 GeV	> 30 GeV
m_{T}	> 140 GeV	> 150 GeV	> 110 GeV
$p_{\mathrm{T}}(\ell\ell)$	> 20 GeV	–	–
$m(jj)$	–	–	> 250 GeV
High-mass region 3: 520 – 1000 GeV			
Variable	0 jets	1 jet	2 jets
$p_{\mathrm{T}}(\ell_1)$	> 35 GeV	> 50 GeV	> 30 GeV
m_{T}	> 140 GeV	> 180 GeV	> 140 GeV
$p_{\mathrm{T}}(\ell\ell)$	> 20 GeV	–	–
$m(jj)$	–	–	> 250 GeV

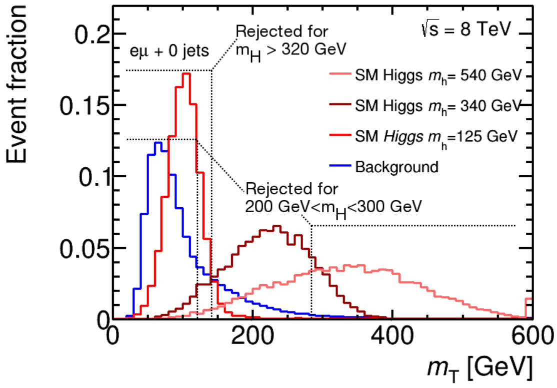

(a) Transverse mass in the 0-jet channel.

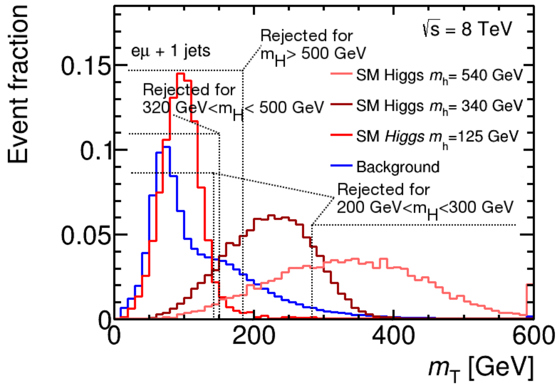

(b) Transverse mass in the 1-jet channel.

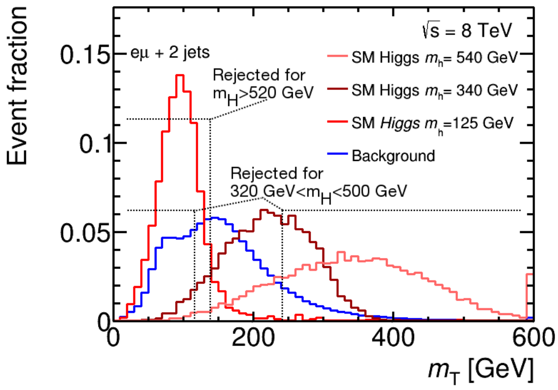

(c) Transverse mass in the 2-jet channel.

Figure 6.6: Normalised distributions of m_{T} for the different jet channels with the marked rejected region. The SM Higgs-boson signals with $m_h = 125$ GeV, $m_h = 340$ GeV and $m_h = 540$ GeV are depicted in different shades of red while the total background is depicted in blue.

The excess of observed events compared to the expected events in the 0-jet channel of Table 6.4 is at most 24%, depending on the selection region. This can be explained by an enhanced WW-boson production cross section [201] of $\sim 22\%$ compared to the theoretical prediction. The enhanced cross section would also explain, why the excess is mainly present in the 0-jet channel where the diboson background is dominant.

Table 6.4: The expected number of signal and background events for an integrated luminosity of 20.3 fb^{-1} in the signal regions. Each column shows the event yield for the selections described in Table 6.3. For each jet channel the expected event yield of a heavy Higgs boson with a mass of m_H = 150 GeV, m_H = 180 GeV, m_H = 240 GeV, m_H = 340 GeV or m_H = 540 GeV respectively in the Type I 2HDM with tan $\beta = 1$ and $\alpha = \pi$ is shown.

0 jets					
Process	Selection Region				
	Low-mass 1	Low-mass 2	High-mass 1	High-mass 2	High-mass 3
SM Higgs Boson	167.8	167.9	52.9	11.2	11.6
Diboson	2496.4	2721.1	3068.5	2499.5	2499.5
Top-quark	374.2	426.8	629.4	645.6	645.6
Z/γ^* + jets	64.7	69.3	79.5	41.5	41.5
W + jets	45.3	53.0	78.4	51.2	51.2
QCD Multijets	1.9	2.0	2.9	2.0	2.1
Total	3150.3	3440.1	3911.5	3251.0	3251.4
Obs.	3930	4242	4591	3696	3696
Heavy Higgs Boson	663.9	733.3	287.4	172.3	50.9
1 jet					
Process	Selection Region				
	Low-mass 1	Low-mass 2	High-mass 1	High-mass 2	High-mass 3
SM Higgs Boson	94.5	94.9	6.2	4.6	0.0
Diboson	1039.2	1182.9	917.4	921.7	572.7
Top-quark	940.8	1095.5	1095.1	1161.2	805.4
Z/γ^* + jets	868.4	872.3	17.8	16.6	9.9
W + jets	63.1	69.4	25.6	17.6	7.6
QCD Multijets	11.0	11.5	1.8	1.1	0.6
Total	3016.9	3326.5	2063.8	2122.8	1396.1
Obs.	3030	3362	2115	2166	1445
Heavy Higgs Boson	360.8	444.3	177.0	136.3	45.8
2 jets					
Process	Selection Region				
	Low-mass 1	Low-mass 2	High-mass 1	High-mass 2	High-mass 3
SM Higgs Boson	12.6	12.6	11.3	3.4	0.0
Diboson	40.4	46.7	72.5	60.5	51.5
Top-quark	93.3	109.9	179.1	152.0	134.7
Z/γ^* + jets	47.9	48.2	39.9	4.2	1.3
W + jets	2.0	2.0	2.2	1.2	0.9
QCD Multijets	0.5	0.5	0.3	0.1	0.0
Total	196.6	219.9	305.3	221.3	188.4
Obs.	174	198	277	193	171
Heavy Higgs Boson	47.9	71.0	39.6	27.5	13.5

6.3 Control Regions

Beside the signal region selection described in the last section, two control regions (CRs) are defined by reverting particular selection criteria. These CRs are enriched with specific processes and they are mainly used to determine the normalisation of the MC simulations with respect to the observed data. Here two different CRs are used: the light Higgs Boson CR and the top-quark CR which are described in the following sections.

6.3.1 Light-Higgs-Boson Control Region

The light-Higgs-Boson CR is constructed in the 0-jet and 1-jet channel by the cuts given in Table 6.5.

Table 6.5: Cuts which define the light Higgs Boson control region.

Variable	0 jets	1 jet
m_T	< 120 GeV	< 145 GeV
$\Delta\phi(\ell_1, \ell_2)$	< 2.4	< 2.4

While the cut on m_T is performed in order to create an orthogonal set of phase space compared to the signal region, the additional cut on $\Delta\phi(\ell_1, \ell_2)$ is applied in order to remove a large fraction of Z + jets background. These cuts enrich the regarded phase space with SM processes, including the SM Higgs boson, which is used to check the modelling of the variables and to estimate the normalisation of the processes. Furthermore, since it is assumed that the light scalar Higgs boson h of the 2HDM coincides with the discovered Higgs boson with a mass of 125 GeV, the shape and rate informations of the light Higgs boson can constrain the allowed coupling modifications predicted by the 2HDM. Therefore, the light-Higgs-Boson CR is included in the statistical analysis, which is described in detail in Chapter 9.

6.3.2 Top-Quark Control Region

The top-quark CR is used in order to estimate the $t\bar{t}$/single top-quark processes, which is the dominant background in the 2-jet channel. It is constructed by inverting the b-jet veto in the 2-jet channel, which means that at least one jet needs to tagged as b jet. This CR is very pure since it contains almost only top-quark candidate events, therefore it is used to determine the rate of $t\bar{t}$/single top-quark events in the final statistical analysis (see Table 6.6).

6.4 Modelling of the Variables

Figure 6.7 shows some basic variables in the different CRs and Table 6.6 shows the event yield of signal and background events in the CRs after the full selection. The MC predictions are normalised to the number of observed events in data and the shaded error bands represent systematic (see Chapter 8) and statistical uncertainties. Below the histograms, the deviation between the simulated events and the data events is shown. The presentation follows the recommendation described in Ref. [202], where the statistical significance, defined as the probability of finding a deviation at least as big as the one observed in the data, under the assumption that the chosen theoretical model describes the system, of the deviation is given in terms of the so-called z-value. The z-value describes the deviation to the right of the mean of a Gaussian distribution in units of standard deviations, which would correspond to the same p-value. Equation (6.2) shows the connection between p- and z-value [202]:

$$p\text{-value} = \int_{z\text{-value}}^{\infty} dx\, \frac{1}{\sqrt{2\pi}} e^{-\frac{x^2}{2}}. \tag{6.2}$$

Significant deviations are characterised by small p-values which correspond to z-values > 3 while common statistical fluctuations lie in the range of 1-2 z-value units. Further, plotting signed z-values has the advantage of being able to spot excesses (positive z-value) or deficits (negative z-value) of data over the expectations while not hiding features which are worth showing.

Below the significance plot the χ^2-probability is shown, which is a measure of accordance between MC prediction and data. It is basically performed as Pearson's χ^2 test [203] with the test statistic

$$\chi^2 = \sum_{i=k}^{M} \frac{n_k - \tilde{\nu}_k}{\tilde{\nu}_k}, \tag{6.3}$$

where M is the number of bins, n_k is the number of observed events and $\tilde{\nu}_k$ is the number of predicted events in bin k. The χ^2-probability is given as:

$$p_{\chi^2} = \int_{\chi^2}^{\infty} dx\, f(x; n_d), \text{ with } f(x; n_d) = \frac{x^{\frac{n_d}{2}-1}}{2^{\frac{n_d}{2}}\Gamma(\frac{n_d}{2})} e^{-\frac{x}{2}}, \tag{6.4}$$

with $n_d = M - 1$ being the number of degrees of freedom, $f(x; n_d)$ being the χ^2-pdf and $\Gamma(x)$ being the well-known Gamma function [204].

The systematic uncertainties are included in the calculation of p_{χ^2} by utilising pseudo experiments which are generated within the systematic variations. For each experiment the χ^2-value from equation (6.3) is calculated, producing a distribution $f_{\text{gen.}}(x; n_d)$ of χ^2 values. Then, the $\chi^2_{\text{obs.}}$-value is computed from the actual data points and p_{χ^2} is determined by:

$$p_{\chi^2} = \int_{\chi^2_{\text{obs.}}}^{\infty} dx\, f_{\text{gen.}}(x; n_d). \tag{6.5}$$

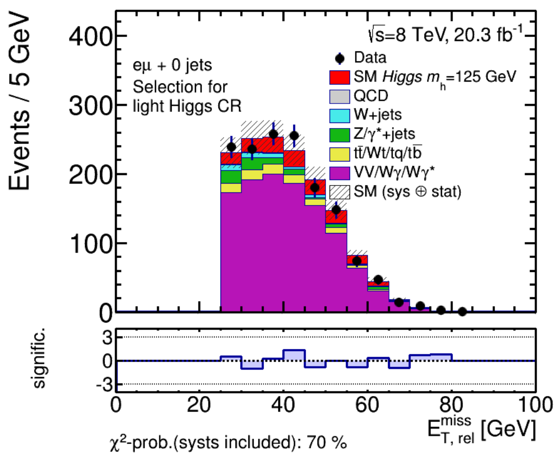

(a) Relative missing transverse momentum.

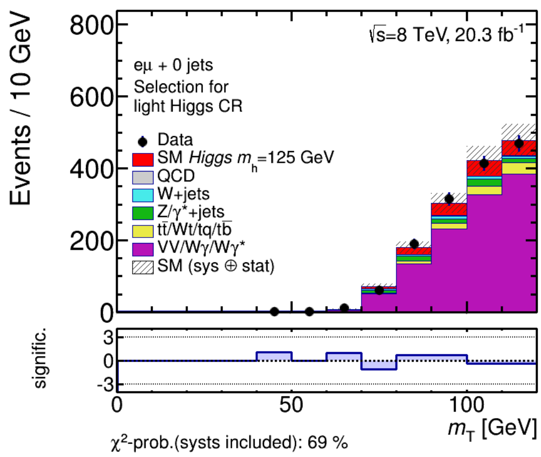

(b) Transverse mass.

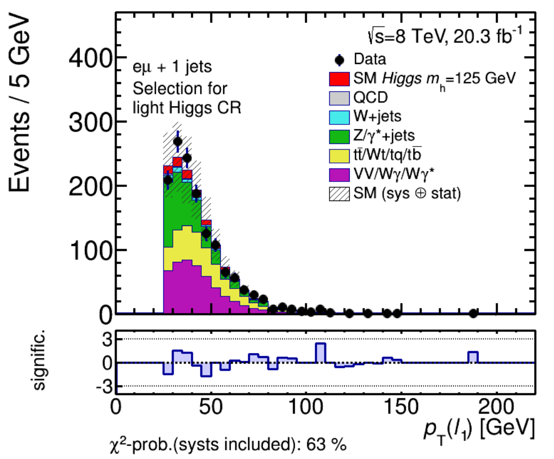

(c) Transverse momentum of the leading lepton.

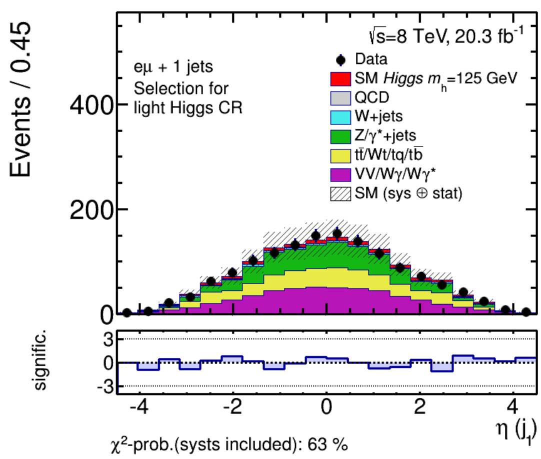

(d) Pseudorapidity of the leading jet.

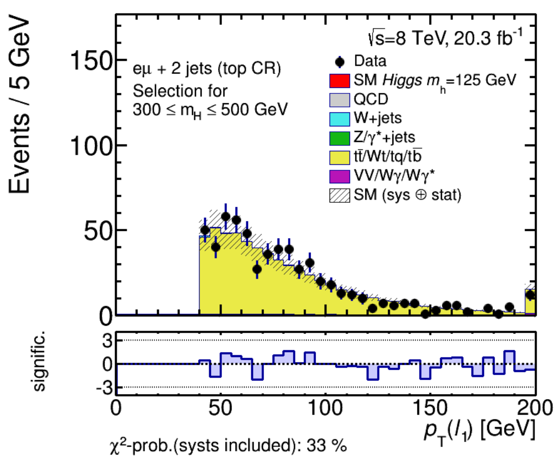

(e) Transverse momentum of the leading lepton.

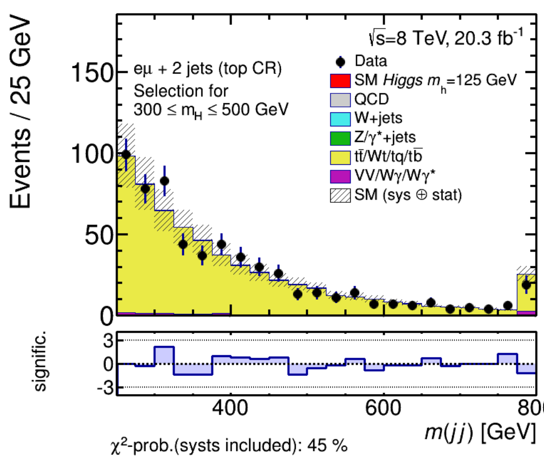

(f) Invariant dijet mass.

Figure 6.7: Basic variables of the light Higgs boson CR (top and center) and the top-quark CR (bottom). The MC predictions are normalised to data and the shaded error bands show the total (systematic and statistical) uncertainty. The significance of the deviation between the simulated events and the data is shown in the subplots as described in Ref. [202]. The last bin of the histograms includes a possible overflow.

Table 6.6: The expected number of signal and background events for an integrated luminosity of 20.3 fb^{-1} in the control regions. Each column shows the event yield for the selections described in Tables 6.3 and 6.5 for the control regions. In the lower table, for each jet channel the expected event yield of a heavy Higgs boson with a mass of $m_H = 150$ GeV, $m_H = 180$ GeV, $m_H = 240$ GeV, $m_H = 340$ GeV or $m_H = 540$ GeV respectively, in the Type I 2HDM with $\tan\beta = 1$ and $\alpha = \pi$ is shown.

Light Higgs boson control region		
Process	Jet channels	
	0 jets	1 jet
SM Higgs Boson	115.5	80.0
$VV/W\gamma/W\gamma^*$	885.8	489.9
$t\bar{t}/Wt/tq/t\bar{b}$	64.0	354.5
Z/γ^* + jets	50.5	405.7
W + jets	23.3	34.0
QCD Multijets	1.9	4.7
Total	1140.9	1368.7
Obs.	1464	1406

Top-quark control region					
Process	Selection Region				
	Low-mass 1	Low-mass 2	High-mass 1	High-mass 2	High-mass 3
SM Higgs Boson	2.1	2.1	1.9	0.6	0.0
$VV/W\gamma/W\gamma^*$	7.6	9.1	15.9	13.4	12.1
$t\bar{t}/Wt/tq/t\bar{b}$	344.4	405.7	662.8	558.9	496.1
Z/γ^* + jets	8.7	8.7	7.3	0.5	0.3
W + jets	1.9	1.8	1.7	1.3	0.5
QCD Multijets	0.1	0.2	0.1	0.0	0.0
Total	364.8	427.5	689.7	574.8	509.1
Obs.	364	431	720	595	541
Heavy Higgs Boson	8.1	10.1	7.0	4.2	1.9

7 | Signal and Background Discrimination

One of the major tasks in this analysis is the separation between signal and background event candidates, in order to obtain regions in the phase space where a decision about the presence of a possible signal can be made. Instead of using a single kinematic variable, a multivariate-analysis (MVA) method based on artificial NNs is chosen [205] which has the advantage of combining the discrimination power of several variables and utilising the correlations between them in order to optimise the separation between signal and background processes. The `NeuroBayes` analysis tool [206, 207] is used in this analysis, since it provides a robust preprocessing of the kinematic input variables and has a better performance in terms of separation power and stability compared to the standard tool `TMVA` [208].

In the following sections the general concept of NNs and the specialities of the `NeuroBayes` package are briefly described. After this, the training procedure – including the selection of input variables and their validation – is described followed by the presentation of the NNs, which are validated in the CRs.

7.1 Functionality of Neural Networks

The `NeuroBayes` package provides a three-layered, feed-forward NN with robust preprocessing of the input variables. The network architecture consists of $(n + 1)$ input nodes for the first layer (one node for each of n input variables and a bias node), a hidden layer with m nodes and a single output node, which gives a continuous distribution between -1 and 1. The number of nodes in the hidden layer can be adjusted by the user, but the dependence on the separation power is small. Therefore, the standard setup of six nodes is not altered. Each node of the hidden layer has connections to all nodes of the input layer, which have different strengths represented by weights w_{ij}, where i and j are the indices of the input and hidden nodes. While the input of the first layer are the preprocessed variables, the input of the hidden layer h_j is a weighted sum of the input variables x_i plus an additional bias term b_j, which describes the connection strength to the bias node and is used to shift the weighted sum to the linear part of the sigmoid function (7.2) in order to avoid saturation effects:

$$h_j(x, b_j) = \sum_i w_{ij} x_j + b_j. \tag{7.1}$$

The output of the hidden nodes is mapped to the interval $[-1, +1]$ by passing its input $h(x)$ to a symmetrised sigmoid function

$$\mathcal{S}(h(x)) = \frac{2}{1 + e^{-h(x)}} - 1, \tag{7.2}$$

which is illustrated in Figure 7.1.

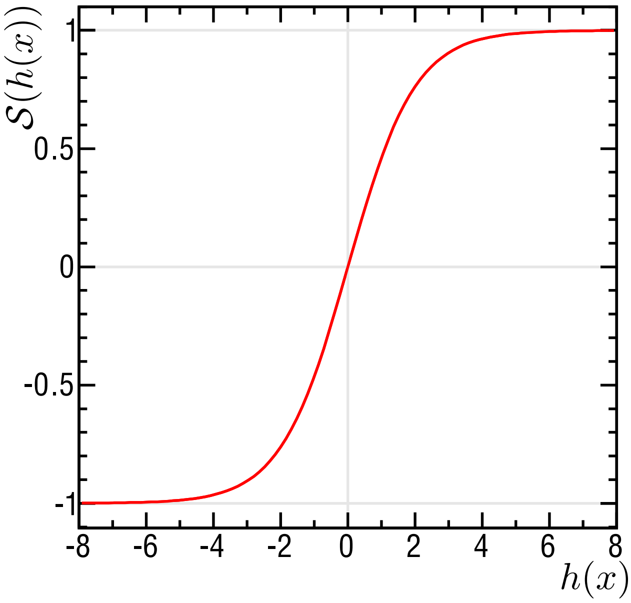

Figure 7.1: Symmetrised sigmoid function $\mathcal{S}(h(x))$ which is used as transfer function for the hidden nodes. Any input value $h(x)$ is mapped to the interval $[-1, 1]$ with a small sensitivity region around zero.

The sigmoid function is also utilised to determine the output of the network's output layer. The single node in this layer is connected with the nodes of the preceding one with weights w_j and the final output for n input variables and m hidden nodes is given as:

$$\begin{aligned} \mathfrak{o} &= \mathcal{S}\left(\sum_{j=1}^{m} w_j \mathcal{S}\left(\sum_{i=1}^{n} w_{ij} x_j + b_j\right)\right) \\ &= \mathcal{S}\left(\sum_{j=1}^{m} w_j \mathcal{S}\left(h_j(x)\right)\right). \end{aligned} \tag{7.3}$$

The construction of the output $\mathfrak{o}$ is such, that it takes values close to 1 for target (signal) events and values close to -1 for non-target (background) events. In order to achieve this, the weights w_{ij}, w_k have to be adjusted according to the target. This process is called training and it is performed using the available MC simulations as so-called training sample. It is described in more detail after the preprocessing of the input variables has been illustrated.

7.1.1 Preprocessing of Variables

The preprocessing of the input variables is one of the main features of `NeuroBayes`. It starts with a non-linear transformation (using the cumulative pdf) of the input variables, such that the transformed variables are distributed uniformly (flattening of the variables), which reduces the influence of statistical outliers. After this, a spline fit to the signal distribution is performed, which further reduces the influence of statistical fluctuations. This distribution is further transformed into a Gaussian distribution with mean of zero and a standard deviation of one, which provides good conditions for an initial learning since it enforces the output of the first-layer nodes to be in the sensitive range of the sigmoid function.

In addition, the correlation matrix for all input variables and their correlations to the target are calculated. With the help of the correlation matrix, the significance of the input variables can be determined by the loss of the total correlation to the target caused by removing the respective variable. In order to find a ranking of the variables which are used for the training, they are decorrelated and the total correlation to the target is computed. Then, one variable after the other is omitted to determine the correlation loss caused by its removal. The variable with the smallest loss is discarded and the procedure is repeated until no variables are left, which leads to a ranking of the variables according to their importance or separation power.

7.1.2 Training of Neural Networks

The training of the NN is performed in order to determine the weights w_{ij} and w_k from equation (7.3). This is done by presenting MC events to the NNs and minimising the so-called entropy loss function [206]:

$$\mathcal{E} = \sum_k \log\left(\frac{1}{2}(1 + \mathfrak{t}_k \cdot \mathfrak{o}_k) + \epsilon\right) \tag{7.4}$$

with the network output $\mathfrak{o}_k$, the target value $\mathfrak{t}_k$ for each event k of the training sample and a small regularisation parameter ϵ, needed to avoid numerical problems at the beginning of the training and which is reduced in each iteration of the training, becoming zero after the first few. The advantage of the entropy loss function is that completely wrong classified events with $\mathfrak{o}_k = 1$ and $\mathfrak{t}_k = -1$ or vice versa lead to an infinite large $\mathcal{E}$, which forces the network to get rid of those wrong classifications very early in its learning process [206]. The small signal-to-background ratio in the samples is artificially enhanced to 50% signal events and 50% background events, while the ratios among the different backgrounds are kept as predicted by the respective cross sections and selection efficiencies.

The minimisation of the entropy loss function $\mathcal{E}$ is performed via back-propagation [209] with an additional momentum term which improves the robustness and the speed of the algorithm. As stated above, the training – and so the minimisation – is an iterative process in order to minimise $\mathcal{E}$ by varying the weights w_{ij} and w_k. For the latter, the update can be calculated easily since the target and its error of the output node are known:

$$\begin{aligned} w_k(t_{r+1}) &= w_k(t_r) + \Delta w_k(t_{r+1}), \text{ with} \\ \Delta w_k(t_{r+1}) &= -\gamma \frac{\partial \mathcal{E}}{\partial w_k(t_r)} + p\Delta w_k(t_r), \end{aligned} \tag{7.5}$$

where $w_k(t_r)$ describes the values of the weight at the rth iteration, $\Delta w_k(t_{r+1})$ describes the update of the weight in the following iteration $r+1$ and $\Delta w_k(t_r)$ the weight update of the previous iteration. The constant γ is used to control the learning speed, while p controls the step width of the gradient descend. The latter term is called momentum term, since this term is equivalent to a friction term for a classical particle in its equation of motion which incorporates information from the previous iterations [210]. In this context, it decelerates the algorithm in areas with frequent gradient changes and it accelerates the algorithm in regions with small gradient changes.

For the update to the weights w_{ij} the hypothetical target values and their corresponding errors for the hidden nodes must be known. While this is not possible directly, it is possible to derive the error of the hidden nodes by back-propagating the error of the output node to the input nodes which takes the following form:

$$\begin{aligned} w_{ij}(t_{r+1}) &= w_{ij}(t_r) + \Delta w_{ij}(t_{r+1}), \text{ with} \\ \Delta w_{ij}(t_{r+1}) &= -\gamma \frac{\partial \mathcal{E}}{\partial w_{ij}(t_r)} + p \Delta w_{ij}(t_r) \\ &= -\gamma \frac{\partial \mathcal{E}}{\partial \mathcal{S}} \frac{\partial \mathcal{S}}{\partial h_j} \frac{\partial h_j}{\partial w_{ij}(t_r)} + p \Delta w_{ij}(t_r). \end{aligned} \tag{7.6}$$

Again, γ and p control the learning speed and weight update and can be adjusted by the user, where small values for γ cause a slower but more accurate behaviour.

As last step, statistically insignificant connections are removed from the NN to ensure that it does not concentrate on irrelevant features of the data. This also avoids overtraining, a common feature of MVA techniques where learning does not adjust to the significant but to random properties of the training sample. In the `NeuroBayes` package it is monitored during the training process if the network is overtrained by using only 80% of the MC events for the training, while using the other 20% as test sample to check for overtraining. The events from the test sample are fed to the previously trained NN and the entropy loss function (7.4) is evaluated. If the evaluation results to be constant in each iteration (ideally 0) the sample is considered as well trained, while a an increase indicates overtraining.

7.2 Setup of the Networks

Since the shape of the heavy Higgs boson signal changes in dependence of its mass as described in Section 6.1 several NNs, each optimised to a specific mass, are trained in order to take this property into account. Table 7.1 shows for which masses the training has been carried out and in which mass range the NN is evaluated. For example the NN trained to separate events with a Higgs boson mass m_H of 150 GeV from background events is also used for Higgs boson masses in the range of 135 GeV $\leqslant m_H \leqslant$ 160 GeV. The choice is adjusted to the available MC samples: In the region below 200 GeV the mass distance between two samples is 5 GeV, from 200 GeV to 600 GeV the distance is 20 GeV and above 600 GeV the distance is 50 GeV. Since the width of the Higgs bosons are smaller at lower masses, more NNs are used in the mass range below 200 GeV, while for higher masses a training every 100 GeV is sufficient.

Table 7.1: Summary of trained NNs for different Higgs-boson masses. The left column shows at which mass the training was carried out and the right column shows in which mass range the corresponding network is used.

m_H used for the training	Mass range
150 GeV	135 GeV $\leqslant m_H \leqslant$ 160 GeV
180 GeV	165 GeV $\leqslant m_H \leqslant$ 195 GeV
240 GeV	200 GeV $\leqslant m_H \leqslant$ 300 GeV
340 GeV	320 GeV $\leqslant m_H \leqslant$ 400 GeV
440 GeV	420 GeV $\leqslant m_H \leqslant$ 500 GeV
540 GeV	520 GeV $\leqslant m_H \leqslant$ 600 GeV
650 GeV	650 GeV $\leqslant m_H \leqslant$ 700 GeV
750 GeV	750 GeV $\leqslant m_H \leqslant$ 800 GeV
850 GeV	850 GeV $\leqslant m_H \leqslant$ 900 GeV
950 GeV	950 GeV $\leqslant m_H \leqslant$ 1000 GeV

Furthermore, for each jet channel a separate training is performed in order to consider the different characteristics of the channels. In the 0-jet channel the training is performed using only the ggF process as target, assuming that the VBF process plays an inferior role in this channel, while in the 1-jet channel both processes are used as targets. In the 2-jet channel the situation is opposite compared to the 0-jet channel, using the VBF process as target. In total 30 (10 mass points times 3 channels) different NNs are used in the signal regions. For the light Higgs boson CR, two additional NNs are trained using the $m_h = 125$ GeV Higgs boson as target in the 0- and 1-jet channel.

Finally, the NN-output distribution delivered by `NeuroBayes` is linearly mapped from its original interval $[-1, 1]$ to $[0, 1]$.

7.2.1 Choice of Input Variables

The separation power of the used NNs is mainly driven by the choice of input variables. If variables with a strong separation power are omitted, the quality of the networks is heavily impaired while on the other hand, at some point the networks reach a saturation, where additional variables are not able to improve the separation power, due to their systematic uncertainties which distort them. Out of the available kinematic variables (about 40) the ones, which were used most frequently in the training (in all mass regions and channels) have been picked, resulting in 20 variables which are presented to all NNs in all jet channels. The reduced number of variables has only a small effect on the quality of the networks, which was checked by comparing the values of the total correlation-to-target of both scenarios. The reduction caused by the removal of variables induces a maximal decrease of one percentage point of the total correlation-to-target.

The used variables can be categorised as follows:

Leptonic Variables: These variables depend only on the leptonic objects of the final state:

- $p_{\mathrm{T}}(\ell_2)$, the transverse momentum of the the sub-leading lepton,
- $|\eta(\ell_1)|$ and $|\eta(\ell_2)|$, the absolute value of the lepton pseudorapidity,
- $\Delta\phi(\ell_1, \ell_2)$, the azimuthal angle between the leptons,
- $\Delta R(\ell_1, \ell_2)$, the angular distance of the leptons,
- $p_{\mathrm{T}}(\ell\ell)$, the transverse momentum of the dilepton system,
- $\Delta p_{\mathrm{T}}(\ell_1, \ell_2)$, the absolute value of the transverse momentum difference between the leptons,
- $\Delta\eta(\ell_1, \ell_2)$, the absolute value of the pseudorapidity difference between the leptons and
- $m(\ell\ell)$, the invariant mass of the dilepton system.

Jet Variables: These variables contain information of one or more jets of the final state:

- $p_{\mathrm{T}}(j_1)$, the transverse momentum of the leading jet,
- $\eta(j_1)$, the pseudorapidity of the jet with the largest transverse momentum,
- $\Delta R(\ell_1, j_1)$, the angular distance between the leading lepton and the leading jet and
- $\Delta R(\ell\ell, j_1)$, the angular distance between the dilepton system and the leading jet.

in case of the 2-jet channel the following variables are also considered:

- $p_{\mathrm{T}}(j_2)$, the transverse momentum of the sub-leading jet,
- $\eta(j_2)$, the pseudorapidity of the sub-leading jet,
- $\Delta\eta(j_1, j_2)$, the pseudorapidity difference between the two jets,
- $\Delta R(j_1, j_2)$, the angular distance between the two jets and
- $m(jj)$, the invariant mass of the dijet system.

Event Variables: These variables depend on a combination of all objects in the final state:

- $E_{\mathrm{T,\,rel}}^{\mathrm{miss}}$, the relative missing transverse momentum as given in equation (4.4),
- m_{T}, the transverse mass as given in equation (6.1) and
- $p_{\mathrm{T}}^{\mathrm{tot}}$, the magnitude of the vector sum of all final state objects:

$$p_{\mathrm{T}}^{\mathrm{tot}} = \left|\vec{p}_{\mathrm{T}}^{\,\mathrm{tot}}\right| = \left|\vec{p}_{\mathrm{T}}(\ell_1) + \vec{p}_{\mathrm{T}}(\ell_2) + \vec{p}_{\mathrm{T}}(j_1) + \vec{p}_{\mathrm{T}}(j_2) + \vec{E}_{\mathrm{T}}^{\mathrm{miss}}\right|. \qquad (7.7)$$

As an example, Table 7.2 shows the ranking of the used variables in the different jet channels for the training performed for a heavy Higgs boson mass of $m_H = 340$ GeV. The ranking for all training points can be found in Appendix A.

7.2.2 Modelling of the Input Variables

After the input variables have been chosen, their modelling in the signal region is reviewed in order to check if the data are correctly described by the MC simulations. As an example, Figures 7.2 to 7.4 show the six most important input variables (obtained from Table 7.2) in the different jet channels for the training performed for a heavy Higgs boson mass of m_H = 340 GeV.

Table 7.2: Variables used for the training of the NN at m_H = 340 GeV in the 0-jet channel (left), the 1-jet channel (centre) and in the 2-jet channel (right), ordered by their importance. The ordering is given by the loss in total correlation to the target, which is 50.3%, 48.5% and 73.9% respectively, for the entire set of variables.

0-jet channel		1-jet channel		2-jet channel	
Variable	corr. loss in %	Variable	corr. loss in %	Variable	corr. loss in %
m_{T}	21.7	m_{T}	19.9	$m(jj)$	12.4
$\Delta\eta(\ell_1, \ell_2)$	14.8	$\eta(j_1)$	19.1	m_{T}	8.9
$\Delta R(\ell_1, \ell_2)$	10.7	$\Delta R(\ell\ell, j_1)$	16.6	$\Delta\eta(j_1, j_2)$	8.4
$\lvert\eta(\ell_1)\rvert$	10.1	$p_{\mathrm{T}}(j_1)$	12.3	$\Delta R(\ell_1, j_1)$	8.2
$\Delta p_{\mathrm{T}}(\ell_1, \ell_2)$	8.9	$\Delta\eta(\ell_1, \ell_2)$	11.2	$\Delta\eta(\ell_1, \ell_2)$	8.1
$\lvert\eta(\ell_2)\rvert$	7.0	$\Delta R(\ell_1, \ell_2)$	9.8	$\eta(j_1)$	6.3
$m(\ell\ell)$	6.3	$\lvert\eta(\ell_1)\rvert$	7.2	$p_{\mathrm{T}}^{\mathrm{tot}}$	5.5
$p_{\mathrm{T}}(\ell_2)$	4.5	$m(\ell\ell)$	6.7	$p_{\mathrm{T}}(\ell_2)$	3.3
$p_{\mathrm{T}}^{\mathrm{tot}}$	4.5	$\Delta p_{\mathrm{T}}(\ell_1, \ell_2)$	4.6	$m(\ell\ell)$	3.1
$p_{\mathrm{T}}(\ell\ell)$	3.4	$p_{\mathrm{T}}(\ell_2)$	3.1	$\Delta R(\ell_1, \ell_2)$	2.8
$E_{\mathrm{T,\,rel}}^{\mathrm{miss}}$	0.6	$\lvert\eta(\ell_2)\rvert$	2.7	$\Delta\phi(\ell_1, \ell_2)$	2.8
		$p_{\mathrm{T}}(\ell\ell)$	0.7	$E_{\mathrm{T,\,rel}}^{\mathrm{miss}}$	1.8
		$\Delta\phi(\ell_1, \ell_2)$	0.6	$p_{\mathrm{T}}(j_2)$	1.2
		$p_{\mathrm{T}}^{\mathrm{tot}}$	0.3	$p_{\mathrm{T}}(j_1)$	1.2
				$\lvert\eta(\ell_2)\rvert$	0.7
				$\Delta p_{\mathrm{T}}(\ell_1, \ell_2)$	0.7
				$\lvert\eta(\ell_1)\rvert$	0.6
				$p_{\mathrm{T}}(\ell\ell)$	0.2

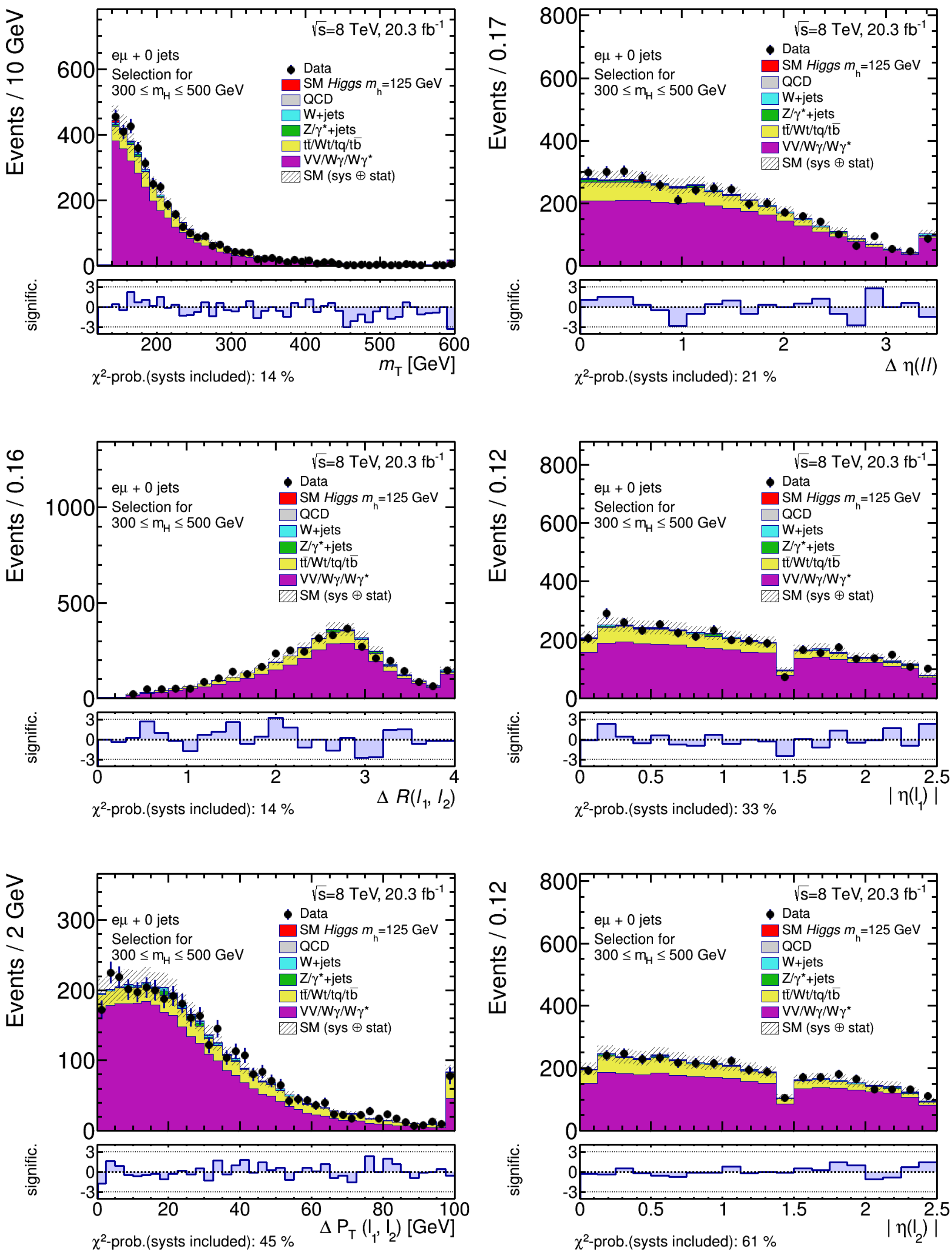

Figure 7.2: The six most important input variables for the NN, trained to obtain a heavy Higgs boson with a mass of $m_H = 340$ GeV in the 0-jet channel. The MC predictions are normalised to fit values as described in Section 7.3 and the shaded error bands show the total (systematic and statistical) uncertainty. The significance of the deviation between the simulated events and the data is shown in the subplots as described in Ref. [202]. The last bin of the histograms includes a possible overflow.

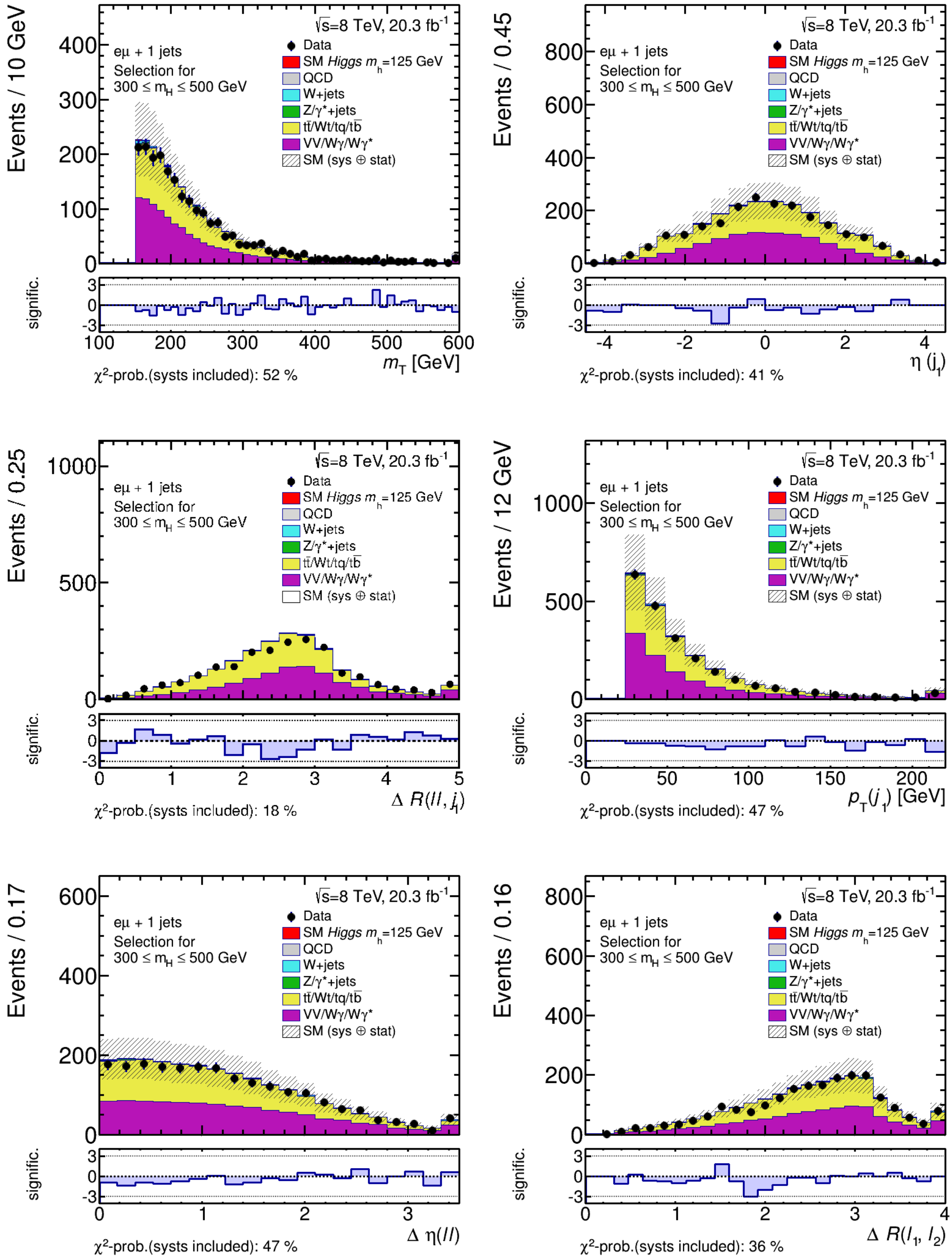

Figure 7.3: The six most important input variables for the NN, trained to obtain a heavy Higgs boson with a mass of $m_H = 340$ GeV in the 1-jet channel. The MC predictions are normalised to fit values as described in Section 7.3 and the shaded error bands show the total (systematic and statistical) uncertainty. The significance of the deviation between the simulated events and the data is shown in the subplots as described in Ref. [202]. The last bin of the histograms includes a possible overflow.

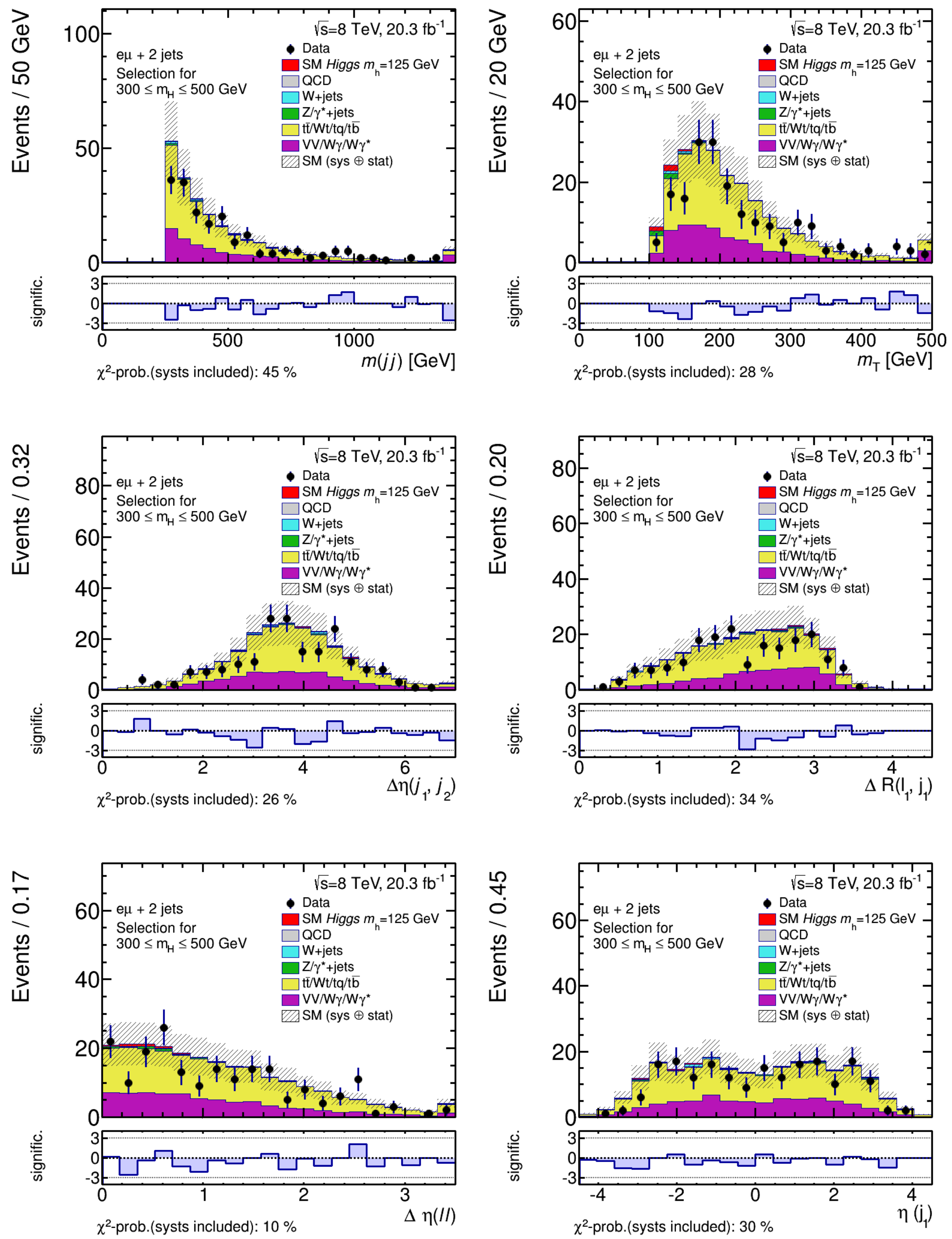

Figure 7.4: The six most important input variables for the NN, trained to obtain a heavy Higgs boson with a mass of $m_H = 340$ GeV in the 2-jet channel. The MC predictions are normalised to fit values as described in Section 7.3 and the shaded error bands show the total (systematic and statistical) uncertainty. The significance of the deviation between the simulated events and the data is shown in the subplots as described in Ref. [202]. The last bin of the histograms includes a possible overflow.

7.2.3 Neural Network related Cuts

As described in Section 6.2.2, the NN-output distributions caused two non-intuitive cuts on the transverse mass m_{T} in the high-mass 1 region and on the invariant dijet mass $m(jj)$ for all mass regions of in the 2-jet channel.

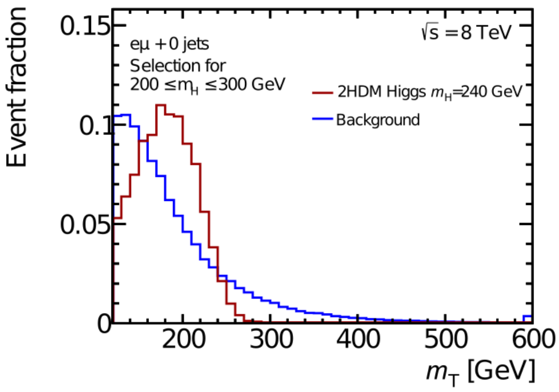

(a) Transverse mass in the 0-jet channel without additional cut on m_{T}.

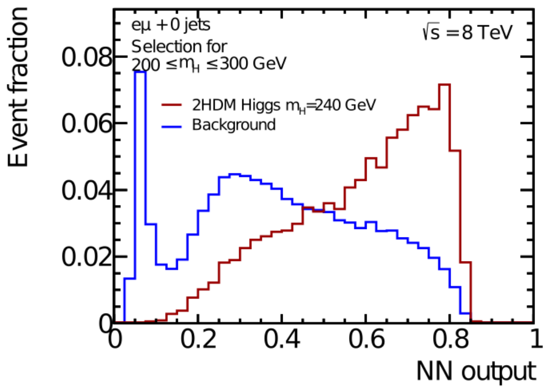

(b) NN-output distribution for the training point at $m_H = 240$ GeV without additional cut on m_{T}.

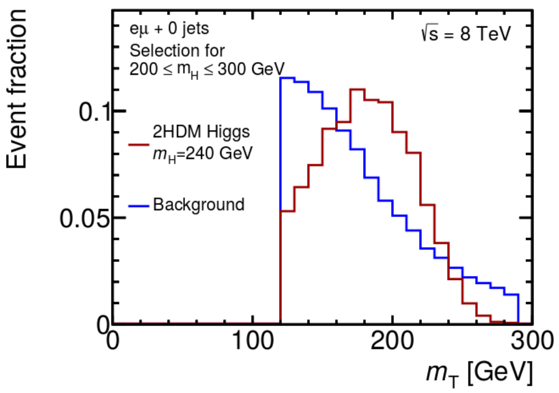

(c) Transverse mass in the 0-jet channel with additional cut on m_{T}.

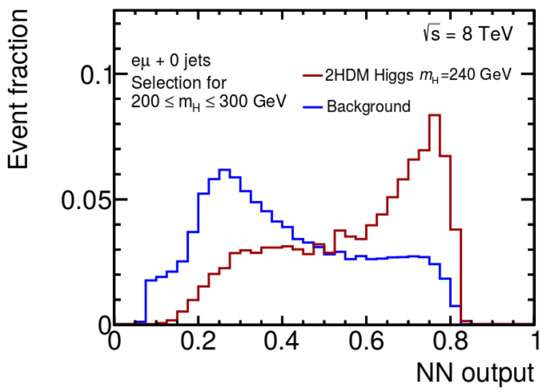

(d) NN-output distribution for the training point at $m_H = 240$ GeV with additional cut on m_{T}.

Figure 7.5: Transverse mass and NN-output distributions in the 0-jet channel before the additional cut on m_{T} ((a) and (b)) and after the additional cut which constrains m_{T} from above ((c) and (d)). The peak around zero in the NN output vanishes after the cut.

Figure 7.5 shows NN-output distributions normalised to unit area for the training point at $m_H = 240$ GeV in the high mass 1 region. The red curve depicts the 2HDM signal with the mass of a heavy Higgs boson of $m_H = 240$ GeV, $\tan\beta = 1$ and $\alpha = \pi$, while the blue curve shows the total background. Figure 7.5(b) shows a spike in the NN-output distribution around zero, which is caused by events which are categorised as completely background-like. Those events can be found in Figure 7.5(a) in the range $m_{\mathrm{T}} > 290$ GeV, where no signal but only background events are found. But in order to avoid this strong shape fluctuation, the additional $m_T < 290$ GeV cut on m_T is performed (see Figure 7.5(c)), which removes the peak in the NN-output distribution as can be seen in Figure 7.5(d). With larger Higgs boson masses the peak of the signal distribution tends to higher values of m_T, as described in Section 6.2.2, and this effect vanishes. Similar behaviour can be observed in the 1-jet channel, where this cut is also applied.

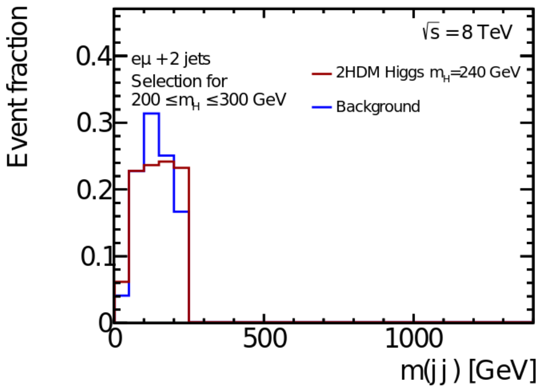

(a) Invariant dijet mass in the region $m(jj) < 250$ GeV.

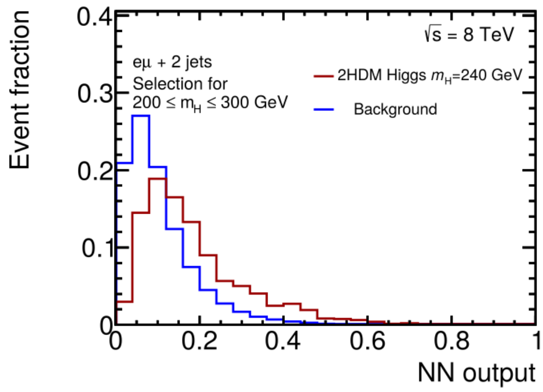

(b) NN-output distribution for the training point at $m_H = 240$ GeV when applied to events with $m(jj) < 250$ GeV.

Figure 7.6: Invariant dijet mass distribution for $m(jj) < 250$ GeV (a) and NN output distribution trained at $m_H = 240$ GeV (b). The NN classifies signal events as well as background events as background-like, if they originate from the phase space region $m(jj) < 250$ GeV.

The second cut, which was chosen in order to improve the shape of the NNs, is the cut $m(jj) > 250$ GeV on the invariant dijet mass. While optimising the rest of the cuts to loose a minimum of signal events, this cut not only removes background events but also a fair amount of signal events. This can be justified by regarding how the NNs treat the events originating from this region in phase space. Figure 7.6(a) shows the invariant dijet mass distribution for $m(jj) < 250$ GeV, while Figure 7.6(b) shows how the events from this region are treated by the NN trained with a heavy Higgs boson mass of 240 GeV for events coming from this region. As can be seen, most of the signal-like events are treated as background-like, leaving the NN unable to classify signal events correctly coming from this phase space region. Therefore, events from this region of phase space are removed in order to focus the NNs on significant regions, where a discrimination between signal and background events is possible.

7.3 Neural Network Output

The main goal of the NNs is the separation between signal and background events. Figure 7.7 shows the NN-output distributions normalised to unit area for the NN trained at $m_H =$

340 GeV. As in the section before, the red curve depicts the 2HDM signal where the mass of the heavy Higgs boson is assumed to be $m_H = 340$ GeV.

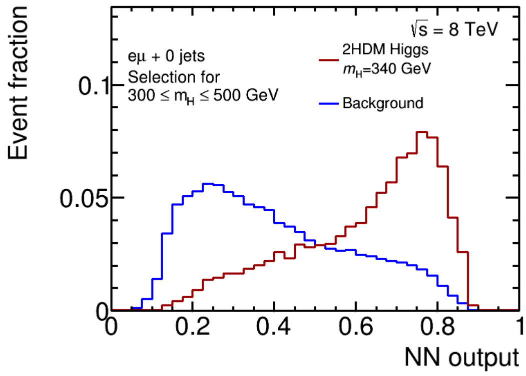

(a)

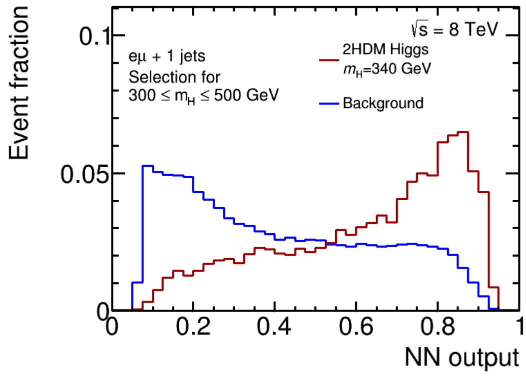

(b)

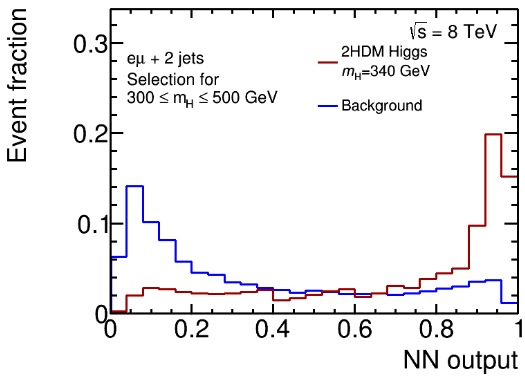

(c)

Figure 7.7: NN-output distributions, normalised to unit area, for $m_H = 340$ GeV. Figure (a) shows the distribution of the 0-jet channel, (b) of the 1-jet channel and (c) of the 2-jet channel. The red curve shows the 2HDM signal with $m_H = 340$ GeV, $\tan\beta = 1$ and $\alpha = \pi$ and the blue curve shows the sum of all background processes.

The normalisation of the plots in Figures 7.2 to 7.4 and in Figure 7.9 is obtained by a binned log-likelihood fit using the NN-output distributions of the light Higgs boson CR (0-jet and 1-jet channel) simultaneously with the event yield of the top-quark CR (2-jet channel). The four scale factors of the different processes are used as free parameters of the fit: β_{SM} for SM-ggF and -VBF processes, β_{diboson} for diboson background processes, β_{top} for processes including at least one top quark and $\beta_{\text{Drell-Yan}}$ for Drell-Yan/Z + jets processes. The SM-Higgs boson processes are summed together due to the small statistics. The W + jets background is fixed, since the normalisation for this process is obtained from data as described in Section 5.3.2. The fit results are shown in Table 7.3, while the NN output distributions of the light Higgs CR and the top-quark CR are shown in Figure 7.8, where for the top-quark CR the NN trained at $m_H = 340$ GeV was chosen as example.

Table 7.3: Scale factors for signal and background processes as obtained from the fit of the the NN-output distributions of the light Higgs boson CR (0-jet and 1-jet channel) simultaneously with the event yield of the top-quark CR (2-jet channel) to the data. Statistical uncertainties on the normalisation factors are shown.

Process	Scale Factor
SM Higgs Boson	1.074 ± 0.029
Diboson Bkg.	1.224 ± 0.033
Top-quark Bkg.	0.989 ± 0.044
Z/γ^* + jets	0.787 ± 0.057

The agreement between the simulated events and the data is checked for all NNs. As an example, Figure 7.9 shows the distributions of the NN discriminant, trained to separate the signal of a heavy Higgs boson with the mass of $m_H = 340$ GeV from the background processes. A decent agreement between simulations and data is found. The ranking of the input variables and the output distributions of the NN distributions which were trained with other mass samples can be found in Appendices A and B respectively.

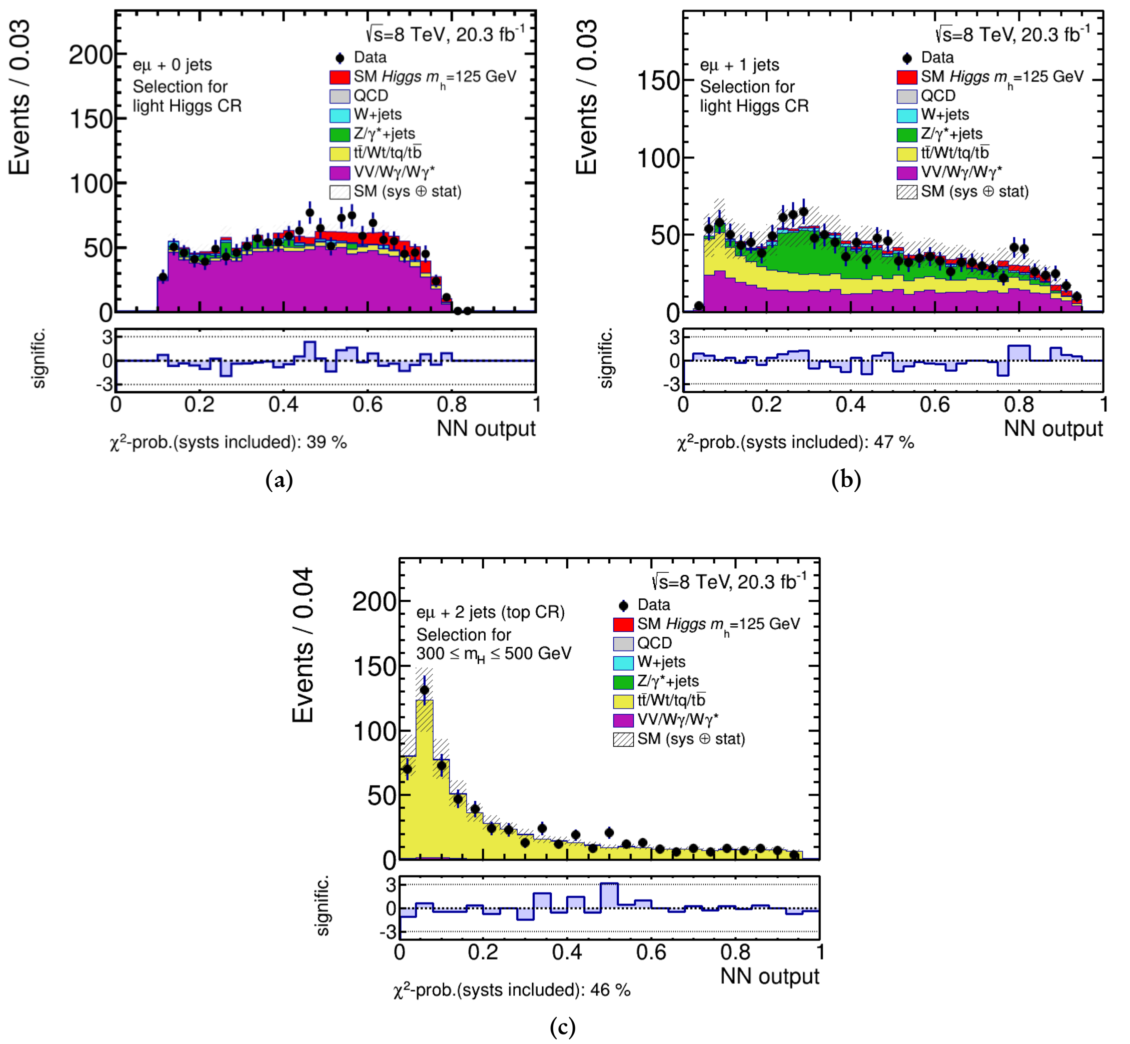

Figure 7.8: NN-output distribution in the light Higgs boson CR (top) and in the top-quark CR (bottom). In the bottom plot the NN trained at $m_H = 340$ GeV was chosen as an example. The MC predictions are normalised to the values given in Table 7.3 and the shaded error bands show the total (systematic and statistical) uncertainty. The significance of the deviation between the simulated events and the data is shown in the subplots as described in Ref. [202]. The last bin of the histograms includes a possible overflow.

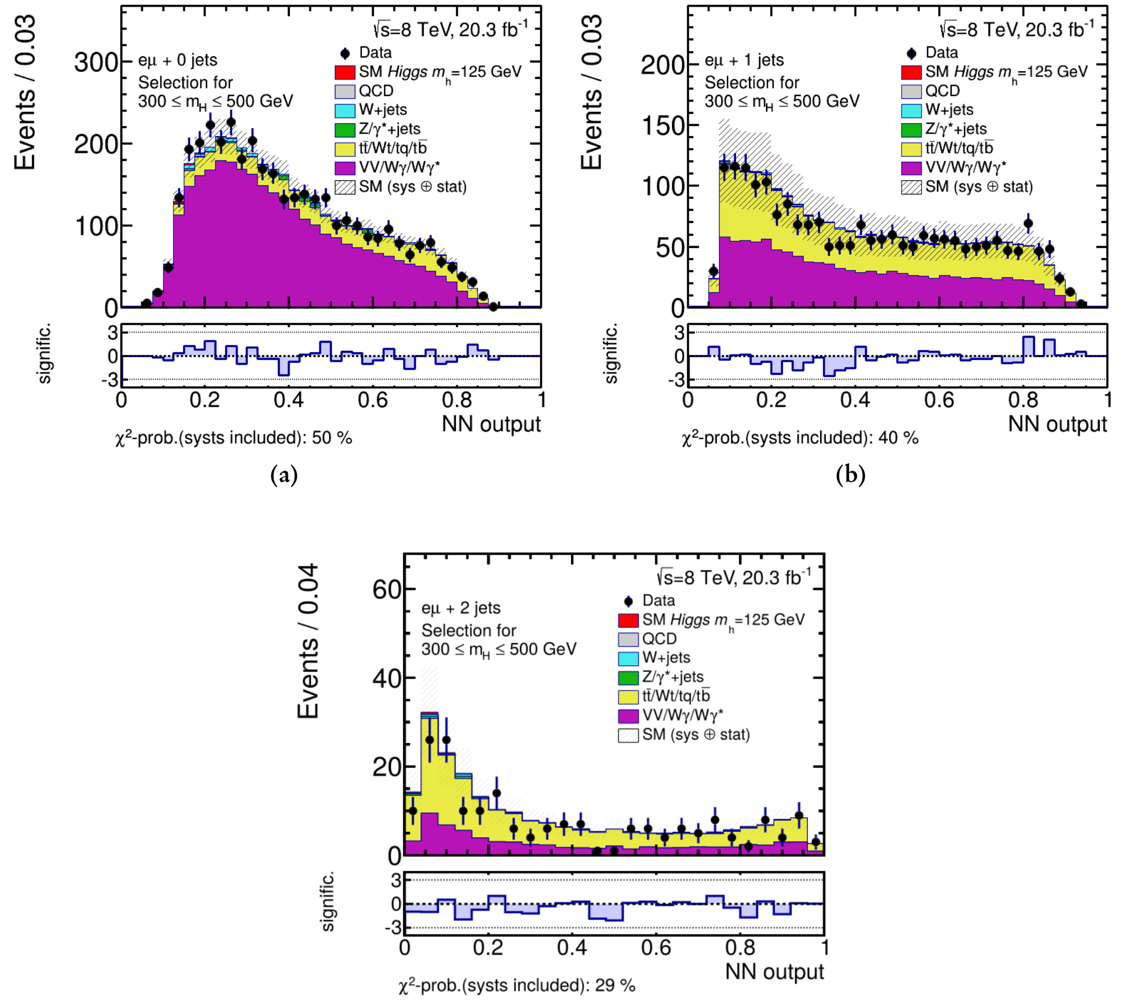

(a) (b) (c)

Figure 7.9: NN-output distribution in the high-mass-2 region in the 0-jet channel (a), the 1-jet channel (b) and in the 2-jet channel for a NN trained at $m_H = 340$ GeV. The MC predictions are normalised to the values given in Table 7.3 and the shaded error bands show the total (systematic and statistical) uncertainty. The significance of the deviation between the simulated events and the data is shown in the subplots as described in Ref. [202]. The last bin of the histograms includes a possible overflow.

8 | Systematic Uncertainties

Systematic uncertainties on the normalisation of the different backgrounds, on the signal acceptance, and on the shape of the NN-discriminant distributions for signal and background processes deteriorate the sensitivity of the search for the Higgs-boson production. Both, rate and shape uncertainties are taken into account as Gaussian variations when generating pseudo experiments that include correlated variations of rate and shapes (see also Section 9.4). Systematic uncertainties due to the residual differences between data and MC simulations for the reconstruction and energy calibration of jets, electrons and muons are propagated through the analysis. The considered systematic uncertainties can be split into the following categories, where the uncertainties associated with jets are dominating. Table 8.2 shows a summary of the impact of the different uncertainties.

8.1 Jet Modelling Uncertainties

The main source of uncertainty on the modelling of jets comes from the JES, including the modelling of pile up, as well as b-jet identification [150]. The JES uncertainty [211] has been evaluated using 2010 ATLAS data. Additional contributions to this uncertainty due to the larger pile-up effects in 2012 data are included and range up to 4% as a function of the transverse momentum for central jets ($\eta = 0.0$) and from 3% to 7% as a function of η with $p_{\mathrm{T}} = 40$ GeV and are taken from Ref. [212].

The JES uncertainties can be split into several categories. The most important one is the η-intercalibration modelling, as described in Section 4.1.3. The uncertainty on the jet-level corrections due to the modelling of additional parton radiation is estimated by comparing di-jet events simulated with `PYTHIA` and `HERWIG`. This modelling uncertainty dominates the η-intercalibration uncertainty and increases with η. Furthermore, the different measurements of the p_{T} balance are subject to uncertainties of the jet resolution and the electron/photon energy scale which are summarised as detector uncertainties. The modelling of the physics processes due to the choice of MC generators, the modelling of the final-state radiation and the modelling of the underlying event as well as the soft radiation is also afflicted with an uncertainty which alters the JES. Finally, the limited size of the data set, used to determine the JES, also carries an uncertainty which is taken into account. In total, twelve different uncertainty components are taken into account for the JES where the up/down variations are performed independently from each other. As an example, the impact of one component of the JES systematic shape uncertainty on the shapes of the NN output distributions in the 2-jet channel trained for a $m_H = 340$ GeV Higgs boson are depicted in Figure 8.1. Further plots with all systematic shape uncertainties can be found in Ref. [205].

Additional uncertainties arise from jets with $p_{\mathrm{T}} < 20$ GeV (soft jets) as well as from soft calorimeter energy deposits that are not associated with reconstructed physics objects and the

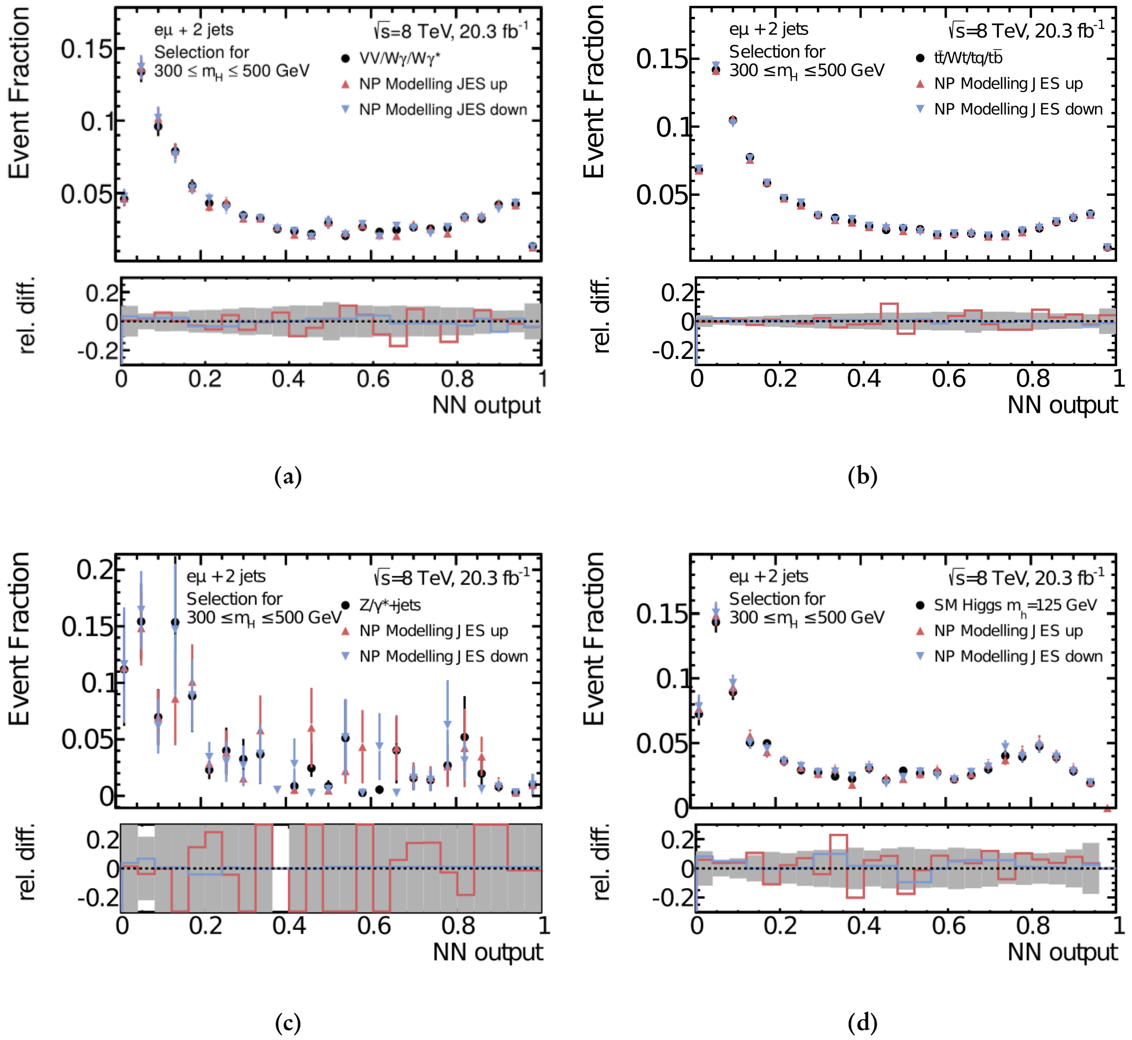

Figure 8.1: Uncertainties on the shape of the NN output distribution trained for an m_H = 340 GeV Higgs boson in the 2-jet channel due to uncertainty of the JES modelling. The figures show the impact on the different background processes: Diboson background (a), top-quark background (b), Drell-Yan/Z + jets background (c) and SM Higgs-boson production (d). The black dots show the nominal NN output distribution, while the markers represent the upward (red) and downward (blue) shape variations, obtained by evaluating the NN on the samples altered by the systematic variation. The ratio panel shows the relative difference between the nominal shape and the shapes shifted by the systematics and the grey band shows the statistical uncertainty of the nominal sample.

jet energy resolution (JER) which range from 5% to 20% depending on p_T and η as described in Ref. [160]. Other minor uncertainties are assigned to the reconstruction of E_T^{miss} and to account for the impact of pile-up collisions on E_T^{miss}.

The uncertainties related to b-jet identification are decomposed into six uncorrelated components, so-called eigenvectors, where the number of the eigenvectors is based on the number of p_T bins used in the calibration. A covariance matrix is constructed for each source of uncertainty and the sum of these matrices form the total covariance matrix. The corresponding eigenvectors of the total covariance matrix are varied within $\pm 1\sigma$ to determine the uncertainties. The rate uncertainties originating from the decomposed components range between below 1% and 8% [200], while the uncertainty for a c-jet (light jet) to be reconstructed as a b-jet ranges between 6% – 14% (9% - 19%), depending on the transverse momentum (and pseudorapidity) of the jet. Each uncertainty corresponding to the eigenvectors is propagated independently through the analysis.

8.2 Lepton Modelling Uncertainties

Uncertainties on the electron and muon reconstruction, identification, and trigger efficiencies are estimated using tag-and-probe methods [156, 213, 214] on samples enriched with $Z \to \ell\ell$, $J/\psi \to \ell\ell$, or $W \to \ell\nu$ ($\ell = e, \mu$) events. Other components include the electron and muon energy scale which are summarised in Table 8.1 as described in Ref. [215].

Table 8.1: Uncertainties on lepton efficiency, energy scale and resolution [215].

Uncertainty Source	Size of the uncertainty
Electron efficiency	reconstruction: 0.1% – 3.0% depending on E_T and η identification: 0.2% – 2.7% depending on E_T and η
Electron energy scale	0.4% depending on E_T and η (except for the crack region)
Electron energy resolution	1% depending on E_T and η
Muon efficiency	$< 2.6\%$ depending on p_T and η
Muon energy scale	$< 3.0\%$ depending on p_T and η
Muon energy resolution	less than 1% depending on p_T and η

8.3 Missing Transverse Momentum Modelling Uncertainties

For the calculation of E_T^{miss} reconstructed physics objects are used whose calorimeter deposits are associated with reconstructed electrons, photons, tau leptons, jets and muons. Therefore all uncertainties related to these objects are propagated through the calculation of the missing transverse momentum. The impact of the soft terms to the total uncertainty are also taken into account and have been obtained by the ATLAS Jet/$E_{\mathrm{T}}^{\mathrm{miss}}$ combined performance group [159]. The uncertainties are up to 17% for the calorimeter based determination of $E_{\mathrm{T}}^{\mathrm{miss}}$ for events with $E_{\mathrm{T}}^{\mathrm{miss}} > 45$ GeV and at most 5% for the track-based determination.

8.4 Migration, Diboson Off-Shell Effect and Luminosity Uncertainties

The normalisation factors are governed by the total number of events and their distribution in the different jet channels. To take the migration of diboson and top events between the jet channels into account, uncertainties are introduced. In case of diboson processes the migration of jets between 0-jet and 1-jet channel is taken into account, which is estimated with an uncertainty of 12%. For top-quark processes the migration between 0-jet, 1-jet and 2-jet channel are considered, the migration from the 2-jet channel into the other jet channels being dominant. The estimated uncertainties are 4%, 3% and 6% for the 0-jet, 1-jet and 2-jet channel respectively. The size of the uncertainties has been determined estimating the fractions of events, migrating between the jet channels from the MC samples.

Due to the same initial and final state the $gg \to H \to WW$ and the $gg \to WW$ processes can have an interference. This effect is considered for the light Higgs (125 GeV) contribution and is estimated using MCFM samples with the interference included. It only affects the $gg \to H \to WW$ and $gg \to WW$ samples, where the latter is a small fraction of the total diboson background. The impact on the rate of $gg \to H \to WW$ and $gg \to WW$ events is 14% in the 0-jet channel, 78% in the 1-jet channel and 50% in the 2-jet channel.

The uncertainty on the integrated luminosity is determined by van der Meer scans [216] and its value is found to be 2.8% [217].

8.5 Cross-Section Uncertainties

In this section, theoretical uncertainties on signal and background processes are presented. Their main sources are the PDFs, QCD renormalisation and factorisation scales, generator modelling and underlying event and parton shower (UEPS).

The relative uncertainty on the signal cross section is determined following [66] and [218] by independently varying QCD renormalisation and factorisation scales. Following the Stewart-Tackmann procedure, described in Ref. [219], independent uncertainties for each jet channel are assumed in the ggF production mode. For high Higgs-boson masses, the relative uncertainties depend on the mass [220] and are 38% in the 0-jet channel, 42% in the 1-jet channel and 78% in the 2-jet channel at a Higgs-boson mass of 600 GeV. The average relative uncertainty for the VBF production processes is assumed to be 10.4% [220].

The scale uncertainties for the WW diboson background production are evaluated by varying the renormalisation and factorisation scales up and down by a factor of 2. The PDF uncertainties are evaluated using CT10 PDF eigenvectors compared to the MSTW2008 PDFs [221]. The UEPS uncertainty is evaluated by comparing the normalisation factors for the nominal POWHEG+PYTHIA6 sample to the predictions from POWHEG interfaced to PYTHIA8 and HERWIG. The total uncertainties range from 2% to 7.1%, with the lowest uncertainties for the 0-jet channel and the highest ones for the 1-jet channel. In the 2-jet channel, dominated by VBF production, the scale variations are 10% for production processes without QCD vertices and 34% for production processes with QCD vertices.

Apart from WW diboson production, the $W\gamma^{(*)}/Z$, ZZ and $Z\gamma$ diboson processes are included as well in the analysis. Uncertainties for $W\gamma$ diboson production are evaluated for each jet channel using MCFM, following the so called Stewart-Tackmann procedure. The resulting uncertainties are 11% in the 0-jet channel, 53% in the 1-jet channel and 100% in the 2-jet channel [215]. In addition, a PDF uncertainty of 3.1% is applied.

Uncertainties on the top-quark production cross sections in the 0-jet channel, arising from the QCD renormalisation and factorisation scale, the PDFs, UEPS and the NLO parton matching are evaluated using a similar procedure as described in the WW diboson background case. In addition, an uncertainty on the relative size of the single top-quark production cross section, compared to the top-quark-antiquark pair production cross section, is applied by varying the single top-quark cross section by $\pm 20\%$ as described in Ref. [220]. The uncertainties on the treatment of interference between top/anti-top quark and single top-quark production are assessed by comparing samples with two different schemes for removing common diagrams from the MC samples. The total uncertainty in this jet channel is 7.5%.

The uncertainties in the 1-jet channel are derived using the same methods as in the 0-jet channel but with a difference in the b-tagging efficiency in the generator-level samples. An average b-tagging efficiency of 82.2% and mis-tag efficiency of 11.6% is assigned to each b-jet and non-b-jet to emulate the b-tagging. These are derived from reconstruction level POWHEG+PYTHIA samples by matching the reconstructed jets to truth jets to classify them as b-jets and non-b-jet. The total uncertainty on the efficiency of the remaining selection is 2%.

In the 2-jet channel the total uncertainties are 5% in the ggF case and 26.2% in the VBF case. For the latter, the main background process is top-quark-antiquark pair production.

The QCD scale uncertainty for the Drell-Yan processes is evaluated through variation of the renormalisation (μ_R) and factorisation (μ_F) scales used in the ALPGEN Z + jets samples with parton multiplicity of 0, 1, or 2. The different values for μ_R and μ_F are [220]:

$$\mu_R = \mu_F = \mu_0,\ \mu_R = \mu_F = 0.5 \cdot \mu_0 \text{ and } \mu_R = \mu_F = 2 \cdot \mu_0 \tag{8.1}$$

with $\mu_0 = \sqrt{m_Z^2 + \sum_j m_{\mathrm{T},j}}^2$, where m_Z is the mass of the Z boson and $m_{\mathrm{T},j}$ is the transverse mass of the jet with index j. The PDF uncertainties are evaluated using the CT10 eigenvectors and its comparison among the MSTW2008, and NNPDF2.3 central values. The generator modelling is evaluated through comparison of the nominal ALPGEN+HERWIG prediction to the

ALPGEN + PYTHIA6 and SHERPA alternatives. The impact of the uncertainties are 21% in the 0-jet channel, 12% in the 1-jet channel and 16% in the 2-jet channel.

As described in Section 5.3.2 the fake factor for the W + jets and QCD multijet background processes is determined from data. In this method, the W + jets and QCD multijet samples are constructed by subtracting a MC control sample from a data sample measured in Z + jets and di-jet events. In order to derive an uncertainty for the fake factor, different MC control samples are compared and POWHEG + PYTHIA8, ALPGEN + PYTHIA6 and ALPGEN + HERWIG are used. The total uncertainty on the fake factor and therefore on the rate is found to be at most 40% for muons and 61% for electrons as [200].

An overview of the systematic rate uncertainties is given in Table 8.2 for each jet channel, using the largest value from all mass regions. Furthermore, the uncertainties are rounded to integers, but all uncertainties smaller than 1% are rounded up.

Table 8.2: Systematic rate uncertainties for background processes in the different jet channels. The uncertainties are rounded to integers in percent but all uncertainties smaller than 1 percent are rounded up. As described in the text, the exact value of the luminosity uncertainty is 2.8% for every process. The Off-shell systematic affects only the $gg \to WW$ process and its impact to the total uncertainty is given in parentheses.

0 jets			
Uncertainty Source	Diboson Bkg.	Top-quark Bkg.	DY/Z + jets
Jet Modelling	10%	12%	31%
b-tagging	1%	1%	1%
Lepton Modelling	6%	1%	8%
$E_{\mathrm{T}}^{\mathrm{miss}}$ Modelling	4%	1%	5%
top migration	–	4%	–
diboson jet migration	12%	–	–
Off-shell	4%	–	–
Luminosity	3%	3%	3%
Total uncertainty	18%(19%)	13%	32%
1 jet			
Uncertainty Source	Diboson Bkg.	Top-quark Bkg.	DY/Z + jets
Jet Modelling	11%	8%	13%
b-tagging	3%	6%	2%
Lepton Modelling	7%	2%	2%
$E_{\mathrm{T}}^{\mathrm{miss}}$ Modelling	4%	1%	4%
top migration	–	3%	–
diboson jet migration	12%	–	–
Off-shell	78%	–	–
Luminosity	3%	3%	3%
Total uncertainty	19%(80%)	11%	14%
2 jets			
Uncertainty Source	Diboson Bkg.	Top-quark Bkg.	DY/Z + jets
Jet Modelling	18%	6%	24%
b-tagging	3%	8%	2%
Lepton Modelling	5%	2%	2%
$E_{\mathrm{T}}^{\mathrm{miss}}$ Modelling	3%	1%	12%
top migration	–	6%	–
Off-shell	50%		
Luminosity	3%	3%	3%
Total uncertainty	19%(53%)	12%	27%

9 | Statistical Methods

The compatibility of the observed data with the different signal predictions, depending on the set of 2HDM parameters, is evaluated by performing hypothesis tests based on pseudo experiments. When searching for a heavy Higgs boson the following hypotheses are compared:

- In the null hypothesis H_0 the Standard Model including a Higgs particle with $m_h = 125$ GeV is assumed.
- In the signal hypotheses H_1 a specific 2-Higgs-Doublet Model, depending on the triplet $(m_H, \tan\beta, \cos(\beta-\alpha))$ is assumed. In the regarded scenarios m_h is fixed at 125 GeV, assuming that the light scalar Higgs boson of the 2HDM coincides with the SM-like Higgs boson.

In order to compare the results of this analysis with the ATLAS analysis [222], which focusses on the search for a heavy SM-like Higgs boson in the same decay channel, the following hypotheses are also regarded:

- In the null hypothesis H_0^* the Standard Model without any Higgs particles is assumed.
- In the alternative hypotheses H_1^* the Standard Model without a light Higgs boson with $m_h = 125$ GeV but with a Higgs boson in the mass range 135 GeV $\leqslant m_H \leqslant$ 1000 GeV is assumed.

The hypothesis tests are carried out using the q-value test statistic, which is defined through the likelihood function L which in turn describes the statistical model. A detailed description of the likelihood function, the test statistic and how exclusion limits for the models are calculated is given in the following sections.

9.1 The Likelihood Function

The binned likelihood function, which describes the statistical model, is given as:

$$L(\vec{\beta}^{\text{sig}}; \vec{\beta}^{\text{bkg}}) = \prod_{k=1}^{M} P(n_k; \mu_k) \cdot \prod_{j=1}^{B} G(\beta_j^{\text{bkg}}; 1; \Delta_j), \tag{9.1}$$

where $\vec{\beta}^{\text{sig}}$ and $\vec{\beta}^{\text{bkg}}$ are the vectors of scale factors for the different signal and background processes

$$\begin{aligned}
\vec{\beta}^{\text{sig}} &= (\beta^{\text{2HDM}}_{\text{ggF,light}}, \beta^{\text{2HDM}}_{\text{ggF,heavy}}, \beta^{\text{2HDM}}_{\text{VBF,light}}, \beta^{\text{2HDM}}_{\text{VBF,heavy}}, \beta^{\text{SM}}_{\text{ggF}}, \beta^{\text{SM}}_{\text{VBF}}) \text{ for } H_0, \text{ and } H_1 \\
\vec{\beta}^{\text{sig}} &= (\beta^{\text{SM}}_{\text{ggF,heavy}}, \beta^{\text{SM}}_{\text{VBF,heavy}}) \text{ for } H_0^* \text{ and } H_1^* \text{ and} \\
\vec{\beta}^{\text{bkg}} &= (\beta_{\text{diboson}}, \beta_{Z+\text{ jets}}, \beta_{\text{top-quark}}) \text{ for all hypotheses}
\end{aligned} \tag{9.2}$$

The signal scale factors are set according to the predicted values of the model:

$$\begin{gathered}\vec{\beta}^{\,\mathrm{sig}}_{H_1} = (1,1,1,1,0,0), \quad \vec{\beta}^{\,\mathrm{sig}}_{H_0} = (0,0,0,0,1,1) \text{ and} \\ \vec{\beta}^{\,\mathrm{sig}}_{H_1^*} = (1,1), \quad \vec{\beta}^{\,\mathrm{sig}}_{H_0^*} = (0,0),\end{gathered} \tag{9.3}$$

while the background scale factors are left floating within their uncertainties.

The sum of the number of bins of the NN output distributions of the signal region, the NN output distributions of the light Higgs boson CR and the event yield of the top-quark CR is denoted with M. The incorporation of the light Higgs boson CR narrows the parameter space, since it takes the features of the light Higgs boson with $m_h = 125$ GeV into account. Further, the rate of top-quark events is almost completely determined by the top-quark CR due to its purity.

The Poisson likelihood $P(n_k; \mu_k)$ is described by,

$$P(n_k; \mu_k) = \frac{e^{-\mu_k} \cdot \mu_k^{n_k}}{n_k!} \tag{9.4}$$

with the number of observed events n_k and the mean number of estimated events μ_k in bin k. Further, the mean value is composed of the sum of the estimated number of events of each regarded process:

$$\begin{gathered}\mu_k = \sum_{j=1}^{S} \mu_{jk}^{\mathrm{sig}} + \sum_{j=1}^{B} \mu_{jk}^{\mathrm{bkg}}, \text{ with} \\ \mu_{jk}^{\mathrm{sig}} = \beta_j^{\mathrm{sig}} \cdot \tilde{\nu}_j^{\mathrm{sig}} \cdot \alpha_{jk}^{\mathrm{sig}} \quad \text{and} \quad \mu_{jk}^{\mathrm{bkg}} = \beta_j^{\mathrm{bkg}} \cdot \tilde{\nu}_j^{\mathrm{bkg}} \cdot \alpha_{jk}^{\mathrm{bkg}}.\end{gathered} \tag{9.5}$$

Here S and B denote the number of signal and background processes respectively. The index j runs over the respective number of processes and the number of expected events of a certain process per bin is given by the product of the predicted events in the selected data set, $\tilde{\nu}_j^{\mathrm{sig}}$ for signal and $\tilde{\nu}_j^{\mathrm{bkg}}$ for background processes, scale factors β_j^{sig} and β_j^{bkg}, and the relative fraction of signal events given by $\alpha_{jk}^{\mathrm{sig}}$ and background events given by $\alpha_{jk}^{\mathrm{bkg}}$ respectively. The set of α_{jk} are also called templates of the processes.

The scale factors β_j^{bkg} for the backgrounds (diboson, $Z+$ jets and top-quark) are the parameters of the likelihood function are fitted to match the observed data, while the $W+$ jets background rate is fixed due to its data-driven nature. The Gaussian functions of the background priors, which incorporate a priori knowledge on the background processes,

$$G(\beta_j^{\mathrm{bkg}}; 1; \Delta_j) = \frac{1}{\sqrt{2\pi}\,\Delta_j} \exp\left(-\frac{(\beta_j^{\mathrm{bkg}} - 1)^2}{2\Delta_j^2}\right) \tag{9.6}$$

have a mean of one and a width of Δ_j which is the relative uncertainty on the cross-section prediction of the background process.

9.2 Hypothesis Tests

The goal of a hypothesis test is to reject the null hypothesis based on the available data set. In order to do that, a single variable function of the data sample – a test statistic – is defined which allows to distinguish the null from the alternative hypothesis. In the regarded case where both hypotheses are *simple*, which means that each of them is described by a single probability distribution and a corresponding pdf, the Neyman-Pearson lemma [223] states that the most powerful test statistic in order to reject the null hypothesis in favour for the alternative hypothesis is the likelihood ratio (or q-value):

$$q = -2\ln\left(\frac{L(\vec{\beta}^{\mathrm{sig}}_{H_1}, \vec{\beta}^{\mathrm{bkg}})}{L(\vec{\beta}^{\mathrm{sig}}_{H_0}, \vec{\beta}^{\mathrm{bkg}})}\right). \tag{9.7}$$

In order to carry out the hypothesis test, the q-value pdfs for the different hypotheses are constructed using large numbers of pseudo experiments. Two ensembles are generated, the first implementing the null hypothesis, the second implementing the alternative hypothesis. Computing the q-value for each pseudo experiment of both ensembles leads to two distinct q-value distributions $q_0(q)$ and $q_1(q)$ corresponding to the null and alternative hypothesis, respectively. The q-value distributions (normalised to unity) $\hat{q}_0(q)$ and $\hat{q}_1(q)$ give the pdfs for both hypotheses which can finally be used to perform the hypothesis test. Therefore, the observed q-value q^{obs}, which is compared with the two pdfs of the hypotheses, is obtained by calculating the q-value from the measured data set.

The common approach to decide if the null hypothesis has to be rejected, is to calculate the p-value for the null (or background only) hypothesis:

$$p_{\mathrm{b}}^{\mathrm{obs}} = p_{\mathrm{b}}(q^{\mathrm{obs}}) = \int_{-\infty}^{q^{\mathrm{obs}}} dq'\, \hat{q}_0(q'), \tag{9.8}$$

which describes the probability to obtain an outcome as much (or even more) signal-like as measured in data assuming the null hypothesis being true. The null hypothesis is rejected if it is smaller than a given significance level α (usually set to 5%). However, this method does not take into account the statistical power $1-p^{\mathrm{obs}}_{\mathrm{s+b}}$, which describes the probability to correctly reject the null hypothesis, the alternative hypothesis being true. The p-value for the alternative (or signal plus background) hypothesis $p^{\mathrm{obs}}_{\mathrm{s+b}}$ is given as:

$$p^{\mathrm{obs}}_{\mathrm{s+b}} = p_{\mathrm{s+b}}(q^{\mathrm{obs}}) = \int_{q^{\mathrm{obs}}}^{\infty} dq'\, \hat{q}_1(q'). \tag{9.9}$$

In order to take the power into account, the so-called $\mathrm{CL_s}$method [224, 225], firstly introduced by LEP experiments, is deployed. Instead of using only $p_{\mathrm{b}}(q)$, the following quantity

$$\mathrm{CL}_s = \frac{p_{\mathrm{s+b}}(q)}{1 - p_{\mathrm{b}}(q)} \tag{9.10}$$

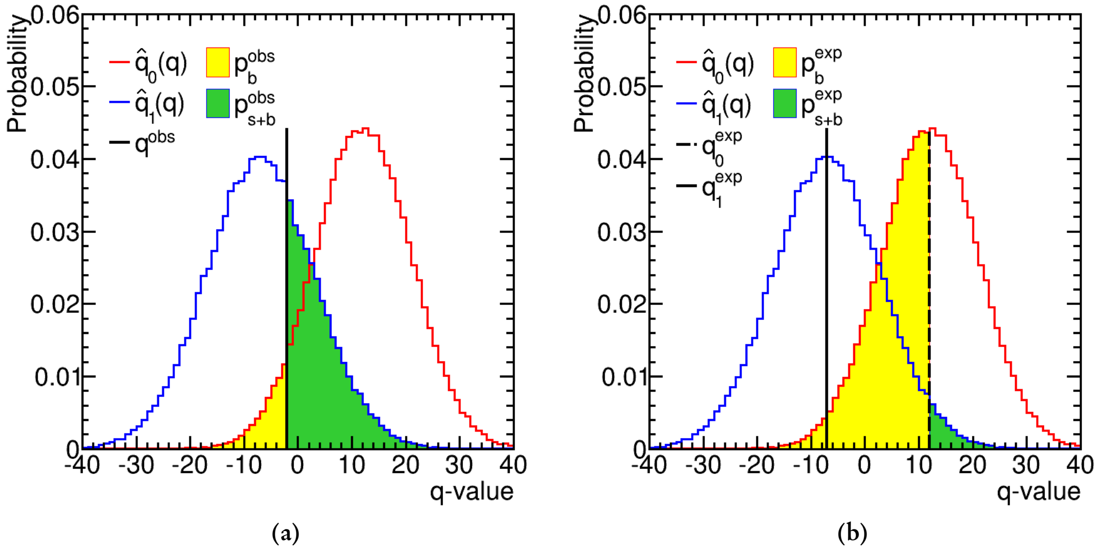

Figure 9.1: Example q-value distributions of $\hat{q}_0(q)$ in red and $\hat{q}_1(q)$ in blue. The observed p-values are depicted in (a), where $p_\mathrm{b}^\mathrm{obs}$ is shown in yellow, while $p_\mathrm{s+b}^\mathrm{obs}$ is shown in green. In (b), the medians of the q-value distributions and the expected p-values are shown.

is used to reason a rejection of the null hypothesis. By construction, the CL$_\mathrm{s}$-value is always larger than $p_\mathrm{s+b}(q)$. Further, due to the inclusion of both p-values, the distinction between the considered hypotheses is more reliable and avoids artificial exclusions [226].

In order to have a graphical representation of the quantities used to calculate the CL$_\mathrm{s}$-value, Figure 9.1 shows a sketch of the q-value distributions as well as the different p-values for a possible observed outcome in (a) and for the expected outcome assuming the null hypothesis, where q^obs is replaced in equations (9.8) and (9.9) by the median q_0^exp of $\hat{q}_0(q)$, in (b).

9.3 Calculation of Cross-Section Limits

If it is not possible to reject the null hypothesis an upper limit on the production cross section is constructed or the phase space where the alternative hypothesis can be excluded is given. In this analysis the former is implemented to test the background-only hypothesis H_0^* against the hypothesis H_1^*, while the latter is implemented to test the SM hypothesis H_0 against the 2HDM, where a particular signal hypothesis H_1, determined by a designated set of 2HDM parameters $(m_H, \tan\beta, \cos(\beta-\alpha))$, is said to be excluded at 95% CL if CL$_\mathrm{s}$< 0.05.

In order to obtain the expected 95% CL upper limits, the cross section is varied until the value is found which corresponds to the 95% CL. If the computed CL$_\mathrm{s}$-value is larger than 0.05 ensembles of pseudo experiments with gradually increased cross sections are generated until the corresponding CL$_\mathrm{s}$-value reaches 0.05, which provides the expected limit. The $\pm 1\sigma$ and

$\pm 2\sigma$ uncertainty bands are calculated following the same strategy and by changing the upper (lower) limit of the integral in equation (9.8) (and (9.9)) to the corresponding quantiles. The same procedure is applied in order to obtain the observed limit utilising the observed q-value q^{obs}.

9.4 Incorporation of Systematic Uncertainties

For each process, four types of uncertainties are considered: Cross-section uncertainties, statistical uncertainties due to the limited amount of MC events, acceptance uncertainties and shape uncertainties.

In order to take care of the cross-section uncertainties, the expected number of events of each process are varied within the appropriate uncertainty. This is performed by generating a random number for each process according to the log-normal distribution, which is favoured over a Gaussian distribution, since it cannot deliver unphysical results of negative expectation values.

The limited amount of simulated MC events is taken into account by a bin-wise altering of the template histograms. Each bin entry is varied within its statistical uncertainty by exchanging the bin entry with a random number drawn from a Gaussian distribution centred at the original bin entry and with a standard deviation corresponding to the statistical uncertainty of the considered bin.

The acceptance uncertainties are implemented by varying the expectation values of each process by throwing a Normal distributed random number for each systematic uncertainty.

Finally, the shape uncertainties are taken into account by systematically altering the up and down fluctuated template histograms obtained from the systematically altered MC samples. A new template histogram is generated in each pseudo experiment by interpolating linearly between the nominal template histograms and the systematically modified template histograms. The full correlation between the acceptance variation and the shape variation is taken into account via a nuisance parameter which acts as weight for each considered systematic uncertainty.

10 | Results

Since there is no indication for a heavy Higgs boson, exclusion limits at 95% CL (obtained with the CL_smethod) are presented for the two scenarios described in the previous chapter: The SM-like scenario, where a search is carried out for a heavy SM-like Higgs boson under the assumption of the SM without a Higgs boson. The second set of scenarios are the 2HDM-like scenarios, where the search for a heavy Higgs boson is performed in a specific 2HDM, defined by the triplet $(m_H, \tan\beta, \cos(\beta - \alpha))$, under the assumption of the SM including a light Higgs boson with a mass of $m_h = 125$ GeV.

10.1 Exclusion Limits for the Standard Model-like Scenario

Figure 10.1 shows the exclusion limits on the cross section times branching ratio in terms of the heavy Higgs boson mass m_H. In order to obtain the limits for the ggF and VBF signal alone, the signal strength of the regarded process is set to 1, while the other one is treated as background.

As can be observed in Figures B.5(b) to B.7(b), the 0-jet channel shows a small deficit in data, assumed to be a statistical downward fluctuation, which is propagated through the NN output distribution in to the exclusion limits obtained from the ggF signal alone in Figure 10.1. The deficit is visible in the higher mass range and therefore the observed limit slightly drops below the 2σ band between 500 and 600 GeV, while it is compatible with the expected limit on the 2σ level elsewhere.

A SM-like Higgs boson with a mass of $m_H \leqslant 850$ GeV ($m_H \leqslant 700$ GeV expected) can be excluded at 95% CL by this analysis.

10.2 Exclusion Limits for the 2-Higgs-Doublet Model Scenarios

The hypothesis tests, as described in the last chapter, are performed for a large part of the 2HDM Type I and II parameter space. The results are presented in the m_H-$\cos(\beta - \alpha)$ plane for fixed values of $\tan\beta$, where the mass range of $135 \leqslant m_H \leqslant 1000$ GeV is considered for the mass of the CP-even Higgs boson H. The mass range is scanned in steps of 5 GeV from $m_H = 135$ GeV to 200 GeV, in steps of 20 GeV in the range from 220 GeV to 600 GeV and in steps of 50 GeV from 650 GeV upward. The scan of the 2HDM coupling parameter is performed in steps of 0.1 in $\cos(\beta-\alpha)$ if $|\cos(\beta-\alpha)| > 0.1$. To get a better understanding of the alignment limit ($\cos(\beta-\alpha) \to 0$), in the range $|\cos(\beta - \alpha)| \leqslant 0.1$ the step width is reduced to 0.01. For $\tan\beta$, values of $1, 3$ and 6 are considered and for each combination of these parameters the CL_svalues are determined and exclusion contours are drawn in the m_H-$\cos(\beta-\alpha)$ plane at 95% CL as depicted in Figure 10.2.

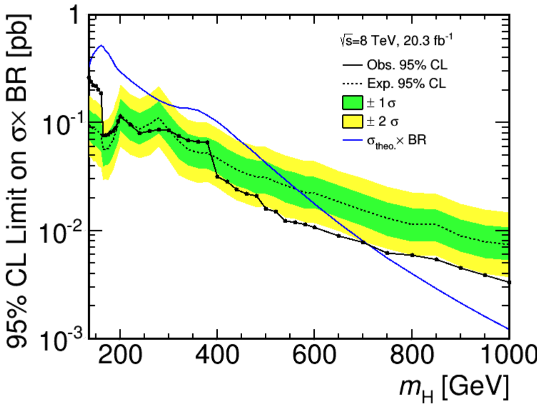

(a) 95% CL upper limits on the cross section times branching ratio using the ggF signal alone.

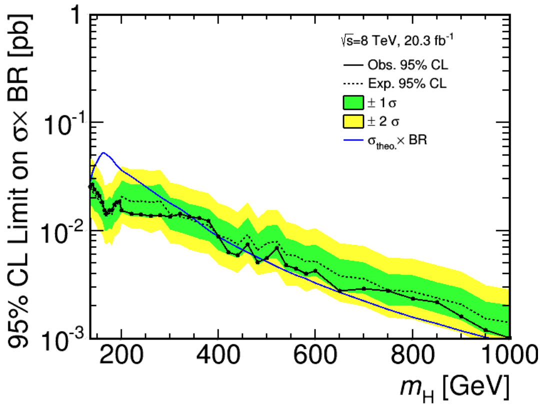

(b) 95% CL upper limits on the cross section times branching ratio using the VBF signal alone.

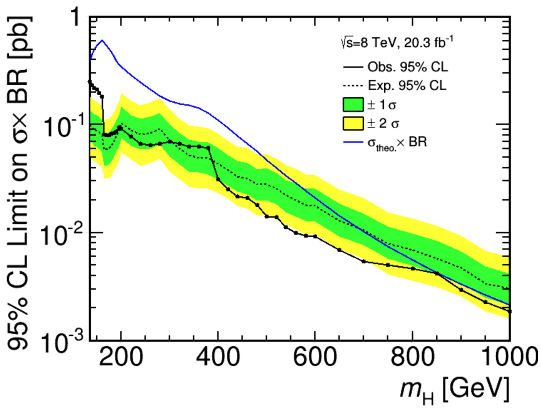

(c) 95% CL upper limits on the cross section times branching ratio using the combination of ggF and VBF signal.

Figure 10.1: 95% CL upper limits on the cross section times branching ratio using the ggF signal (a), the VBF signal (b) and their combination (c). The solid line shows the observed limit, while the dotted line shows the expected limit with the $\pm 1\sigma$ and $\pm 2\sigma$ uncertainty bands in green and yellow respectively. The blue line shows the theoretical cross section times branching ratio as predicted by the SM.

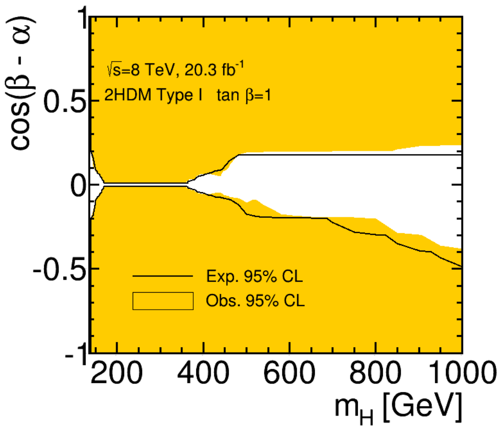

(a) 2HDM Type I, $\tan\beta = 1$.

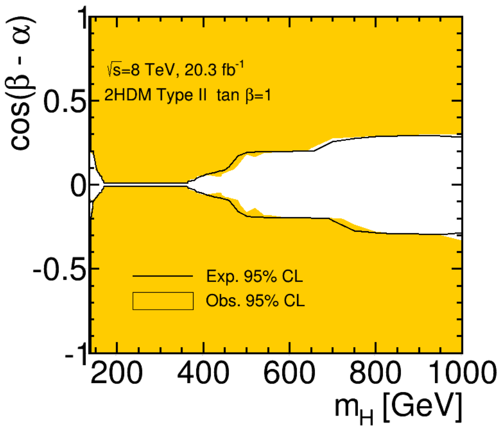

(b) 2HDM Type II, $\tan\beta = 1$.

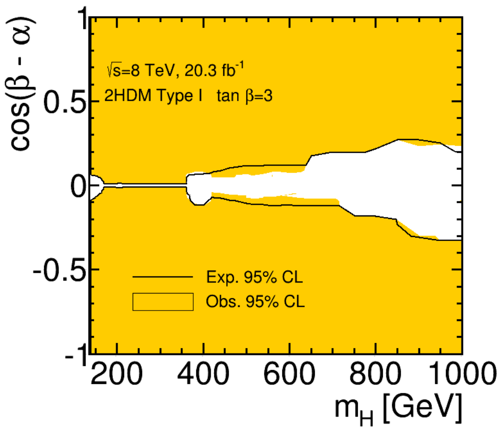

(c) 2HDM Type I, $\tan\beta = 3$.

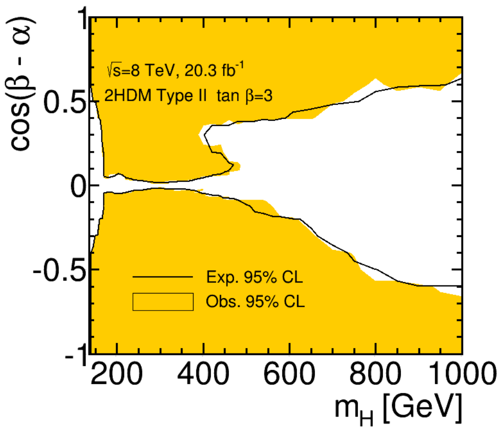

(d) 2HDM Type II, $\tan\beta = 3$.

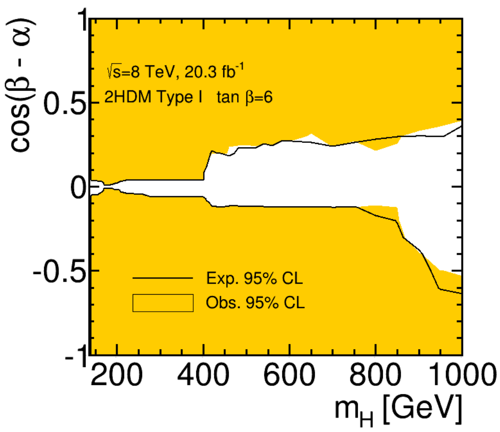

(e) 2HDM Type I, $\tan\beta = 6$.

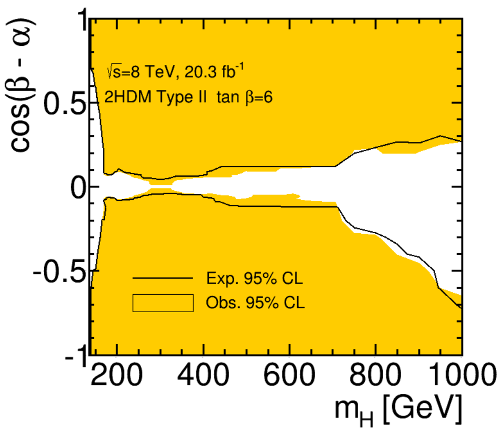

(f) 2HDM Type II, $\tan\beta = 6$.

Figure 10.2: Exclusion contours of 2HDM Type I (left column) and Type II (right column) for different values of $\tan\beta$ in the m_H-$\cos(\beta - \alpha)$ plane. The coloured area shows the observed exclusion, while the area limited by the black line shows the expected exclusion at 95% CL.

In the mass region from 135 to 350 GeV almost all parts of the m_H-$\cos(\beta-\alpha)$ plane can be excluded for all regarded values of $\tan\beta$ and for both 2HDM types. However, in the alignment limit no exclusion is possible in the considered decay channel, since the coupling of the heavy 2HDM Higgs boson to the vector bosons scales with $\cos(\beta-\alpha)$. Further, an exclusion up to 1000 GeV is possible in some parts of the m_H-$\cos(\beta-\alpha)$ plane for all $\tan\beta$ values as well, while the excluded region slightly shrinks with increasing $\tan\beta$.

To get an understanding of the sensitivity of the analysis the expected exclusion contours are also computed and shown as black lines in Figure 10.2. In this calculation the median q_0^{exp} of the $\hat{q}_0(q)$ distribution (see Section 9.2) instead of q^{obs} is used.

The impact of the different systematic uncertainties has been investigated to see which have the largest influence on the computed exclusion limits. For this purpose a sample parameter point ($m_H = 460$ GeV, $\cos(\beta-\alpha) = -0.1$, $\tan\beta = 1$ in 2HDM Type I) has been picked and the corresponding $\mathrm{CL_s}$values have been evaluated with different sets of systematics/uncertainties enabled. The results are given in Table 10.1.

Table 10.1: Impact of different systematic uncertainties on the exclusion power at the parameter point $m_H = 460$ GeV, $\cos(\beta-\alpha) = -0.1$, $\tan\beta = 1$ in 2HDM Type I. Each group of systematics has been evaluated solitarily.

Systematics	CL in %
Jet Modelling	98.1
b-tagging	98.2
Lepton Modelling	98.4
$E_{\mathrm{T}}^{\mathrm{miss}}$ Modelling	99.5
Cross section	98.8
Migration syst.	98.1
Off-shell syst.	99.9
Lumi	99.9
Full syst.	96.1
No syst.	100

11 | Conclusion

The discovery of a scalar Higgs-boson like particle with $m_h \approx 125$ GeV in July 2012 was not only a huge success for CERN, LHC and all involved experiments, but also for the SM which can now be regarded as complete in the sense, that all predicted particles have been found and their properties have been measured. Unfortunately, it is incomplete in the sense, that it cannot explain all observed properties of our universe like the baryon asymmetry [23] or dark matter [24] and it has unsatisfactory issues like the strong CP problem [22] (the question why QCD does not break CP symmetry). However, the framework of 2HDMs allows to address at least two of the issues mentioned above, namely the baryon asymmetry in the universe [26] and the strong CP problem [27].

The analysis presented in this thesis shows an extension of the search presented in Ref. [37], which strongly enhances the examined phase space of 2HDMs from $m_H \leqslant 300$ GeV to $m_H \leqslant 1000$ GeV. The search for a heavy scalar Higgs boson H of the 2HDMs is carried out in the $h/H \to WW \to \mu\nu e\nu$ decay channel and under the assumption, that the Higgs particle h with a mass of approximately 125 GeV is the light scalar particle predicted by the 2HDMs. These models are tested against the SM including a SM-like Higgs boson with a mass of 125 GeV using 20.3 fb^{-1} of collision data recorded by the ATLAS detector with a centre-of-mass energy of 8 TeV in 2012.

Since no evidence for an additional heavy Higgs boson H could be found in the investigated mass range of 135 GeV to 1000 GeV, excluded phase space regions at 95% CL are given in the m_H-$\cos(\beta - \alpha)$ plane for Type I and Type II 2HDMs for different values of $\tan\beta$. In both model types, large parts of the m_H-$\cos(\beta - \alpha)$ planes can be excluded for masses up to 1000 GeV.

The phase space regarded in the search mentioned above is fully included in this analysis. Only a small area in the mass range of 135 GeV to 350 GeV where no exclusion is possible is left due to the alignment limit and the vanishing coupling of the heavy Higgs boson to vector bosons. Because of the alignment limit, it is not possible to remove all "blank spots" of the m_H-$\cos(\beta - \alpha)$ planes only relying on $h/H \to WW/ZZ$ decay channels. For further exclusion, decay channels which involve the coupling to fermions need to be regarded or constraints from other searches have to be imposed.

The limits on the 2HDM phase space presented in this thesis are the most advanced ones currently available. Further, the direct search performed in this analysis enables a coherent consideration of the different 2HDM coupling modifications and the kinematics for the light and heavy Higgs bosons. Finally, while both – a direct search and a pure coupling analysis of the light Higgs boson – have the possibility to constrain the possible parameter space of 2HDMs, only a direct search renders the possibility to find a heavy state as predicted by the considered models.

Bibliography

[1] A. Djouadi. 'The Anatomy of electro-weak symmetry breaking. I: The Higgs boson in the Standard Model'. In: *Phys.Rept.* 457 (2008), pages 1–216. arXiv: `hep-ph/0503172 [hep-ph]`.

[2] K. A. Olive et al. 'Review of Particle Physics'. In: *Chinese Physics C* 38.9 (2014), page 090001. URL: `http://stacks.iop.org/1674-1137/38/i=9/a=090001`.

[3] J. C. Maxwell. 'A dynamical theory of the electromagnetic field'. In: *Phil. Trans. Roy. Soc. Lond.* 155 (1865), pages 459–512.

[4] J. D. Jackson. *Classical Electrodynamics*. 3rd edition. John Wiley & Sons, 1999.

[5] M. Planck. 'Über das Gesetz der Energieverteilung im Normalspectrum'. In: *Annalen der Physik* 309.3 (1901), pages 553–563. URL: `http://dx.doi.org/10.1002/andp.19013090310`.

[6] C. Cohen-Tannoudji, B. Diu and F. Laloe. *Quantenmechanik. Bände 1 & 2*. 3. Auflage. de Gruyter, Berlin, 2007/2008.

[7] A. Einstein. 'Zur Elektrodynamik bewegter Körper'. In: *Annalen der Physik* 322 (1905), pages 891–921.

[8] T. Schörner-Sadenius, editor. *The Large Hadron Collider: Harvest of Run 1*. Berlin: Springer, 2015. URL: `http://www.springer.com/gb/book/9783319150017`.

[9] S. L. Glashow. 'Partial Symmetries of Weak Interactions'. In: *Nucl. Phys.* 22 (1961), pages 579–588.

[10] A. Salam and J. Ward. 'Electromagnetic and Weak Interactions'. In: *Physics Letters* 13.2 (1964), pages 168–171. URL: `http://www.sciencedirect.com/science/article/pii/0031916364907115`.

[11] S. Weinberg. 'A Model of Leptons'. In: *Phys.Rev.Lett.* 19 (1967), pages 1264–1266.

[12] M. Kobayashi and T. Maskawa. 'CP-Violation in the Renormalizable Theory of Weak Interaction'. In: *Progress of Theoretical Physics* 49.2 (1973), pages 652–657. eprint: `http://ptp.oxfordjournals.org/content/49/2/652.full.pdf+html`.

[13] F. Englert and R. Brout. 'Broken Symmetry and the Mass of Gauge Vector Mesons'. In: *Phys. Rev. Lett.* 13 (1964), pages 321–322.

[14] P. W. Higgs. 'Broken symmetries and the masses of gauge bosons'. In: *Phys. Rev. Lett.* 13 (1964), pages 508–509.

[15] G. Guralnik, C. Hagen and T. Kibble. 'Global conservation laws and massless particles'. In: *Phys. Rev. Lett.* 13 (1964), pages 585–587.

[16] A. Astbury. 'Found: W and Z. The Discovery of the W and Z Intermediate Vector Bosons at CERN's Proton Anti-Proton Collider'. In: *Phys. Bull.* 34 (1983), pages 434–436.

[17] E. Radermacher. 'The Experimental Discovery of the Intermediate Vector Bosons W^+, W^- and Z^0 at the CERN $p\bar{p}$ Collider'. In: *Prog. Part. Nucl. Phys.* 14 (1985), pages 231–328.

[18] D0 Collaboration. 'Search for High Mass Top Quark Production in $p\overline{p}$ Collisions at $\sqrt{s} = 1.8$ TeV'. In: *Phys. Rev. Lett.* 74 (13 Mar. 1995), pages 2422–2426. URL: `http://link.aps.org/doi/10.1103/PhysRevLett.74.2422`.

[19] CDF Collaboration. 'Observation of Top Quark Production in $\overline{p}p$ Collisions with the Collider Detector at Fermilab'. In: *Phys. Rev. Lett.* 74 (14 Apr. 1995), pages 2626–2631. URL: `http://link.aps.org/doi/10.1103/PhysRevLett.74.2626`.

[20] ATLAS Collaboration. 'Observation of a new particle in the search for the Standard Model Higgs boson with the ATLAS detector at the LHC'. In: *Phys.Lett.* B716 (2012), pages 1–29. arXiv: `1207.7214 [hep-ex]`.

[21] CMS Collaboration. 'Observation of a new boson at a mass of 125 GeV with the CMS experiment at the LHC'. In: *Phys.Lett.* B716 (2012), pages 30–61. arXiv: `1207.7235 [hep-ex]`.

[22] R. D. Peccei and H. R. Quinn. 'CP Conservation in the Presence of Pseudoparticles'. In: *Phys. Rev. Lett.* 38 (25 June 1977), pages 1440–1443. URL: `http://link.aps.org/doi/10.1103/PhysRevLett.38.1440`.

[23] L. Canetti, M. Drewes and M. Shaposhnikov. 'Matter and Antimatter in the Universe'. In: *New J. Phys.* 14 (2012), page 095012. arXiv: `1204.4186 [hep-ph]`.

[24] G. Bertone, D. Hooper and J. Silk. 'Particle dark matter: Evidence, candidates and constraints'. In: *Phys. Rept.* 405 (2005), pages 279–390. arXiv: `hep-ph/0404175 [hep-ph]`.

[25] T. Lee. 'A Theory of Spontaneous T Violation'. In: *Phys.Rev.* D8 (1973), pages 1226–1239.

[26] M. Trodden. 'Electroweak baryogenesis: A Brief review'. In: *33rd Rencontres de Moriond: Electroweak Interactions and Unified Theories Les Arcs, France, March 14-21, 1998*. 1998. arXiv: `hep-ph/9805252 [hep-ph]`.

[27] J. E. Kim. 'Light pseudoscalars, particle physics and cosmology'. In: *Phys. Rep.* 150 (Nov. 1986), 1–177. 99 p. URL: `https://cds.cern.ch/record/173118`.

[28] N. Craig et al. 'Multi-Lepton Signals of Multiple Higgs Bosons'. In: *JHEP* 1302 (2013), page 033. arXiv: `1210.0559 [hep-ph]`.

[29] W. Altmannshofer et al. 'A Minimal Flavor Violating 2HDM at the LHC'. In: *Phys.Rev.* D86 (2012), page 115009. arXiv: `1210.2465 [hep-ph]`.

[30] B. Swiezewska. 'Yukawa independent constraints for 2HDMs with a 125 GeV Higgs boson'. In: (2012). arXiv: 1209.5725 [hep-ph].

[31] H. Cheon and S. K. Kang. 'Constraining parameter space in type-II two-Higgs doublet model in light of a 125 GeV Higgs boson'. In: (2012). arXiv: 1207.1083 [hep-ph].

[32] A. Celis, V. Ilisie and A. Pich. 'LHC constraints on two-Higgs doublet models'. In: *JHEP* 07 (2013), page 053. arXiv: 1302.4022 [hep-ph].

[33] M. Krawczyk, D. Sokołowska and B. Świeżewska. '2HDM with Z_2 symmetry in light of new LHC data'. In: *J. Phys. Conf. Ser.* 447 (2013), page 012050. arXiv: 1303.7102 [hep-ph].

[34] A. Barroso et al. '2HDM at the LHC - the story so far'. In: *1st Toyama International Workshop on Higgs as a Probe of New Physics 2013 (HPNP2013) Toyama, Japan, February 13-16, 2013*. 2013. arXiv: 1304.5225 [hep-ph].

[35] J. Baglio et al. 'Benchmarks for Higgs Pair Production and Heavy Higgs boson Searches in the Two-Higgs-Doublet Model of Type II'. In: *Phys. Rev.* D90.1 (2014), page 015008. arXiv: 1403.1264 [hep-ph].

[36] P. Ferreira et al. 'Implications of the LHC two-photon signal for two-Higgs-doublet models'. In: *Phys.Rev.* D85 (2012), page 077703. arXiv: 1112.3277 [hep-ph].

[37] ATLAS Collaboration. *Search for Higgs bosons in Two-Higgs-Doublet models in the $H \to WW \to e\nu\mu\nu$ channel with the ATLAS detector*. ATLAS Conference Note. Geneva, Mar. 2013. URL: https://cds.cern.ch/record/1525887.

[38] T. Aaltonen et al. 'Search for Higgs bosons predicted in two-Higgs-doublet models via decays to tau lepton pairs in 1.96-TeV p anti-p collisions'. In: *Phys.Rev.Lett.* 103 (2009), page 201801. arXiv: 0906.1014 [hep-ex].

[39] T. Aaltonen et al. 'Search for a two-Higgs-boson doublet using a simplified model in $p\bar{p}$ collisions at $\sqrt{s} = 1.96$ TeV'. In: (2012). arXiv: 1212.3837 [hep-ex].

[40] S. Chang et al. 'Two Higgs doublet models for the LHC Higgs boson data at $\sqrt{s} = 7$ and 8 TeV'. In: (2013). arXiv: 1310.3374 [hep-ph].

[41] ATLAS Collaboration. *Constraints on New Phenomena via Higgs Coupling Measurements with the ATLAS Detector*. ATLAS Conference Note. Geneva, Mar. 2014. URL: https://cds.cern.ch/record/1670531.

[42] P. W. Higgs. 'Broken symmetries, massless particles and gauge fields'. In: *Phys. Lett.* 12 (1964), pages 132–133.

[43] Wikimedia Commons. *Standard Model of Elementary Particles*. URL: https://commons.wikimedia.org/wiki/File:Standard_Model_of_Elementary_Particles.svg (visited on 23/09/2015).

[44] S. Dulat et al. 'Higgs Boson Cross Section from CTEQ-TEA Global Analysis'. In: *Phys.Rev.* D89.11 (2014), page 113002. arXiv: 1310.7601 [hep-ph].

[45] J. Gao et al. 'CT10 next-to-next-to-leading order global analysis of QCD'. In: *Phys. Rev.* D89.3 (2014), page 033009. arXiv: 1302.6246 [hep-ph].

[46] Durham University. *The Durham HepData Project*. Durham, 6th Aug. 2015. URL: http://hepdata.cedar.ac.uk/pdf/pdf3.html (visited on 23/09/2015).

[47] D. J. Gross and F. Wilczek. 'Ultraviolet Behavior of Nonabelian Gauge Theories'. In: *Phys.Rev.Lett.* 30 (1973), pages 1343–1346.

[48] H. D. Politzer. 'Reliable Perturbative Results for Strong Interactions?' In: *Phys.Rev.Lett.* 30 (1973), pages 1346–1349.

[49] H. Fritzsch, M. Gell-Mann and H. Leutwyler. 'Advantages of the color octet gluon picture'. In: *Physics Letters B* 47.4 (1973), pages 365–368. URL: http://www.sciencedirect.com/science/article/pii/0370269373906254.

[50] M. E. Peskin and D. V. Schroeder. *An Introduction to Quantum Field Theory*. Westview Press, 1995.

[51] F. Englert and R. Brout. 'Broken symmetry and the mass of gauge vector mesons'. In: *Phys. Rev. Lett.* 13 (1964), pages 321–323.

[52] P. W. Higgs. 'Spontaneous symmetry breakdown without massless bosons'. In: *Phys. Rev.* 145 (1966), pages 1156–1163.

[53] R. Ellis, W. Stirling and B. Webber. *QCD and Collider Physics*. Cambridge University Press, Cambridge, 2003.

[54] D. J. Griffiths. *Introduction to elementary particles*. 2nd edition. Wiley-VCH-Verlag, Weinheim, 2008.

[55] C. Quigg. 'Spontaneous Symmetry Breaking as a Basis of Particle Mass'. In: *Rept.Prog.Phys.* 70 (2007), pages 1019–1054. arXiv: 0704.2232 [hep-ph].

[56] N. Cabibbo. 'Unitary Symmetry and Leptonic Decays'. In: *Phys. Rev. Lett.* 10 (12 June 1963), pages 531–533. URL: http://link.aps.org/doi/10.1103/PhysRevLett.10.531.

[57] A. Djouadi, M. Spira and P. Zerwas. 'Production of Higgs bosons in proton colliders: QCD corrections'. In: *Phys. Lett.* B264 (1991), pages 440–446.

[58] S. Dawson. 'Radiative corrections to Higgs boson production'. In: *Nucl. Phys.* B359 (1991), pages 283–300.

[59] M. Spira et al. 'Higgs boson production at the LHC'. In: *Nucl.Phys.* B453 (1995), pages 17–82. arXiv: hep-ph/9504378 [hep-ph].

[60] R. V. Harlander and W. B. Kilgore. 'Next-to-next-to-leading order Higgs production at hadron colliders'. In: *Phys.Rev.Lett.* 88 (2002), page 201801. arXiv: hep-ph/0201206 [hep-ph].

[61] C. Anastasiou and K. Melnikov. 'Higgs boson production at hadron colliders in NNLO QCD'. In: *Nucl.Phys.* B646 (2002), pages 220–256. arXiv: hep-ph/0207004 [hep-ph].

[62] V. Ravindran et al. 'NNLO corrections to the total cross-section for Higgs boson production in hadron hadron collisions'. In: *Nucl.Phys.* B665 (2003), pages 325–366. arXiv: hep-ph/0302135 [hep-ph].

[63] S. Catani et al. 'Soft gluon resummation for Higgs boson production at hadron colliders'. In: *JHEP* 0307 (2003), page 028. arXiv: hep-ph/0306211 [hep-ph].

[64] U. Aglietti et al. 'Two loop light fermion contribution to Higgs production and decays'. In: *Phys.Lett.* B595 (2004), pages 432–441. arXiv: `hep-ph/0404071 [hep-ph]`.

[65] S. Actis et al. 'NLO Electroweak Corrections to Higgs Boson Production at Hadron Colliders'. In: *Phys.Lett.* B670 (2008), pages 12–17. arXiv: `0809.1301 [hep-ph]`.

[66] S. Dittmaier et al. 'Handbook of LHC Higgs Cross Sections: 1. Inclusive Observables'. In: (2011). arXiv: `1101.0593 [hep-ph]`.

[67] LHC Higgs Cross Section Working Group et al. 'Handbook of LHC Higgs Cross Sections: 2. Differential Distributions'. In: *CERN-2012-002* (CERN, Geneva, 2012). arXiv: `1201.3084 [hep-ph]`.

[68] M. Ciccolini, A. Denner and S. Dittmaier. 'Strong and electroweak corrections to the production of Higgs + 2jets via weak interactions at the LHC'. In: *Phys.Rev.Lett.* 99 (2007), page 161803. arXiv: `0707.0381 [hep-ph]`.

[69] M. Ciccolini, A. Denner and S. Dittmaier. 'Electroweak and QCD corrections to Higgs production via vector-boson fusion at the LHC'. In: *Phys. Rev.* D77 (2008), page 013002. arXiv: `0710.4749 [hep-ph]`.

[70] K. Arnold et al. 'VBFNLO: A Parton level Monte Carlo for processes with electroweak bosons'. In: *Comput. Phys. Commun.* 180 (2009), pages 1661–1670. arXiv: `0811.4559 [hep-ph]`.

[71] P. Bolzoni et al. 'Higgs production via vector-boson fusion at NNLO in QCD'. In: *Phys.Rev.Lett.* 105 (2010), page 011801. arXiv: `1003.4451 [hep-ph]`.

[72] O. Brein, A. Djouadi and R. Harlander. 'NNLO QCD corrections to the Higgs-strahlung processes at hadron colliders'. In: *Phys.Lett.* B579 (2004), pages 149–156. arXiv: `hep-ph/0307206 [hep-ph]`.

[73] T. Han and S. Willenbrock. 'QCD correction to the $pp \rightarrow WH$ and ZH total cross-sections'. In: *Phys. Lett.* B273 (1991), pages 167–172.

[74] M. Ciccolini, S. Dittmaier and M. Kramer. 'Electroweak radiative corrections to associated WH and ZH production at hadron colliders'. In: *Phys.Rev.* D68 (2003), page 073003. arXiv: `hep-ph/0306234 [hep-ph]`.

[75] ATLAS and CMS Collaborations. 'Combined Measurement of the Higgs Boson Mass in pp Collisions at $\sqrt{s} = 7$ and 8 TeV with the ATLAS and CMS Experiments'. In: *Phys.Rev.Lett.* 114 (2015), page 191803. arXiv: `1503.07589 [hep-ex]`.

[76] ATLAS Collaboration. 'Evidence for the spin-0 nature of the Higgs boson using ATLAS data'. In: *Phys.Lett.* B726 (2013), pages 120–144. arXiv: `1307.1432 [hep-ex]`.

[77] CMS Collaboration. 'Study of the Mass and Spin-Parity of the Higgs Boson Candidate Via Its Decays to Z Boson Pairs'. In: *Phys. Rev. Lett.* 110.8 (2013), page 081803. arXiv: `1212.6639 [hep-ex]`.

[78] ATLAS Collaboration. *Measurements of the Higgs boson production and decay rates and coupling strengths using pp collision data at $\sqrt{s} = 7$ and 8 TeV in the ATLAS experiment.* ATLAS Conference Note. Geneva, Mar. 2015. URL: `https://cds.cern.ch/record/2002212`.

[79] ATLAS Collaboration. 'Search for the Standard Model Higgs boson decay to $\mu^+\mu^-$ with the ATLAS detector'. In: *Phys.Lett.* B738 (2014), pages 68–86. arXiv: 1406.7663 [hep-ex].

[80] ATLAS Collaboration. 'Search for Higgs boson decays to a photon and a Z boson in pp collisions at $\sqrt{s}$=7 and 8 TeV with the ATLAS detector'. In: *Phys.Lett.* B732 (2014), pages 8–27. arXiv: 1402.3051 [hep-ex].

[81] J. R. Andersen et al. *Handbook of LHC Higgs Cross Sections: 3. Higgs Properties*. Edited by S. Heinemeyer et al. Geneva, 2013. arXiv: 1307.1347 [hep-ph].

[82] Y. Wu and L. Wolfenstein. 'Sources of CP violation in the two Higgs doublet model'. In: *Phys.Rev.Lett.* 73 (1994), pages 1762–1764. arXiv: hep-ph/9409421 [hep-ph].

[83] D. Eriksson, J. Rathsman and O. Stal. '2HDMC: Two-Higgs-Doublet Model Calculator Physics and Manual'. In: *Comput.Phys.Commun.* 181 (2010), pages 189–205. arXiv: 0902.0851 [hep-ph].

[84] L. Lavoura. 'Signatures of discrete symmetries in the scalar sector'. In: *Phys.Rev.* D50 (1994), pages 7089–7092. arXiv: hep-ph/9405307 [hep-ph].

[85] G. Branco et al. 'Theory and phenomenology of two-Higgs-doublet models'. In: *Phys.Rept.* 516 (2012), pages 1–102. arXiv: 1106.0034 [hep-ph].

[86] J. F. Gunion and H. E. Haber. 'The CP conserving two Higgs doublet model: The Approach to the decoupling limit'. In: *Phys.Rev.* D67 (2003), page 075019. arXiv: hep-ph/0207010 [hep-ph].

[87] S. Davidson and H. E. Haber. 'Basis-independent methods for the two-Higgs-doublet model'. In: *Phys.Rev.* D72 (2005), page 035004. arXiv: hep-ph/0504050 [hep-ph].

[88] ATLAS Collaboration. 'Search for top quark decays $t \to qH$ with $H \to \gamma\gamma$ using the ATLAS detector'. In: *JHEP* 1406 (2014), page 008. arXiv: 1403.6293 [hep-ex].

[89] R. Goldouzian. *Search for FCNC in top quark production and decays*. ATLAS & CMS Conference Report. Geneva, Nov. 2014. URL: https://cds.cern.ch/record/1975984.

[90] S. L. Glashow and S. Weinberg. 'Natural Conservation Laws for Neutral Currents'. In: *Phys.Rev.* D15 (1977), page 1958.

[91] R. V. Harlander et al. 'SusHi: A program for the calculation of Higgs production in gluon fusion and bottom-quark annihilation in the Standard Model and the MSSM'. In: (2012). arXiv: 1212.3249 [hep-ph].

[92] R. V. Harlander and W. B. Kilgore. 'Higgs boson production in bottom quark fusion at next-to-next-to leading order'. In: *Phys.Rev.* D68 (2003), page 013001. arXiv: hep-ph/0304035 [hep-ph].

[93] N. G. Deshpande and E. Ma. 'Pattern of Symmetry Breaking with Two Higgs Doublets'. In: *Phys.Rev.* D18 (1978), page 2574.

[94] M. Sher. 'Electroweak Higgs potential and vacuum stability'. In: *Physics Reports* 179.5–6 (1989), pages 273–418. URL: http://www.sciencedirect.com/science/article/pii/0370157389900616.

[95] I. Ginzburg and I. Ivanov. 'Tree-level unitarity constraints in the most general 2HDM'. In: *Phys.Rev.* D72 (2005), page 115010. arXiv: hep-ph/0508020 [hep-ph].

[96] L. Evans and P. Bryant. 'LHC Machine'. In: *JINST* 3 (2008). Edited by L. Evans, S08001.

[97] K. Aamodt et al. 'The ALICE experiment at the CERN LHC'. In: *JINST* 3 (2008), S08002.

[98] ATLAS Collaboration. 'The ATLAS Experiment at the CERN Large Hadron Collider'. In: *JINST* 3 (2008), S08003.

[99] CMS Collaboration. 'The CMS experiment at the CERN LHC'. In: *JINST* 3 (2008), S08004.

[100] LHCb Collaboration. 'The LHCb Detector at the LHC'. In: *JINST* 3 (2008), S08005.

[101] E. Halkiadakis, G. Redlinger and D. Shih. 'Status and Implications of Beyond-the-Standard-Model Searches at the LHC'. In: *Ann.Rev.Nucl.Part.Sci.* 64 (2014), pages 319–342. arXiv: 1411.1427 [hep-ex].

[102] W. Davey. 'BSM Higgs boson searches at LHC and the Tevatron'. In: *2nd Conference on Large Hadron Collider Physics Conference (LHCP 2014) New York City, New York, USA, June 2-7, 2014*. 2014. arXiv: 1409.6016 [hep-ex].

[103] H. Bohr and H. Nielsen. 'Hadron production from a boiling quark soup: A thermodynamical quark model predicting particle ratios in hadronic collisions'. In: *Nuclear Physics B* 128.2 (1977), pages 275–293. URL: http://www.sciencedirect.com/science/article/pii/0550321377900323.

[104] LHCb Collaboration. 'First Evidence for the Decay $B_s^0 \to \mu^+\mu^-$'. In: *Phys. Rev. Lett.* 110.2 (2013), page 021801. arXiv: 1211.2674 [hep-ex].

[105] M. Benedikt et al. *LHC Design Report*. Geneva: CERN, 2004. URL: https://cds.cern.ch/record/823808.

[106] K. Schindl. *The PS Booster as Pre-Injector for LHC*. Geneva, Apr. 1997. URL: https://cds.cern.ch/record/323757.

[107] R. Cappi. 'The PS in the LHC injector chain'. In: *Part. Accel.* 58.CERN-PS-97-016-CA (Apr. 1997), 79–89. 13 p. URL: https://cds.cern.ch/record/323933.

[108] T. P. R. Linnecar. 'Preparing the SPS for LHC'. In: *Part. Accel.* 58.CERN-SL-97-018-RF (Apr. 1997), 91–101. 7 p. URL: https://cds.cern.ch/record/327491.

[109] J. Haffner. 'The CERN accelerator complex. Complexe des accélérateurs du CERN'. In: (Oct. 2013). URL: https://cds.cern.ch/record/1621894.

[110] M. Lamont. 'Status of the LHC'. In: *J.Phys.Conf.Ser.* 455 (2013), page 012001.

[111] J. Pequenao. 'Computer generated image of the whole ATLAS detector'. Mar. 2008. URL: https://cds.cern.ch/record/1095924.

[112] J. Pequenao. 'Computer generated image of the ATLAS inner detector'. Mar. 2008. URL: https://cds.cern.ch/record/1095926.

[113] N. Wermes and G. Hallewel. *ATLAS pixel detector: Technical Design Report*. Geneva: CERN, 1998. URL: https://cds.cern.ch/record/381263.

[114] ATLAS Collaboration. 'ATLAS pixel detector electronics and sensors'. In: *J. Instrum.* 3.07 (2008), P07007. URL: https://cds.cern.ch/record/1119279.

[115] S. Corréard et al. *b-tagging with DC1 data*. ATLAS Public Note. Marseille, Nov. 2003. URL: https://cds.cern.ch/record/686346.

[116] M. Capeans et al. *ATLAS Insertable B-Layer Technical Design Report*. Geneva, Sept. 2010. URL: https://cds.cern.ch/record/1291633.

[117] ATLAS Collaboration. *Expected performance of the ATLAS b-tagging algorithms in Run-2*. Geneva, July 2015. URL: https://cds.cern.ch/record/2037697.

[118] T. P. Calvet. *Expected b-tagging performance for ATLAS in LHC Run 2*. Geneva, Oct. 2015. URL: https://cds.cern.ch/record/2058102.

[119] A. Ahmad et al. 'The silicon microstrip sensors of the ATLAS semiconductor tracker'. In: *Nucl. Instr. Meth. Phys. Res. A: Accelerators, Spectrometers, Detectors and Associated Equipment* 578.1 (2007), pages 98–118. URL: http://www.sciencedirect.com/science/article/pii/S0168900207007644.

[120] E. Abat et al. 'The ATLAS Transition Radiation Tracker (TRT) proportional drift tube: design and performance'. In: *J. Instrum.* 3.02 (2008), P02013. URL: https://cds.cern.ch/record/1094549.

[121] J. Pequenao. 'Computer Generated image of the ATLAS calorimeter'. Mar. 2008. URL: https://cds.cern.ch/record/1095927.

[122] B. Aubert et al. 'Construction, assembly and tests of the ATLAS electromagnetic barrel calorimeter'. In: *Nucl.Instrum.Meth.* A558 (2006), pages 388–418.

[123] A. Artamonov et al. 'The ATLAS forward calorimeters'. In: *JINST* 3 (2008), P02010.

[124] P. Adragna et al. 'The ATLAS hadronic tile calorimeter: From construction toward physics'. In: *IEEE Trans.Nucl.Sci.* 53 (2006), pages 1275–1281.

[125] S. Palestini. 'The muon spectrometer of the ATLAS experiment'. In: *Nuclear Physics B - Proceedings Supplements* 125 (2003). Innovative Particle and Radiation Detectors, pages 337–345. URL: http://www.sciencedirect.com/science/article/pii/S0920563203910139.

[126] J. Pequenao. 'Computer generated image of the ATLAS Muons subsystem'. Mar. 2008. URL: https://cds.cern.ch/record/1095929.

[127] M. Bruschi. 'The ATLAS luminosity monitor'. In: *Nucl.Instrum.Meth.* A623 (2010), pages 371–373.

[128] O. Adriani et al. 'The LHCf detector at the CERN Large Hadron Collider'. In: *JINST* 3 (2008), S08006.

[129] S. Franz and P. Barrillon. 'ATLAS ALFA-measuring absolute luminosity with scintillating fibres'. In: *Nucl.Instrum.Meth.* A610 (2009), pages 35–40.

[130] ATLAS Collaboration. 'Measurement of the total cross section from elastic scattering in pp collisions at $\sqrt{s} = 7$ TeV with the ATLAS detector'. In: *Nucl. Phys.* B889 (2014), pages 486–548. arXiv: 1408.5778 [hep-ex].

[131] P. Jenni et al. *ATLAS high-level trigger, data-acquisition and controls: Technical Design Report*. Technical Design Report ATLAS. Geneva: CERN, 2003. URL: https://cds.cern.ch/record/616089.

[132] J. C. Vermeulen et al. *The baseline dataflow system of the ATLAS trigger and DAQ*. ATLAS Public Note. Geneva, Oct. 2003. URL: https://cds.cern.ch/record/685564.

[133] ATLAS Collaboration. *Electron efficiency measurements with the ATLAS detector using the 2012 LHC proton-proton collision data*. ATLAS Conference Note. Geneva, June 2014. URL: https://cds.cern.ch/record/1706245.

[134] ATLAS Collaboration. 'Measurement of the muon reconstruction performance of the ATLAS detector using 2011 and 2012 LHC proton-proton collision data'. In: *Eur.Phys.J.* C74.11 (2014), page 3130. arXiv: 1407.3935 [hep-ex].

[135] ATLAS Collaboration. 'Electron and photon energy calibration with the ATLAS detector using LHC Run 1 data'. In: *Eur.Phys.J.* C74.10 (2014), page 3071. arXiv: 1407.5063 [hep-ex].

[136] A. Collaboration. *ATLAS Data Quality Operations in 2012*. ATLAS Internal Note. Geneva, Jan. 2015. URL: https://cds.cern.ch/record/1982821.

[137] ATLAS Collaboration. *Luminosity Public Results*. 2012. URL: https://twiki.cern.ch/twiki/bin/view/AtlasPublic/LuminosityPublicResults.

[138] M. Limper, S. Bentvelsen and A. P. Colijn. 'Track and vertex reconstruction in the ATLAS inner detector'. Presented on 12 Oct 2009. PhD thesis. Amsterdam: Amsterdam U., 2009. URL: https://cds.cern.ch/record/1202457.

[139] R. E. Kalman. 'A New Approach to Linear Filtering and Prediction Problems'. In: *Transactions of the ASME – Journal of Basic Engineering* 82.Series D (1960), pages 35–45. URL: http://www.cs.unc.edu/%5C~%7B%7Dwelch/kalman/media/pdf/Kalman1960.pdf.

[140] R. Frühwirth. 'Application of Kalman filtering to track and vertex fitting'. In: *Nucl. Instr. Meth. Phys. Res. A: Accelerators, Spectrometers, Detectors and Associated Equipment* 262.2–3 (1987), pages 444–450. URL: http://www.sciencedirect.com/science/article/pii/0168900287908874.

[141] G. Piacquadio, K. Prokofiev and A. Wildauer. 'Primary vertex reconstruction in the ATLAS experiment at LHC'. In: *Journal of Physics: Conference Series* 119.3 (2008), page 032033. URL: http://stacks.iop.org/1742-6596/119/i=3/a=032033.

[142] W. Waltenberger, R. Frühwirth and P. Vanlaer. 'Adaptive vertex fitting'. In: *Journal of Physics G: Nuclear and Particle Physics* 34.12 (2007), N343. URL: http://stacks.iop.org/0954-3899/34/i=12/a=N01.

[143] ATLAS Collaboration. *ATLAS Stand-Alone Event Displays: 2012 $Z \rightarrow \mu\mu$ event with high pileup*. Geneva, Aug. 2015. URL: https://twiki.cern.ch/twiki/pub/AtlasPublic/EventDisplayStandAlone/2012_highPileup.png.

[144] ATLAS Collaboration. 'Electron reconstruction and identification efficiency measurements with the ATLAS detector using the 2011 LHC proton-proton collision data'. In: *Eur.Phys.J.* C74.7 (2014), page 2941. arXiv: 1404.2240 [hep-ex].

[145] M. Cacciari, G. P. Salam and G. Soyez. 'The anti-k_T jet clustering algorithm'. In: *JHEP* 04 (2008), page 063. arXiv: 0802.1189 [hep-ph].

[146] S. D. Ellis and D. E. Soper. 'Successive combination jet algorithm for hadron collisions'. In: *Phys.Rev.* D48 (1993), pages 3160–3166. arXiv: hep-ph/9305266 [hep-ph].

[147] Y. L. Dokshitzer et al. 'Better jet clustering algorithms'. In: *JHEP* 9708 (1997), page 001. arXiv: hep-ph/9707323 [hep-ph].

[148] M. Wobisch and T. Wengler. 'Hadronization corrections to jet cross-sections in deep inelastic scattering'. In: (1998). arXiv: hep-ph/9907280 [hep-ph].

[149] ATLAS Collaboration. *Jet energy scale and its systematic uncertainty for jets produced in proton-proton collisions at $\sqrt{(}s) = 7$ TeV and measured with the ATLAS detector*. ATLAS Conference Note. Geneva, July 2010. URL: https://cds.cern.ch/record/1281329.

[150] ATLAS Collaboration. 'Jet energy measurement with the ATLAS detector in proton-proton collisions at $\sqrt{s} = 7$ TeV'. In: *Eur. Phys. J.* C73.3 (2013), page 2304. arXiv: 1112.6426 [hep-ex].

[151] M. Petteni. *Setting of the ATLAS Jet Energy Scale*. ATLAS Public Note. Geneva, Mar. 2011. URL: https://cds.cern.ch/record/1340537.

[152] *Tagging and suppression of pileup jets with the ATLAS detector*. ATLAS Conference Note. Geneva, May 2014. URL: https://cds.cern.ch/record/1700870.

[153] ATLAS Collaboration. *Commissioning of the ATLAS high-performance b-tagging algorithms in the 7 TeV collision data*. ATLAS Conference Note. Geneva, July 2011. URL: https://cds.cern.ch/record/1369219.

[154] ATLAS Collaboration. *Measurement of the b-tag Efficiency in a Sample of Jets Containing Muons with 5 fb^{-1} of Data from the ATLAS Detector*. ATLAS Conference Note. Geneva, Mar. 2012. URL: https://cds.cern.ch/record/1435197.

[155] ATLAS Collaboration. *Calibration of the performance of b-tagging for c and light-flavour jets in the 2012 ATLAS data*. ATLAS Conference Note. Geneva, July 2014. URL: https://cds.cern.ch/record/1741020.

[156] ATLAS Collaboration. *Preliminary results on the muon reconstruction efficiency, momentum resolution, and momentum scale in ATLAS 2012 pp collision data*. ATLAS Conference Note. Geneva, Aug. 2013. URL: https://cds.cern.ch/record/1580207.

[157] S. Hassani et al. 'A muon identification and combined reconstruction procedure for the ATLAS detector at the LHC using the (MUONBOY, STACO, MuTag) reconstruction packages'. In: *Nucl. Instr. Meth. Phys. Res. A: Accelerators, Spectrometers, Detectors and Associated Equipment* 572.1 (2007), pages 77–79. URL: http://www.sciencedirect.com/science/article/pii/S0168900206019863.

[158] B. Resende. *Muon identification algorithms in ATLAS*. ATLAS Public Note. Geneva, Sept. 2009. URL: https://cds.cern.ch/record/1209632.

[159] ATLAS Collaboration. *Performance of Missing Transverse Momentum Reconstruction in ATLAS studied in Proton-Proton Collisions recorded in 2012 at 8 TeV*. ATLAS Conference Note. Geneva, Aug. 2013. URL: https://cds.cern.ch/record/1570993.

[160] HSG3 Working Group. *Object Selections in the $H \rightarrow WW(*)$ analysis with* 20.3 fb^{-1} *of data collected with the ATLAS detector at* $\sqrt{s} = 8$ *TeV*. ATLAS Internal Note. Geneva, Nov. 2013. URL: https://cds.cern.ch/record/1624408.

[161] ATLAS Collaboration. *ATLAS Data Summary*. 2012. URL: https://atlas.web.cern.ch/Atlas/GROUPS/DATAPREPARATION/DataSummary/2012/run-table.html.

[162] ATLAS Collaboration. *Performance of the ATLAS Electron and Photon Trigger in p-p Collisions at* $sqrts = 7$ *TeV in 2011*. ATLAS Conference Note. Geneva, May 2012. URL: https://cds.cern.ch/record/1450089.

[163] D. Damazio et al. *Performance of the ATLAS Electron and Photon Triggers in pp Collisions at* $\sqrt{s} = 8$ *TeV in 2012*. ATLAS Internal Note. Geneva, Oct. 2013. URL: https://cds.cern.ch/record/1609629.

[164] ATLAS Collaboration. 'Performance of the ATLAS muon trigger in *pp* collisions at $\sqrt{s} = 8$ TeV'. In: *Eur. Phys. J. C* 75 (2015), page 120. arXiv: 1408.3179 [hep-ex].

[165] S. D. Drell and T.-M. Yan. 'Massive Lepton-Pair Production in Hadron-Hadron Collisions at High Energies'. In: *Phys. Rev. Lett.* 25.5 (Aug. 1970), pages 316–320.

[166] J. C. Collins, D. E. Soper and G. F. Sterman. 'Factorization of Hard Processes in QCD'. In: *Adv.Ser.Direct.High Energy Phys.* 5 (1989), pages 1–91. arXiv: hep-ph/0409313 [hep-ph].

[167] M. Mangano and T. Stelzer. 'Tools for the simulation of hard hadronic collisions'. In: *Ann.Rev.Nucl.Part.Sci.* 55 (2005), pages 555–588.

[168] S. Catani et al. 'QCD matrix elements + parton showers'. In: *JHEP* 0111 (2001), page 063. arXiv: hep-ph/0109231 [hep-ph].

[169] M. L. Mangano, M. Moretti and R. Pittau. 'Multijet matrix elements and shower evolution in hadronic collisions: $Wb\bar{b} + n$ jets as a case study'. In: *Nucl.Phys.* B632 (2002), pages 343–362. arXiv: hep-ph/0108069 [hep-ph].

[170] F. Krauss. 'Matrix elements and parton showers in hadronic interactions'. In: *JHEP* 0208 (2002), page 015. arXiv: hep-ph/0205283 [hep-ph].

[171] S. Hoeche et al. 'QCD matrix elements and truncated showers'. In: *JHEP* 0905 (2009), page 053. arXiv: 0903.1219 [hep-ph].

[172] S. M. T. Sjostrand and P. Z. Skands. 'PYTHIA 6.4 physics and manual'. In: *JHEP* 0605 (2006), page 026.

[173] T. Sjostrand, S. Mrenna, and P. Z. Skands. 'A Brief Introduction to PYTHIA 8.1'. In: *CERN-LCGAPP* 04 (2007), page 1. arXiv: 0710.3820.

[174] B. Andersson et al. 'Parton Fragmentation and String Dynamics'. In: *Phys. Rept.* 97 (1983), pages 31–145.

[175] B. Andersson. 'The Lund model'. In: *Camb. Monogr. Part. Phys. Nucl. Phys. Cosmol.* 7 (1997), pages 1–471.

[176] G. Corcella et al. 'HERWIG 6: an event generator for hadron emission reactions with interfering gluons (including super-symmetric processes) '. In: *JHEP* 0101 (2001), page 010.

[177] J. Butterworth, J. R. Forshaw and M. Seymour. 'Multiparton interactions in photoproduction at HERA'. In: *Z.Phys.* C72 (1996), pages 637–646. arXiv: `hep-ph/9601371 [hep-ph]`.

[178] J.-C. Winter, F. Krauss and G. Soff. 'A Modified cluster hadronization model'. In: *Eur. Phys. J.* C36 (2004), pages 381–395. arXiv: `hep-ph/0311085 [hep-ph]`.

[179] P. Nason. 'A New method for combining NLO QCD with shower Monte Carlo algorithms'. In: *JHEP* 0411 (2004), page 040. arXiv: `hep-ph/0409146 [hep-ph]`.

[180] C. Oleari. 'The POWHEG-BOX'. In: *Nucl.Phys.Proc.Suppl.* 205-206 (2010), pages 36–41. arXiv: `1007.3893 [hep-ph]`.

[181] T. Binoth, M. Ciccolini, N. Kauer and M. Krämer. 'Gluon-induced W-boson pair production at the LHC'. In: *JHEP* 12 (2006), page 046. eprint: `hep-ph/0611170v1`.

[182] T. Gleisberg et al. 'Event generation with SHERPA 1.1'. In: *JHEP* 0902 (2009), page 007. arXiv: `0811.4622 [hep-ph]`.

[183] B. P. Kersevan and E. Richter-Was. 'The Monte Carlo event generator AcerMC version 2.0 with interfaces to PYTHIA 6.2 and HERWIG 6.5'. In: *arXiv:hep-ph/0405247* (2004).

[184] M. Mangano et al. 'ALPGEN, a generator for hard multi-parton processes in hadronic collisions'. In: *JHEP* 0307 (2003), page 001.

[185] S. Hoeche et al. 'Matching parton showers and matrix elements'. In: *HERA and the LHC: A Workshop on the implications of HERA for LHC physics: Proceedings Part A*. 2006. arXiv: `hep-ph/0602031 [hep-ph]`.

[186] J. M. Campbell and R. Ellis. 'MCFM for the Tevatron and the LHC'. In: *Nucl.Phys.Proc.Suppl.* 205-206 (2010), pages 10–15. arXiv: `1007.3492 [hep-ph]`.

[187] J. M. Campbell, R. K. Ellis and C. Williams. 'Gluon-Gluon Contributions to W+ W- Production and Higgs Interference Effects'. In: *JHEP* 1110 (2011), page 005. arXiv: `1107.5569 [hep-ph]`.

[188] K. Arnold et al. 'VBFNLO: A parton level Monte Carlo for processes with electroweak bosons – Manual for Version 2.5.0'. In: (2011). arXiv: `1107.4038`.

[189] J. Baglio et al. 'Release Note - VBFNLO 2.7.0'. In: (2014). arXiv: `1404.3940 [hep-ph]`.

[190] S. Alioli et al. 'NLO Higgs boson production via gluon fusion matched with shower in POWHEG'. In: *JHEP* 0904 (2009), page 002. arXiv: `0812.0578 [hep-ph]`.

[191] P. Nason and C. Oleari. 'NLO Higgs boson production via vector-boson fusion matched with shower in POWHEG'. In: *JHEP* 1002 (2010), page 037. arXiv: `0911.5299 [hep-ph]`.

[192] S. Agostinelli et al. 'GEANT 4, A Simulation Toolkit'. In: *Nucl. Instrum. Meth.* A506 (2003), page 250.

[193] J. Allison et al. 'Geant4 developments and applications'. In: *IEEE Trans.Nucl.Sci.* 53 (2006), page 270.

[194] ATLAS Collaboration. 'The ATLAS Simulation Infrastructure'. In: *The European Physical Journal C* 70.3 (2010), pages 823–874. URL: `http://dx.doi.org/10.1140/epjc/s10052-010-1429-9`.

[195] N. Kauer and G. Passarino. 'Inadequacy of zero-width approximation for a light Higgs boson signal'. In: *JHEP* 1208 (2012), page 116. arXiv: `1206.4803 [hep-ph]`.

[196] S. Goria, G. Passarino and D. Rosco. 'The Higgs boson lineshape'. In: *Nucl. Phys.* B864 (2012), pages 530–579. arXiv: `1112.5517 [hep-ph]`.

[197] G. Passarino. 'Higgs interference effects in $gg \to ZZ$ and their uncertainty'. English. In: *Journal of High Energy Physics* 2012.8, 146 (2012). URL: `http://dx.doi.org/10.1007/JHEP08(2012)146`.

[198] ATLAS Collaboration. 'Measurement of the WW cross section in $\sqrt{s} = 7$ TeV pp collisions with ATLAS'. In: *Phys. Rev. Lett.* 107 (2011), page 041802. arXiv: `1104.5225 [hep-ex]`.

[199] ATLAS Collaboration. 'Observation and measurement of Higgs boson decays to WW* with the ATLAS detector'. In: *Phys. Rev.* D92.1 (2015), page 012006. arXiv: `1412.2641 [hep-ex]`.

[200] M. Chelstowska et al. *Background estimation in the $H \to WW^{(*)} \to \ell\nu\ell\nu$ analysis with 20.7fb^{-1} of data collected with the ATLAS detector at $\sqrt{s} = 8$ TeV*. ATLAS Internal Note. Geneva, Dec. 2013. URL: `https://cds.cern.ch/record/1636127`.

[201] ATLAS Collaboration. *Measurement of the W^+W^- production cross section in proton-proton collisions at $\sqrt{s} = 8$ TeV with the ATLAS detector*. ATLAS Conference Note. Geneva, July 2014. URL: `https://cds.cern.ch/record/1728248`.

[202] G. Choudalakis and D. Casadei. 'Plotting the differences between data and expectation'. In: *European Physical Journal Plus* 127, 25 (Feb. 2012), page 25. arXiv: `1111.2062 [physics.data-an]`.

[203] K. Pearson. 'On the criterion that a given system of deviations from the probable in the case of a correlated system of variables is such that it can be reasonably supposed to have arisen from random sampling'. In: *Philosophical Magazine Series 5* 50.302 (1900), pages 157–175. eprint: `http://dx.doi.org/10.1080/14786440009463897`.

[204] E. W. Weisstein. *Gamma Function – from Wolfram MathWorld*. 2015. URL: `http://mathworld.wolfram.com/GammaFunction.html` (visited on 23/09/2015).

[205] S. Diglio et al. *Update of the search for Higgs bosons predicted in Two-Higgs-Doublet models in the $H \to WW \to e\nu\mu\nu$ channel with the full 8 TeV data set*. ATLAS Internal Note. Geneva, June 2014. URL: `https://cds.cern.ch/record/1708884`.

[206] M. Feindt. 'A Neural Bayesian Estimator for Conditional Probability Densities'. In: (2004). arXiv: `physics/0402093`.

[207] M. Feindt and U. Kerzel. 'The NeuroBayes Neural Network Package'. In: *Nucl. Instrum. Meth. A* 559 (2006), pages 190–194.

[208] A. Hoecker et al. 'TMVA: Toolkit for Multivariate Data Analysis'. In: *PoS* ACAT (2007), page 040. arXiv: physics/0703039.

[209] Rumelhart David E., Hinton Geoffrey E. and Williams Ronald J. 'Learning representations by back-propagating errors'. In: *Nature* 323.6088 (Oct. 1986). 10.1038/323533a0, pages 533–536.

[210] N. Qian. 'On the momentum term in gradient descent learning algorithms'. In: *Neural Networks* 12.1 (1999), pages 145–151. URL: http://www.sciencedirect.com/science/article/pii/S0893608098001166.

[211] ATLAS Collaboration. *Update on the jet energy scale systematic uncertainty for jets produced in proton-proton collisions at $\sqrt{s} = 7$ TeV measured with the ATLAS detector*. ATLAS Conference Note. Geneva, Feb. 2011. URL: https://cds.cern.ch/record/1330713.

[212] ATLAS Collaboration. *Approved 2013 JES Uncertainty of the Jet/E_T^{miss} group*. Geneva, 11th Aug. 2015. URL: https://twiki.cern.ch/twiki/bin/view/AtlasPublic/JetEtmissApproved2013JESUncertainty.

[213] ATLAS Collaboration. 'Electron performance measurements with the ATLAS detector using the 2010 LHC proton-proton collision data'. In: *Eur. Phys. J.* C72 (2012), page 1909. arXiv: 1110.3174 [hep-ex].

[214] ATLAS Collaboration. *Measurements of the photon identification efficiency with the ATLAS detector using 4.9 fb^{-1} of pp collision data collected in 2011*. ATLAS Conference Note. Geneva, Aug. 2012. URL: https://cds.cern.ch/record/1473426.

[215] HSG3 Working Group. *Analysis of $H \to WW \to \ell\nu\ell\nu$ ggF and VBF production modes with 20 fb^{-1} and 5 fb^{-1} of data collected with the ATLAS detector at $\sqrt{s} = 8$ and 7 TeV*. ATLAS Internal Note. Geneva, May 2014. URL: https://cds.cern.ch/record/1702035.

[216] ATLAS Collaboration. *Luminosity Determination in pp Collisions at $\sqrt{s} = 7$ TeV using the ATLAS Detector in 2011*. ATLAS Conference Note. Geneva, Aug. 2011. URL: https://cds.cern.ch/record/1376384.

[217] ATLAS Collaboration. 'Luminosity Determination in pp Collisions at $\sqrt{s} = 7$ TeV Using the ATLAS Detector at the LHC'. In: *Eur. Phys. J.* C71 (2011), page 1630. arXiv: 1101.2185 [hep-ex].

[218] HSG3 Working Group. *Update of the $H \to WW \to \ell\nu\ell\nu$ analysis with 21 fb^-1 of $\sqrt{s} = 8$ TeV data and 4.6 fb^{-1} of $\sqrt{s} = 7$ TeV data collected with the ATLAS Detector*. ATLAS Internal Note. Geneva, Feb. 2013. URL: https://cds.cern.ch/record/1515017.

[219] I. W. Stewart and F. J. Tackmann. 'Theory Uncertainties for Higgs and Other Searches Using Jet Bins'. In: *Phys.Rev.* D85 (2012), page 034011. arXiv: 1107.2117 [hep-ph].

[220] M. Chelstowska et al. *Theoretical studies for the $H \to WW$ measurement with the ATLAS detector*. ATLAS Internal Note. Geneva, Nov. 2013. URL: https://cds.cern.ch/record/1627073.

[221] A. Martin et al. 'Parton distributions for the LHC'. In: *Eur. Phys. J.* C63 (2009), pages 189–285. arXiv: `0901.0002 [hep-ph]`.

[222] ATLAS Collaboration. 'Search for a high-mass Higgs boson decaying to a W boson pair in pp collisions at $\sqrt{s} = 8$ TeV with the ATLAS detector'. In: CERN-PH-EP-2015-185 (Sept. 2015). arXiv: `1509.00389 [hep-ex]`.

[223] J. Neyman and E. S. Pearson. 'On the Problem of the Most Efficient Tests of Statistical Hypotheses'. In: *Philosophical Transactions of the Royal Society of London. Series A, Containing Papers of a Mathematical or Physical Character* 231 (1933), pages 289–337. URL: `http://www.jstor.org/stable/91247`.

[224] T. Junk. 'Confidence level computation for combining searches with small statistics'. In: *Nucl.Instrum.Meth.* A434 (1999), pages 435–443. arXiv: `hep-ex/9902006 [hep-ex]`.

[225] A. L. Read. 'Presentation of search results: the CL_s technique'. In: *Journal of Physics G: Nuclear and Particle Physics* 28.10 (2002), page 2693. URL: `http://stacks.iop.org/0954-3899/28/i=10/a=313`.

[226] B. Mistlberger and F. Dulat. 'Limit setting procedures and theoretical uncertainties in Higgs boson searches'. In: (Apr. 2012). arXiv: `1204.3851 [hep-ph]`.

A | Ranking of Variables in Neural Network Training

In Tables A.1 to A.10 the ranking of variables in the different jet channels for the different training points as described in Table 7.1 is given. Table A.11 shows the ranking for the training in the light Higgs boson CR.

Table A.1: Variables used for the training of the NN at $m_H = 150$ GeV in the 0-jet channel (left), the 1-jet channel (centre) and in the 2-jet channel (right), ordered by their importance. The ordering is given by the loss in total correlation to the target, which is 44.6%, 55.3% and 72.0% respectively, for the entire set of variables.

0-jet channel		1-jet channel		2-jet channel	
Variable	corr. loss in %	Variable	corr. loss in %	Variable	corr. loss in %
m_T	22.2	m_T	33.8	m_T	22.2
$\|\eta(\ell_1)\|$	19.1	$p_T(j_1)$	20.2	$m(jj)$	12.6
$m(\ell\ell)$	15.3	$\eta(j_1)$	18.0	$\Delta\eta(j_1, j_2)$	8.1
$p_T(\ell\ell)$	12.8	$\Delta R(\ell\ell, j_1)$	15.6	$\Delta R(\ell_1, j_1)$	7.8
$\Delta p_T(\ell_1, \ell_2)$	12.3	$m(\ell\ell)$	11.8	$m(\ell\ell)$	7.0
p_T^{tot}	10.0	$\Delta p_T(\ell_1, \ell_2)$	10.5	$\eta(j_1)$	6.4
$\|\eta(\ell_2)\|$	6.3	$\Delta R(\ell_1, \ell_2)$	6.3	$\Delta R(\ell_1, \ell_2)$	3.8
$p_T(\ell_2)$	4.5	$p_T(\ell\ell)$	5.4	$E_{T, rel}^{miss}$	3.2
$\Delta R(\ell_1, \ell_2)$	3.5	$\|\eta(\ell_1)\|$	5.0	$p_T(\ell\ell)$	3.0
$\Delta\eta(\ell_1, \ell_2)$	2.1	$\Delta\eta(\ell_1, \ell_2)$	3.5	$p_T(\ell_2)$	2.7
$E_{T, rel}^{miss}$	1.8	$p_T(\ell_2)$	2.3	$\Delta p_T(\ell_1, \ell_2)$	2.6
		$\Delta\phi(\ell_1, \ell_2)$	1.6	$\|\eta(\ell_2)\|$	2.3
		p_T^{tot}	1.1	$\|\eta(\ell_1)\|$	1.9
		$\|\eta(\ell_2)\|$	0.9	$\Delta\eta(\ell_1, \ell_2)$	1.7
				$p_T(j_2)$	1.6
				p_T^{tot}	1.2
				$\Delta\phi(\ell_1, \ell_2)$	0.9
				$p_T(j_1)$	0.2

Table A.2: Variables used for the training of the NN at $m_H = 180$ GeV in the 0-jet channel (left), the 1-jet channel (centre) and in the 2-jet channel (right), ordered by their importance. The ordering is given by the loss in total correlation to the target, which is 43.5%, 51.4% and 70.4% respectively, for the entire set of variables.

0-jet channel		1-jet channel		2-jet channel	
Variable	corr. loss in %	Variable	corr. loss in %	Variable	corr. loss in %
$m(\ell\ell)$	15.4	m_{T}	19.2	m_{T}	10.2
$\Delta p_{\mathrm{T}}(\ell_1, \ell_2)$	15.0	$p_{\mathrm{T}}(j_1)$	16.1	$\Delta\eta(j_1, j_2)$	7.2
$\lvert\eta(\ell_1)\rvert$	14.4	$\eta(j_1)$	15.6	$E_{\mathrm{T,\,rel}}^{\mathrm{miss}}$	6.3
$p_{\mathrm{T}}(\ell_2)$	13.9	$\Delta R(\ell\ell, j_1)$	13.7	$m(jj)$	6.0
$p_{\mathrm{T}}(\ell\ell)$	13.5	$p_{\mathrm{T}}(\ell_2)$	9.2	$\eta(j_1)$	5.9
m_{T}	12.9	$m(\ell\ell)$	7.6	$m(\ell\ell)$	5.3
$p_{\mathrm{T}}^{\mathrm{tot}}$	7.1	$\Delta p_{\mathrm{T}}(\ell_1, \ell_2)$	7.2	$\Delta R(\ell_1, j_1)$	4.6
$\lvert\eta(\ell_2)\rvert$	3.3	$\lvert\eta(\ell_1)\rvert$	4.8	$p_{\mathrm{T}}(\ell_2)$	4.4
$\Delta R(\ell_1, \ell_2)$	2.0	$E_{\mathrm{T,\,rel}}^{\mathrm{miss}}$	4.1	$p_{\mathrm{T}}(\ell\ell)$	3.5
$E_{\mathrm{T,\,rel}}^{\mathrm{miss}}$	1.6	$\Delta R(\ell_1, \ell_2)$	3.2	$\Delta p_{\mathrm{T}}(\ell_1, \ell_2)$	3.2
$\Delta\eta(\ell_1, \ell_2)$	1.1	$\Delta\eta(\ell_1, \ell_2)$	2.2	$\Delta R(\ell_1, \ell_2)$	2.3
		$p_{\mathrm{T}}^{\mathrm{tot}}$	2.1	$\Delta\phi(\ell_1, \ell_2)$	2.0
		$\Delta\phi(\ell_1, \ell_2)$	1.5	$p_{\mathrm{T}}(j_1)$	1.9
		$p_{\mathrm{T}}(\ell\ell)$	0.6	$\lvert\eta(\ell_2)\rvert$	1.4
				$\lvert\eta(\ell_1)\rvert$	1.1
				$p_{\mathrm{T}}^{\mathrm{tot}}$	0.9
				$p_{\mathrm{T}}(j_2)$	0.8
				$\Delta\eta(\ell_1, \ell_2)$	0.3

Table A.3: Variables used for the training of the NN at $m_H = 240$ GeV in the 0-jet channel (left), the 1-jet channel (centre) and in the 2-jet channel (right), ordered by their importance. The ordering is given by the loss in total correlation to the target, which is 38.9%, 41.2% and 71.1% respectively, for the entire set of variables.

0-jet channel		1-jet channel		2-jet channel	
Variable	corr. loss in %	Variable	corr. loss in %	Variable	corr. loss in %
m_T	22.6	$\Delta R(\ell\ell, j_1)$	17.8	$m(jj)$	10.9
$\|\eta(\ell_1)\|$	13.4	$\eta(j_1)$	16.6	m_T	9.8
$p_T(\ell\ell)$	11.3	m_T	14.5	$\Delta\eta(j_1, j_2)$	7.5
$p_T(\ell_2)$	9.4	$p_T(j_1)$	13.9	$\Delta R(\ell_1, j_1)$	6.8
$\Delta p_T(\ell_1, \ell_2)$	8.7	$m(\ell\ell)$	8.3	$\Delta\eta(\ell_1, \ell_2)$	6.0
$\Delta R(\ell_1, \ell_2)$	8.1	$\Delta R(\ell_1, \ell_2)$	5.8	$\eta(j_1)$	5.8
$m(\ell\ell)$	7.5	$\|\eta(\ell_1)\|$	5.5	$E_{\mathrm{T,\,rel}}^{\mathrm{miss}}$	5.2
$\|\eta(\ell_2)\|$	7.4	$\Delta\eta(\ell_1, \ell_2)$	5.0	$p_T(\ell\ell)$	4.6
$\Delta\eta(\ell_1, \ell_2)$	6.3	$E_{\mathrm{T,\,rel}}^{\mathrm{miss}}$	3.9	p_T^{tot}	3.0
p_T^{tot}	3.6	$p_T(\ell_2)$	2.6	$m(\ell\ell)$	2.9
$E_{\mathrm{T,\,rel}}^{\mathrm{miss}}$	1.1	$\Delta p_T(\ell_1, \ell_2)$	2.5	$p_T(\ell_2)$	2.8
		$p_T(\ell\ell)$	1.4	$\Delta p_T(\ell_1, \ell_2)$	2.1
		p_T^{tot}	1.0	$\Delta R(\ell_1, \ell_2)$	1.9
		$\|\eta(\ell_2)\|$	0.9	$p_T(j_2)$	1.6
				$\|\eta(\ell_1)\|$	1.2
				$\Delta\phi(\ell_1, \ell_2)$	1.0
				$p_T(j_1)$	0.5
				$\|\eta(\ell_2)\|$	0.1

Table A.4: Variables used for the training of the NN at $m_H = 340$ GeV in the 0-jet channel (left), the 1-jet channel (centre) and in the 2-jet channel (right), ordered by their importance. The ordering is given by the loss in total correlation to the target, which is 50.3%, 48.5% and 73.9% respectively, for the entire set of variables.

0-jet channel		1-jet channel		2-jet channel	
Variable	corr. loss in %	Variable	corr. loss in %	Variable	corr. loss in %
m_T	21.7	m_T	19.9	$m(jj)$	12.4
$\Delta\eta(\ell_1, \ell_2)$	14.8	$\eta(j_1)$	19.1	m_T	8.9
$\Delta R(\ell_1, \ell_2)$	10.7	$\Delta R(\ell\ell, j_1)$	16.6	$\Delta\eta(j_1, j_2)$	8.4
$\|\eta(\ell_1)\|$	10.1	$p_T(j_1)$	12.3	$\Delta R(\ell_1, j_1)$	8.2
$\Delta p_T(\ell_1, \ell_2)$	8.9	$\Delta\eta(\ell_1, \ell_2)$	11.2	$\Delta\eta(\ell_1, \ell_2)$	8.1
$\|\eta(\ell_2)\|$	7.0	$\Delta R(\ell_1, \ell_2)$	9.8	$\eta(j_1)$	6.3
$m(\ell\ell)$	6.3	$\|\eta(\ell_1)\|$	7.2	p_T^{tot}	5.5
$p_T(\ell_2)$	4.5	$m(\ell\ell)$	6.7	$p_T(\ell_2)$	3.3
p_T^{tot}	4.5	$\Delta p_T(\ell_1, \ell_2)$	4.6	$m(\ell\ell)$	3.1
$p_T(\ell\ell)$	3.4	$p_T(\ell_2)$	3.1	$\Delta R(\ell_1, \ell_2)$	2.8
$E_{T, rel}^{miss}$	0.6	$\|\eta(\ell_2)\|$	2.7	$\Delta\phi(\ell_1, \ell_2)$	2.8
		$p_T(\ell\ell)$	0.7	$E_{T, rel}^{miss}$	1.8
		$\Delta\phi(\ell_1, \ell_2)$	0.6	$p_T(j_2)$	1.2
		p_T^{tot}	0.3	$p_T(j_1)$	1.2
				$\|\eta(\ell_2)\|$	0.7
				$\Delta p_T(\ell_1, \ell_2)$	0.7
				$\|\eta(\ell_1)\|$	0.6
				$p_T(\ell\ell)$	0.2

Table A.5: Variables used for the training of the NN at $m_H = 440$ GeV in the 0-jet channel (left), the 1-jet channel (centre) and in the 2-jet channel (right), ordered by their importance. The ordering is given by the loss in total correlation to the target, which is 62.5%, 59.6% and 78.3% respectively, for the entire set of variables.

0-jet channel		1-jet channel		2-jet channel	
Variable	corr. loss in %	Variable	corr. loss in %	Variable	corr. loss in %
m_{T}	20.3	m_{T}	23.0	$m(jj)$	8.1
$\Delta\eta(\ell_1, \ell_2)$	12.7	$\eta(j_1)$	19.5	$\Delta\eta(j_1, j_2)$	6.0
$\Delta R(\ell_1, \ell_2)$	12.2	$\Delta R(\ell\ell, j_1)$	13.0	m_{T}	5.6
$\lvert\eta(\ell_1)\rvert$	9.0	$\Delta R(\ell_1, \ell_2)$	9.2	$\Delta R(\ell_1, j_1)$	4.5
$\Delta p_{\mathrm{T}}(\ell_1, \ell_2)$	9.0	$p_{\mathrm{T}}(j_1)$	9.0	$\Delta\eta(\ell_1, \ell_2)$	4.4
$\lvert\eta(\ell_2)\rvert$	8.5	$\lvert\eta(\ell_1)\rvert$	8.4	$\Delta R(\ell_1, \ell_2)$	3.6
$m(\ell\ell)$	4.5	$\lvert\eta(\ell_2)\rvert$	6.9	$\eta(j_1)$	3.2
$p_{\mathrm{T}}^{\mathrm{tot}}$	2.7	$\Delta\eta(\ell_1, \ell_2)$	6.5	$p_{\mathrm{T}}(j_2)$	2.4
$E_{\mathrm{T,\,rel}}^{\mathrm{miss}}$	1.9	$\Delta p_{\mathrm{T}}(\ell_1, \ell_2)$	4.5	$p_{\mathrm{T}}^{\mathrm{tot}}$	2.4
$\Delta\phi(\ell_1, \ell_2)$	1.0	$p_{\mathrm{T}}(\ell_2)$	3.7	$\lvert\eta(\ell_2)\rvert$	1.6
$p_{\mathrm{T}}(\ell\ell)$	0.7	$m(\ell\ell)$	2.8	$m(\ell\ell)$	1.6
		$p_{\mathrm{T}}^{\mathrm{tot}}$	2.6	$E_{\mathrm{T,\,rel}}^{\mathrm{miss}}$	1.4
		$\Delta\phi(\ell_1, \ell_2)$	2.0	$\Delta\phi(\ell_1, \ell_2)$	1.2
		$p_{\mathrm{T}}(\ell\ell)$	0.9	$\Delta p_{\mathrm{T}}(\ell_1, \ell_2)$	1.1
				$p_{\mathrm{T}}(\ell_2)$	1.0
				$p_{\mathrm{T}}(j_1)$	1.0
				$\lvert\eta(\ell_1)\rvert$	0.8
				$p_{\mathrm{T}}(\ell\ell)$	0.3

Table A.6: Variables used for the training of the NN at $m_H = 540$ GeV in the 0-jet channel (left), the 1-jet channel (centre) and in the 2-jet channel (right), ordered by their importance. The ordering is given by the loss in total correlation to the target, which is 70.6%, 63.2% and 81.4% respectively, for the entire set of variables.

0-jet channel		1-jet channel		2-jet channel	
Variable	corr. loss in %	Variable	corr. loss in %	Variable	corr. loss in %
m_{T}	21.2	m_{T}	24.3	$m(jj)$	9.3
$\Delta R(\ell_1, \ell_2)$	9.2	$\eta(j_1)$	18.6	m_{T}	7.4
$\lvert\eta(\ell_2)\rvert$	9.1	$\Delta R(\ell\ell, j_1)$	11.1	$\Delta R(\ell_1, j_1)$	5.4
$\lvert\eta(\ell_1)\rvert$	8.7	$p_{\mathrm{T}}(j_1)$	9.6	$\Delta\eta(j_1, j_2)$	5.4
$\Delta p_{\mathrm{T}}(\ell_1, \ell_2)$	8.7	$\Delta R(\ell_1, \ell_2)$	9.6	$\eta(j_1)$	3.2
$\Delta\eta(\ell_1, \ell_2)$	8.2	$\lvert\eta(\ell_1)\rvert$	8.2	$\lvert\eta(\ell_2)\rvert$	2.8
$p_{\mathrm{T}}(\ell\ell)$	2.7	$\lvert\eta(\ell_2)\rvert$	7.6	$\lvert\eta(\ell_1)\rvert$	2.6
$E_{\mathrm{T,\,rel}}^{\mathrm{miss}}$	2.7	$\Delta\eta(\ell_1, \ell_2)$	6.5	$\Delta R(\ell_1, \ell_2)$	2.6
$p_{\mathrm{T}}(\ell_2)$	2.1	$\Delta p_{\mathrm{T}}(\ell_1, \ell_2)$	4.0	$E_{\mathrm{T,\,rel}}^{\mathrm{miss}}$	2.4
$p_{\mathrm{T}}^{\mathrm{tot}}$	1.8	$m(\ell\ell)$	3.4	$\Delta\eta(\ell_1, \ell_2)$	2.4
$\Delta\phi(\ell_1, \ell_2)$	0.8	$p_{\mathrm{T}}(\ell_2)$	2.0	$p_{\mathrm{T}}(\ell_2)$	2.3
		$p_{\mathrm{T}}(\ell\ell)$	1.4	$p_{\mathrm{T}}^{\mathrm{tot}}$	2.0
		$\Delta\phi(\ell_1, \ell_2)$	1.3	$\Delta\phi(\ell_1, \ell_2)$	1.7
		$E_{\mathrm{T,\,rel}}^{\mathrm{miss}}$	0.6	$\Delta p_{\mathrm{T}}(\ell_1, \ell_2)$	1.5
				$p_{\mathrm{T}}(j_2)$	1.2
				$p_{\mathrm{T}}(\ell\ell)$	0.6
				$p_{\mathrm{T}}(j_1)$	0.3
				$m(\ell\ell)$	0.2

Table A.7: Variables used for the training of the NN at $m_H = 650$ GeV in the 0-jet channel (left), the 1-jet channel (centre) and in the 2-jet channel (right), ordered by their importance. The ordering is given by the loss in total correlation to the target, which is 76.4%, 69.9% and 85.0% respectively, for the entire set of variables.

0-jet channel		1-jet channel		2-jet channel	
Variable	corr. loss in %	Variable	corr. loss in %	Variable	corr. loss in %
m_{T}	14.1	m_{T}	20.4	m_{T}	9.6
$\lvert\eta(\ell_1)\rvert$	6.6	$\eta(j_1)$	11.6	$m(jj)$	7.4
$\lvert\eta(\ell_2)\rvert$	6.3	$\lvert\eta(\ell_1)\rvert$	7.0	$\Delta R(\ell_1, j_1)$	5.4
$\Delta p_{\mathrm{T}}(\ell_1, \ell_2)$	6.0	$\Delta R(\ell\ell, j_1)$	6.4	$\Delta\eta(j_1, j_2)$	5.4
$\Delta R(\ell_1, \ell_2)$	4.3	$\lvert\eta(\ell_2)\rvert$	6.2	$\lvert\eta(\ell_2)\rvert$	3.7
$\Delta\eta(\ell_1, \ell_2)$	3.8	$\Delta R(\ell_1, \ell_2)$	6.0	$\lvert\eta(\ell_1)\rvert$	3.2
$p_{\mathrm{T}}^{\mathrm{tot}}$	3.0	$p_{\mathrm{T}}(\ell_2)$	3.8	$\eta(j_1)$	3.1
$p_{\mathrm{T}}(\ell\ell)$	2.3	$p_{\mathrm{T}}(j_1)$	3.6	$E_{\mathrm{T,\,rel}}^{\mathrm{miss}}$	2.6
$m(\ell\ell)$	1.8	$\Delta p_{\mathrm{T}}(\ell_1, \ell_2)$	3.0	$\Delta\phi(\ell_1, \ell_2)$	2.1
$E_{\mathrm{T,\,rel}}^{\mathrm{miss}}$	1.3	$E_{\mathrm{T,\,rel}}^{\mathrm{miss}}$	2.5	$p_{\mathrm{T}}^{\mathrm{tot}}$	1.5
$\Delta\phi(\ell_1, \ell_2)$	0.3	$\Delta\phi(\ell_1, \ell_2)$	2.2	$\Delta R(\ell_1, \ell_2)$	1.5
		$\Delta\eta(\ell_1, \ell_2)$	2.2	$\Delta p_{\mathrm{T}}(\ell_1, \ell_2)$	1.4
		$p_{\mathrm{T}}^{\mathrm{tot}}$	1.6	$p_{\mathrm{T}}(j_1)$	1.4
		$p_{\mathrm{T}}(\ell\ell)$	0.9	$\Delta\eta(\ell_1, \ell_2)$	1.3
				$p_{\mathrm{T}}(\ell\ell)$	0.8
				$p_{\mathrm{T}}(\ell_2)$	0.6
				$p_{\mathrm{T}}(j_2)$	0.5
				$m(\ell\ell)$	0.4

Table A.8: Variables used for the training of the NN at $m_H = 750$ GeV in the 0-jet channel (left), the 1-jet channel (centre) and in the 2-jet channel (right), ordered by their importance. The ordering is given by the loss in total correlation to the target, which is 78.9%, 75.1% and 87.3% respectively, for the entire set of variables.

0-jet channel		1-jet channel		2-jet channel	
Variable	corr. loss in %	Variable	corr. loss in %	Variable	corr. loss in %
m_{T}	14.4	m_{T}	20.7	m_{T}	10.6
$\Delta p_{\mathrm{T}}(\ell_1, \ell_2)$	5.8	$\eta(j_1)$	9.3	$\Delta\eta(j_1, j_2)$	6.7
$\lvert\eta(\ell_2)\rvert$	5.3	$\lvert\eta(\ell_1)\rvert$	6.9	$m(jj)$	5.7
$\lvert\eta(\ell_1)\rvert$	4.8	$\lvert\eta(\ell_2)\rvert$	5.9	$\Delta R(\ell_1, j_1)$	4.0
$\Delta\eta(\ell_1, \ell_2)$	3.5	$\Delta R(\ell\ell, j_1)$	5.8	$\lvert\eta(\ell_2)\rvert$	3.8
$p_{\mathrm{T}}(\ell\ell)$	3.1	$\Delta\phi(\ell_1, \ell_2)$	3.9	$\lvert\eta(\ell_1)\rvert$	3.4
$\Delta R(\ell_1, \ell_2)$	2.5	$p_{\mathrm{T}}(j_1)$	3.5	$\eta(j_1)$	2.5
$\Delta\phi(\ell_1, \ell_2)$	2.4	$\Delta p_{\mathrm{T}}(\ell_1, \ell_2)$	2.4	$\Delta R(\ell_1, \ell_2)$	2.0
$p_{\mathrm{T}}^{\mathrm{tot}}$	1.8	$\Delta\eta(\ell_1, \ell_2)$	2.1	$\Delta\phi(\ell_1, \ell_2)$	1.9
$E_{\mathrm{T,\,rel}}^{\mathrm{miss}}$	1.0	$\Delta R(\ell_1, \ell_2)$	1.9	$p_{\mathrm{T}}^{\mathrm{tot}}$	1.6
$p_{\mathrm{T}}(\ell_2)$	0.3	$m(\ell\ell)$	1.4	$\Delta p_{\mathrm{T}}(\ell_1, \ell_2)$	1.4
		$E_{\mathrm{T,\,rel}}^{\mathrm{miss}}$	1.3	$p_{\mathrm{T}}(\ell_2)$	1.3
		$p_{\mathrm{T}}(\ell\ell)$	1.0	$p_{\mathrm{T}}(\ell\ell)$	1.0
		$p_{\mathrm{T}}(\ell_2)$	0.9	$\Delta\eta(\ell_1, \ell_2)$	1.0
				$p_{\mathrm{T}}(j_2)$	0.9
				$E_{\mathrm{T,\,rel}}^{\mathrm{miss}}$	0.9
				$p_{\mathrm{T}}(j_1)$	0.7
				$m(\ell\ell)$	0.4

Table A.9: Variables used for the training of the NN at $m_H = 850$ GeV in the 0-jet channel (left), the 1-jet channel (centre) and in the 2-jet channel (right), ordered by their importance. The ordering is given by the loss in total correlation to the target, which is 80.6%, 76.6% and 88.7% respectively, for the entire set of variables.

0-jet channel		1-jet channel		2-jet channel	
Variable	corr. loss in %	Variable	corr. loss in %	Variable	corr. loss in %
m_{T}	15.0	m_{T}	21.2	m_{T}	12.1
$\lvert\eta(\ell_2)\rvert$	5.0	$\eta(j_1)$	9.4	$m(jj)$	6.9
$\lvert\eta(\ell_1)\rvert$	4.9	$\lvert\eta(\ell_1)\rvert$	6.0	$\Delta\eta(j_1, j_2)$	4.7
$\Delta p_{\mathrm{T}}(\ell_1, \ell_2)$	4.4	$\lvert\eta(\ell_2)\rvert$	5.8	$\lvert\eta(\ell_2)\rvert$	3.6
$\Delta\phi(\ell_1, \ell_2)$	2.8	$\Delta R(\ell\ell, j_1)$	3.5	$\Delta R(\ell_1, j_1)$	3.5
$p_{\mathrm{T}}(\ell\ell)$	2.4	$\Delta R(\ell_1, \ell_2)$	3.4	$\eta(j_1)$	2.7
$p_{\mathrm{T}}^{\mathrm{tot}}$	2.2	$\Delta\phi(\ell_1, \ell_2)$	3.3	$p_{\mathrm{T}}^{\mathrm{tot}}$	2.7
$\Delta R(\ell_1, \ell_2)$	2.1	$\Delta p_{\mathrm{T}}(\ell_1, \ell_2)$	2.6	$\lvert\eta(\ell_1)\rvert$	2.6
$\Delta\eta(\ell_1, \ell_2)$	2.1	$p_{\mathrm{T}}(\ell_2)$	2.3	$\Delta\phi(\ell_1, \ell_2)$	2.2
$E_{\mathrm{T,\,rel}}^{\mathrm{miss}}$	1.5	$p_{\mathrm{T}}(j_1)$	2.3	$p_{\mathrm{T}}(\ell\ell)$	2.0
$p_{\mathrm{T}}(\ell_2)$	0.6	$E_{\mathrm{T,\,rel}}^{\mathrm{miss}}$	1.9	$p_{\mathrm{T}}(\ell_2)$	1.8
		$p_{\mathrm{T}}(\ell\ell)$	1.5	$\Delta p_{\mathrm{T}}(\ell_1, \ell_2)$	1.7
		$p_{\mathrm{T}}^{\mathrm{tot}}$	1.0	$m(\ell\ell)$	1.5
		$\Delta\eta(\ell_1, \ell_2)$	0.7	$p_{\mathrm{T}}(j_1)$	1.1
				$\Delta R(\ell_1, \ell_2)$	0.9
				$E_{\mathrm{T,\,rel}}^{\mathrm{miss}}$	0.8
				$\Delta\eta(\ell_1, \ell_2)$	0.7
				$p_{\mathrm{T}}(j_2)$	0.0

Table A.10: Variables used for the training of the NN at $m_H = 950$ GeV in the 0-jet channel (left), the 1-jet channel (centre) and in the 2-jet channel (right), ordered by their importance. The ordering is given by the loss in total correlation to the target, which is 82.8%, 78.1% and 89.3% respectively, for the entire set of variables.

0-jet channel		1-jet channel		2-jet channel	
Variable	corr. loss in %	Variable	corr. loss in %	Variable	corr. loss in %
m_{T}	16.2	m_{T}	20.9	m_{T}	9.9
$\Delta p_{\mathrm{T}}(\ell_1, \ell_2)$	5.8	$\eta(j_1)$	9.6	$m(jj)$	6.8
$\lvert\eta(\ell_2)\rvert$	4.2	$\lvert\eta(\ell_2)\rvert$	6.1	$\Delta\eta(j_1, j_2)$	5.0
$p_{\mathrm{T}}(\ell\ell)$	3.5	$\lvert\eta(\ell_1)\rvert$	5.3	$\lvert\eta(\ell_1)\rvert$	3.3
$\lvert\eta(\ell_1)\rvert$	3.4	$\Delta\phi(\ell_1, \ell_2)$	4.0	$\lvert\eta(\ell_2)\rvert$	3.1
$p_{\mathrm{T}}(\ell_2)$	2.6	$\Delta R(\ell\ell, j_1)$	3.4	$\Delta R(\ell_1, j_1)$	2.7
$\Delta\phi(\ell_1, \ell_2)$	2.6	$p_{\mathrm{T}}(j_1)$	2.6	$\Delta\phi(\ell_1, \ell_2)$	1.9
$m(\ell\ell)$	2.5	$\Delta p_{\mathrm{T}}(\ell_1, \ell_2)$	1.7	$p_{\mathrm{T}}^{\mathrm{tot}}$	1.8
$E_{\mathrm{T,\,rel}}^{\mathrm{miss}}$	2.1	$\Delta R(\ell_1, \ell_2)$	1.6	$\Delta p_{\mathrm{T}}(\ell_1, \ell_2)$	1.6
$\Delta R(\ell_1, \ell_2)$	1.9	$p_{\mathrm{T}}^{\mathrm{tot}}$	1.3	$p_{\mathrm{T}}(\ell\ell)$	1.5
$p_{\mathrm{T}}^{\mathrm{tot}}$	1.8	$\Delta\eta(\ell_1, \ell_2)$	1.2	$\eta(j_1)$	1.0
		$p_{\mathrm{T}}(\ell\ell)$	1.1	$p_{\mathrm{T}}(\ell_2)$	0.9
		$p_{\mathrm{T}}(\ell_2)$	0.7	$\Delta R(\ell_1, \ell_2)$	0.9
		$E_{\mathrm{T,\,rel}}^{\mathrm{miss}}$	0.7	$E_{\mathrm{T,\,rel}}^{\mathrm{miss}}$	0.7
				$p_{\mathrm{T}}(j_2)$	0.4
				$\Delta\eta(\ell_1, \ell_2)$	0.3
				$m(\ell\ell)$	0.2
				$p_{\mathrm{T}}(j_1)$	0.1

Table A.11: Variables used for the training of the NN at $m_H = 125$ GeV in the 0-jet channel (left) and in the 1-jet channel (right), ordered by their importance. The ordering is given by the loss in total correlation to the target, which is 34.2% and 50.4% respectively, for the entire set of variables.

0-jet channel		1-jet channel	
Variable	corr. loss in %	Variable	corr. loss in %
$m(\ell\ell)$	18.0	m_{T}	55.6
$p_{\mathrm{T}}(\ell\ell)$	15.5	$\Delta R(\ell\ell, j_1)$	41.9
$\lvert\eta(\ell_1)\rvert$	14.3	$p_{\mathrm{T}}(j_1)$	38.5
$\lvert\eta(\ell_2)\rvert$	12.8	$m(\ell\ell)$	29.3
$\Delta p_{\mathrm{T}}(\ell_1, \ell_2)$	10.1	$\eta(j_1)$	28.1
m_{T}	9.1	$\lvert\eta(\ell_1)\rvert$	8.1
$E_{\mathrm{T,\,rel}}^{\mathrm{miss}}$	8.0	$E_{\mathrm{T,\,rel}}^{\mathrm{miss}}$	7.7
$p_{\mathrm{T}}^{\mathrm{tot}}$	7.3	$p_{\mathrm{T}}^{\mathrm{tot}}$	7.2
$p_{\mathrm{T}}(\ell_2)$	4.8	$\lvert\eta(\ell_2)\rvert$	6.9
$\Delta\phi(\ell_1, \ell_2)$	3.5	$\Delta R(\ell_1, \ell_2)$	6.1
$\Delta R(\ell_1, \ell_2)$	1.2	$\Delta p_{\mathrm{T}}(\ell_1, \ell_2)$	4.9
		$p_{\mathrm{T}}(\ell\ell)$	3.5
		$\Delta\phi(\ell_1, \ell_2)$	3.1
		$p_{\mathrm{T}}(\ell_2)$	2.6

B | Separation of Signal and Background Events in the Neural Networks

In Figures B.1 to B.10 the NN-output distributions, once normalised to unit area with a 2HDM signal with $\tan\beta = 1$ and $\alpha = \pi$ (red curve) and the total background (blue curve) is shown for the different training points and once normalised to the fit values from Table 7.3.

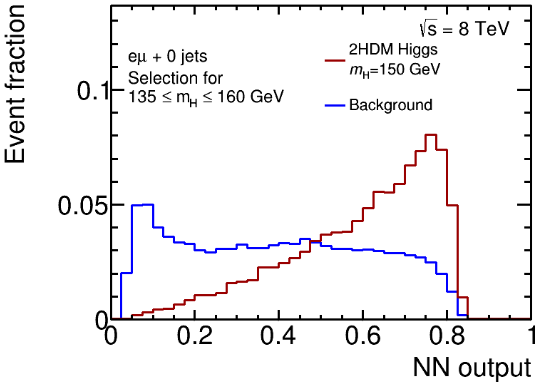

(a)

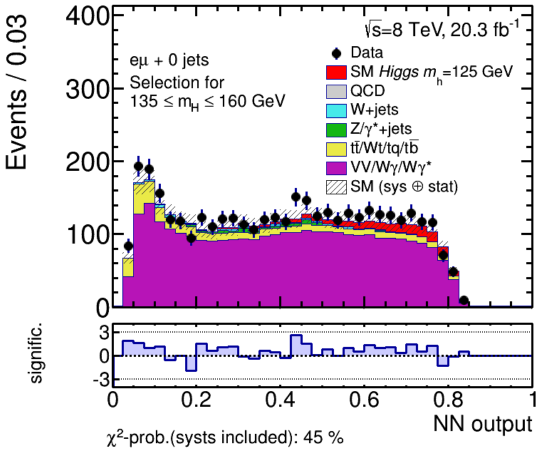

(b)

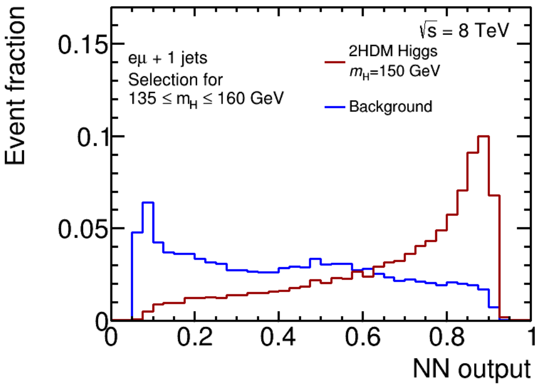

(c)

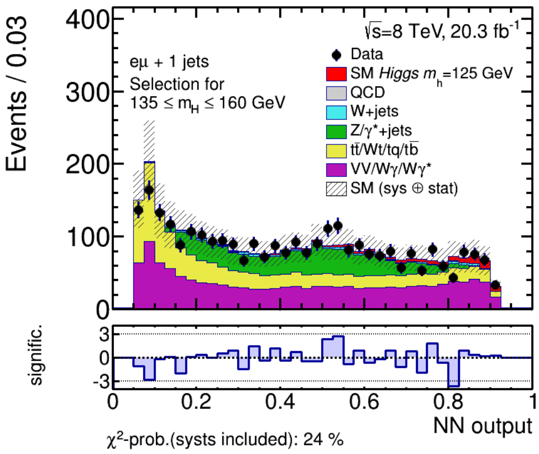

(d)

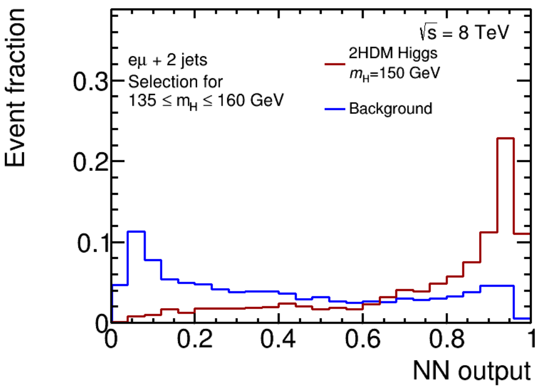

(e)

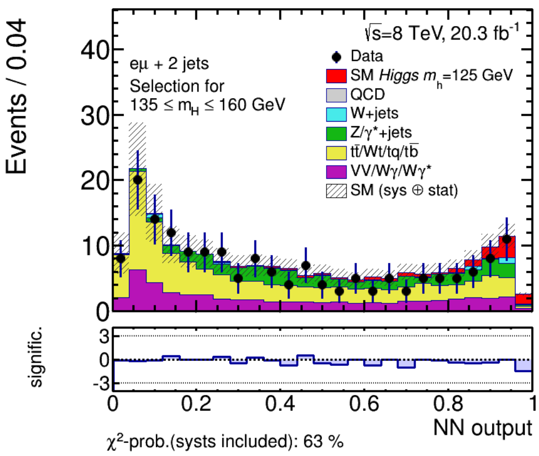

(f)

Figure B.1: NN-output distributions, normalised to unit area (left column) and normalised to fit values from Table 7.3 (right column), for $m_H = 150$ GeV. Figures (a) and (b) show the distribution of the 0-jet channel, (c) and (d) of the 1-jet channel and (e) and (f) of the 2-jet channel. The red curve shows the 2HDM signal with $m_H = 150$ GeV, $\tan\beta = 1$ and $\alpha = \pi$ and the blue curve shows the sum of all background processes.

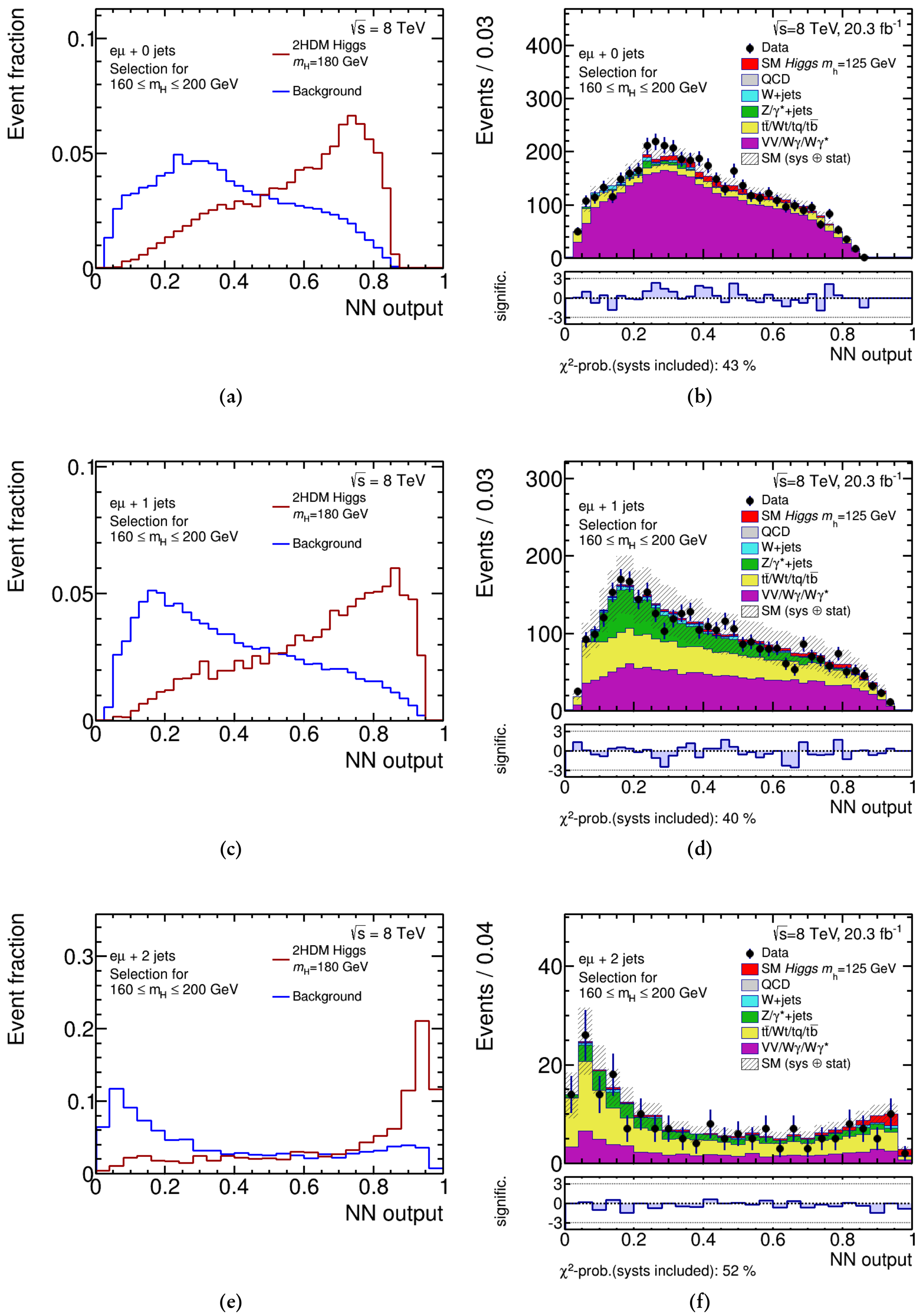

Figure B.2: NN-output distributions, normalised to unit area (left column) and normalised to fit values from Table 7.3 (right column), for $m_H = 180$ GeV. Figures (a) and (b) show the distribution of the 0-jet channel, (c) and (d) of the 1-jet channel and (e) and (f) of the 2-jet channel. The red curve shows the 2HDM signal with $m_H = 180$ GeV, $\tan\beta = 1$ and $\alpha = \pi$ and the blue curve shows the sum of all background processes.

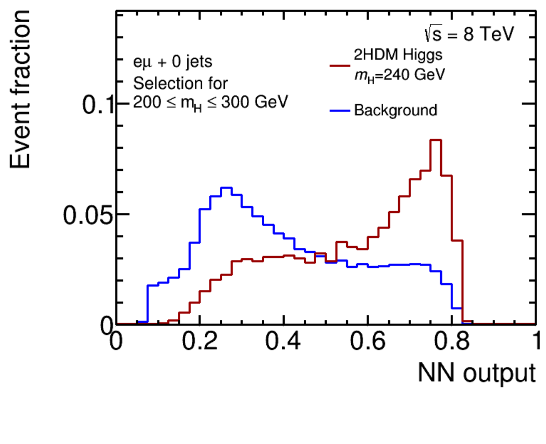

(a)

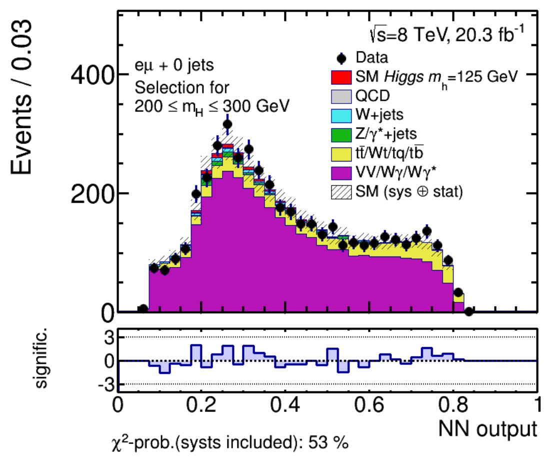

(b)

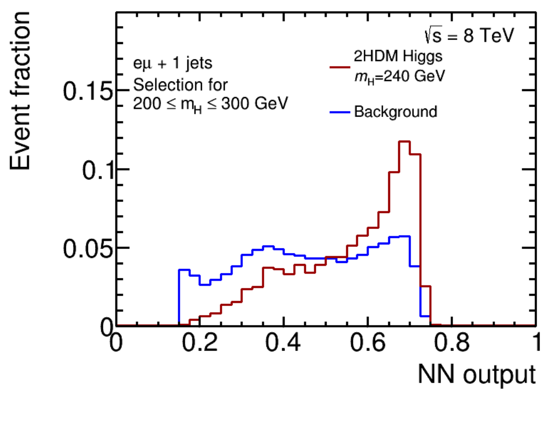

(c)

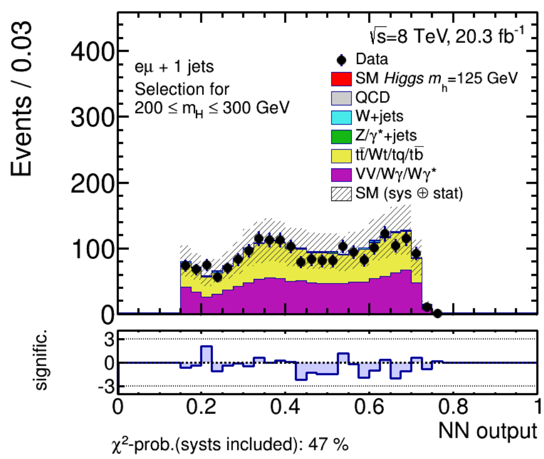

(d)

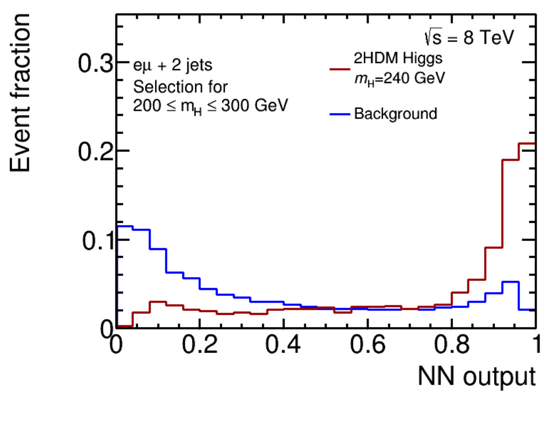

(e)

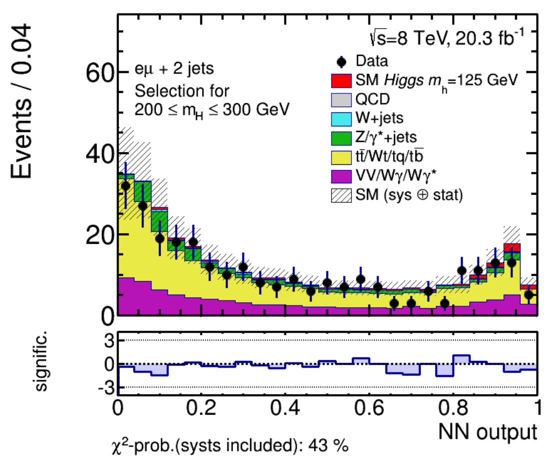

(f)

Figure B.3: NN-output distributions, normalised to unit area (left column) and normalised to fit values from Table 7.3 (right column), for $m_H = 240$ GeV. Figures (a) and (b) show the distribution of the 0-jet channel, (c) and (d) of the 1-jet channel and (e) and (f) of the 2-jet channel. The red curve shows the 2HDM signal with $m_H = 240$ GeV, $\tan\beta = 1$ and $\alpha = \pi$ and the blue curve shows the sum of all background processes.

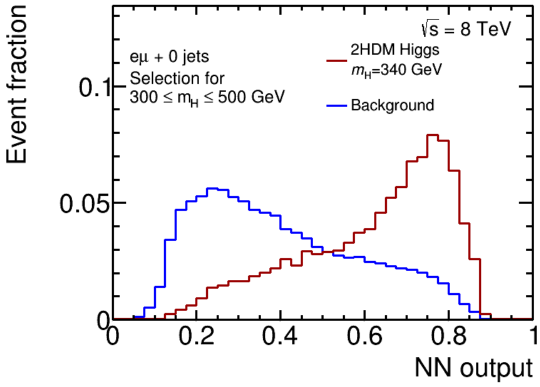

(a)

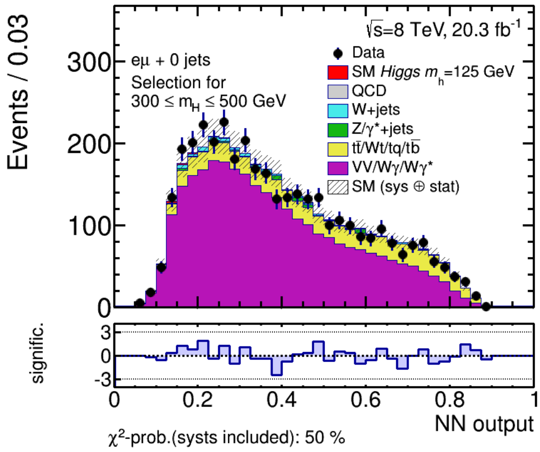

(b)

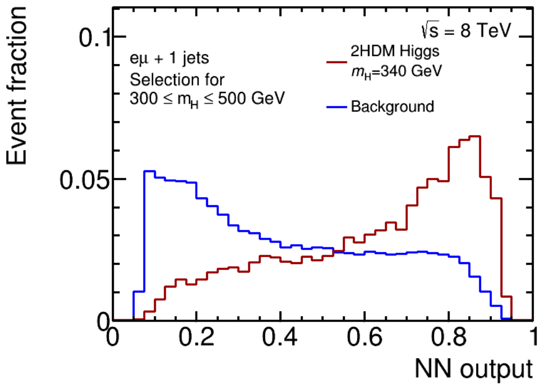

(c)

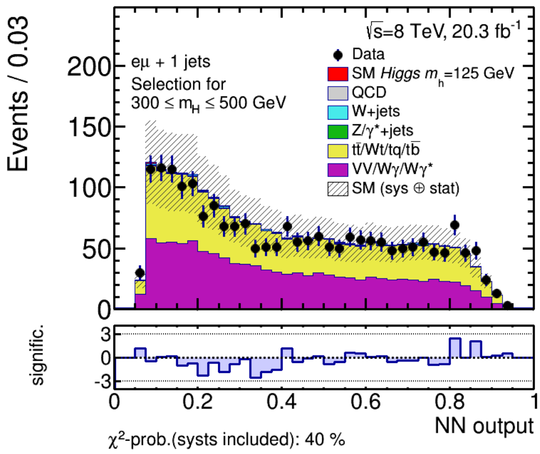

(d)

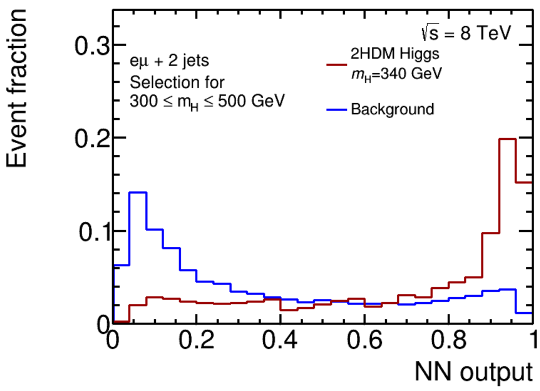

(e)

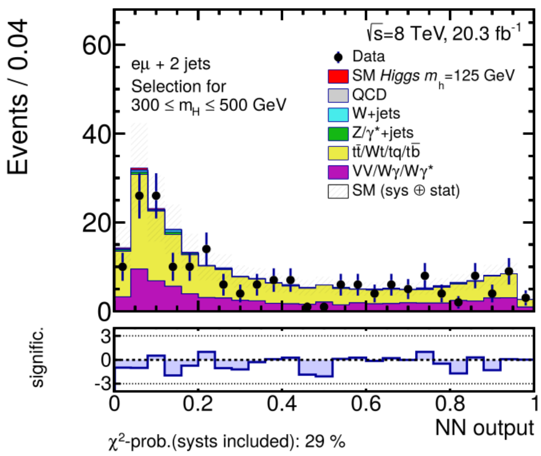

(f)

Figure B.4: NN-output distributions, normalised to unit area (left column) and normalised to fit values from Table 7.3 (right column), for $m_H = 340$ GeV. Figures (a) and (b) show the distribution of the 0-jet channel, (c) and (d) of the 1-jet channel and (e) and (f) of the 2-jet channel. The red curve shows the 2HDM signal with $m_H = 340$ GeV, $\tan\beta = 1$ and $\alpha = \pi$ and the blue curve shows the sum of all background processes.

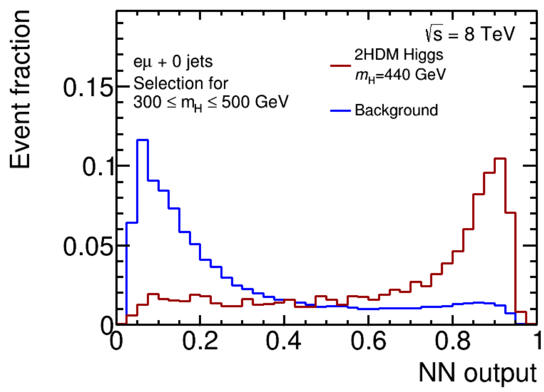

(a)

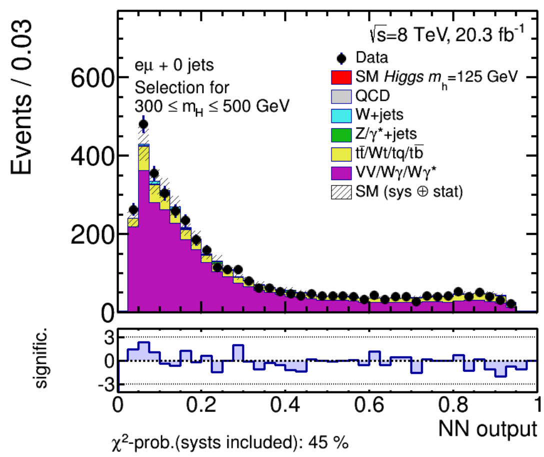

(b)

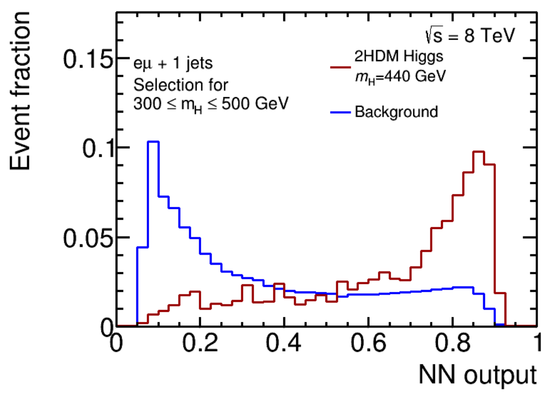

(c)

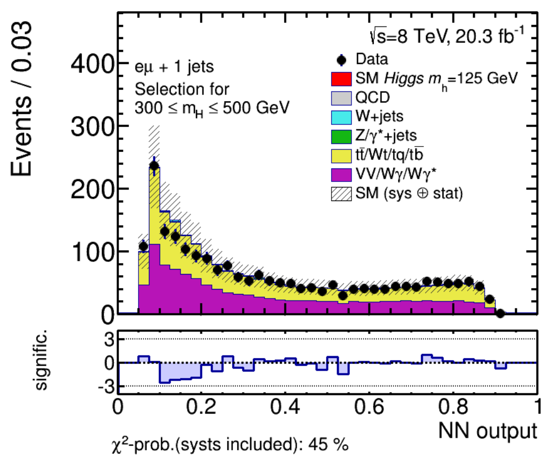

(d)

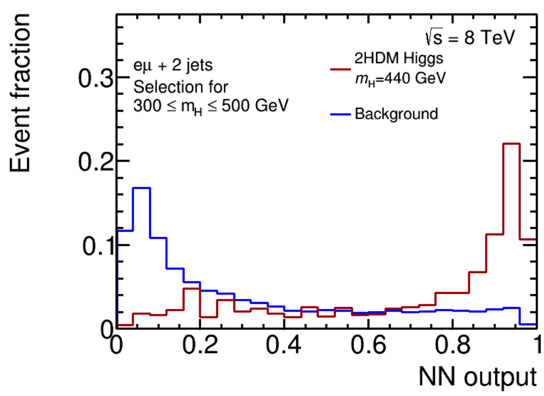

(e)

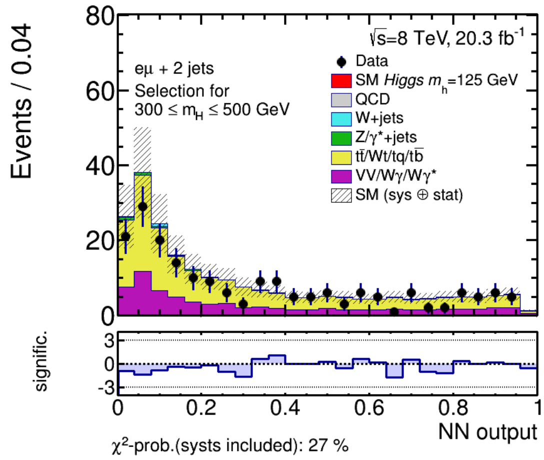

(f)

Figure B.5: NN-output distributions, normalised to unit area (left column) and normalised to fit values from Table 7.3 (right column), for $m_H = 440$ GeV. Figures (a) and (b) show the distribution of the 0-jet channel, (c) and (d) of the 1-jet channel and (e) and (f) of the 2-jet channel. The red curve shows the 2HDM signal with $m_H = 440$ GeV, $\tan\beta = 1$ and $\alpha = \pi$ and the blue curve shows the sum of all background processes.

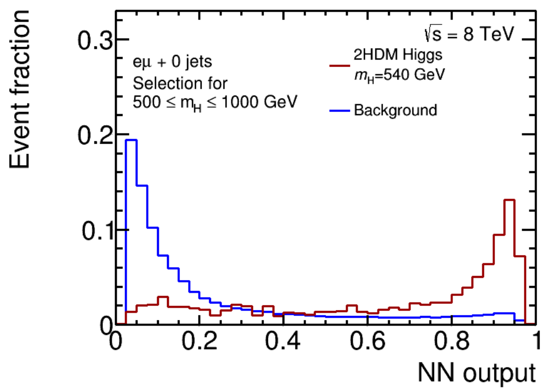

(a)

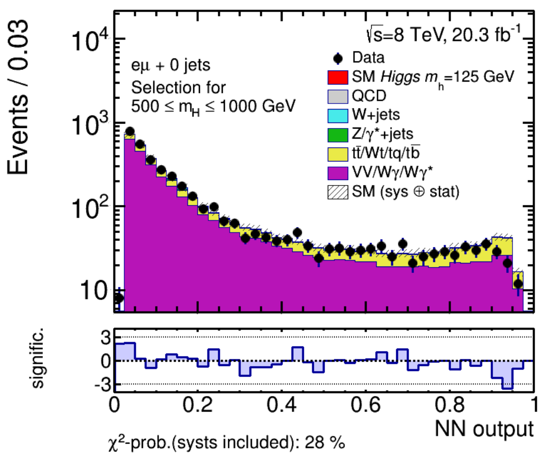

(b)

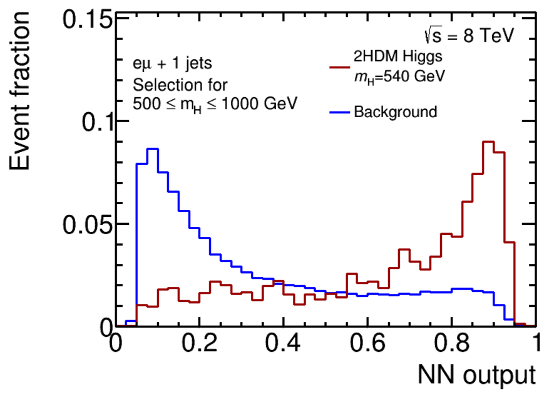

(c)

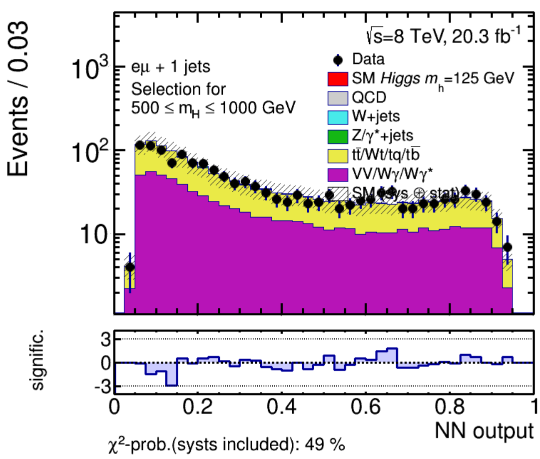

(d)

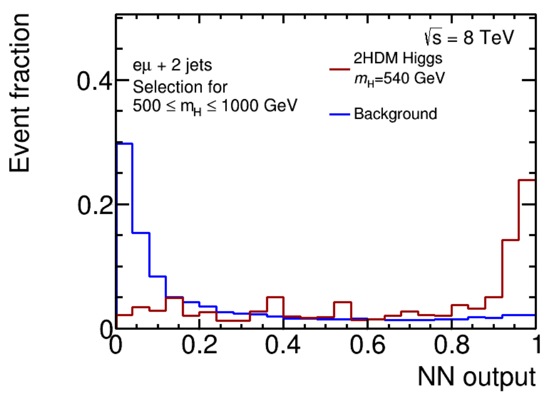

(e)

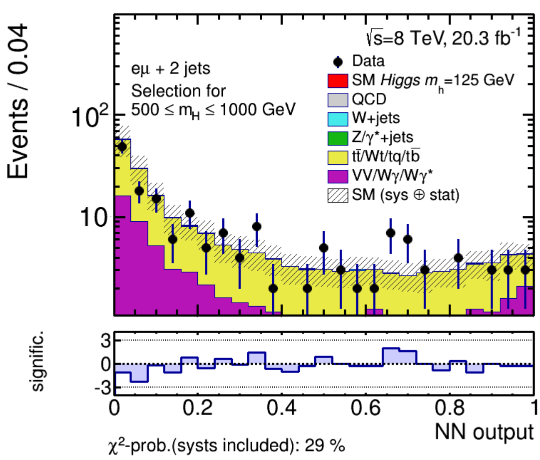

(f)

Figure B.6: NN-output distributions, normalised to unit area (left column) and normalised to fit values from Table 7.3 (right column), for $m_H = 540$ GeV. Figures (a) and (b) show the distribution of the 0-jet channel, (c) and (d) of the 1-jet channel and (e) and (f) of the 2-jet channel. The red curve shows the 2HDM signal with $m_H = 540$ GeV, $\tan\beta = 1$ and $\alpha = \pi$ and the blue curve shows the sum of all background processes.

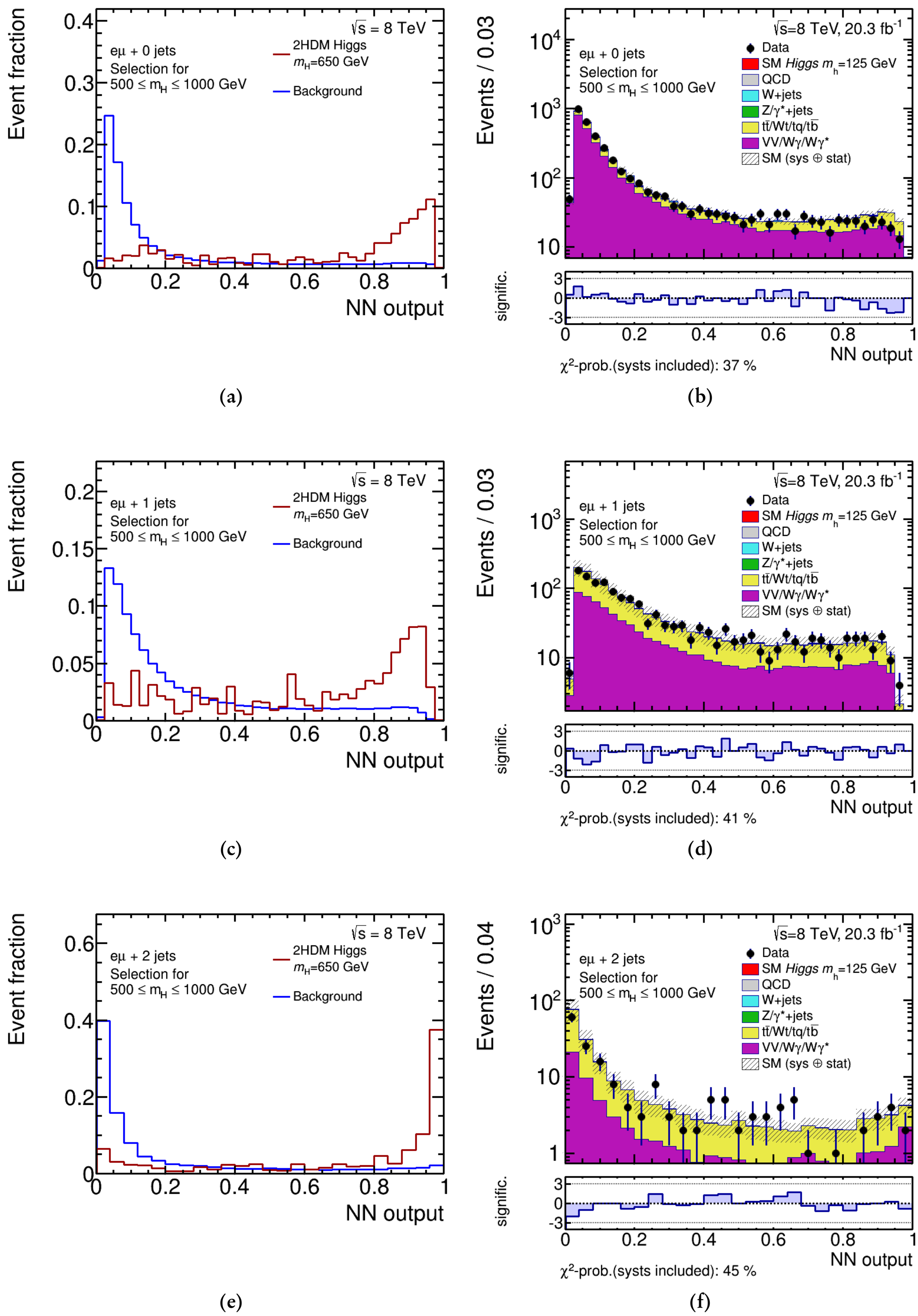

Figure B.7: NN-output distributions, normalised to unit area (left column) and normalised to fit values from Table 7.3 (right column), for $m_H = 650$ GeV. Figures (a) and (b) show the distribution of the 0-jet channel, (c) and (d) of the 1-jet channel and (e) and (f) of the 2-jet channel. The red curve shows the 2HDM signal with $m_H = 650$ GeV, $\tan\beta = 1$ and $\alpha = \pi$ and the blue curve shows the sum of all background processes.

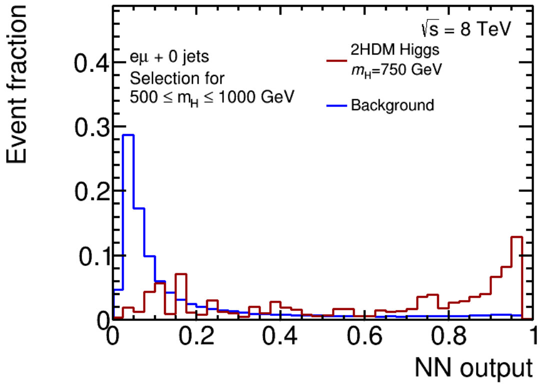

(a)

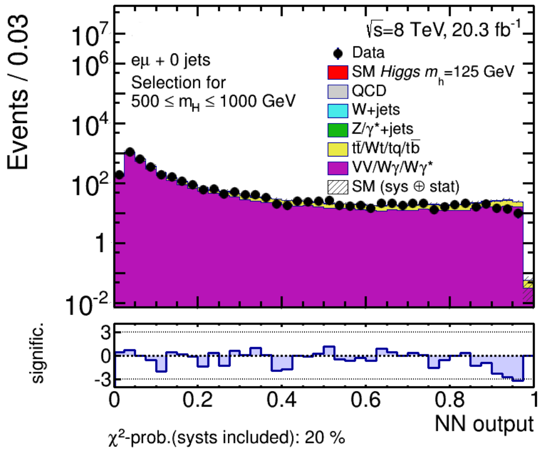

(b)

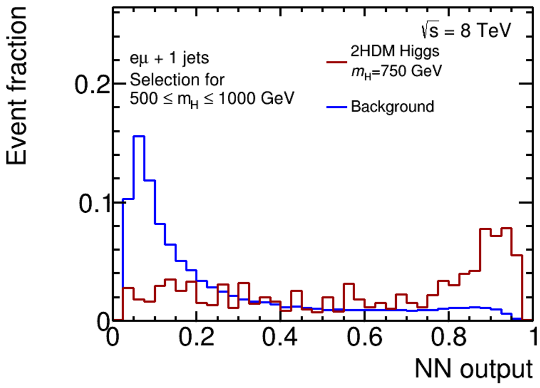

(c)

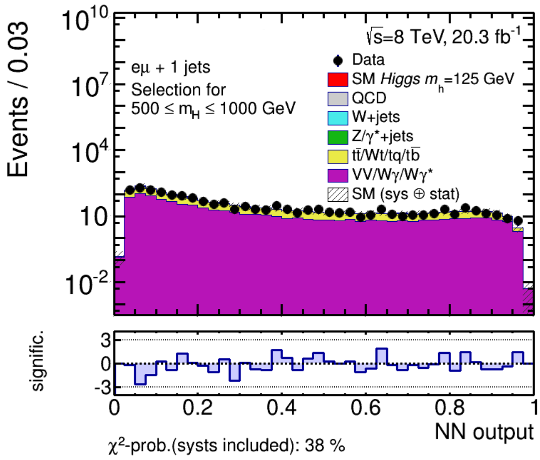

(d)

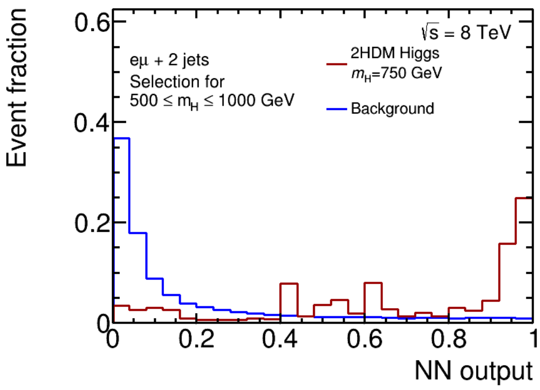

(e)

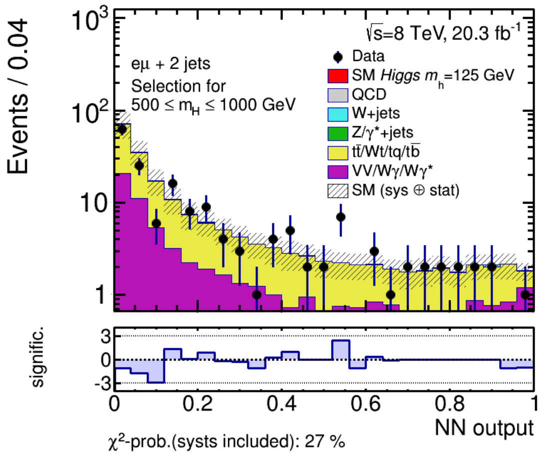

(f)

Figure B.8: NN-output distributions, normalised to unit area (left column) and normalised to fit values from Table 7.3 (right column), for $m_H = 750$ GeV. Figures (a) and (b) show the distribution of the 0-jet channel, (c) and (d) of the 1-jet channel and (e) and (f) of the 2-jet channel. The red curve shows the 2HDM signal with $m_H = 750$ GeV, $\tan\beta = 1$ and $\alpha = \pi$ and the blue curve shows the sum of all background processes.

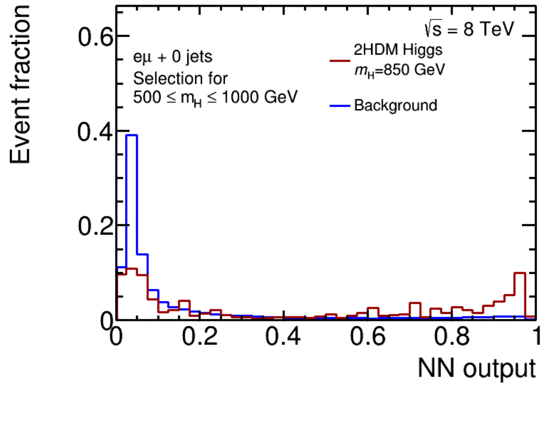

(a)

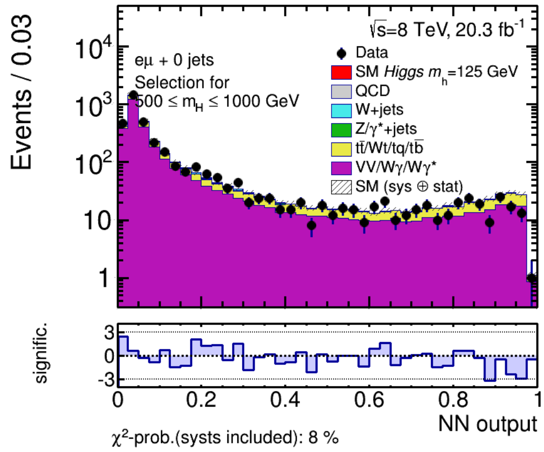

(b)

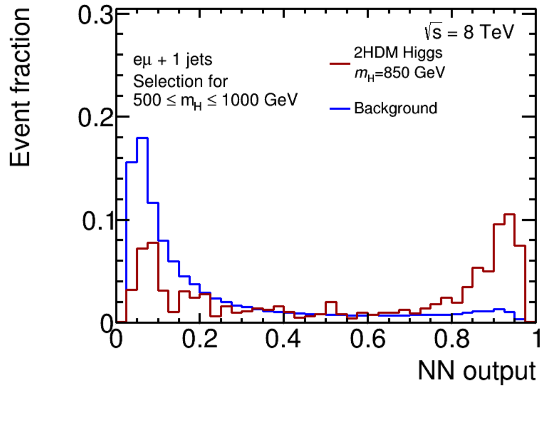

(c)

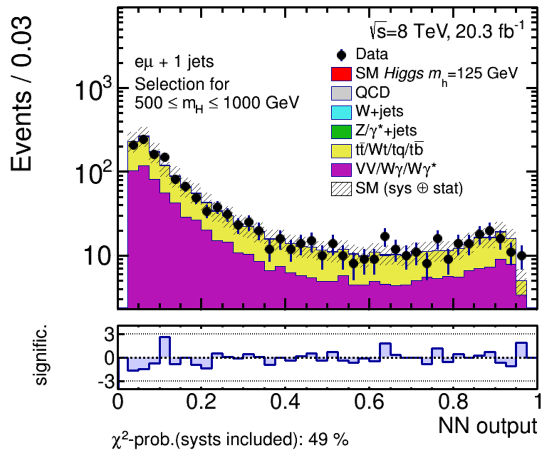

(d)

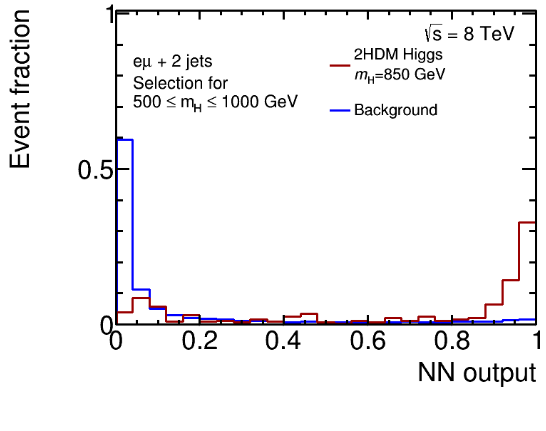

(e)

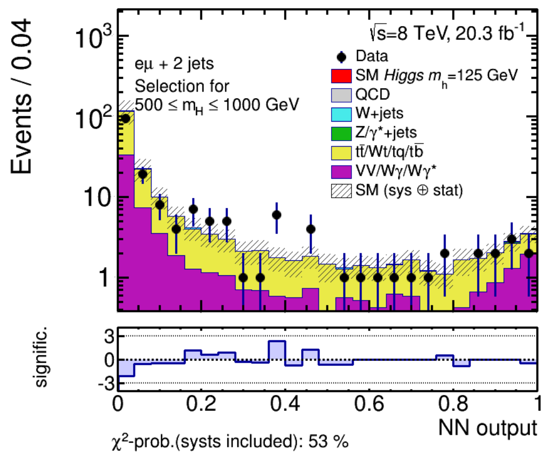

(f)

Figure B.9: NN-output distributions, normalised to unit area (left column) and normalised to fit values from Table 7.3 (right column), for $m_H = 850$ GeV. Figures (a) and (b) show the distribution of the 0-jet channel, (c) and (d) of the 1-jet channel and (e) and (f) of the 2-jet channel. The red curve shows the 2HDM signal with $m_H = 850$ GeV, $\tan\beta = 1$ and $\alpha = \pi$ and the blue curve shows the sum of all background processes.

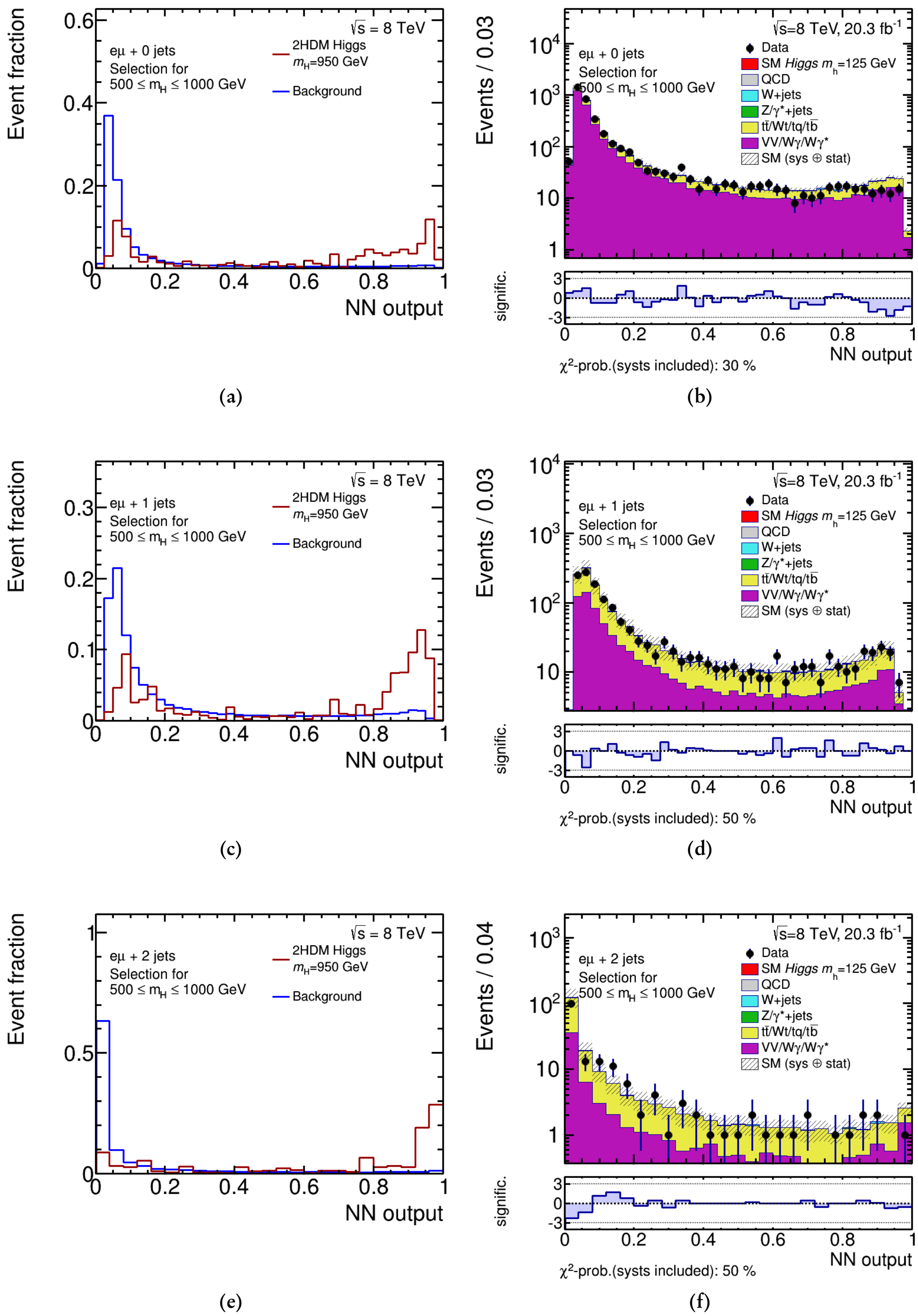

Figure B.10: NN-output distributions, normalised to unit area (left column) and normalised to fit values from Table 7.3 (right column), for $m_H = 950$ GeV. Figures (a) and (b) show the distribution of the 0-jet channel, (c) and (d) of the 1-jet channel and (e) and (f) of the 2-jet channel. The red curve shows the 2HDM signal with $m_H = 950$ GeV, $\tan\beta = 1$ and $\alpha = \pi$ and the blue curve shows the sum of all background processes.

Erklärung

Hiermit erkläre ich nach § 7, Absatz (2) der Promotionsordnung des Fachbereich C der Bergischen Universität Wuppertal vom 18. Februar 2008, dass ich die vorliegende Arbeit selbstständig verfasst und keine anderen als die angegebenen Quellen und Hilfsmittel verwendet, sowie alle wörtlich oder inhaltlich übernommene Stellen als solche gekennzeichnet habe und dass die Dissertation in der gegenwärtigen oder einer anderen Fassung keinem anderen Fachbereich einer wissenschaftlichen Hochschule vorliegt.

Wuppertal, 2. Oktober 2015

(Gunar Ernis)

Danksagung

Mein besonderer Dank gilt in erster Linie Prof. Dr. Wolfgang Wagner, der mir Gelegenheit gab die vorliegende Arbeit zu schreiben und mich in den letzten Jahren dabei sehr gut betreut hat. Dein Interesse und die stetige Unterstützung haben sehr zum Gelingen dieser Arbeit beigetragen. Ich möchte mich außerdem für die verschiedenen Aufenthalte am CERN, die Möglichkeit an Konferenzen teilzunehmen und Vorträge zu halten und den Besuch der CERN School of Computing bedanken. Diese einmaligen Erfahrungen werde ich sicher nicht vergessen.

Weiterhin gilt mein Dank Dr. Dominic Hirschbühl, der mir nicht nur treffsicher die richtigen Fragen gestellt hat sondern auch zu jeder Tages- und Nachtzeit bereit war auf meine Fragen zu antworten und behilflich zu sein. Außerdem konnte ich durch deine Anregungen und Korrekturen dieser Arbeit den letzten Schliff verleihen.

I would like to thank Dr. Corinne Mills for being second referee of the thesis and for her support of the analysis during her convenorship (and beyond) of the HSG3 in ATLAS. Thank you for your interest and your questions regarding the analysis, they helped a lot to understand and eliminate problems.

Meinen Korrekturlesern Dr. Ofir Gabison, Dr. Frank Ellinghaus, Julia Fischer und Frank Volkmer gebührt auch ein großes Dankeschön. Ihr habt mir nicht nur über meine Betriebsblindheit hinweg geholfen und die Arbeit dadurch (hoffentlich) verständlicher gemacht, sondern mich auch von den kleinen (und großen) Fehlern befreit, die sich bei so einem langen Text zwangsweise einschleichen. Alle verbleibenden Fehler gehen selbstverständlich auf mein Konto!

Meinen Mitstreitern auf dem Weg zu akademischem Ruhm – Julia Fischer und Frank Volkmer – danke ich für die Hilfe bei (physikalischen) Problemen und die bisweilen etwas ausartende Abendgestaltung

Meiner Frau Anja danke ich von ganzem Herzen für ihre Unterstützung in jeder Lebenslage. Danke, dass du darauf geachtet hast dass ich den Kopf auch mal frei bekomme.

Zu guter Letzt möchte ich mich herzlich bei meinen Eltern bedanken. Ohne euch und eure großartige Unterstützung wäre mein Studium, geschweige denn eine Doktorarbeit, niemals möglich gewesen.